Czech Technical University in Prague
Faculty of Nuclear Sciences and Physical Engineering
Department of Physical Electronics

Degree Programme: Applied natural sciences
Field of Study: Physical Engeneering

Ph.D. THESIS

Laser Ion Acceleration: Theory and Simulation

Laserové urychlování iontů: teorie a simulace

Author:	Ing. Martina Greplová Žáková
Supervisor:	doc. Ing. Jan Pšikal, Ph.D.
Supervisor specialist:	doc. Ing. Ondřej Klimo, Ph.D.
Supervisor specialist:	Dr. Daniele Margarone
Submitted in:	September 2021

Prohlášení

Prohlašuji, že jsem svou doktorskou práci vypracovala samostatně a použila jsem pouze uvedené podklady.

Nemám závažný důvod proti použití tohoto školního díla ve smyslu § 60 Zákona č. 121/200 Sb., o právu autorském, o právech souvisejících s právem autorským a o změně některých zákonů (autorský zákon).

V Praze dne ....

Ing. Martina Greplová Žáková

Bibliografický záznam	
Autorka	Ing. Martina Greplová Žáková, České vysoké učení technické v Praze, Fakulta jaderná a fyzikálně inženýrská, Katedra fyzikální elektroniky Centrum ELI Beamlines, Fyzikální ústav Akademie věd České republiky
Název práce	Laserové urychlování iontů: teorie a simulace
Studijní program	Aplikace přírodních věd
Studijní obor	Fyzikální inženýrství
Školitel	doc. Ing. Jan Pšikal, Ph.D., České vysoké učení technické v Praze, Fakulta jaderná a fyzikálně inženýrská, Katedra fyzikální elektroniky Centrum ELI Beamlines, Fyzikální ústav Akademie věd České republiky
Školitel specialista	doc. Ing. Ondřej Klimo, Ph.D., České vysoké učení technické v Praze, Fakulta jaderná a fyzikálně inženýrská, Katedra fyzikální elektroniky Centrum ELI Beamlines, Fyzikální ústav Akademie věd České republiky
Školitel specialista	Dr. Daniele Margarone, Centrum ELI Beamlines, Fyzikální ústav Akademie věd České republiky Centre for Plasma Physics, School of Mathematics and Physics Queen's University Belfast
Akademický rok	2021
Počet stran	186
Klíčová slova	divergence protonového svazku, laserem řízené iontové svazky, Particle-in-cell simulace, magnetické multipóly, prostorový design terčů, předplasma

Bibliographic Entry	
Author	Ing. Martina Greplová Žáková, Czech Technical University in Prague, Faculty of Nuclear Sciences and Physical Engineering, Department of Physical Electronics ELI Beamlines Centre, Institute of Physics, Czech Academy of Sciences
Title of Dissertation	Laser Ion Acceleration: Theory and Simulation
Degree Programme	Applied natural sciences
Field of Study	Physical Engeneering
Supervisor	doc. Ing. Jan Pšikal, Ph.D., Czech Technical University in Prague, Faculty of Nuclear Sciences and Physical Engineering, Department of Physical Electronics ELI Beamlines Centre, Institute of Physics, Czech Academy of Sciences
Supervisor specialist	doc. Ing. Ondřej Klimo, Ph.D., Czech Technical University in Prague, Faculty of Nuclear Sciences and Physical Engineering, Department of Physical Electronics ELI Beamlines Centre, Institute of Physics, Czech Academy of Sciences
Supervisor specialist	Dr. Daniele Margarone, ELI Beamlines Centre, Institute of Physics, Czech Academy of Sciences Centre for Plasma Physics, School of Mathematics and Physics Queen's University Belfast
Academic Year	2021
Number of Pages	186
Keywords	proton beam divergence, laser-driven ion beams, Particle-in-cell simulations, magnetic multipoles, advanced target designs, preplasma

Abstrakt
Laserem řízené iontové svazky se staly slibným zdrojem pro řadu budoucích aplikací se značným socio-ekonomickým dopadem. Tyto sekundární zdroje byly hojně studovány různými přístupy, například numerickými simulacemi, které poskytují cenný vhled do mechanismů urychlování a do kýžené modulace parametrů iontového svazku. V dizertační práci jsou prezentovány dvou a tří-dimenzionální Particle-in-cell (PIC) simulace implementující interakci vysoce-intenzivních femtosekundových laserových impulsů s designově pokročilými terči (konkrétně s rovnými či prohnutými fóliemi na jejichž zadní straně je připevněn kanál různého tvaru). Hlavním cílem je vylepšit parametry protonového svazku pomocí tvarovaní terčů, především úhlovou divergenci a prostorovou uniformitu svazku, a to ideálně bez žádného významného poklesu maximální energie částic. Detailní studium EM polí odhalilo jednak formování magnetického multipólu (kvadrupól se silnou oktupólovou složkou) a dále také dlouhotrvající transverzální elektrické fokusační pole uvnitř vodícího válce kanálového terče, narozdíl od polí pozorovaných v případě referenční rovné fólie. Tyto jevy byly studovány a porovnány mezi sebou v závislosti na energii částic. Značný důraz byl rovněž kladen na pochopení fyzikálních principů zodpovědných za laserem řízené urychlování iontů z kanálových terčů a relevantních přidružených jevů. Nakonec byl studován efekt předplazmatu, generovaného laserovým předpulsem, na parametry urychlených protonů. To bylo provedeno implementací výstupu 2D Magnetohydrodynamického kódu (simulace efektu laserového předpulsu na terč) do 2D PIC simulace, kde se modelovala interakce hlavního laserového impulsu s terčem obsahujícím předplazma. V práci je dále popsána relevantní teorie týkající se laserem řízeného iontového urychlování, laserového plazmatu, laserových parametrů a vlastností magnetických polí, stejně jako numerické pozadí Particle-in-cell simulací. Diskuze nad experimentální proveditelností i nad budoucími aplikacemi laserem urychlených iontových svazků je rovněž zahrnuta.

Abstract
Laser-driven ion beams have become a promising source in numerous foreseen applications with a high socioeconomic impact. These secondary sources have been widely investigated by various approaches including numerical simulations which provide a valuable insight into acceleration mechanisms and targeted modulations of ion beam features. Two and three dimensional Particle-in-cell (PIC) simulations, implementing the interaction of high-intensity femtosecond laser pulses with advanced target designs (particularly, of flat or curved plastic foils with various channels attached to their rear sides), are presented within this thesis. The main goal is to improve proton beam parameters directly using target shaping, specifically angular divergence and spatial uniformity of the produced beam, optimally accompanied by no significant drop of the maximum energy of particles. A detailed investigation of EM fields revealed the formation of magnetic multipoles, namely a magnetic quadrupole with a strong octupole component, and a long-lasting focusing transverse electric field inside a guiding cylinder of a channel-like target in contrast to a reference flat foil. These features have been studied and compared to each other as a function of proton energy. In addition, a substantial emphasis has been given to the understanding of the physical phenomena behind specific laser-driven proton acceleration from channel-like targets and relevant accompanying features. Eventually, the effect of a preplasma generated by the laser prepulse on accelerated protons has been investigated by implementing the output from a 2D Magnetohydrodynamic code (i.e., simulating the target response to the laser prepulse) into 2D PIC, where simulation of the main pulse interaction with the preplasma target has been performed. The relevant theory of laser-driven ion acceleration, laser plasmas, laser parameters, magnetic field features as well as numerical Particle-in-cell simulations are included. Moreover, the discussion of experimental feasibility and various foreseen applications of laser-driven ion beams is provided.

Contents

Acknowledgements

I would like to express my gratitude to my supervisor, doc. Ing. Jan Pšikal, Ph.D., for his patience, fruitful discussions, advice and for his help in general, which he provided during the writing of this thesis. I would like to also thank my supervisors specialists; particularly to doc. Ondřej Klimo, Ph.D. for his expert advice; and especially to Dr. Daniele Margarone, PhD. for providing experimental insight, kind comments, support, willingness and friendly approach during my employment at the ELI Beamlines project. Furthermore, my deep thanks definitely belong to Dr. Francesco Schillaci, who gave me the initial and crucial impulse to move my dissertation in the right direction and supported me on that way. Also, I would like to thank the scientific team of *Department of Ion Acceleration and Applications of High Energy Particles* I belong in, my past university lecturers and, in particular, to my colleague Ing. Jiří Vyskočil, Ph.D., who I met my first day at ELI and I am grateful I have him in my life for the whole time also as a friend. Last, but not least, I would like to deeply appreciate the support of my loving family, incredible friends and my great husband, who meets and exceeds the definition of both.

Introduction

The idea of accelerating protons and ions by a coherent light has gained a huge interest since high-intensity pulsed lasers were developed and ever since continuously attracts attention, because of its implications in basic research. Scientists investigate the interaction of relativistic laser pulses with matter, which produce extremely high electric and magnetic fields in plasmas resulting in the acceleration of particles on very compact scales. The same laser system may produce not only protons, heavier ions and electrons, but also other radiation such as X-rays, γ-rays or neutrons, which implies an extreme versatility of laser driven sources and their employment in societal applications. Generally, implementing laser-accelerated ion beams opens new possibilities and leads to foreseen applications, for instance, in medicine (e.g. hadrontherapy, proton-boron capture therapy), astrophysics, fast ignition of Inertial Confinement Fusion (ICF) targets, laser triggering and control of nuclear reactions, production and probing of warm dense matter, material science [1], [2], or non-destructive methods applied in heritage testing [3], [4], [5] and possibly also in botanical, environmental or forensic sciences. With the continuous development of laser technologies, facilities delivering femtosecond pulses of ultra-high peak power of several PWs are being commissioned or are already operational, such as ELI Beamlines in the Czech Republic, part of the Extreme Light Infrastructure project. Similar laser installations will enable the acceleration of ions to energy levels of several hundreds MeV per nucleon [6], possibly leading to many appealing applications with a high socio-economic impact.

Since various applications generally require different beam parameters, the control and the adjustment of beam features are fundamental in order to, for example, achieve particular maximum energy, improve spatial uniformity and homogeneity of the produced beam, decrease its divergence, make the spectrum monoenergetic-like or increase the number of particles per bunch, i.e., the total charge. Therefore, various improvements may be optimal for each specific application even though the remaining parameters indicate worse values. Of course, experimental shot-to-shot stability, reproducibility and a precise characterization of the produced particle beam are essential.

This thesis aims for an innovative design of overdense targets, which would lead to the improvement of ion beams accelerated from the interaction with ultra-intense, femtosecond laser pulses with PW power. Specifically, the efforts are primarily focused on the reduction of angular spread and on the improvement of spatial uniformity of the protons without any significant lowering of maximum energies, or other important parameters.

Generally, the dissertation is divided into five numbered chapters containing the theory of laser-driven ion acceleration, related plasmas and laser phenomena, a numerical description of the method, i.e., Particle-in-cell simulations, a brief introduction into possible applications and, of course, the largest part, which refers to performed simulations of advanced targets, achieved results and a discussion about the manufacturability of such targets and possible

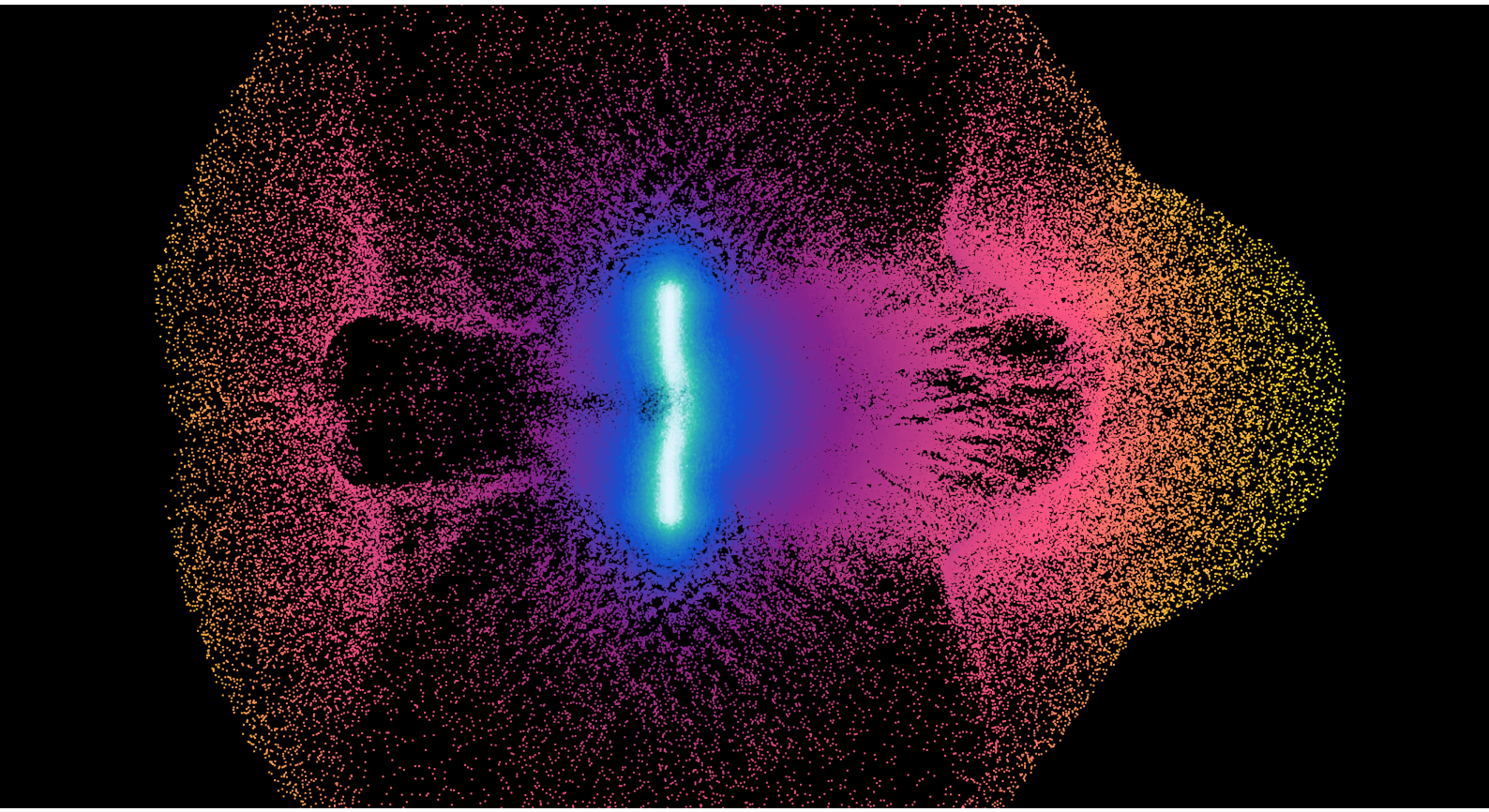

Figure 1: Artistic visualization of laser-driven proton acceleration from a flat plastic target using L3 HAPLS laser parameters [7], [8] (ELI Beamlines). Because the energetic spectrum of accelerated protons is broad, various proton energies are depicted by different colors; the warmer the color, the higher the energy. Data originates from Particle-in-cell simulation of the author; visualization created by Mariana Kecová.

utilization in experiments.
In particular, the first chapter summarizes the theoretical background related to the physics of laser-driven ion acceleration, mainly, to accelerating mechanisms and the role of hot electron population. The list of discussed accelerating scenarios includes regimes relevant for high laser intensities, i.e., $\approx 10^{18} - 10^{23}$ W/cm^2, which are suitable, but not restricted to, femtosecond laser pulses being employed in the following simulations reported in the practical part 4. Particularly, Target Normal Sheath Acceleration, Radiation Pressure Acceleration (including both Light Sail and Hole Boring scenarios), Break-Out Afterburner, Magnetic Vortex Acceleration, Collisionless Shock Acceleration and (Direct) Coulomb Explosion mechanisms are discussed. In the majority of these regimes, the hot electron population plays a significant role, which is the reason why the explanation of both electron heating mechanisms at the critical surface and their transport and recirculation through the target is provided in subchapter 1.3. Furthermore, the overview of often used terms (e.g. relativistic transparency, ponderomotive force) and basic definitions of various plasma parameters are provided at the beginning of the chapter in order to prevent any confusion, which may arise from the text when the terms are not properly understood.

The second chapter presents the additional phenomena which is important in order to support and to explain particular results obtained from Particle-in-cell simulations. Physics related to the laser pulse itself and to the magnetic field generation is also provided. The former topic includes a description of a realistic laser pulse profile causing the generation of a preplasma, especially on the target front side, and of consequent relativistic self-focusing of the laser pulse in such an ionized expanded material. Furthermore, the expected preplasma impacts on laser-driven ion beam parameters are discussed. The latter part deals with magnetic field generation in laser-plasmas and with the characterization of multipole magnetic field, typically produced by complex (permanent or electro-) magnets being used, for instance, in accelerator beamlines. In fact, this section is provided in order to demonstrate strong similarities with magnetic field formation which has been observed in presented simulations of laser-driven ion acceleration reported in chapter 4.
The third chapter refers to the simulation method of Particle-in-cell (PIC), being a main tool for studied phenomena. Besides a standard description of numerical approach, particular computational steps, advantages and possible instabilities, also a guide to estimate the requested number of cluster nodes is provided. Eventually, the subchapter presenting a topic of a joint simulation between PIC and Magnetohydrodynamic (MHD) codes, which has been employed for the investigation of effects of a laser prepulse on ion beam parameters, is introduced.
The most extensive fourth chapter presents the results of 2D and 3D PIC simulations performed in EPOCH code [9]. The analysis was done in MATLAB, unless explicitly stated otherwise. A primarily presented parametric 2D study implements advanced plastic target designs consisting of a flat or a curved foil and of various channels attached to their rear sides. These targets have been compared to a single flat foil from the point of view of various parameter improvements in the produced ion beam. As a result, a significant divergence reduction accompanied with no major energy or particle number lowering has been demonstrated for the straight channel target which was also consequently simulated in 3D. Three dimensional geometry allows a deep investigation of the favorable establishment of an electromagnetic (EM) field inside the guiding cylinder in comparison with the reference flat foil. In particular, the differences between generated fields are affected by variations in electron motion. Moreover, the magnetic field shows evident similarities to multipole magnets and contributes to both divergence lowering and improving spatial uniformity of the particle beam. This phenomenon was described in laser-target interaction for the first time according to the author's best knowledge. The effect was studied with dependence on particle energy and the process of acceleration has been investigated from multiple perspectives. In particular, the following interesting features have been, for example, explored: (i) electric and magnetic field inversions, (ii) the influence of the direction of linear laser polarization and (iii) the effect of the shape of electric sheath field in transverse direction on particle beam parameters. Finally, in order to investigate the effect of a realistic laser pulse, the optimal channel target design with a preplasma on its front side has been simulated in 2D PIC. The preplasma density input was taken from the output of 2D MHD simulation performing the target interaction with a laser prepulse. Therefore, the important comparison between an ideal and a realistic laser contrast ratios is provided. The chapter ends with the discussion on manufacturing possibilities of suggested target designs and on possible effects of implementing different laser parameters than those, which have been used for the study presented here.
The fifth chapter provides a short insight into future applications of improved laser-driven ion beams. Particularly, three applications, in which the author of this thesis has been partially

involved in, are discussed deeper: Laser-driven hadrontherapy, Proton pulsed radiolysis of water and Non-destructive heritage testing.
The thesis ends with a brief Summary of the main results and Conclusions, Bibliography section and a List of author's publications and granted projects.

Chapter 1

Theoretical background of laser ion acceleration

Over the past years, various mechanisms of laser-driven particle acceleration have been studied theoretically, numerically and experimentally. In order to provide optimal interaction conditions of a specific regime, parameters of both laser pulses and targets (i.e., their shape & material) are being improved correspondingly. With the recent advent of short pulse petawatt class lasers and ultra-high field intensities, it is foreseen that many of theoretical/numerical predictions would be confirmed also experimentally. Specifically, a 10 PW peaked-power laser system ATON (10 PW, 150 fs, 1.5 kJ, 1 shot per minute) [10] is currently under commissioning at ELI Beamlines. Nevertheless, the most important lasers for the scope of this dissertation are 1 PW, short pulse, high repetition rate systems such as HAPLS (30 fs, 30 J, 10 Hz) [7], [8] at ELI Beamlines, GEMINI laser (15 J, 30 fs,) at RAL, VEGA-3 (30 fs, 30 J, 1 Hz) at CLPU or J-KAREN-P (30 fs, 30 J, 0.1 Hz) [11] at QST and others.

1.1 Overview of the most important terms and plasma parameters

The aim of this work is to study and deeply understand the processes present during laser-plasma interaction leading to ion acceleration.
Firstly, we should know the basic physical background of plasma, which is a quasi-neutral system of charged or neutral particles which are coupled together by their electric and magnetic fields and show collective behavior. Below a brief table of the most common plasma parameters and terms 1.1.1 – 1.1.9 is presented. Additional subchapters covering, for example, Relativistic Transparency or Ponderomotive force will follow. For a more detailed description, derivation or deeper understanding readers may see [12], [13], [14], [15], [16], [17].

1.1.1 Quasineutrality

If the total charge in a small volume (e.g., in the sphere of the radius at least one Debye length λ_{De} (1.2)) is much lower than both the total charges of all ions or of all electrons, then we call this system *quasineutral*. This condition has more equivalents (for instance, $n_e \approx Zn_i$, $\Delta n \ll n_e$, $\Delta n \ll n_i$, $L \gg \lambda_{De}$, ...), which will be discussed in the following text. In fact,

Variable or term	Notation	Formula	Note
Quasineutrality	–	$n_e \approx Z n_i$ $\tau \gg \omega_{pe}^{-1}$	
Debye length	λ_{De}	$\lambda_{De} = \sqrt{\frac{\varepsilon_0 k_b T_e}{n_e e^2}}$	
Plasma parameter	N_D	$N_D = \frac{4\pi}{3}\lambda_{De}^3 n_e$	ideal plasma: $N_D \gg 1$
Plasma scale length	L	decay formula for a specific parameter e.g. $n_e(r) = n_0 \exp(-r/L)$	quasineutrality conservation: $L \gg \lambda_{De}$
Electron plasma frequency	ω_{pe}	$\omega_{pe} = \sqrt{\frac{e^2 n_e}{\varepsilon_0 m_e}}$	often ω_p notation is used, i.e., $\omega_p \equiv \omega_{pe}$
Ion plasma frequency	ω_{pi}	$\omega_{pi} = \sqrt{\frac{Z m_e}{m_i}}\omega_{pe}$	
Critical density	n_c	$n_c = \frac{\varepsilon_0 m_e}{e^2}\omega^2$	$\omega_p = \omega$
Collision frequency	ν	$\nu_{ei} \simeq \frac{Z^2 e^4 n_i \ln\Lambda}{m_e^2 v_e^3}$ $\nu_{ee} = \nu_{ei}/Z$	assumption: $v_e \gg v_{Te}$
Thermal velocity of electron	v_{Te}	$v_{Te} = \sqrt{\frac{k_B T_e}{m_e}}$	
Collective behavior	–	$\omega_{pe} > \nu_c$	
Skin depth	l_s	$l_s = \frac{c}{\omega_p}\left(1 - \frac{\omega^2}{\omega_p^2}\cos^2\theta\right)^{-1/2}$	$l_s \approx \frac{c}{\omega_p}$ for $\frac{n_e}{n_c} \gg 1$
Dimensionless laser amplitude	a_0	$a_0 = eE/m_e c\omega$	

Table 1.1: Plasma parameters and terms; e – electron charge, Z – ion charge state, n_e/ n_i – electron/ion density, n_0 – initial electron density, ε_0 – vacuum permittivity, m_e/m_i – mass of electron/ ion, τ – characteristic time, ω – laser frequency, E – laser electric field, k_b – Boltzmann constant, c – speed of light, ν – collision frequency (ν_{ee} electron-electron and ν_{ei} electron-ion), T_e – electron temperature, v_e – electron speed, $\ln\Lambda$ – Coulomb logarithm, θ – laser angle of incidence.

quasineutrality is not assumed for very fast phenomena, where charges are separated only for a very short moment and the situation changes quickly. Therefore, if the assumption of quasineutrality is needed, the plasma characteristic time τ has to be much larger than the laser period, i.e., $\tau \gg \omega_{pe}^{-1}$, where ω_{pe} is the electron plasma frequency (1.7).

1.1.2 Debye length

Debye length is the scale over which mobile charge carriers screen out the external electric fields in plasmas and other conductors. In other words, it is the length over which the field contribution of a single charge is shielded by the surrounding electrons [18] or equivalently, the length over which the electric potential $\varphi(r)$ decreases in magnitude by $1/e$ [13].
Charges can be spontaneously separated only at a distance allowed by their thermal energy, i.e., the distance, where all the heat energy changes into the potential one. Taking Δ as the thickness of electron layer moving from ion background, the potential energy of an electron

is equal to its thermal energy, when it moves over a single Δ [16], [17]:

$$U_{pot} = -eE\Delta = \frac{e^2 n_e \Delta^2}{\varepsilon_0} = k_B T_e, \tag{1.1}$$

then, the electron Debye length λ_{De} is given by:

$$\lambda_{De} \equiv \Delta = \sqrt{\frac{\varepsilon_0 k_b T_e}{n_e e^2}}, \qquad \varphi(r) = \frac{Ze}{r} \exp(\frac{-r}{\lambda_{De}}), \tag{1.2}$$

where e, n_e, T_e are the electron charge, density and temperature, respectively; Z is the charge number, ε_0 denotes vacuum permittivity and k_b is Boltzmann constant. Although Debye length can be defined for ion component as well, the mobility of ions is usually negligible compared to the process's timescale, therefore this part is often neglected.
The so-called Debye sphere is the sphere having a diameter equal to Debye length. The number of particles N_D confined inside this volume is important, for example, in order to decide whether the plasma is *ideal* (i.e., $N_D \gg 1$) or not:

$$N_D = \frac{4\pi}{3} \lambda_{De}^3 n_e. \tag{1.3}$$

1.1.3 Plasma scale length

Scale lengths are generally distances over which a quantity of a specific parameter decreases by a factor of e (Euler's number). Plasma scale lengths, usually noted only as L, are defined in correspondence to various plasma parameters (e.g. density, electric potential, temperature). For example, plasma density scale length L (the word *density* is usually omitted) is defined with decay formula [19], [20], for example:

$$n(r) = n_0 \exp(-r/L), \tag{1.4}$$

where n is distance-varying density and n_0 is the constant, for instance, in the case of pre-plasma, the initial density of homogeneous non-expanded target. In fact, the density plasma scale length can be defined also as the length over which the density deviations between electron and ion components $\Delta n = |n_e - n_i|$ are acceptable in terms of overall quasineutrality:

$$\frac{\Delta n}{n} \approx \left(\frac{\lambda_{De}}{L}\right)^2. \tag{1.5}$$

The condition of quasineutrality may be formulated as $\Delta n \ll n_e$ or as $\Delta n \ll n_i$ (i.e., $n_e \approx Z n_i$), hence, according to (1.5), it is equivalent to $L \gg \lambda_{De}$. In other words, plasma quasineutrality is defined only on a much larger scale than Debye length λ_{De}. That is also one of the plasma scale lengths, but related to electric potential. If we treat plasma on a smaller scale than λ_{De}, we may find deviations from neutrality increasing with the decreasing scale [21].
Plasma scale length is often defined also as a ratio between the value and its gradient, for instance, $L_{n_e} = n_e/|\nabla n_e|$ or $L_{T_e} = T_e/|\nabla T_e|$ in the case of electron density or temperature, respectively [12].

1.1.4 Plasma frequency

Electron plasma frequency ω_{pe} could be derived from the equation of electron motion and from the differential equation for linear harmonic oscillator [16]:

$$v = \frac{\mathrm{d}\Delta}{\mathrm{d}t} \quad \Rightarrow \quad m_e \frac{\mathrm{d}v}{\mathrm{d}t} = -eE = -e\frac{\sigma}{\varepsilon_0} = -\frac{e^2 n_e \Delta}{\varepsilon_0} \quad \Rightarrow \quad \frac{\mathrm{d}^2\Delta}{\mathrm{d}t^2} + \frac{e^2 n_e}{\varepsilon_0 m_e}\Delta = 0, \tag{1.6}$$

$$\omega_{pe} = \sqrt{\frac{e^2 n_e}{\varepsilon_0 m_e}}, \tag{1.7}$$

where n_e, m_e are the electron density and mass, respectively, and σ is the charge per unit area bounded with electric field E in plasma as $E = \sigma/\varepsilon_0$, where ε_0 is vacuum permittivity. Ion plasma frequency ω_{pi} is defined analogically:

$$\omega_{pi} = \sqrt{\frac{n_i Z^2 e^2}{m_i \varepsilon_0}} = \sqrt{\frac{Z m_e}{m_i}}\omega_{pe}, \tag{1.8}$$

where Z is the ion charge state and m_i, n_i are the ion mass and density, respectively.

1.1.5 Critical Density

In order to distinguish opaque and transparent plasma regions for the incident laser light, the relation between the angular frequency ω of the interacting laser pulse and the plasma frequency ω_p of the target is crucial. The so-called *critical density* n_c denotes the boundary between underdense and overdense plasma for the given laser parameters and it can be derived from the equality between ω and ω_p:

$$\omega = \omega_p \quad \Rightarrow \quad \omega^2 = \frac{e^2 n_c}{\varepsilon_0 m_e},$$

$$n_c = \frac{\varepsilon_0 m_e}{e^2}\omega^2 = \frac{(2\pi)^2 \varepsilon_0 m_e c^2}{\lambda^2 e^2}. \tag{1.9}$$

In other words, the value of critical density n_c differs depending on the laser wavelength λ. Electromagnetic (EM) waves with frequency higher than plasma frequency ω_p interact with underdense plasmas conductively in contrast to EM waves with frequency lower than ω_p which assign dielectric behavior with overdense plasmas (the inertia of electrons retards their response). As a result, the underdense plasma is rather transparent to the radiation [17], [18].

1.1.6 Collision frequency

When the plasma temperature is not relativistic, the thermal equilibrium is ensured mainly by particle collisions. Therefore, it is useful to introduce the collision frequencies which are expressed by the rate of the momentum transfer between particles. Assuming the scattering at small angles (i.e., lower than 90°) and that the electron velocity is higher than the thermal

velocity, i.e., $v_e \gg v_{Te}$, the relations for electron-ion ν_{ei} and electron-electron ν_{ee} collision frequencies are following [12], [18]:

$$\nu_{ei} \simeq \frac{Z^2 e^4 n_i \ln\Lambda}{m_e^2 v_e^3}, \tag{1.10}$$

$$\nu_{ee} = \nu_{ei}/Z, \tag{1.11}$$

where v_e, m_e is the electron velocity and mass, Z is the charge state of ions, $\ln\Lambda$ (where $\Lambda \propto N_D$) is Coulomb logarithm and n_i is the ion density. For example, the typical values of dimensionless Coulomb logarithm for laser plasmas (femtosecond interactions) ranging between $1 - 10$ [22], [23]. In the case of very fast particles, the collision frequency (generally noted as ν) decreases rapidly with the increasing electron velocity as:

$$\nu \sim v_e^{-3}, \tag{1.12}$$

therefore, in the means of electron temperature T_e:

$$\nu \sim T_e^{-2/3}. \tag{1.13}$$

Hence, for the relativistic-speed particles we can work under the approximation of *collisionless plasma* as in the case of the simulations presented within this work.

1.1.7 Macroscopic parameters, Maxwell distribution function

Plasma is usually described by macroscopic parameters (typically electron and ion densities n_e, n_i and their temperatures T_e, T_i, respectively) which can be specified in thermodynamic equilibrium only. In fact, the particle temperature can be defined via the Maxwellian distribution function in kinetic energy $f(\varepsilon_{kin})$ [18]:

$$f(\varepsilon_{kin}) = \frac{2}{\sqrt{\pi}(k_B T)^{3/2}} \sqrt{\varepsilon_{kin}} \exp\left(-\frac{\varepsilon_{kin}}{k_B T}\right), \tag{1.14}$$

where T may be the temperature of electrons or ions and ε_{kin} their kinetic energy, which can be also expressed by equipartition theorem. Therefore, the relation, e.g., for the mean thermal velocity v_{Te} of electrons moving in one direction only is:

$$\varepsilon_{kin} = \frac{1}{2} m_e v_{Te}^2 = \frac{1}{2} k_b T_e \quad \Rightarrow \quad v_{Te} = \sqrt{\frac{k_B T_e}{m_e}}, \tag{1.15}$$

where k_B is Boltzmann constant and m_e is the electron mass.

1.1.8 Collective behavior

Each plasma particle interacts with a large number of other particles in contrast to a neutral gas. To clarify, particles in a neutral gas can interact only in terms of binary collisions with the typical distance r^{-6} (Van der Waals force). On the other hand plasma particles feel the long-range Coulomb field on typical distance r^{-2} which results in a much higher number of interaction events. Therefore, plasmas show a simultaneous response of many particles to an external stimulus. The term collective behavior denotes the interaction of a particle by macroscopic electromagnetic fields (i.e., long-range fields) rather than by microscopic ones (i.e., short-term fields, such as in a binary collision). A collective action is then characterized by the electron plasma frequency ω_{pe} which is stronger than the binary operation characterized by the collision frequency ν_c, i.e., $\omega_{pe} > \nu_c$ [16], [17], [24].

1.1.9 Skin depth

The decay length of EM fields in the overdense plasma region is called collisionless skin depth and it is defined as [12]:

$$l_s = \frac{c}{\omega_p}\left(1 - \frac{\omega^2}{\omega_p^2}\cos^2\theta\right)^{-1/2}, \tag{1.16}$$

$$l_s \approx \frac{c}{\omega_p} \qquad \text{for} \qquad \frac{n_e}{n_c} \gg 1, \tag{1.17}$$

where ω is the laser frequency, c is the speed of light and θ is the angle of incidence of the laser light; the rest of variables has been already defined elsewhere.

1.1.10 Dimensionless laser amplitude

Dimensionless laser amplitude a_0 is the parameter which is often given in laser-plasma physics instead of the intensity in order to characterize the laser pulse:

$$a_0 = \frac{eE}{m_e c\omega}, \tag{1.18}$$

where e, m_e, c are the elemental charge, the electron mass, the speed of light and E, ω are the laser electric field and the laser frequency, respectively. Moreover, dimensionless laser amplitude is bounded with the intensity of the laser pulse I by following relation, which varies depending on the laser polarization [25], [26]:

$$I = 1.37 \cdot \kappa \cdot \left(\frac{a_0}{\lambda[\mu\text{m}]}\right)^2 \cdot 10^{18} \quad [\text{W/cm}^2], \tag{1.19}$$

where κ is the parameters distinguishing between linear ($\kappa = 1$) and circular ($\kappa = 2$) polarization of the laser wave.

1.1.11 Relativistic Transparency (RT)

When a laser pulse interacts with an overdense target, the light is initially reflected from the plasma surface, because the electron plasma density n_e is higher than the critical density n_c, i.e., $n_e > n_c$. Nevertheless, the interaction continues and electrons are accelerated in a laser wave nearly to the speed of light, which leads to the relativistic increase of their rest mass m_{e0} by Lorentz factor γ, i.e., $m_e = \gamma m_{e0} = \frac{1}{\sqrt{1-v^2/c^2}} m_{e0}$. Lorentz factor can be evaluated also in terms of the laser pulse equivalently. Specifically, for linear polarization $\gamma_L = \sqrt{1 + a_0^2/2}$ and $\gamma_C = \sqrt{1 + a_0^2}$ for circular polarization [18]. Therefore, the effective electron density is changed correspondingly to the value n_e/γ and the plasma refractive index η is corrected to the value $\eta = \sqrt{1 - n_e/(\gamma n_c)}$. Simultaneously, the target is expanding, which further decreases its electron density n_e. As a consequence, laser pulse can penetrate deeper into the target, i.e., up to the point where effective electron density reaches the value of $n_c\gamma$. This phenomenon is called *relativistic transparency* (see Fig. 1.1) and it is crucial for understanding of accelerating mechanisms using high intensities, e.g. of Break-Out Afterburner regime. In fact, RT is the phenomenon which allows the laser pulse propagate through otherwise opaque

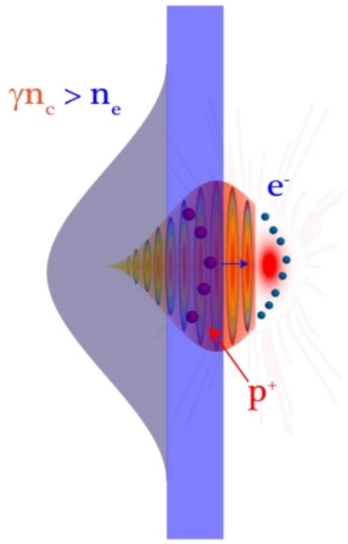

Figure 1.1: Schematic representation of Relativistic transparency phenomenon during the laser-target interaction [28].

overdense plasma [27].
As a demonstrating example of RT dynamics, the evolution of normalized plasma density ($n_e/(\gamma n_c)$) and heating of electrons during the interaction (represented by Lorentz factor γ) is shown in Fig. 1.2. The results comes from the 2D PIC simulation of the interaction of 200 TW laser pulse having intensity $I = 2 \cdot 10^{20}$ W/cm^2 and the FWHM duration of 650 fs (corresponding to TRIDENT laser system at Los Alamos National Laboratory) with a 100 nm thin carbon foil. There are two important lines in the figure which characterize induced RT during the interaction with the laser pulse. Firstly, the effective normalized plasma density ($n_e/\gamma n_c$; light blue curve), and secondly, its Lorentz gamma factor (γ; green curve). Classically underdense plasma meets the condition $n_e/n_c < 1$ (i.e., corresponding to $\gamma \cdot n_e/\gamma n_c < 1$ in the figure), whilst classically overdense plasma fulfills $n_e/n_c > 1$ (i.e., corresponding to $\gamma \cdot n_e/\gamma n_c > 1$ in the figure). Taking the relativistic effects into account, the conditions for induced RT are:

$$\left(\gamma \cdot \frac{n_e}{\gamma n_c} > 1\right) \quad \wedge \quad \left(\frac{n_e}{\gamma n_c} \approx 1 \quad \vee \quad \frac{n_e}{\gamma n_c} < 1\right), \tag{1.20}$$

which corresponds to the interval $\langle t_1, t_2 \rangle$ in Fig. 1.2 ($n_e/n_c = 1$ at both t_1 and t_2). The interval $\langle 0, t_0 \rangle$ stands for classically overdense plasma and the interval $\langle t_2, \infty \rangle$ for classically underdense. At the time t_0, only the first slab of the target becomes relativistically transparent. In fact, the process of RT takes just a tenth of a picosecond and its dynamics is studied in [27] both experimentally and numerically.
The commonly presented field-amplitude threshold a_{th}^{homo} of RT is derived from a traveling-wave approach and it is valid for homogeneous plasma only [29], [30]:

$$a_{th}^{homo} = \sqrt{n_\omega^2 - 1}, \tag{1.21}$$

where n_ω is a critical parameter defined as $n_\omega = \omega_p^2/\omega^2 = n_e/n_c$.
Nevertheless, it was shown that if the plasma is non-uniform, the threshold of relativistic

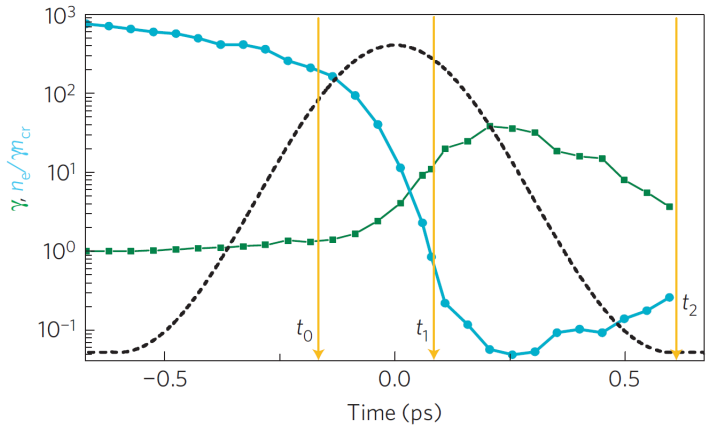

Figure 1.2: Evolution of plasma density and Lorentz gamma factor leading to Relativistic transparency phenomenon. The peak value of the on-axis effective normalized plasma density ($n_e/\gamma n_c$; light blue curve), and its Lorentz gamma factor (γ; green curve) taken from 2D PIC simulations (represented by dots) for the Trident-like laser pulse (black dashed line) interacting with a 100 nm thin carbon foil, [27].

induced transparency by circularly polarized laser pulses is essentially modified due to the ponderomotive force acting on electrons. In fact, PF pushes the electrons further into the plasma which steepens the electron density profile resulting in the shorter laser penetration distance and correspondingly higher threshold a_{th} [31]:

$$a_{th} = \frac{1}{2}\left[\frac{2}{3}(1+a_d^2)(2a_d^2 - n_\omega) - a_d^4\right]^{1/2}, \qquad a_{th}^2 \simeq \frac{27}{64} n_\omega^4, \tag{1.22}$$

where a_d is the field amplitude at the point where the electron density vanishes. For instance, in the case of the plasma having $n_\omega = 10$, the threshold of the laser penetration is more than forty times higher than that defined for homogeneous plasma [31]; see Fig. 1.3 where the comparison of the RT threshold amplitudes for homogeneous and non-uniform plasma as functions of the critical parameter n_ω are shown.

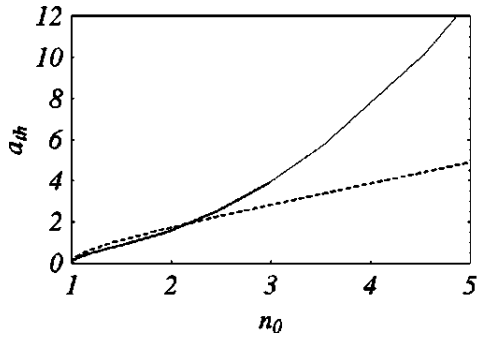

Figure 1.3: Maximum incident amplitude as a function of the critical parameter $n_0 \equiv n_\omega = \omega_p^2/\omega^2 = n_e/n_c$. The continuous line represents the threshold relevant for non-uniform plasma a_{th} (the relation (1.22)), whilst the dashed line for homogeneous plasma a_{th}^{homo} (the relation (1.21)) [27].

1.1.12 Ponderomotive force (PF)

The so-called Ponderomotive force (PF) is a low-frequency non-linear force that acts on charged particles in a non-homogeneous high-frequency EM field. This force is involved in a number of physical phenomena bounded with laser-driven proton/ion acceleration [13]:

- momentum transfer to the target [32], [33], [34],
- self-focusing and filamentation [35],
- changes of plasma density profiles, e.g. formation of solitons and cavitons [36], [37], [38],
- magnetic field generation [39], [40], [41], [42], see the section Magnetic field generation, mainly parts 2.3.1.2 and 2.3.2.1,
- parametric instabilities [43],
- second-harmonic (HHG) generation [44] and others.

The ponderomotive force is related to the gradient of the radiation pressure P_L of an interacting laser pulse with plasma. If the plasma is homogeneous, the value of P_L is dependent on the irradiance I_L and on the laser reflection R from the sharp boundary of the target [13]:

$$P_L = \frac{I_L}{c}(1+R). \tag{1.23}$$

In the case of inhomogeneous plasma, the situation is not such simple and the detailed knowledge of the electromagnetic fields is needed in order to calculate the radiation pressure properly.
Ponderomotive force can be derived for a single particle in EM field [13]. Let's assume that the field is monochromatic and that the plasma has magnetic permeability $\mu = 1$, i.e., $\vec{B} = \mu\vec{H} = \vec{H}$. Then, with the use of Maxwell's equations (in c.g.s units), $\vec{E}$ and $\vec{B}$ fields satisfy:

$$\vec{E}(\vec{r},t) = \vec{E}_s(\vec{r})\cos\omega t, \tag{1.24}$$

$$\vec{B}(\vec{r},t) = \vec{B}_s(\vec{r})\sin\omega t = -\frac{c}{\omega}\nabla\times\vec{E}_s(\vec{r})\sin\omega t. \tag{1.25}$$

The electrons are moving in EM field according to Lorentz equation:

$$F = m_e\frac{\mathrm{d}\vec{v}}{\mathrm{d}t} = -e\left(\vec{E}_s\cos\omega t + \frac{\vec{v}}{c}\times\vec{B}_s\sin\omega t\right). \tag{1.26}$$

In the case of a non-relativistic electron, the magnetic term in (1.26) is smaller than the electric term and thus it can be neglected in the first order solution ($\vec{v} = \vec{v}_1$, $\vec{r} = \vec{r}_1$). The electron oscillates in the direction of the vector $\vec{E}_s$ with velocity $\vec{v}_1$ according to the following equation:

$$m_e\frac{\mathrm{d}\vec{v}_1}{\mathrm{d}t} + e\vec{E}_s(\vec{r}_0)\cos\omega t = 0, \tag{1.27}$$

$$\vec{v}_1 = \frac{\mathrm{d}\vec{r}_1}{\mathrm{d}t} \quad\rightarrow\quad \vec{v}_1 = -\frac{e\vec{E}_s(\vec{r}_0)\sin\omega t}{m_e\omega}, \qquad \vec{r}_1 = \frac{e\vec{E}_s(\vec{r}_0)\cos\omega t}{m_e\omega}. \tag{1.28}$$

Since the ponderomotive force is non-linear, the second order solution, including the *perturbations*, is needed:

$$\vec{v} = \vec{v}_1 + \vec{v}_2, \qquad \vec{E}_s = \vec{E}_s(\vec{r}_0) + (\vec{r}_1 \cdot \nabla)\vec{E}_s(\vec{r} = \vec{r}_0), \qquad \vec{B}_s = \vec{B}_s(\vec{r}_0). \tag{1.29}$$

Substituting these second order variables (1.29) into the equation of motion (1.26):

$$m_e \frac{\mathrm{d}(\vec{v}_1 + \vec{v}_2)}{\mathrm{d}t} = -e\left(\vec{E}_s(\vec{r}_0)\cos\omega t + (\vec{r}_1 \cdot \nabla)\vec{E}_s(\vec{r}_0)\cos\omega t + \frac{\vec{v}_1 + \vec{v}_2}{c} \times \vec{B}_s(\vec{r}_0)\sin\omega t\right). \tag{1.30}$$

Taking $\frac{\mathrm{d}\vec{v}_1}{\mathrm{d}t}$ from (1.27) and neglecting all members having a higher order than the second, the following relation for the non-linear force is valid:

$$m_e \frac{\mathrm{d}\vec{v}_2}{\mathrm{d}t} = -e\left[(\vec{r}_1 \cdot \nabla)\vec{E}_s(\vec{r}_0)\cos\omega t + \frac{\vec{v}_1 \times \vec{B}_s(\vec{r}_0)\sin\omega t}{c}\right]. \tag{1.31}$$

By substituting $\vec{r}_1$, $\vec{v}_1$ from (1.27) and $\vec{B}_s(\vec{r}_0)\sin\omega t$ from (1.24) into (1.31) and averaging this equation over time ($\langle\sin^2\omega t\rangle_t = \langle\cos^2\omega t\rangle_t = 1/2$, $\langle\sin\omega t\cos\omega t\rangle_t = 0$), we get the relation for *Ponderomotive force (PF)*:

$$m_e \frac{\mathrm{d}\vec{v}_2}{\mathrm{d}t} = -e\left[\left(\frac{e\vec{E}_s(\vec{r}_0)\cos\omega t}{m_e\omega^2} \cdot \nabla\right)\vec{E}_s(\vec{r}_0)\cos\omega t + \frac{e\vec{E}_s(\vec{r}_0)\sin\omega t}{m_e\omega c} \times \left(\frac{c}{\omega}\nabla \times \vec{E}_s(\vec{r}_0)\sin\omega t\right)\right],$$

$$m_e\left\langle\frac{\mathrm{d}\vec{v}_2}{\mathrm{d}t}\right\rangle_t = -e\left[\left(\frac{e\langle\cos^2\omega t\rangle_t}{m_e\omega^2}\vec{E}_s(\vec{r}_0) \cdot \nabla\right)\vec{E}_s(\vec{r}_0) + \frac{e\langle\sin^2\omega t\rangle_t}{m_e\omega^2}\vec{E}_s(\vec{r}_0) \times \left(\nabla \times \vec{E}_s(\vec{r}_0)\right)\right],$$

$$m_e\left\langle\frac{\mathrm{d}\vec{v}_2}{\mathrm{d}t}\right\rangle_t = -\frac{e^2}{2m_e\omega^2}\left[(\vec{E}_s(\vec{r}_0) \cdot \nabla)\vec{E}_s(\vec{r}_0) + \vec{E}_s(\vec{r}_0) \times \left(\nabla \times \vec{E}_s(\vec{r}_0)\right)\right]. \tag{1.32}$$

As simply visible in (1.32), ponderomotive force can be defined as the sum of two forces. The first term on the right hand side corresponds to the force which results in electron movement along a linear trajectory, whereas the second term corresponds to a general $\vec{E} \times \vec{B}$ force which distorting the ideal linear motion [13].
Moreover, if we use the vector identity [15]:

$$\vec{E}_s \times (\nabla \times \vec{E}_s) = \frac{1}{2}\nabla\vec{E}_s^2 - (\vec{E}_s \cdot \nabla)\vec{E}_s, \tag{1.33}$$

the relation for PF becomes simple:

$$F_{pf} = m_e\left\langle\frac{\mathrm{d}\vec{v}_2}{\mathrm{d}t}\right\rangle = -\frac{e^2}{4m_e\omega^2}\nabla\vec{E}_s^2. \tag{1.34}$$

The relation (1.34) demonstrates that PF is a potential force, i.e., that the energy of oscillating charged particles in the high-frequency field is given by their positions. Such energy is therefore a potential energy U and there is a force $F_{pf} = -\nabla U$, so-called *ponderomotive*, which pushes charged particles from the stronger field to the weaker one. From the point of view of laser-target interaction during laser-driven ion acceleration, PF has the inward direction and tends to push and to pile up electrons inside the plasma and thus steepens the density profile. Consequently, PF creates a charge separation layer which results in an electrostatic field acting on ions and accelerating them [13].

1.2 Laser-driven ion acceleration mechanisms

Protons and ions can be accelerated by the laser radiation as a consequence of various physical phenomena and from diverse regions of the target. Since laser-driven ion acceleration is mostly the result of generated intense longitudinal electric field, the acceleration scenarios can be sorted by the origin of this field. In the majority of current laser systems, the laser radiation usually affects protons and ions indirectly, i.e., due to the charge separation caused by the motion of directly-affected electrons. Nevertheless, if the laser pulse is sufficiently intense (i.e., exceeding 10^{21} W/cm^2 [45]), the field can accelerates protons and ions directly. The effectiveness of conversion efficiency from the energy of light to the energy of particles depends, among others, also on the target itself (e.g., its material, density, shape..) or more generally speaking on the relation between the laser pulse and the target. In other words, it is crucial if the target is transparent or opaque for the specific laser light or similarly, if particles undergo sheath or volumetric acceleration and how efficient it is, see Fig. 1.4.
In principle, a several acceleration mechanisms have been already investigated and properly described. The basic ones [46] reported in this work are: Target Normal Sheath Acceleration (TNSA), Radiation Pressure Acceleration (RPA) (including Light Sail regime (LS) for thin targets and Hole Boring (HB) mechanism for thick targets), Coulomb Explosion (CE) & Direct Coulomb Explosion (DCE) and Magnetic Vortex Acceleration (MVA). Additionally, some other mechanisms, which can be perceived as the combination of the previous basic ones or the enhancement of them, are introduced – namely Break-Out-Afterburner (BOA) and Collisionless Shock Acceleration (CSA), [47]. In fact, a combination of multiple acceleration mechanisms can be observed in real experiments [48], because the actual parameters never precisely meet the requirements of only one scenario.

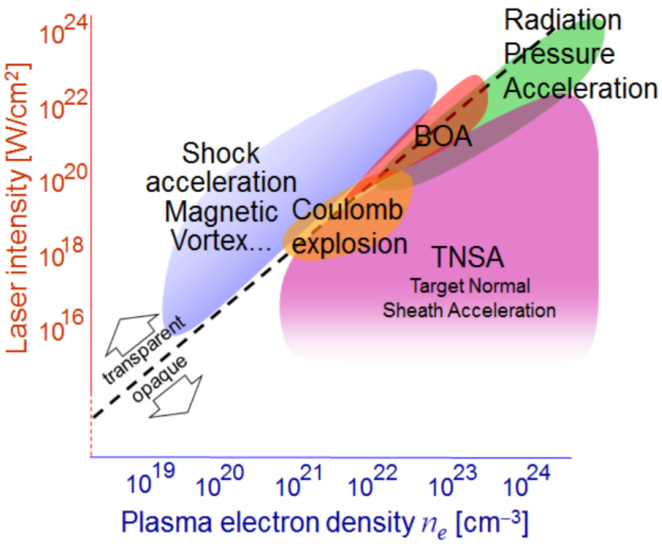

Figure 1.4: The schematic occurrence of the laser-driven ion acceleration mechanisms depending on the relation between the laser pulse intensity and the electron density of the used target [28].

1.2.1 Target Normal Sheath Acceleration (TNSA)

Target Normal Sheath Acceleration (TNSA) is the laser-driven scenario accelerating protons and heavier ions from the rear side of the solid target due to the longitudinal electric sheath field. This field originates from a charge separation induced by the hot electron generation heated by the laser light on the target front side, see Fig. 1.6. Thus, TNSA mechanism is initialized by an ultraintense laser pulse interacting with a solid target of various properties [49]. The process of acceleration depends on various parameters, mainly on the laser pulse itself (i.e., the electric field amplitude, the pulse duration, the energy on target, etc.) or on the target features (i.e., the material and electron density/ density profile of the target, its shape and dimensions, etc.).

Electron transport through the target
In fact, there are no laser systems capable to accelerate ions directly. Consequently, TNSA relies on the electron component and on the electric field resulting from charge separation. In fact, the laser radiation is efficiently converted to a kinetic energy of relativistic collisionless *hot electrons population* which is extremely important for ion acceleration. The electron temperature is scaled with laser intensity and the order of this scaling depends on Electron temperature scaling models described later in the section 1.3.2. For example, often used ponderomotive scaling of electrons predicts a logarithmic-slope temperature that is roughly equal to the ponderomotive potential of the laser pulse [50]. Hot electrons are moving nearly without collisions through the target material due to their high velocity and they are compensated by a cold electron return current. In the case of metal targets, these current consists of free material electrons, whereas in the case of insulator targets, mainly from electrons originating from thermal or field (i.e., collisional and optical) ionization. Therefore, usually two-temperature electron distribution is used in TNSA models [50].
During the laser-target interaction, hot electrons are generated in the area of the laser incidence, having the dimension comparable to the size of the laser focus. When the laser pulse impinges the critical surface, it pushes the target inwards resulting in the steepening of an electron density profile. Furthermore, the motion of ablated plasma causes a shockwave moving into the foil, which leads to ionization and consequently to a modification of the initial electrical conductivity. If the target is thin enough to be fully ionized by the laser pulse or even by a pedestal of amplified spontaneous emission (ASE) or a laser prepulse, the hot electrons can move inside/circulate the target without collisions. If the target is thick and consequently not fully ionized, the binary collisions with particles of material are no longer negligible, when the hot electrons penetrate into a cold solid region. Either way, these electrons are transported to the rear side of the target eventually where they form a dense charge-separation sheath. A toroidal magnetic field B_θ is generated by outflowing electrons. This field is the originator of a kinematic force $E \times B_\theta$ which spreads the electrons into *a fountain* (so-called fountain effect [51]); see Fig. 1.5. As soon as electrons reach the rear side of the target and pass the target-vacuum boundary, they can be attracted back by the strong electric field and they can recirculate the target repeatedly [52]. In fact, the most energetic ones escape, but the majority of them returns towards the target (because of (de)acceleration by electrostatic force) or even reaches the target front side. More about hot electrons and electron heating mechanisms could be found below and in Electron heating/accelerating mechanisms at the critical surface.

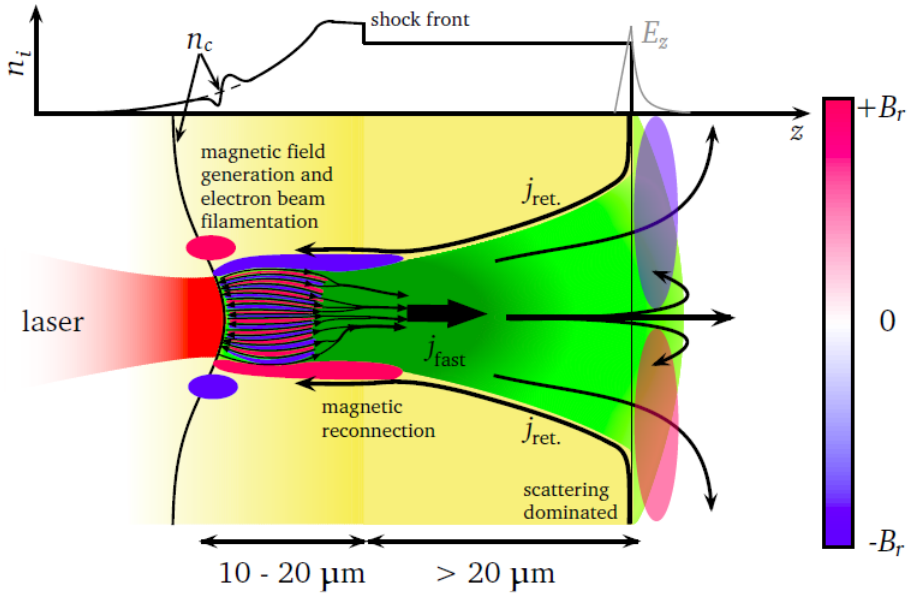

Figure 1.5: Schematic figure showing laser-generated hot (fast) electrons transport; [52]

Ion acceleration by longitudinal electric sheath field & scaling

The electrons at the target rear side cause an unbalance in charge resulting in a strong electrostatic potential, (i.e., a charge-separation over a Debye length) which consequently leads to the acceleration of heavier protons and ions. In other words, a double layer of positive (ions) and negative (electrons) charges is generated at the target rear side, which leads to an electrostatic field having the magnitude of several teravolts per meter [50], [52]. The direction of the accelerated ions trajectory is typically normal to the initially unperturbed target rear surface (i.e., the forward acceleration follows the direction of the electric field). Therefore, the ion trajectories crucially depend on the local shape of the rear surface and on the electric field spatial distribution driven by the time-dependent electron density [52]. The accelerated ions are leaving the target together with co-moving electrons forming a quasineutral plasma cloud. Because the plasma density in the volume drops dramatically after the detachment from the target and the temperature stays high, recombination effects are negligible for propagation lengths in the range of several meters [53].

The acceleration stage lasts approximately from hundred(s) of fs to ones of ps. In fact, the main acceleration time period τ_{acc} is of the order of the laser pulse duration τ [50] and for laser intensities $I \geq 3 \times 10^{19}$ W/cm^2 scales like following [52]:

$$\tau_{acc} = 1.3 \times (\tau + t_{min}), \tag{1.35}$$

where t_{min} is the constant equal to 60 fs, which was found to be the minimum time that the energy transfer from the electrons to the ions takes when using ultrashort pulses [52], [54], [55].

Maximum energy of accelerated ions strongly depends on the hot electron temperature T_{hot}, nevertheless, various models of hot electrons scaling are present. These models vary from different pulse durations, relativistic or not relativistic laser intensities or even a specific model of energy absorption, see sections Hot electrons generation and their transport and

Electron heating/accelerating mechanisms at the critical surface. When T_{hot} is known, the maximum ion energy E_{max} scales as [52]:

$$E_{max} = 2k_B T_{hot} \ln^2 \left(\tau + \sqrt{1+\tau^2}\right), \qquad \tau = \omega_{pi} t/\sqrt{2e}, \tag{1.36}$$

where ω_{pi} denotes ion plasma frequency. The equation is based on electrons expansion model by Mora [56], [57], [58].
The variety of accelerated ion species depends on the material and the purity of the target. Naturally, protons are accelerated the most easily because of their highest charge-to-mass ratio. Thus, for an efficient acceleration of heavy ions (and not the light hydrogen contaminants on the foil surface) one must operate with a very pure target which could be obtained by various techniques like target heating or laser ablation [59].

The relation between the target thickness and the laser dimensionless amplitude has been generally studied in order to achieve ideal ratio to capture as light ions by as large ponderomotive force as possible. Both experiments and simulations show that there is an optimal target thickness d_0 (nm range) for given laser parameters at which the energy of protons is maximal and any further decreasing or increasing of this thickness causes only lower proton energy [60], [61], [62], [63]. The optimal thickness d_0 is related to the dimensionless normalized electron areal density σ and to dimensionless laser amplitude a_0; $a_0 \sim \sigma = \frac{n_e}{n_c}\frac{d}{\lambda}$, where n_e, n_c and λ are electron density, critical density nd laser wavelength, respectively. Therefore, when investigating the efficiency of TNSA mechanism, it is beneficial to define a parameter ξ as a dimensionless ratio between the normalized areal density σ and the normalized laser pulse amplitude a_0:

$$\xi = \sigma/a_0, \tag{1.37}$$

$$\sigma = n_e d/(n_c \lambda), \qquad a_0 = eE/(m_e c\omega), \tag{1.38}$$

where d is normalized amplitude of laser electric field E and the target thickness d_0 ($d = |E|/d_0$), n_e and n_c are electron and critical densities of the target and λ and ω are laser wavelength and frequency, respectively. Naturally, three possible cases can occur [63]:

$$\xi \ll 1, \qquad \xi \gg 1, \qquad \xi \approx 1.$$

Firstly, when $\xi \ll 1$, the laser pulse is intense enough or the target has significantly low density to let the pulse pass though the target without proper TNSA interaction. Secondly, when $\xi \gg 1$, the laser pulse will be reflected from the front surface of the overdense steady target and TNSA regime occurs. In such case, the ion acceleration may be described by the plasma expansion model for thicker targets [64]. Eventually, the optimal TNSA conditions occur at the boundary of these two cases, because it is the fulfillment of the optimal target thickness discussed earlier, i.e., when $\xi \approx 1$, or more specifically when $0.1 < \xi < 10$ [63]. In this case, the laser pulse is both partially reflected and partially transmitted. Electrons still feel the laser field, quiver in it and are pushed forward by the ponderomotive force.

The optimal interacting conditions are even more advantageous to be fulfilled in real experiments, where the target density drops even before the main pulse comes due to the laser prepulse when the contrast ratio is not sufficient (i.e., the ratio between the main peak intensity and the femtosecond prepulse intensity). In fact, even a contrast 10^9, related to the

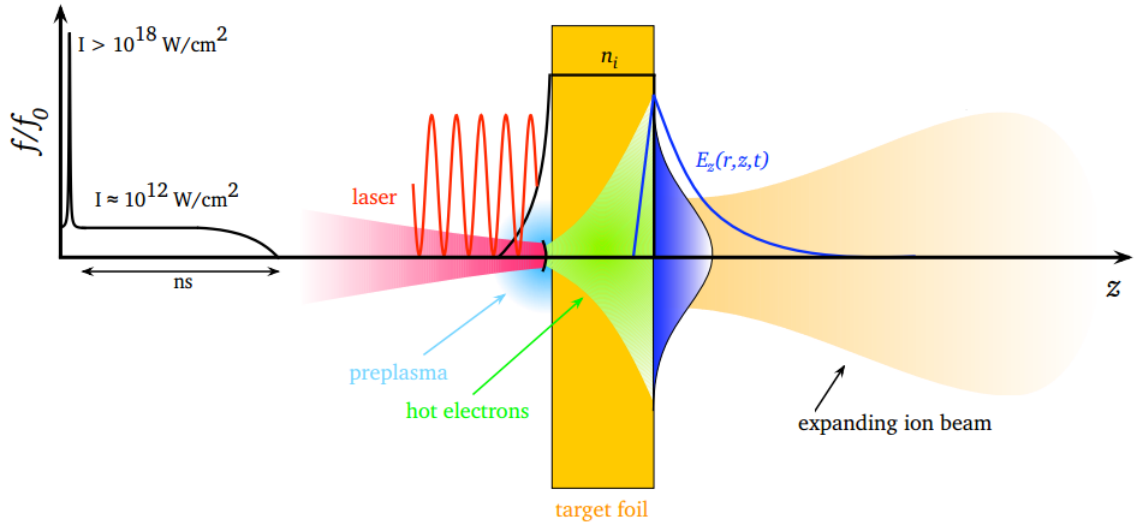

Figure 1.6: Schematic sketch of Target Normal Sheath Acceleration (TNSA) scenario. The example of representative laser pulse is shown on the left side: the peak intensity reaches $> 10^{18}$ W/cm^2, whilst a nanosecond pedestal has typically $\approx 10^{12}$ W/cm^2 [52]

intensity 10^{20} W/cm^2, can excite a plasma resulting in the target expansion towards the main pulse. Nevertheless, the profile of realistic laser pulse is more complex, because, among the multiple prepulses, it contains also laser pedestal [65], see the section Realistic laser profile including prepulse and pedestal.

1.2.2 Radiation Pressure Acceleration (RPA)

Even though a majority of laser-driven ion acceleration experiments have reported TNSA scenario, Radiation Pressure Acceleration mechanism (RPA) based on the pressure of laser light become more effective when more intense, and optimally also circularly polarized, laser pulses are applied. In fact, a dominance of RPA mechanism for high intensities above 10^{23} W/cm^2 were demonstrated by PIC simulations [60], [66], although the regime occurs already from the intensity $\approx 10^{20-\mathbf{21}}$ W/cm^2 [60] as reported for thin targets also experimentally [67]. At mid-high intensities, both RPA and TNSA mechanisms often occur simultaneously, but with various effectiveness. Since RPA employs the radiation pressure, the acceleration takes place at the *front* side of the target in contrast to TNSA, where the ions are accelerated mainly from the *back* side (TNSA acceleration from the front side is possible only when the laser contrast is extremely high).
The efforts in achieving RPA-dominated regime also at lower intensities were made. Such attempts are based on the idea of suppressing the generation of high-energy electrons that contribute to TNSA efficiency, but strongly reduce RPA. This can be achieved by using circularly polarized (CP) laser pulses at normal incidence, because the components of Lorenz force, i.e., $\vec{j} \times \vec{B}$ force, oscillating perpendicularly to the target surface vanish (in the case of plane wave) or are efficiently suppressed (in the case of a finite laser spot size). This leads to the crucial reduction in the electron heating (which suppresses TNSA) whilst the electrostatic force (created in order to balance the local radiation pressure from the laser pulse) accelerates ions, i.e., RPA regime occurs [1], [68], [69]. Moreover, RPA mechanism has been already used

for efficient acceleration of thin foils [68], since CP laser pulses accelerate efficiently all ions in a skin layer [68], [69]. In this context, the term *thin foils* implies that the target must be thin enough in order to bunch and accelerate all ions via several cycles, which is typically low hundreds or tens of nm; similarly ultrathin foils (also studied recently by RPA) refers to the target thicknesses down to ones of nm [68].
In a nutshell, RPA mechanism is based on the radiation pressure affecting the nontransparent front target surface [1], which could even mean the whole foil if it is sufficiently thin. This pressure, being proportional to the inverse value of the particle mass, is bounded with the overall Ponderomotive force (PF) acting on the medium and affecting the lightest particles more effectively. PF forces the electrons to accumulate themselves in the skin layer which causes a charge-separation leading to the creation of the electric field accelerating the ions eventually. Therefore, the ions are accelerated from the space-limited slab only, which is the reason why monoenergetic features in the energy spectrum are so typical for RPA and not for TNSA regime [68].
The maximum energy of accelerated ions strongly depends on the laser and the target parameters. Consequently, there are many means which can both enhance or limit the efficiency of the laser light energy conversion into the energy of ions. Namely, these processes include (i) target transparency, (ii) sub-luminal laser group velocity, (iii) transverse target expansion and (iv) laser off-normal incidence and polarization of the pulse. A deeper explanation, an origin, scaling laws and consequences of all these effects could be found in [46]. Here, only relativistic transparency is briefly commented later in the section Relativistic Transparency (RT).
The feature of Relativistic transparency of the target is a crucial parameter in RPA efficiency, because the material should stay opaque for the laser pulse during the acceleration in order to achieve a sufficient energy transfer from the laser light to the foil. On the other hand, opaque foils are more often thick or/and made from heavy materials. This leads to the problems with a higher number of ions which are irradiated within the laser focal spot which results in the lower energy per ion. Naturally, the efforts in increasing the ion energy follow the idea that the foil should be opaque for the radiation, but simultaneously this radiation should affect only as low number of ions as possible. In other words, the ideal condition lies at the boundary between the foil transparency and its opacity [46], which leads to the investigation of Relativistic transparency phenomenon.

Radiation Pressure Acceleration regime can be sorted further into two additional sub-mechanisms depending on the target thickness: *Light sail* for thin targets and *Hole Boring* for thick targets, see Fig. 1.7.

- *Light sail (LS) mechanism* for thin targets
  Light sail mechanism is a sub-scenario of RPA, efficient in the case of ultrathin targets, or more precisely, in the case of targets whose thickness is comparable to their skin depth $l_s = \frac{c}{\omega_{pe}}$ [70] (i.e., to the depth inside a plasma where electromagnetic radiation can penetrate, typically ones or low tens of nm). When the target is sufficiently thin, all the ions are accelerated before the end of the laser pulse. This means that a part of the target is accelerated as a slab, thus the complete hole boring occurs. In fact, this is the reason why the mechanism has been named after the analogy with a sailing boat, since the longer pulse pushes in front of itself the whole foil, similarly as a wind does a sail, and it accelerates the target as a whole. Moreover, the laser pulse has enough power

to accelerate ions to even higher energies than in the case of thick target, because they are not screened by a background plasma anymore. A thin target has large surface and low mass and thus can receive a significantly higher boost from radiation pressure than a thick target [1]. Moreover, analytical models show that LS mechanism provides high conversion efficiency in the relativistic limit [1].

- *Hole Boring (HB) mechanism* for thick targets
  Hole Boring mechanism is a sub-scenario of RPA, efficient in the case of thick targets in contrast to LS. In other words, the target thickness has to be much larger than the skin layer $l_s = \frac{c}{\omega_{pe}}$, where ion acceleration by the space-charge separation field occurs. The pressure of the laser pulse pushes the overdense target surface inward and steepens its density profile. The surface undergoes a parabolic deformation which allows the laser pulse to penetrate deeper into the target. In contrast to LS regime, where the target is thin enough that all the ions are accelerated before the end of the laser cycle, in the case of HB regime, the pulse pushes neighboring surface layers and accelerates more ions via repeated cycle.
  The front of the imploding plasma surface moves in the laboratory frame with the so-called *hole-boring velocity* v_{hb}, which may be derived by balancing the EM momentum (radiation pressure) with mass momentum flow in a planar geometry in the instantaneous rest frame (IRF) [71], [72], [73]. Therefore, the plasma that is at rest in the lab frame now approaches the plasma surface at $-v_{hb}$ in the IRF. The relativistic equilibrium of these flows in instantaneous rest frame gives [1], [74], [68]:

$$\begin{aligned} \frac{2I}{c}\frac{1-v_{hb}/c}{1+v_{hb}/c} &= 2\gamma_{hb}^2 m_i n_i v_{hb}^2, \\ \gamma_{hb} &= \frac{1}{\sqrt{1-\frac{v_{hb}^2}{c^2}}} \end{aligned}$$

$$v_{hb} = \frac{\sqrt{\Pi}}{1+\sqrt{\Pi}}c, \qquad \Pi = \frac{I}{m_i n_i c^3} = \frac{n_c m_e}{n_i m_i} a_0^2. \tag{1.39}$$

The ponderomotive force originating from the laser pulse forces electrons to concentrate in the skin layer until it is balanced by the charge separation field which in turn accelerates ions. This produces a sharp density increase at the end of the skin layer, where hydrodynamical breaking occurs [68]. Consequently, the dense bunch of fast ions is formed (having a relatively narrow spectrum), it penetrates into the plasma bulk and subsequently escapes from the skin layer. The maximum ion energy is then given by [1], [72]:

$$E_{max} = 2m_i c^2 \frac{\Pi}{1+2\sqrt{\Pi}}, \tag{1.40}$$

which means that the most energetic ions are moving with the velocity two times bigger than the hole-boring velocity v_{hb}. The factor of 2 came from a Gallilean transformation of IRF back to the laboratory frame [74]. In other words, in the rest frame of reference, the 1D ion momentum changes from $-mv_x\gamma_{hb}$ to $mv_x\gamma_{hb}$, whereas in the laboratory

frame, the ion momentum in one direction changes from zero to $2mv_x\gamma_{hb}$, see [75]. This is the reason why in the laboratory frame the ions move with velocity equal to $2v_{hb}$:

$$E_{max} = 2m_ic^2\frac{\Pi}{1+2\sqrt{\Pi}} = \frac{1}{2}m_i\left(2c\sqrt{\frac{\Pi}{1+2\sqrt{\Pi}}}\right)^2, \qquad \rightarrow \qquad v = 2c\sqrt{\frac{\Pi}{1+2\sqrt{\Pi}}},$$

$$v \approx 2c\left(\frac{\sqrt{\Pi}}{1+\sqrt{\Pi}+...}\right) \approx 2v_{hb}. \tag{1.41}$$

In fact, after escaping the skin layer, the ions are not accelerated anymore, since the laser field is screened by the overdense plasma. Finally, electron quasiequlibrium is reached again and the process repeats itself as long as the laser pulse is still present, which is the reason why HB regime is often described as *pulsed* scenario in contrast to LS. This phenomenon is confirmed by PIC simulations and it is very efficient for targets having density above n_c (i.e., tens of n_c such as e.g. pure solid/liquid hydrogen) [1]. The presented Hole Boring relativistic model is not able to resolve the dynamics in the charge separation layer. However, advanced models describing the dynamics exist [1], [69].

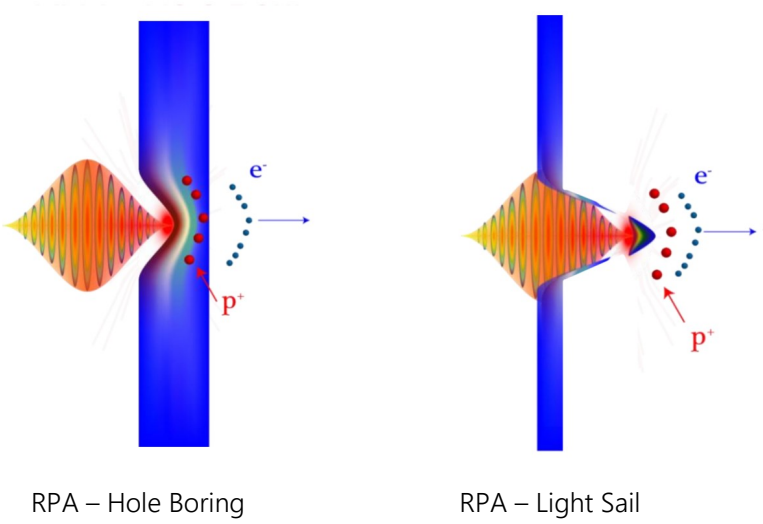

Figure 1.7: The illustrative interaction of a laser pulse with a thick and a thin target demonstrating differences between RPA - Hole Boring and RPA - Light sail mechanisms, respectively [28].

1.2.3 Break-Out Afterburner (BOA)

Widely discussed laser acceleration regime based on Relativistic transparency is known as Break-Out Afterburner (BOA) acceleration [76], [77], [78], [79].
BOA mechanism usually plays a crucial role when a relatively long (low hundreds of fs) ultrahigh intensity laser pulse ($\sim 10^{20}$ W/cm^2) interacts with an ultrathin solid target (density

$\sim 10^{23}$ cm^{-3} and 100's nm-scale). In experiments, BOA occurrence strongly requires an ultra-high laser contrast in order to do not destroy or ionize/expand a thin target before the main pulse arrives.
The target electrons are heated to high temperatures by the incoming laser pulse, which drives a hydrodynamic longitudinal expansion of the target along the laser propagation axis. As already discussed in TNSA mechanism, these energetic electrons are called *hot* and they are produced in the laser field at the target front side. With becoming more and more electrons hot, the electron density decreases and the electron Lorentz factor γ increases. This phenomenon leads to already described Relativistic transparency and it allows the laser light penetrate deeper to the classically opaque target and further enlarge the hot electron generation. In fact, BOA regime is bounded with a massive electron heating.
In the case of a thin target of an optimal thickness (as will be discussed later), the laser field can convert nearly all electrons into hot generation and the whole target becomes relativistically transparent. This corresponds to the region $n_e/\gamma n_c \geq 1$ in Fig. 1.2 presented in the Relativistic transparency section. The simulations shown in this figure have proved, that when the target becomes relativistically transparent to the laser (denoted as time t_1), electrons are heated only at the front side of the target (that is classically underdense) and ions are accelerated by the electric field E_x. Moreover, PIC simulations demonstrated, that ions gain only $\sim 10\%$ from the final kinetic energy at this stage. From the time t_1 to the time t_2, a dramatic BOA acceleration of ions occurs and lasts until the target is not expanded enough that becomes classically underdense and thus the efficiency of the laser energy transfer into the ion energy is low. In the stage of BOA acceleration (i.e., $t \in \langle t_1, t_2 \rangle$), an enhanced volumetric heating of electrons appears and leads to the strong longitudinal electric field that co-moves with ions, thus accelerates them more efficiently. Furthermore, due to the RT, the acceleration field holds longer and has bigger field gradient with a longer effective acceleration distance than those of TNSA. The ideal target density interval for BOA acceleration is thus $n_c < n_e < n_c^\gamma$, where $n_c^\gamma = n_c \gamma$ denotes relativistic critical density, [1], [78], [80].
The earlier mentioned optimal target thickness is bounded with the target density as well as with the laser parameters, for instance, with the laser contrast, the pulse duration, the energy in the pulse and the focus diameter. Generally, the target should not be too thin to experience the time t_2 (the notation consistent with Fig. 1.2) before the pulse peak arrives, because it would massively reduce the energy transfer from the light into the particles. If it happens, the target becomes transparent too early, which leads to the unwanted expansion, the shorter acceleration period and to the lower average intensities of the laser pulse. On the other hand, the target should not be also too thick to experience the time t_1 (the notation consistent with Fig. 1.2) after the arrival of the pulse peak. If so, the foil becomes transparent at the end of the pulse when the laser intensity is already low or even does not experience RT at all. As a consequence, the optimal acceleration is reached when the peak of the laser pulse interacts with the material between times t_1 and t_2. It corresponds to the optimal BOA target thicknesses about a few skin depths (usually from tens to low hundreds of nm) [80].
A combination of PIC simulations and experimental results gave the following energy scaling for BOA regime [80]:

$$E_{max} \approx 5\tau^{0.28}(a_0 - 1)\text{MeV} \propto I^{0.5}\tau^{0.28} \tag{1.42}$$

where τ is the laser pulse duration (FWHM) in units of femtoseconds, a_0 is the dimensionless laser amplitude and I is the laser intensity. The expression is valid only for relativistic laser intensities, ideally in the interval $a_0 \in \langle 1, 30 \rangle$ or at least $a_0 < 100$ (i.e., for intensities not

exceeding 10^{22} W/cm^2), and for single species and a single charge. In other words, the model does not include any physics related to multi-species targets or to ionization [80].

The physical features typical for BOA as well as crucial differences between BOA and TNSA/RPA mechanisms help us to distinguish Break-Out Afterburner scenario from the others [78]:

- BOA is characterized by a strong increase of the maximum ion energy due to the massive electron heating (in comparison to TNSA). This is connected, for instance, to:
  - In both BOA and RPA regimes, the laser light interacts directly with the electrons co-propagating with the ions, in contrast to TNSA scenario, where the laser field interacts with electrons only during the limited time, when they are in a skin-depth layer. Consequently, in the case of BOA and RPA, a collective motion of electrons and therefore the better coupling of energy from the laser to the particles were observed [78].
  - Accelerating fields of BOA and RPA generally hold longer (nevertheless it is also dependent on the pulse duration), have bigger field gradients and longer effective acceleration distances than those of TNSA [78]. Therefore, we can expect higher energies of accelerated ions by BOA or RPA in comparison to TNSA.
- In RPA and BOA, the high-Z species feel, at least, the same accelerating fields as protons do, contrarily to TNSA where the protons shield the field from the heavier species. Therefore, BOA and RPA scenarios are more efficient for acceleration of heavier ions compared to TNSA (e.g., $v_{ion}/v_{proton} > 0.5$ in the case of BOA).
- A diverse dynamics of the laser-target interaction during BOA leads to a fundamentally different angular distributions of the ions compared to TNSA [81]; In the case of BOA, the fastest ions are emitted off-axis in a plane orthogonal to the laser polarization.
- RT is crucial feature of BOA, in contrast to RPA and TNSA regimes, where the target stays both classically and relativistically overdense.

1.2.4 Magnetic Vortex Acceleration (MVA)

Magnetic Vortex Acceleration (MVA) is the regime producing high-energy collimated ion beams from the laser interaction with relatively thick targets (i.e., much thicker than the laser pulse length) having *near critical density*. The mechanism is based on a self-generated magnetic field at the target rear side which strongly contributes to a charge separation and a creation of the electrostatic field. One of the main requirements, in order to reach ideal conditions for MVA scenario, is to get nearly critical target in its density ($n_e \approx n_c$). Therefore, gas jet targets [82], foam targets ($n_e = (0.9 - 30)n_c$) [83], expanded targets with preplasma or targets fabricated from various materials in order to obtain desired density profile with favorable gradients have to be considered [1], [84], [85]. Another important thing is to use tightly focused laser beams in order to get long and stable pulse propagation through the plasma without filamentation.
A focused relativistically intense laser pulse interacts with near critical plasma and it forms a channel just behind its own front – firstly in electron and then in ion densities. The electrons are expelled in the transverse direction and, since the reaction of ions is slow because of their higher inertia, the electrons leave the inner space of the channel filled with protons

and ions, i.e., they leave it positive in charge. The high electron current flows along the laser propagation axis and drags the ions behind. The ions naturally form a sharp spike in density just behind the electrons, the laser pulse itself and behind the growing magnetic vortex. These ions are effectively accelerated in the well-collimated filament along the channel axis by an electrostatic sheath field $E \simeq \nabla B^2/(8\pi e n_e)$, when they reach the plasma-vacuum interface (i.e., when they exit the self-dig channel in the plasma slab). The simulations show that the acceleration stage lasts only less than 100 fs [84]. In fact, the accelerating electric field comes from the rapidly varying magnetic field pressure, that pushes both electrons and ions outside the magnetic vortex (along the vortex axis) and thus redistributes the electrons (being much lighter and thus faster than ions) in the plasma; see typical fountain trajectories of electrons in Fig. 1.8, [84], [85]. In fact, these electron vortices move along the channel axis, i.e., in the direction perpendicular to the plasma density gradient. Consequently, the generated magnetic field has hundreds of megagauss (and even ones of gigagauss inside the channel) [84], [86]. The amplitude of magnetic field B_1 inside the target can be derived from Ampere's law. When the magnetic vortex expands, the amplitude B_1 decreases according to Ertel's theorem at the rear side of the target to the value B_2 [84]:

$$B_1 = -\mu_0 e n_1 c^2 \sqrt{\gamma}/\omega_{p1}, \tag{1.43}$$

$$B_2 = B_1 \frac{n_1 + n_2}{2n_1}, \tag{1.44}$$

where ω_{p1} is plasma frequency, i.e., $\omega_{p1} = \sqrt{n_1 e^2/m_e \varepsilon_0}$, and n_1, n_2 ($n_1 > n_2$) denote densities occurring in an optimal density profile of the target (see Fig. 1.9).

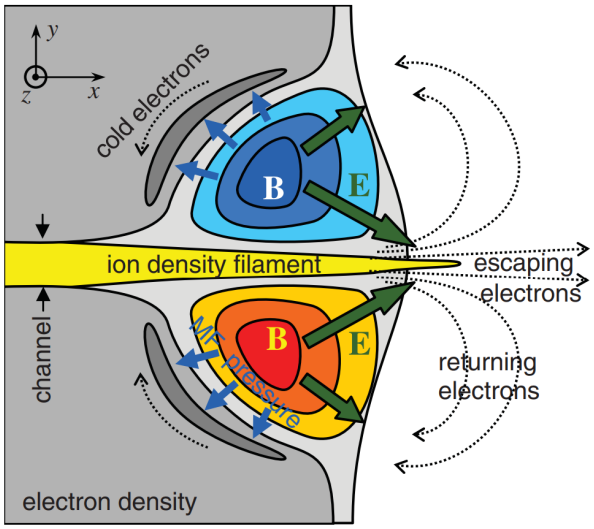

Figure 1.8: Schematic sketch of Magnetic Vortex Acceleration scenario based on a self-generated magnetic field [85]

In order to reach effective MVA acceleration, the condition of the near critical density has to be additionally strengthen by the optimal density profile of the target. Such density profile has to show *bell* or *gaussian*-like shape, whilst the proper density gradients are crucial as well. In fact, PIC simulations show that MVA acceleration was not observed in the case of targets having only *homogeneous* density profile, even though the density was near critical

[84]. Moreover, if the density gradient is too large, the magnetic vortex expands too fast in lateral dimension and the magnetic field disappears very quickly at the rear side of the target. As a consequence, the vortex has no time to form ion filament. On the other hand, if the density gradient is too small, the vortex does not expand at all, thus any ion spike in the density is generated. As an example, the effective MVA acceleration were observed in PIC simulations performing the interaction with 100 TW laser pulse (30 fs, 800 nm, focal spot 1.67 μm) with a 97 μm-thick hydrogen target having an optimized density profile presented in Fig. 1.9 [84]. The theoretical model predicting the scaling law for maximum ion energy

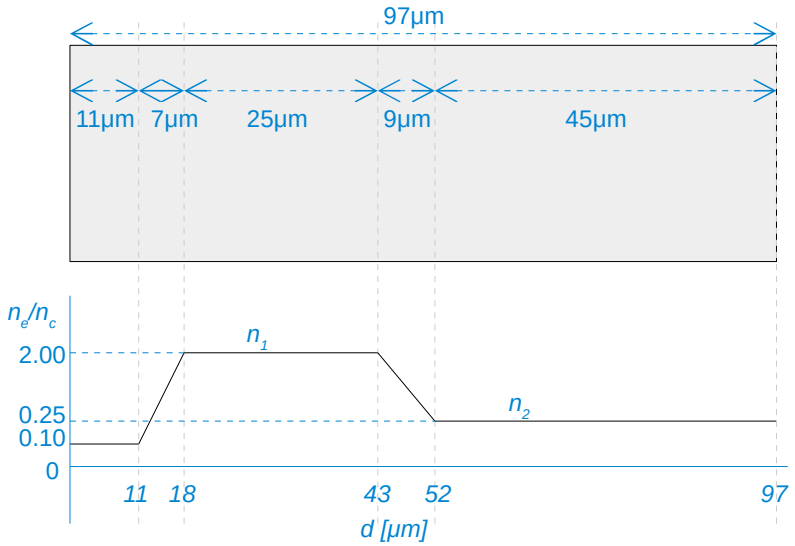

Figure 1.9: Sketch of dimensions and corresponding density profile of a H-target used for sufficient MVA acceleration studied by PIC simulation in [84]

per nucleon accelerated in MVA regime has been confirmed by the set of above described PIC simulations (see Fig. 1.10, where the scaling is plotted as a function of the incident laser power) and it is following [84]:

$$E_{max}/A = m_p c^2 \left(\frac{1}{\sqrt{1-\beta_i^2}} - 1 \right) \approx \left(\frac{Z}{A} \right) m_e c^2 \frac{(n_1+n_2)^2 \gamma}{2 n_1 n_2} \approx \frac{Z}{A} \left(\frac{m_e c^2 a_L}{2\sqrt{2}} \frac{n_1}{n_2} \right), \quad (1.45)$$

where Z, A m_e and m_p are the ion charge, the ion mass number, the electron mass and the proton mass, respectively. The normalized vector potential of the laser pulse is denoted as $a_L = eA_L/(m_e c)$ and due to the vortex formation it is typically higher than the normalized vector potential of the laser pulse in vacuum a_0 ($a_L \approx 2.5 a_0$, see [84]). Lorentz factor is bounded with a_L for linearly polarized laser pulse by the relation $\gamma = \sqrt{1 + a_L^2/2}$. The approximations of (1.45) are valid for $n_1 \gg n_2$ and $a_L \gg 1$. The scaling predicts approximately $5 - 10$ times higher ion energies in comparison to the sheath field acceleration mechanisms using solid targets. This means, that even 200 MeV ions are achievable with 100 TW class lasers in MVA regime using an optimized plasma density profile [84].

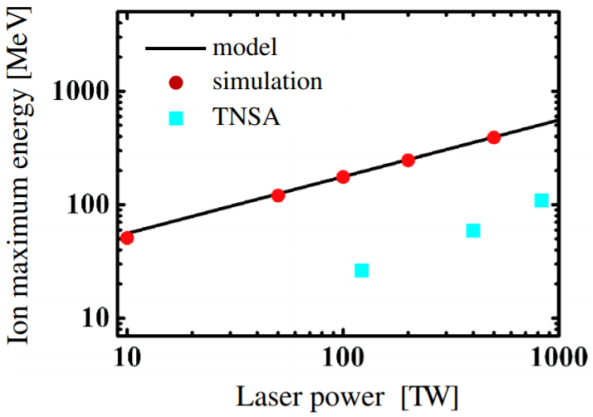

Figure 1.10: Energy scaling for the magnetic vortex acceleration. The solid line shows the maximum ion energy predicted by the theoretical model by (1.45), and the red circles show PIC simulation results. The blue squares show ion acceleration experiments using solid targets, where TNSA model is applied (TNSA data taken from [54]) [84].

1.2.5 Collisionless Shock Acceleration (CSA)

The regime of Collisionless Shock Acceleration (CSA) has been studied mainly in astrophysics, because it covers a wide range of related phenomena such as shocks around supernova remnants, particle acceleration in solar wind and terrestrial bow shocks, which are formed when the solar wind encounters the magnetosphere of the Earth [87], [88].
The limited-size spot is irradiated by a laser light which creates a large radiation pressure gradient, similarly to already described RPA-HB mechanism. The radiation pressure gradient evolves in a collisionless shock wave moving at the shock velocity v_{sho} close to the hole-boring velocity v_{hb} (1.39) and remaining nearly the same during the propagation through the target [1]. In other words, the shocks themselves are driven by the piston action of the radiation pressure, but after that they can propagate independently of the laser pulse. This is the difference from RPA-HB where the front movement is driven by the laser pulse directly. Therefore, HB-RPA lasts as long as the pulse is still present, in contrast to CSA. Generally, $v_{sho} > v_{hb}$ and the propagation of the shock can be observed ahead of the hole boring front. Consequently, the CSA leads to higher ion velocity than HB [89].
In the case of strongly relativistic intensities ($a_0 \gg 1$) and the assumption of $v_{sho} \simeq v_{hb}$, the condition for supersonic shocks occurrence is following [1], :

$$\sqrt{2}a_0 > n_e/n_c. \tag{1.46}$$

As a response to the charge separation driven by the shock at the front target side, an electric field is formed. A part of plasma ions is accelerated due to the reflection from the shock wave front under the action of the generated electric field, which is co-moving with the wave. In the shock frame, the ions are reflected when the value of the electrostatic potential barrier Φ_{max} at the front side satisfies $Ze\Phi_{max} > m_i v_i^2/2$ (v_i is the ion velocity in the shock frame). Therefore, the accelerated ion component acquires in the laboratory frame the velocity $v_{i,sh}$, which is approximately two times higher than the shock one, i.e., $v_{i,sh} = 2v_{sho}/(1 + v_{sho}^2/c^2) \approx 2v_{sho}$ [1], [89], [90]. Therefore, the ions are accelerated by the shock to the energy $E_{max} = m_i c^2(\gamma_{i,sh} - 1) = m_i c^2((1 - v_{i,sh}^2/c^2)^{-1/2} - 1)$. In the case of

non-relativistic shock velocity and $a_0 \gg 1$, the following approximation is valid [89]:

$$E_{max} \approx \frac{2Z}{3} m_e c^2 \frac{n_c}{n_e} a_0^2. \tag{1.47}$$

In fact, the ion population accelerated to the twice higher velocity than the velocity of the shock front has been clearly tracked and separated from other ions in PIC simulations, which is in reality the way how CSA mechanism had been predicted [71], [91]. Furthermore, the energy spectra show narrow features which made this scenario interesting for future applications [90].
Moreover, already reflected ions can be post-accelerated by the transient sheath field at the rear side of the target (TNSA), which produces a plateau in the ion spectrum. This phenomenon was observed experimentally [92] and it proves the importance of the front-contribution to the typical TNSA acceleration. The simulations reporting a combination of CSA-TNSA regimes characterized by a high-energy tail of accelerated particles (but with lower efficiency than pure TNSA) have been published [93], [94]. Furthermore, CSA often occurs as the combination of CSA-HB or/and CSA-HB-TNSA because of a gradual expansion of the target, see Fig. 1.11, where the maximum proton energies expected from the theory and the occurence of these three acceleration mechanisms are depicted as a function of the relativistic density ratio $n_e/(\gamma n_c)$ for $a_0 = 10$ [89].

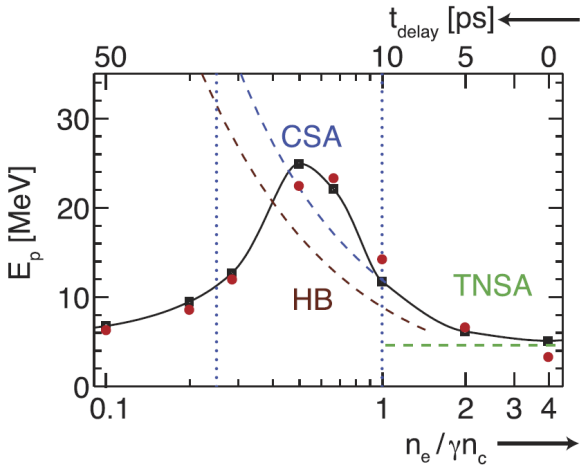

Figure 1.11: Maximum proton energies expected from theory as function of the relativistic target density for $a_0 = 10$ due to different acceleration mechanisms: Target Normal Sheath Acceleration (TNSA) (green), Collisionless Shock Acceleration (CSA) (blue), Hole Boring (HB) (brown). The time axis corresponds to the time delay between the heating pulse with $a_0 = 0.1$ initiating a hydrodynamic expansion and the second laser pulse. The maximum proton energies in the simulations measured inside the target are compared for a cubed (black squares) and a spherical target (red dots). The details can be found in [89].

1.2.6 Coulomb Explosion (CE) & Direct Coulomb Explosion (DCE)

Coulomb expansion (CE) regime plays an important role when the laser radiation is so intense, that resulting Ponderomotive force expels nearly all electrons from the irradiated spot. Consequently, a strong electric field inside the foil originated from a charge separation is created.

The positively charged target is left behind and it undergoes a fast expansion, because the resting constituents start to separate themselves from each other due to Coulomb repulsion. The process of CE is usually associated with laser-driven acceleration from target clusters [95] [96], [97], although the works performing multilayered targets can be found as well [98]. In fact, the mixing of heavy and light materials when fabricating multilayered targets is usually used [47], [98], [99], because the higher amplitudes of electric field and thus higher energies of protons and ions can be reached with the higher values of the parameter $\chi = Zm_e/m_i$. The proton acceleration time is relatively long ($t \sim 100/\omega_p$), therefore the dynamics of ion cluster and the evolution of the electric field are usually neglected in acceleration models [98].
The maximum ion energy of a non-neutral spherical cluster with the radius R_0 and homogeneous ion density n_i is [95]:

$$E_{max}^{CE} = 4\pi Z^2 e^2 n_i R_0^3/3 \approx 300 Z^2 \times \left(\frac{n_i}{5 \times 10^{22}\ \mathrm{cm}^{-2}}\right)^{1/2} \left(\frac{R_0}{1\ \mu\mathrm{m}}\right) \mathrm{MeV}, \tag{1.48}$$

where Z is the ion charge state.
Currently, the notation of so-called Directed Coulomb expansion (DCE) regime can be found. In DCE, the stress is given on the fact, that the laser pulse does not only expel the electrons from the target undergoing CE, but more importantly, the radiation pressure accelerates the ion core as well (predominantly in the laser propagation direction), see Fig. 1.12. Therefore, we can consider DCE mechanism as an effective combination of RPA scenario and CE effect. Consequently, the proton energy originating from DCE scenario scales as [47]:

$$E^{DCE} = E^{CE} + (p_f/m_p)\sqrt{2m_p E^{CE}}, \tag{1.49}$$

where E^{CE} is the energy which protons obtained from CE and p_f is the momentum of the foil due to RPA.

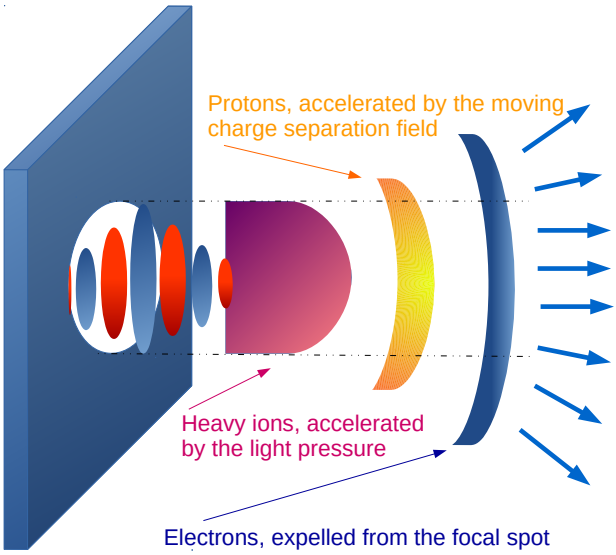

Figure 1.12: Schematic sketch of Direct Coulomb Explosion (DCE) acceleration.

1.3 Role of electrons in laser-driven proton and ion acceleration

1.3.1 Electron heating/accelerating mechanisms at the critical surface

The efficiency of coupling of the laser energy to the target material is crucial when studying laser-driven ion acceleration. Up to nowadays, there is no single model which is able to adequately describe all main absorption phenomena. There are various mechanisms describing both electrons heating or acceleration. These mechanisms can be roughly divided into two groups depending on the laser intensity (or equivalently on the laser irradiance):

- If the laser intensity is below 10^{15} W/cm^2 (or more precisely, when the laser irradiance satisfies $I\lambda^2 \leq 10^{15}$ W/cm^2 μm^2), the plasma is *usually* heated by *electron-ion collisions* and absorption mechanisms such as *Collisional absorption* [13], [100] and *Normal skin effect* [100] cause heating of all electrons. The electron mean free path is shorter than the skin depth in the interaction region. A relatively long time is needed for the efficient heating, which corresponds to the longer pulses ($\sim ns$), usually employed in such interactions. Then, more than 80% of the laser pulse energy can be delivered into the plasma.

  Since PIC simulations in this work consider laser pulses of $I \sim 10^{21}$ W/cm^2, only corresponding collisionless mechanisms will be discussed in detail.

- If the laser intensity is higher than 10^{15} W/cm^2, the plasma is heated predominantly by *collisionless absorption mechanisms*, because the electrons gain a high energy from the laser field. Consequently, collisions become ineffective during the interaction. In other words, the electron mean free path is longer than the skin depth in the interaction region. The electron velocity v_e (here, containing both oscillation and thermal velocities) and the temperature T_e scale with the collision frequency ν_{ei} as follows [12]:

$$\nu_{ei} \sim T_e^{-2/3}, \qquad \nu_{ei} \sim v_e^{-3}. \tag{1.50}$$

  The so-called effective collision frequency ν_{eff} corrects the relation for the collision frequency ν_{ei}, when the electron oscillation velocity v_{os} becomes (with the growing laser intensity) significant and it is thus treated separately from the thermal velocity component v_{Te}. When the electron quiver velocity becomes comparable to or even higher than the thermal velocity (e.g. $v_{os} \gg v_{Te}$ for laser intensities above $\sim 10^{16}$ W/cm^2 [101]), the effective collision frequency is reduced [100]:

$$\nu_{eff} \simeq \nu_{ei} \frac{v_{Te}^3}{(v_{os}^2 + v_{Te}^2)^{3/2}}. \tag{1.51}$$

  therefore, for the relativistic velocity v_{os} the frequency (1.51) becomes negligible.
  There are various collisionless processes which can couple the laser energy to the plasma. If the plasma has a step-like or a very steep density profile, the absorption of the laser energy takes place due to Brunel vacuum heating, $\vec{j} \times \vec{B}$ heating, Anomalous skin effect or Sheath inverse-bremsstrahlung. On the other hand, if the plasma density profile has the scale length larger than the laser wavelength, Resonant absorption plays a crucial role. Furthermore, it is important to point out, that the presented mechanisms of hot

electron generation are an approximation of complex physical phenomena since they presume only the incident laser light and do not solve any interference of the incident and the reflected part of this wave. In following subchapters, the mentioned mechanisms will be discussed from the lowest laser intensity to the highest.
In contrast to collisional heating mechanisms, in collisionless scenarios, only a part of electrons gains the majority of absorbed energy. These electrons are called *hot electrons* and they are crucial for laser-driven ion acceleration mechanisms. In fact, the knowledge of the hot electron temperature is important in order to predict, for example, maximum ion energies. Its dependence on, typically, the laser intensity or on any other parameter differs from the used scaling model. The list of various scaling laws below and above the laser intensity of 10^{20} W/cm^2 will be discussed separately in the following section Hot electrons scalings.

1.3.1.1 Resonance absorption

Resonance absorption (RA) is a linear collisionless absorption mechanism able to accelerate electrons. The occurrence of RA is strongly dependent on the laser pulse parameters. Specifically, it is crucial to distinguish between two cases of linear polarization: *s*-polarized and *p*-polarized laser light, see Fig. 1.13. In the case of *s*-polarized light, the electric field oscillates along z-axis and its component along the density gradient ∇n_e is zero. On the contrary, when a *p*-polarized laser pulse is obliquely incident (forming the angle φ_0 with the target normal) on a continuously increasing plasma density profile, the z-component of the electric field vector is zero. Then, the electromagnetic field has a non-zero electric field component in the plane $x - y$ (i.e., a non-zero component along the density gradient ∇n_e). Here, the direction of the electric field oscillations is given by the fact, that $\vec{E}$ is perpendicular to the wave vector $\vec{k_0}$. This corresponds to the condition of $\vec{E} \cdot \nabla n_e \neq 0$, which has to be fulfilled in order to drive resonant plasma oscillations, which, in turn, accelerate electrons [1].

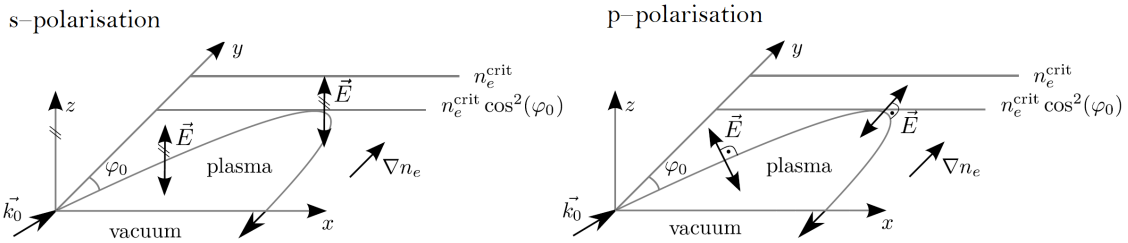

Figure 1.13: Schematic drawing of the electric field vector direction in the case of s-polarized and p-polarized laser light [102]

In other words, Resonance absorption takes place when a laser wave with the incidence angle φ_0 passes through an underdense plasma and when it reaches the vicinity of the critical surface, i.e., the place where the electron density can be expressed as $n_e = n_e^{crit}\cos^2\varphi_0$. Therefore, the laser pulse reaches the critical surface for normal incidence only, i.e., for $\varphi_0 = 0°$. Eventually, the electron plasma wave is resonantly excited by the evanescent electric wave (the laser field) in the critical density area. The electrons oscillate around the equilibrium position in the plasma having the plasma frequency equal to the frequency of the laser in the critical area (and hence to that of the evanescent wave as well). The electron plasma wave grows over a few laser periods and it can be damped by various mechanisms – for lower laser

intensities by collisions and Landau damping, for higher intensities by particle trapping and wave breaking [12], [103]. Resonance absorption is efficient for long pulses (> ps) and large (pre)plasma scale lengths (> μm) [12].
As already mentioned, resonantly absorbed energy in the case of s-polarized light is naturally equal to zero. Nevertheless, in the case of p-polarized light and of long density scale lengths, i.e., $k_0 L \gg 1$ ($k_0 = 2\pi/\lambda$ is the laser wave vector and L satisfies $L = n_e^{crit}/|\nabla n_e^{crit}|$), the amount of absorbed energy depends on the parameter $\xi = (k_0 L)^{1/3} \sin\varphi_0$. Then, the fractional absorption η_{ra} is given as a function of the parameter ξ and thus depends on the characteristic plasma length L, the laser wavelength λ and on the angle of incidence φ_0 [12]:

$$\eta_{ra} = \frac{1}{2}\phi^2(\xi), \qquad \phi \simeq 2.3\xi \exp(-2\xi^3/3), \tag{1.52}$$

as illustrated in Fig. 1.14 (a).

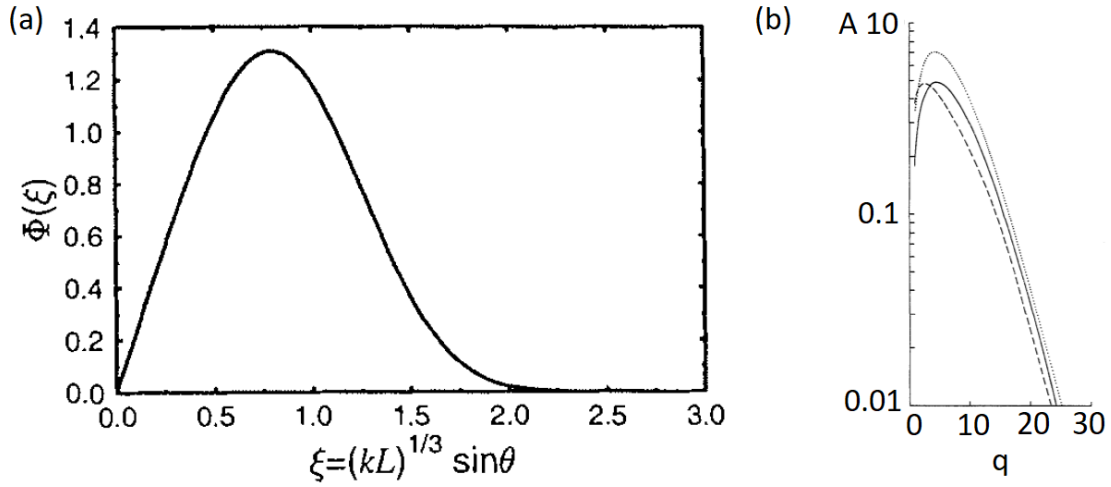

Figure 1.14: (a) The Denisov function: Self-similar behavior of Resonance absorption for long density scale lengths (i.e., $k_0 L \gg 1$) [12]; (b) The dependence of absorption coefficient A on the angle parameter q. The solid line represents the exact solution of A, the dashed line shows the calculation when the Denisov's solution was used and the dotted line represents the new model of RA (1.53) [103].

Furthermore, there are other models of Resonance absorption. For example, one of them deals with the energy of the beam at the reflection point Q_{refl}, the reflection angle φ_0 (i.e., the angle between the incident laser beam and the density gradient), the characteristic plasma length L and the laser frequency ω in order to estimate the resonantly absorbed energy ΔQ_{res} from p-polarized laser light in the terms of absorption coefficient A [103]:

$$A \equiv \frac{\Delta Q_{res}}{Q_{refl}} = 18q\frac{F_{Airy}^3(q)}{|F'_{Airy}(q)|}, \tag{1.53}$$

$$q = (\frac{\omega}{c}L)^{2/3} \sin^2(\varphi_0), \qquad L = n_e^{crit}/|\nabla n_e^{crit}|, \tag{1.54}$$

where F_{Airy} and F'_{Airy} denote Airy function and its derivation, respectively. The dependence of the absorption coefficient A on the angle parameter q is illustrated in Fig. 1.14 (b), which

compares the exact solution of this coefficient with the model (1.53) and with the Denisov's solution.

1.3.1.2 Anomalous skin effect and Sheath inverse-bremsstrahlung

Anomalous skin effect (ASE) and Sheath inverse-bremstrahlung (SIB) are complementary collisionless mechanisms to Brunel vacuum and $\vec{j}\times\vec{B}$ heating processes in the sense of various demands on the density profiles. In fact, whereas Brunel and $\vec{j}\times\vec{B}$ scenarios play a crucial role for step-like density profiles (related usually to short laser pulses with high contrast ratios), ASE and SIB take place for an expanded material with steep density gradients ($L/\lambda \ll 1$), i.e., when the light pressure P_L is lower than the plasma pressure P_e [12]:

$$\frac{P_L}{P_e} = \frac{660 I_{18}}{160 n_{23} T_{keV}} < 1, \tag{1.55}$$

where I_{18} is the laser intensity in units of 10^{18} W/cm^2, n_{23} is the electron density in units of 10^{23} cm^{-3} and T_{keV} is the electron temperature in keV. Both SIB and ASE become important for laser intensities above 10^{17-18} W/cm^2 [104]. If (1.55) is violated, for example, in the case of higher irradiances, Brunel vacuum heating or Resonance absorption are expected instead of ASE or SIB. The relation (1.55) can be replaced equivalently by:

$$\frac{v_{os}^2}{v_{Te}^2} < \frac{n_e}{n_c}. \tag{1.56}$$

In the case of Anomalous skin effect, both the electron mean free path $\lambda_{mfp} = v_{Te}/\nu_{ei}$ and the mean thermal excursion length v_{Te}/ω are larger (due to the temperature increase) than the skin depth $l_s = c/\omega_p$, i.e., $\lambda_{mfp} > l_s$ and $v_{Te}/\omega > l_s$, respectively. Therefore, the laser pulse penetrates deeper into the plasma and the relation between the induced currents and the electric field becomes nonlocal. Consequently, the electrons originated from the interaction region can surmount the skin layer in the time shorter than a laser period [12].
On the contrary, in the case of Sheath inverse-bremsstrahlung, electrons pass a skin layer in the longer time than only one laser period (i.e., $\omega l_s/v_{Te} \gg 1$). The energy transfer from the laser to the electrons takes place via series of irreversible kicks as they are inelastically reflected from the Debye sheath near the plasma-vacuum interface. In fact, due to the condition $\omega l_s/v_{Te} > 1$ or $\omega l_s/v_{Te} < 1$, SIB and ASE mechanisms are referred as two limits of the same absorption mechanism [12].

1.3.1.3 Brunel vacuum heating

The Brunel vacuum heating is a non-linear collisionless mechanism, which leads to the generation of hot electrons and takes place when the p-polarized laser pulse is obliquely incident on the target surface. If a thermal electron arrives at the edge of the plasma in the right moment of the laser cycle (specifically, in its half), it is dragged out into the vacuum to the distance larger than the Debye length. Moreover, a self-consistent electric field is created when many electrons are ejected simultaneously. As a consequence of the oscillating laser field and of the self-consistent electric field, the same electron would be turned and accelerated back into the plasma when the laser field reverses its direction. Because the electric field is strongly shielded inside the overdense plasma, these accelerated electrons are not dragged back during the next half-cycle, but they propagate further into the plasma, where they can be absorbed,

for instance, by collisions. In reality, DC currents along the target surface generate an additional magnetic field which can deflect electrons trajectories and prevent them from returning to the target [1], [12], [17].
This mechanism efficiently works for high laser irradiances (i.e., above 10^{16} W/cm$^2\mu$m^2) [12], [105]), because the amplitude of oscillating electrons ($A_e = a_0 c/\omega = v_{osc}/\omega$) driven by the electric laser field is larger than the density scale length L, i.e., $v_{osc}/\omega > L$. This condition implies that the density profile has to be very steep or even step-like, in contrast to Resonant absorption. In fact, oscillating electrons bring away the energy of the laser pulse and transform it to the kinetic energy of the plasma when they reach the overdense plasma region [18], [106].
The oblique incidence of the laser pulse is crucial factor of Brunel vacuum heating occurrence since the electrons have to be dragged out from the plasma. This would not work for normal incidence, because the oscillating field vector would be parallel with the target surface. The angular dependence of vacuum heating predicted by Brunel model is shown in Fig. 1.15 (a) and the fractional absorption rate used there satisfies [12]:

$$\eta_{vh} = \frac{1}{\pi a_0} f \left[(1 + f^2 a_0^2 \sin^2\theta)^{1/2} - 1 \right] \frac{\sin\theta}{\cos\theta}, \tag{1.57}$$

where $f = 1 + \sqrt{1 - \eta_a}$ is the field amplification factor reflecting the fractional laser absorption η_a.

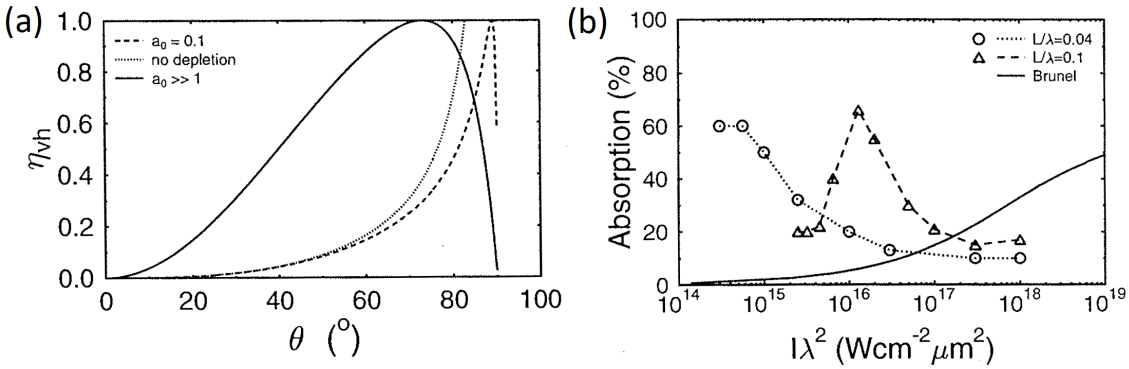

Figure 1.15: (a) Angular dependence of vacuum heating predicted by Brunel model [12]; (b) Absorption fraction vs. laser irradiance according to Brunel (1.57) with $\theta = 45°$ (solid line); and according to simulations [105] for various density scale lengths (dotted and dashed lines) with $n_e/n_c = 2$, [12].

When only the electric field is taken into account, we can write for the strongly relativistic limit (i.e., for $f a_0 \sin\theta \gg 1$):

$$\eta_{vh}^{rel} = \frac{4\pi\alpha'}{(\pi + \alpha')^2}, \tag{1.58}$$

where $\alpha' = \sin^2\theta/\cos\theta$, θ is the angle of oblique laser incidence and $f = 2(\frac{\alpha'}{\pi} + 1)^{-1}$.
However, for realistic density profiles with finite gradients and for more complex models of absorption (containing also other mechanisms), the situation is more complicated. For example, the transition and the combination of Resonance absorption with Vacuum heating

is expected [12], [105], see Fig. 1.15 (b). As demonstrated in this figure, the absorption fraction varies also with a different scale length of the plasma. Generally, the high absorption is expected not only for the optimal angles of incidence θ but also for the high values of the laser irradiance. In fact, it was demonstrated that the most favorable incidence angle for modest densities and intensities (i.e., laser irradiances 10^{14-18} W/cm$^2\mu$m^2 and density scale lengths $L/\lambda = 0.1-2$) is around 45° [105], [107] rather than the grazing incidence angle $\sim 70°$ suggested by Fig. 1.15 (a) showing the simplified Brunel's model.

1.3.1.4 $\vec{j} \times \vec{B}$ heating

Relativistic $\vec{j} \times \vec{B}$ heating is very similar to Brunel vacuum heating in the sense that electrons are heated by a direct laser field acting on a step-like plasma density profile. The driving term of this mechanism is a high-frequency $\vec{v} \times \vec{B}$ magnetic component of Lorentz force. The $\vec{j} \times \vec{B}$ mechanism differs from Brunel vacuum heating in two main signs – firstly, the high efficiency is reached for normal incidence of the laser pulse and secondly, the electrons are ejected into vacuum twice per laser period. Due to the secondly mentioned feature, Brunel and $\vec{j} \times \vec{B}$ heating could be distinguished in numerical simulations.
The self-consistent field is generated as a response to the ejection of electrons. This field, together with oscillating $\vec{j} \times \vec{B}$ force, pushes the electrons back into the preplasma, where they feel no restoring forces after passing through a plasma skin layer [12]. The force which ejects electrons twice per laser period in the normal direction, can be expressed as [18]:

$$F_p \sim \frac{m_e \omega c a_0^2}{\sqrt{1 + a_0^2}}, \tag{1.59}$$

and the average electron energy is proportional to the ponderomotive potential given by $U_p = m_e c^2 \left(\sqrt{1 + a_0^2} - 1 \right)$. Relativistic $\vec{j} \times \vec{B}$ heating works for any laser polarization except circular and becomes important for relativistic pulse intensities, i.e., when $a_0 \gg 1$ (where a_0 is given by $I\lambda^2 = 1.38 \cdot 10^{18} \cdot a_0^2$) [18].

1.3.2 Hot electrons scalings

In the case of laser intensities higher than 10^{15-16} W/cm^2, collisionless mechanisms described in the previous subchapter Electron heating/accelerating mechanisms at the critical surface prevail and lead to the efficient energy transfer to a fraction of electrons. These electrons are called *hot* and they originate from the area of laser incidence, having the dimension comparable to the size of the laser focus. In fact, they are responsible for carrying energy from skin layers deeper to the target. Notwithstanding hot electrons are accelerated by coherent electric field, they have Maxwellian velocity distribution with characteristic temperature T_h, significantly higher than the temperature of background plasma T_e, i.e., $T_h \gg T_e$. It is a consequence of particle acceleration in a standing wave which has a stochastic nature and shows a strong cycle-to-cycle fluctuations both in particle trajectories and their energies [108]. Hence, Maxwellian velocity distribution is a result of averaging the single particle distributions over time [12]. In laser-produced plasmas, an energy distribution of electrons has generally a shape close to the bi-Boltzmann-Maxwell distribution, where temperature T_e characterizes the plasma itself (i.e., T_e corresponds to *thermal* or *cold* electrons in the interaction region), whereas T_h describes the temperature of the hot electron population [109], [110], see the

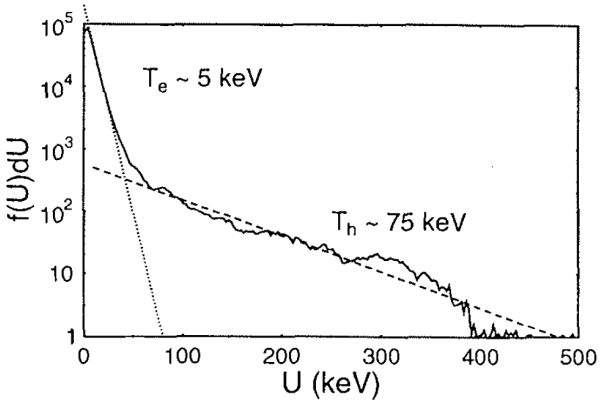

Figure 1.16: Example of typical bi-Maxwell electron distribution resulting from collisionless heating by a laser [12].

example of the bi-Maxwellian electron distribution in Fig. 1.16.
In order to explain further the physical mechanisms behind the particle acceleration, both the temperature and the number of hot electrons are crucial. These values significantly depend on the length of the interacting laser pulse and its intensity.

1.3.2.1 Electron temperature scaling models for laser intensities below 10^{20} W/cm^2

- *Longer pulses* (i.e., the pulses having several *ps* or more) provide enough time to establish the equilibrium, i.e., the balance, between the laser and the plasma pressure. In contrast to short pulses, electrons have enough time to move in response to the laser pressure. As long as the condition $n_h \ll n_e$ on the mean electron densities is fulfilled, the least numerous hot electrons population n_h is responsible for the energy balance, whilst the cold electron bulk with higher density n_e assures the pressure (or momentum) equilibrium [12].
  Assuming long pulses, Forslund-Kindel-Lee scaling for hot electron temperature is usually used [111]:

$$T_h^{FKL}[\text{keV}] \simeq 14(I_{16}\lambda_\mu^2)^{1/3}T_e^{1/3}, \tag{1.60}$$

  where I_{16} denotes the laser intensity in units of 10^{16} W/cm^2 and λ_μ the laser wavelength in micrometers.

- In the case of *short pulses* (i.e., the pulses having fs-scale), the steady-state situation is not possible any longer, because the equilibrium can not be established in such short times. Also, the density and the field profiles are much sharper.
  There are various models, which predict the scaling of hot electron temperature T_h assuming short pulses and preferably lower laser intensities, i.e., without taking into account relativistic effects.

  – Brunel scaling can be used [12]:

$$T_h^B[\text{keV}] \simeq 3.7 I_{16}\lambda_\mu^2, \tag{1.61}$$

where I_{16} denotes the laser intensity in units of 10^{16} W/cm^2 and λ_μ the laser wavelength in micrometers.

– For oblique laser incidence on a steep, but finite, density gradient, we can use Gibbon & Bell scaling [12]:

$$T_h^{GB}[\text{keV}] \simeq 7(I_{16}\lambda_\mu^2)^{1/3}, \tag{1.62}$$

where I_{16} denotes the laser intensity in units of 10^{16} W/cm^2 and λ_μ the laser wavelength in micrometers.

– Lastly, Wilks or so-called *ponderomotive* scaling is based on the ponderomotive potential U_p being formed when the laser pulse is reflected from the target surface. This scaling is expected to be valid for laser pulses at normal incidence and intensities above 10^{18} W/cm^2 (where $\vec{j} \times \vec{B}$ heating mechanism is important) [72]:

$$T_h^{W}[\text{keV}] \simeq 511 \left[(1 + 0.73 I_{18}\lambda_\mu^2)^{1/2} - 1\right] \approx \sqrt{U_p}, \tag{1.63}$$

where I_{18} denotes laser intensity in units of 10^{18} W/cm^2 and λ_μ the laser wavelength in micrometers.

The summary of presented scaling laws together with experimental results of femtosecond laser interaction with matter are depicted in Fig. 1.17.

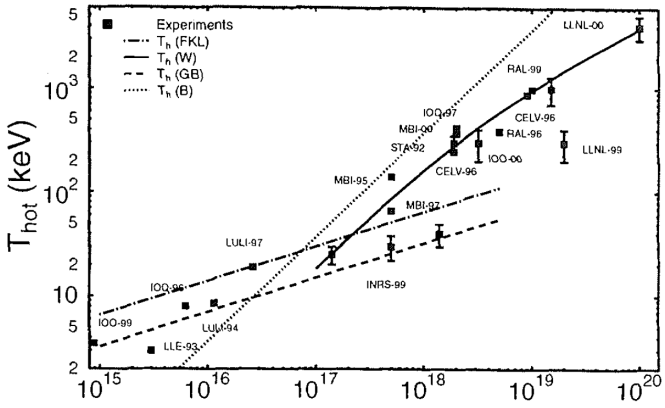

Figure 1.17: Hot electron temperature scalings and measurements (squares): Long pulses: Forslund-Kindel-Lee scaling according to (1.60), Short pulses: Brunel scaling according to (1.61), Gibbon & Bell scaling according to (1.62) and Wilks scaling according to (1.63); [12]

Although the Fig. 1.17 gives a clear insight into the situation it covers only the cases with the laser intensity below 10^{20} W/cm^2, which is insufficient for current laser systems.

- Experimental data show, that the electron temperature scaling with the cube root of the laser intensity used by Gibbon & Bell (1.62) works properly also for higher intensities as shown by Beg [112]:

$$T_h^{Beg}[\text{keV}] = 215(I_{18}\lambda_\mu^2)^{1/3}. \tag{1.64}$$

1.3.2.2 Electron temperature scaling laws for relativistic laser intensities above 10^{20} W/cm^2

The Beg scaling (1.64) was moreover extended towards a fully relativistic model (i.e., for laser intensities $> 10^{20}$ W/cm^2) [113]. Therefore, relativistic Beg's scaling for hot electron temperature is often used for nowadays laser systems:

$$T_h^{BegR}[\mathrm{eV}] = \frac{m_e c^2}{e}\left\{\left[1+\frac{2}{m_e c}\left(\frac{m_e I}{n_c c}\right)^{1/2}\right]^{1/2}-1\right\}. \tag{1.65}$$

Although the ponderomotive scaling (1.63) can be potentially extrapolated to relativistic intensities as well, it significantly overestimates the electron temperature for $a_0 \gg 1$. For example, the electron temperature is nearly one order higher in comparison to both experiments and PIC simulations for $a_0 = 100$ [114].
All above described scalings rely strongly on a specific model of energy absorption, although it can be described by various processes (e.g., Resonant absorption, Brunel vacuum heating, $\vec{j}\times\vec{B}$ heating and others). The scaling law which does not suffer from this issue and works for relativistic intensities is Kluge's scaling [114]. Specifically, it is based on a weighted average of kinetic energy of an ensemble of electrons, thus it overcomes the need for a specific absorption model. In nutshell, it uses Lorentzian scalar steady state distribution function $f_t \propto 1/\gamma$ of the electron energy $\gamma(t)$ to derive a general expression for the electron mean energy $\langle\gamma\rangle$ (1.70). This mean energy is then identified with the hot electron temperature and the scaling is derived from the electron quiver motion in the EM wave, thus it is dependent on the laser intensity. When assuming an adiabatic laser ramp-up, normal incidence and a step-like density profile of a highly overdense plasma, following Kluge's scaling is valid [114]:

$$T_h^{Kl} + 1 = 1 + \frac{a_0^2}{4} + O(a^4) \qquad \text{for } a_0 \ll 1, \tag{1.66}$$

$$T_h^{Kl} + 1 = \frac{\pi a_0}{2\ln 16 + 2\ln a_0} + O(a^{-3}) \qquad \text{for } a_0 \gg 1, \tag{1.67}$$

where O-notation refers the growth rate of the error function and the temperature T_h^{Kl} is in units of $[m_e c^2]$. Furthermore, the *correction including ASE/prepulse* cases, i.e., when a certain amount of preplasma at the target front side is present, were published and it shows even better agreement with experiments and simulations (see Fig. 1.18) [114]:

$$p_x(t) = S - \frac{2}{S}, \tag{1.68}$$

$$S = \sqrt{\sqrt{(3a_0\sin\omega_0 t)^2 + 8} + 3a_0\sin\omega_0 t}, \tag{1.69}$$

where $p_x(t)$ is the electron momentum in transverse axis, when the laser pulse propagates along $z-$axis. The single electron energy evolution can be written as $\gamma(t) = \sqrt{1+\vec{p}^2}$, therefore $p_z(t) = p_x(t)^2/2$ assuming an adiabatic laser ramp-up. The scaling shown in Fig. 1.18 by the dotted line were hence obtained by averaging the inverse $\gamma(t)^{-1}$ over time and taking its inverse according to [114]:

$$\langle\gamma\rangle = \frac{2\pi}{\int_0^{2\pi}\frac{1}{\gamma}\mathrm{d}t}. \tag{1.70}$$

This important relation states that the average kinetic energy of the accelerated electrons is equal to the inverse of the unweighted average of the inverse of the single electron energy $\gamma(t)$ with respect to the laboratory time t in the laboratory frame; the factor 2π is the period of electron energy distribution function being the same as the period of the laser wave. Consequently, the average energy of an electron ensemble cannot be derived simply by averaging the single electron energy over the laboratory time [114].

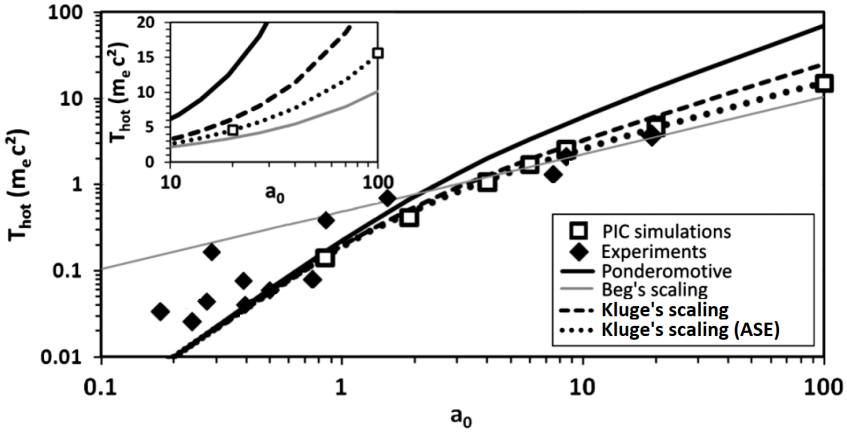

Figure 1.18: Comparison of various electron temperature scalings for high laser intensities showing the selected experimental values (diamonds) and PIC simulations (squares). Simulation(s) parameters and experiments references can be found in [114].

1.3.3 Transport of electrons through the target

A generation of hot electrons is an inevitable consequence of a laser interaction with a plasma. For further understanding of physical phenomena bounded with the electron transport and also with accelerating regimes themselves, it is crucial to study the parameters of the hot electrons such as their number, the charge (the current density is typically ~ 10 kA/μm^2 [115]) or the temperature as well as the generated fields. In the optimal situation, hot electrons carry $20-40\%$ of the laser energy. These electrons can reach the rear side of a sufficiently thin target (for given laser parameters) or they are stopped inside a thick target by binary collisions with particles of the material, which are no longer negligible. In reality, the situation is more complicated, because the induced electric ($E \sim 1$ TV/m) and magnetic ($B \sim 10$ kT) fields could deflect or suppress hot electrons flows [12], [115].
During the laser-plasma interaction, a very strong electric current i is generated [12]:

$$i_h = \frac{\pi\sigma^2 I \eta_a}{T_h}. \tag{1.71}$$

For example, when a half of the laser energy is converted into the hot electrons (i.e., $\eta_a = 50\%$), the hot electron temperature is $T_h \simeq 100$ keV and the laser pulse having the intensity $I = 10^{18}$ W/cm^2 is focused into the laser spot area of $\pi\sigma^2$; for example, we can expect the generation of the electron beam having the radius 25 μm and hence, according to (1.71), carrying the electric current $i_h = 10$ MA.
In fact, there is a maximum uncompensated current, so-called *Alfven current*, depending

only on electrons, that can be transported in the vacuum without deflecting at the edges by magnetic field [116]:

$$i_{Alf} = \frac{4\pi\varepsilon_0 m_e c^2 \gamma v_b}{e} \approx 17\frac{\gamma v_b}{c}[\text{kA}], \tag{1.72}$$

where v_b is the velocity of a monoenergetic electron beam with a finite radius. Generally, Alfven current i_{Alf} (1.72) has a lower value than the hot electrons current i_h (1.71); for instance, when the electron temperature will be $T_h \simeq 100$ keV, as in the previous example, Alfven current would be ~ 11 kA. This naturally leads to the conclusion, that another return current, compensating the hot electrons flow, have to be present in the plasma. In fact, free plasma electrons create the almost completely neutralizing beam having a comparable charge and current density, but propagating in the opposite direction than the hot electron flow. Nevertheless, the accessibility of these free plasma electrons depends on the material. Whereas for initially ionized plasmas, these electrons are free and thus well accessible, in the case of insulators, the local thermodynamic equilibrium has to be violated in order to get the electrons from their bound states. That can be done, for instance, by electric field ionization or by collisions between atoms and beam electrons [18]. As a response to hot and return currents, a longitudinal electric field is rapidly induced. Its magnitude is given by Ohm's law:

$$j_r = -j_h = \sigma_e E, \tag{1.73}$$

where σ_e is the conductivity of the target material bounded with the characteristic relaxation time $\tau_e = \varepsilon_0/\sigma_e$. In fact, for cold metals, it gives an extremely fast charge density response, typically $\tau_e \sim 1$ as, [12], [18].
The situation can be assumed as an electrostatic equilibrium. Consequently, the nonlinear diffusion equation can be solved, with the use of Maxwellian distribution and Ohm's law, by separating variables [12]. The effective penetration depth R_h of fast electrons (being valid when the laser pulse is still interacting with the foil) is then [12], [117]:

$$R_h = \frac{3T_h^2\sigma_e}{I_a}\ [\text{SI}] = \left(\frac{T_h}{100\ \text{keV}}\right)^2 \left(\frac{\sigma_e}{10^6\ \Omega^{-1}\ \text{m}^{-1}}\right) \frac{10^{18}\ \text{W/cm}^2}{I_a}\ 3\ \mu\text{m}, \tag{1.74}$$

where I_a is the absorbed laser intensity. The conductivity σ_e of the solid aluminum has been found experimentally as $0.5 \cdot 10^6 - 1 \cdot 10^6\ \Omega^{-1}\text{m}^{-1}$ for the temperatures in the range of $10 - 100$ eV [118]. Therefore, hot electrons are expected to penetrate up to $R_h \sim 10\ \mu$m inside the aluminum target, for the laser intensities around 10^{18} W/cm^2 and the absorption $\sim 40\%$ (which is a typical value for such laser intensity [119]). This penetration depth is much smaller than the collisional range of fast electrons [117].
When a target is thinner than the effective penetration depth, hot electrons can reach the rear side of the target, where they form a dense charge-separation sheath. Subsequently, a toroidal magnetic field B_θ is generated by outflowing electrons. This field is an originator of the kinematic force $E \times B_\theta$ which spreads the electrons into *a fountain* shape (so-called fountain effect [51]). This phenomenon is extremely important, e.g., for Target Normal Sheath Acceleration and Magnetic Vortex Acceleration where it is discussed in detail.
Unfortunately, the balance between the hot electron beam and the return current formed by free plasma electrons is unstable. The electron beam can break up into filaments (having the characteristic size of $0.1 - 1\mu$m [120]) in the direction of laser propagation because of Weibel instability [121]. This instability occurs due to the electron density perturbations,

which are perpendicular to the propagation direction. Furthermore, the perturbations could be further enhanced near the source, where the hot electron beam density n_h is high and on the contrary, the electron plasma density n_e is sufficiently low. Therefore, the growth rate of Weibel instability is given by the ratio n_h/n_e [18]. On the other hand, PIC simulations show that Weibel-originated hot electron filaments can subsequently coalesce due to mutual magnetic attraction [122]. In reality, a combination or a periodic repetition of the filaments generation and their merging occurs.
Notwithstanding, the hot electron current j_h is nearly canceled by the return flow j_r, there is still a little imbalance between them, which leads to the growth of the magnetic field via Faraday's law [12]:

$$\frac{\partial \vec{B}}{\partial t} = -\nabla \times \vec{E} = \nabla \times (\frac{\vec{j_h}}{\sigma_e}). \tag{1.75}$$

The displacement current $\partial E/\partial t$ is neglected in (1.75), because it is significant only before the return current had established itself.

Chapter 2

Selection of physical phenomena related to laser-driven acceleration

2.1 Relativistic self-focusing of laser pulse

2.1.1 Conditions required for optical channeling and self-focusing

Relativistic self-focusing of light, also known as optical guiding or channeling, is a consequence of ponderomotive force and a relativistic change in refractive index. These changes lead to the additional focusing of a laser pulse during its propagation through a self-induced channel in underdense plasma if the pulse has sufficient power. Such threshold power is called *critical* and, in the case of uniform ionized plasma, it can be expressed as [12], [123]:

$$P_c\ [\mathrm{GW}] = 17\frac{n_c}{n_e} \simeq 17\left(\frac{\omega_0}{\omega_p}\right)^2. \tag{2.1}$$

In other words, if the incident power P_0 is higher than the critical power P_c, the optical channeling occurs. For example, in the case of plasma with the electron density of 10^{25} m^{-3} and radiation at the wavelength of 800 nm, the relation (2.1) is satisfied for the laser pulse having the power higher than 3 TW. Since the laser intensity is defined as the optical power per unit area, which is transmitted through an imagined surface perpendicular to the propagation direction (i.e., a focal spot), the idealistic intensity of such laser pulse has the order of 10^{19} W/cm^2 for the focal spot of 3 μm. Such values are reachable with modern short-pulse lasers, which can exceed PW powers. For instance, a laser pulse of 30 fs and energy of 30 J has a peak power of 1 PW (the idealistic intensity corresponds to the order of 10^{22} W/cm^2 for the focal spot of 3 μm).
The high intensity laser pulse interacts with the electrons in the plasma and ensures their movement resulting in a relativistic change in the electron rest mass, i.e., from m_e to γm_e. In fact, the plasma frequency ω_p and the refractive index η are changed correspondingly. Assuming dispersion relation for a relativistic light wave $\omega^2 = c^2k^2 + \omega_p^{rel}$, the modified value

for the relativistic refractive index η^{rel} satisfies [12]:

$$\eta(r) \equiv \frac{ck}{\omega}, \tag{2.2}$$

$$\omega_p^{rel} = \sqrt{\frac{n_e e^2}{\gamma m_e \varepsilon_0}} = \frac{\omega_p}{\sqrt{\gamma}}, \qquad \gamma = \sqrt{1 + \frac{a(r)^2}{2}}, \tag{2.3}$$

$$\eta^{rel}(r) = \sqrt{1 - \frac{\omega_p^2}{\omega^2 \gamma}} = \sqrt{1 - \frac{\omega_p^2}{\omega^2 \sqrt{1 + a(r)^2/2}}}, \tag{2.4}$$

where n_e is the electron density, e is elementary charge, ε_0 is vacuum permittivity, ω is the laser frequency and $a(r) = a_0 \exp(-r^2/2\sigma_0^2)$ is the radially dependent dimensionless laser amplitude with σ_0 being the radius of a circular spot size.
The equations (2.2) – (2.4) demonstrate that with the increasing radial distance r from the laser propagation axis, the relativistic refractive index $\eta^{rel}(r)$ decreases. In other words, the refractive index $\eta^{rel}(r)$ is peaked on axis ($\mathrm{d}\eta/\mathrm{d}r < 0$) which indicates the occurrence of the focusing effect. Using Taylor series for a square root, the phase velocity v_φ of the wavefronts passing through a focusing media can be expressed, with the use of refractive index $\eta^{rel}(r)$, as [12]:

$$\frac{v_\varphi}{c} = \frac{1}{\eta^{rel}(r)} \simeq 1 + \frac{\omega_p^2}{2\omega^2}\left(1 - \frac{a^2(r)}{4}\right). \tag{2.5}$$

Obviously, the phase velocity is radially dependent and it predicts that the wave fronts move slower at the center than at the edges of the beam. Therefore, the laser radiation can be bent by this phase velocity difference by the maximum angle α [12]:

$$\alpha = \frac{\omega_p a_0}{8\omega}. \tag{2.6}$$

The focusing occurs, when the focusing angle α is grater than the divergence angle β, which results in the laser power threshold, similarly as in (2.1). Since the original laser power $P_0 \propto a_0 \sigma_0^2$, with the use of (2.6), the relation for this threshold is:

$$\alpha > \beta \tag{2.7}$$

$$\beta = \frac{\sigma_0}{Z_R}, \qquad Z_R = k\sigma_0^2, \tag{2.8}$$

$$a_0^2 \left(\frac{\omega_p \sigma_0}{c}\right)^2 > 8, \tag{2.9}$$

where Z_R is Rayleigh length, i.e., the length at which the focal area $\pi\sigma_0^2$ is doubled in size. It is worth mentioning, that the relativistic change in the refractive index η^{rel} is equivalent to the change in the phase velocity v_φ defined by (2.5). Hence, both the spatial and the temporal profiles of the laser intensity change during the self-focusing and during the laser propagation through the plasma.
Besides the change in the relativistic refractive index (i.e., in the wave front phase velocity), also the electron plasma density profile is modified due to ponderomotive force. When a laser pulse propagates through an underdense media, transverse ponderomotive force pushes light electrons from the place of high EM field, i.e., from the laser propagation axis, to the

area of lower EM field, i.e., to the sides. This causes the density drop on the laser axis and the corresponding electron density increase at the edges/outside from the borders of the laser propagation channel. If the laser pulse is sufficiently intense (no matter if because of additional focusing optics or of the self-focusing itself), the complete expulsion of electrons from the beam center towards the edges is expected. Such expulsion lasts as long as the laser pulse is present, assuming that ions are immobile, because of their high mass. Consequently, the laser pulse leaves behind a massive positively charged area which will undergo Coulomb repulsive explosion afterwards [12].
It is evident, that when a laser pulse propagates through a plasma, diverging photons gradually enter the region with various refractive indexes along the direction perpendicular to the laser propagation axis, see Fig. 2.1. Since the refractive index decreases with the increasing distance from the laser axis, the channel border has at exact level such refractive index that the reflection occurs. This phenomenon leads to the natural self-focusing and the plasma acts as a convex lens. Snell law illustrates well the described situation:

$$\frac{\sin\theta_1}{\sin\theta_0} = \frac{\eta_0}{\eta_1}, \tag{2.10}$$

where the total reflection case corresponds to $\sin\theta_1 = 1$. The phenomenon is schematically depicted also in Fig. 2.1, where the notation used in (2.10) is demonstrated.

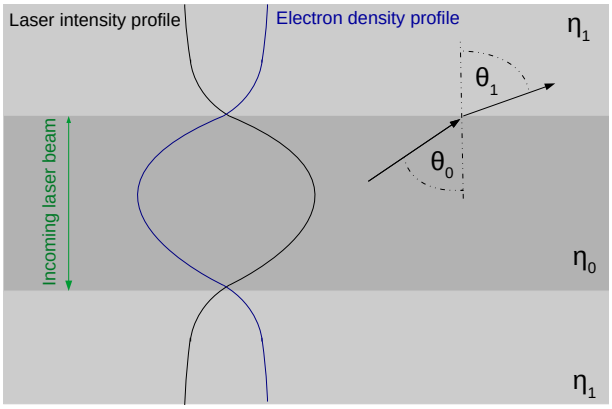

Figure 2.1: Schematic sketch of the self-focusing phenomenon of a sufficient-power laser pulse propagating in a plasma; η_1 and η_2 are refractive indexes related to each other as $\eta_0 > \eta_1$; θ_0 is the angle of incidence and θ_1 is the angle of refraction on the boundary between various refractive indexes.

In reality, the laser pulse would be focused and defocused repetitively until it loses enough energy. This can take even a few Rayleigh ranges [123].
The situation is more complicated in the case of short pulses, because the refractive index can be modified not only by the relativistic quiver motion of electrons, but also by the longitudinal bunching in plasma density [12]. Therefore, the requirement of reaching the critical power P_c in order to initiate self-focusing is strongly dependent on the spatial position along the laser pulse length [12], [124].

2.1.2 Filamentation of self-focused laser pulse

Among the conditions required for the laser pulse channeling through the plasma, it is also crucial to study the stability of the light propagation through the medium. The situation will be demonstrated on the example of the relativistic and charge-displacement channeling of intense short-pulses in homogeneous underdense plasmas.

- A *stable* propagation means the formation of the channel containing the power P_{ch} (being approximately $30-50\%$ [125] of the incident power P_0), which exceeds the critical power P_c:

$$P_{ch} \in \langle 0.3; 0.5 \rangle \cdot P_0, \qquad P_{ch} > P_c. \tag{2.11}$$

  Then, there are two possibilities:

  - only a single channel is formed (having $30-50\%$ of the incident power)
  - a main channel (having $30-50\%$ of the incident power) accompanied by a few smaller channels (containing the power comparable to P_c, similarly as the filaments produced during an unstable propagation) is created.

- The situation is defined as *unstable*, when the multiple channels are formed and each of them contains the power P_{ch}, which is comparable to the critical one, i.e., $P_{ch} \approx P_c$ [125].

In the case of stability, an increase of the incident power P_0 leads to an increase of the power P_{ch} confined in the main channel, i.e., $\mathrm{d}P_{ch}/\mathrm{d}P_0 > 0$. Contrarily, in the case of unstable situation, an increase of the incident power leads to a decrease of the confined power. In fact, with increasing P_0 (and the fixed value ρ_0), the number of filaments grows, but it does not lead to a higher power trapped in the individual channel. It was reported, that a sufficiently high level of the initial power can lead to an unstable behavior resulting in the filamentation [125].
Two dimensionless parameters are defined in order to describe a stable and an unstable laser light propagation in a plasma:

1. the normalized incident power of the laser pulse ζ; $\zeta = P_0/P_c$, where P_c denotes the critical power required for the occurrence of the relativistic charge-displacement self-channeling (see (2.1)),

2. the material parameter ρ_0; $\rho_0 = \sigma_0 \omega_{p,0}/c$, where σ_0 stands for the radius of the focal zone and $\omega_{p,0}$ is the unperturbed plasma frequency [125].

It was investigated, that the stability of the laser propagation through a plasma slightly depends also on its spatial profile [125], see the stability maps for hyper-Gaussian and Gaussian beams in Fig. 2.2. Nevertheless, the laser propagation through the plasma is stable for a very wide range of ρ_0, no matter the laser spatial profile, when the parameter ζ satisfies $1 < \zeta \lesssim 10$. The stability is moreover highly tolerant against a substantial level of azimuthal perturbations. Furthermore, it is worth mentioning that for $0.5\ \rho_{e,0} \lesssim \rho_0 < \rho_{e,0}$ (where $\rho_{e,0}$ is a dimensionless radius of the zeroth eigenmode of the laser radiation defined by (3.6) – (3.11) in [125]), the propagation does not lead to the self-focusing at all [125], see Fig. 2.2.
Besides studies performing homogeneous plasmas, also pre-formed plasma channels [125] and

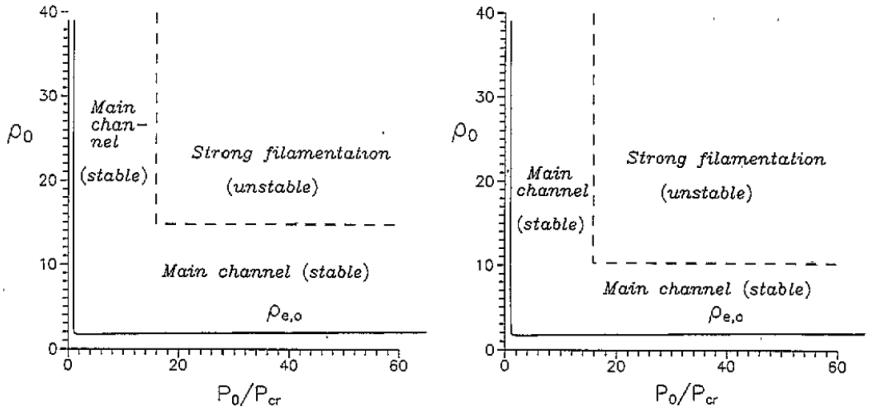

Figure 2.2: Stability maps for relativistic and charge displacement self-channeling of *Left:* hyper-Gaussian beams ($N = 8$) or *Right:* Gaussian beams ($N = 2$) in initially homogeneous plasmas; [125].

purely relativistic self-channeling were studied [126]. Nevertheless, the self-focusing generated solely by relativistic mechanisms was demonstrated to be strongly unstable when $\zeta \gg 1$. In other words, a ponderomotively driven charge displacement studied in [125] is crucial for stabilizing the propagation.

2.2 The role of laser prepulse & preplasma in laser-driven acceleration

2.2.1 Realistic laser profile including prepulse and pedestal

The profile of a realistic laser pulse does not only varies in the shape from ideal Gaussian or SuperGaussian beams, but it also includes multiple compressed prepulses, a pedestal of amplified spontaneous emission (ASE) and a so-called coherent pedestal, which is the slope rising slower compared to an ideal Gaussian pulse [127], see the example of realistic laser pulse profile in Fig. 2.3.
The so-called *laser contrast* is the ratio between the peak pulse intensity and any prepulse or pedestal (ASE) intensity [65] which makes it a crucial parameter for laser-driven ion acceleration experiments. Within this work, as well as more frequently in the literature, a laser contrast refers to the ratio between the main laser peak and the strongest femtosecond laser prepulse (because it typically reaches the second highest value). In fact, the realistic laser pulse features have to be taken into account when designing/using the targets, because, when the laser contrast is low, the prepulse may destroy the thin foils or the structures both at the front and at the rear side of the thicker targets before the main pulse arrives. Naturally, the laser prepulse is thus widely taken as an unwanted feature and in practice, it is usually suppressed (i.e., partly filtered out) by expensive plasma mirrors [128]. On the other hand, the specific conditions may assure that correspondingly generated preplasma can be advantageous for laser accelerated particle beam in terms of, for example, enhanced particle energy and more homogeneous density profile as will be discussed in the following section.

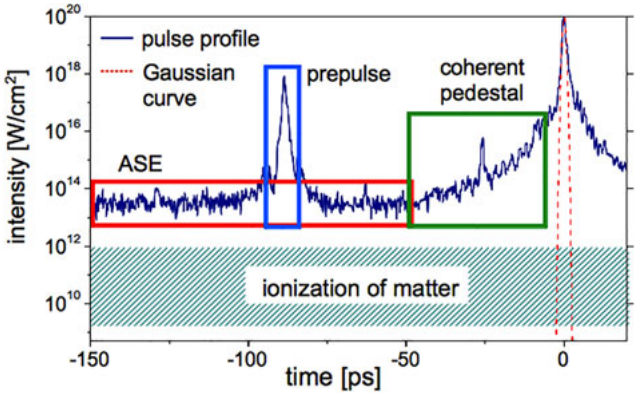

Figure 2.3: Temporal profile of the PHELIX pulse in 2010 before the application of pulse cleaning techniques. The curve has been scaled to a peak intensity of 10^{20} W/cm^2. The shaded area illustrates the ionization threshold for typical target materials. The red dashed line shows a Gaussian function with the same FWHM as the pulse (blue) [127].

2.2.2 The impact of generated preplasma on laser-driven particle acceleration

The difficulties bounded with the laser prepulse in laser-driven acceleration experiments lie in the fact that it heats, evaporates and ionizes the target which leads to the various changes in laser-target interaction as well as in the acceleration process. In fact, the created preplasma cloud at the target front side (being formed typically on the timescale of nanoseconds) may change significantly the parameters of the propagating main laser pulse before it reaches the solid density region (if it is still present) and/or modify the interaction itself. Hence, the parameters of the accelerated particle beams would be changed accordingly. Naturally, the high laser prepulse is detrimental for targets having structures on the front side, because they can be destroyed before the main pulse comes. Indeed, the same issue is relevant also for the structures at the target back side, when the shock wave, generated in the material by the laser prepulse, arrives at the rear side before the main laser pulse interaction [129], [130], [131]. This can affect, for instance, proton divergence which was intended to be reduced by the target design.
The higher particle divergence is one disadvantage of the preplasma presence, which is important for the scope of this dissertation. In fact, the increasing divergence of hot electrons has been demonstrated to be approximately linearly dependent on the growing preplasma scale length. That can be explained by a larger interaction volume being available for longer scale lengths [132], [133]. The result came from simulations, which are nevertheless in great agreement with data obtained from experiments. Both flat targets and targets with drilled cone towards the foil center (by the laser prepulse) having preplasma at the front side have been performed and compared to the experimental data. There, the divergence has been extracted from the difference between K_α spectra recorded at different position inside the target. This was done by placing fluor layer in various depths inside the target. Additionally, it was shown that, for the same scale lengths, the laser intensities between $\sim 10^{18-21}$ W/cm^2 have nearly no effect on laser-accelerated electron beam divergence [132]. Previous work [134] also demonstrated that the hot electron divergence increases with preplasma presence. There, it was connected to the rising size and the higher strength of the quasistatic magnetic fields

originated from Weibel instability connected to the increasing scale length of the preplasma. Higher hot electron divergence bounded with the preplasma naturally affects proton and ion divergence.
Generally, the exact profile of the realistic laser pulse is hardly predictable. Nevertheless, the prepulse duration may be controlled by ultra-fast Pockel's cells [129]. Even though the laser prepulse is usually taken as a disadvantage in laser-driven particle acceleration experiments (e.g. due to a higher particle divergence [132], [133], [134], a disintegration of the target and corresponding lowering of the conversion efficiency from the light to the particles or due to not efficient formation of TNSA-accelerating field formed at the target rear side [72], [135]), it can be also beneficial in some occasional cases, if it is sufficiently controlled. Namely, preplasma can contribute to the increasing of the main pulse absorption [136], [137], [138] or assure relativistic self-focusing of the main pulse as mentioned earlier [139].
For example, the duration of the laser prepulse influences the maximum proton energy. In fact, for each duration of the laser prepulse exists an optimal target thickness where the cut-off proton energy is significantly enhanced. Specifically, this feature has been studied for sub-ns and low ones of ns prepulses in [129]. Thinner targets than the optimal value result in lower energies because the preplasma is created not only at the front but also at the back side of the target which is the problem because it limits the accelerating field of rear-TNSA [72], [135]. Similarly, thicker targets than the optimal value do not have any big impact on proton energies with varying prepulse duration, because the step-like density profile at the rear side is still conserved. In such case, the trend of the increasing thickness leading to the decreasing proton energies is therefore the classical effect known e.g. from TNSA theory and experiments with optimal laser pulses (i.e., having high laser contrast) [129]. To summarize, the *optimal thickness of the target* means as thin target as possible which still has, after the interacting with laser prepulse, the step-like density profile at the rear side (in order to get the high accelerating TNSA field) as well as the preplasma at the front side. That allows to non-linear effects such as self-focusing and pulse front steepening occur [139], [140]. As a result, the duration of the main pulse is shortened and the spot size is reduced leading to the increase of the main laser pulse intensity and the enhancement of particle energies.
Moreover, the proton beam spatial profiles depends on the target dimension as well. In the case of the optimal target thickness for a given prepulse duration, the proton spatial profile has rather collimated features around target normal rather than the blurry image present when the target was too thin [129]. The difference lies in the specific location of efficient acceleration – whereas protons are accelerated only from the target front side when the thickness is thinner than the optimal one, acceleration takes place from both target surfaces in the case of targets having optimal or bigger thicknesses. On the other hand, the optimal target thickness seems to be independent from the laser intensity, which affects primarily the maximum proton energy.
Currently, a higher attention is paid to short fs-prepulses. A numerical model [141] valid for femtosecond prepulses describes the evolution of targets as a function of laser intensity and time. Experiments enhancing proton energies by varying intensity of fs-prepulse between $\sim 10^{13}-10^{16}$ W/cm^2 have been reported (the main laser pulse had intensity of $4.5{\cdot}10^{19}$ W/cm^2 and the target thickness was 2 μm) [140].
In the context of laser prepulse and generated preplasma, the role of standing wave (created due to the interference of incident and reflected laser pulse) in the generation of hot electrons has been studied [142]. In the case of high laser intensities relevant for this dissertation ($\sim 10^{21}$ W/cm^2) and step-like density profiles, the hot electron motion is affected by the

inward deformation of the target front surface by the radiation pressure. In fact, this causes not-optimal interference of the incident and the reflected laser light. In the case of normal incidence, electrons are accelerated at vacuum-plasma boundary by $\vec{j} \times \vec{B}$ mechanism. When the exponentially increasing density profile is present at the target front, all accelerated electrons originate from the preplasma region, which results in a significantly higher temperature. Two populations of electrons were observed [142]. The first one rises at the laser pulse front, the second one originates from the laser pulse surroundings and forms bunches separated by $\lambda/2$, which resembles again $\vec{j} \times \vec{B}$ heating (as in the case with the step-like density profile, even tough the electrons were accelerated rather in preplasma than in the overdense target). Due to the standing wave and the formed channel in the preplasma, the second "bunched" population are injected to the high field region (i.e., towards the laser propagation axis) where they are accelerated further towards the overdense target. It was also demonstrated, that a longer preplasma scale length results in higher electron energies because of the longer interaction length of electrons with the standing wave [142].
To summarize, the laser prepulse can indirectly lead to the temporal change of the main laser beam parameters (e.g. to self-focusing of the beam) and therefore to the establishment of the required conditions for enhanced electron heating resulting in the proton energy increase or possibly in the establishment of different, more efficient, acceleration regimes.

2.3 Magnetic field generation in laser-plasmas

2.3.1 Generation of magnetic field in overdense plasma

A generation of magnetic fields having megagauss or even gigagauss range [100] (i.e., from hundreds to tens of thousands of Tesla) is an essential phenomenon during laser-plasma interaction. In fact, a number of phenomena can lead to a magnetic-field generation in dense plasmas as summarized in [143]. In a nutshell, all mechanisms have in common a breaking or an absence of symmetry followed by the creation of electron current loops. In the case of short pulses interaction, at least three general cases can be distinguished [100].
Firstly, magnetic fields generation resulting from Direct currents (DC) in steep density gradients or from Hot electron currents occurs on the hydrodynamic time scales. In other words, such mechanisms usually last longer than the duration of currently used short laser pulses. On the contrary, the magnetic field generation driven by the Radial thermal transport takes place predominantly at early times (i.e., the times shorter than the pulse length) in the solid (overdense) region.
Experimental values of MG magnetic fields in a short laser pulse interaction with plasma were obtained due to the measurements of Faraday rotation [144], [145], [146], although this method can be used only for the underdense part of the density profile. It is because the polarized electric field rotates when propagating along the magnetic field in a dielectric or a plasma medium (therefore this medium has to be transparent for the laser radiation). The angle of rotation is proportional to the magnitude of the magnetic field [13]. Two regions of magnetic field with reversed sign were found, which is in a good agreement with the below described theory as well as with hydrodynamic simulations [147]. High magnetic fields were experimentally investigated also using polarization measurements of the self-generated high order laser harmonics, which allows to see further inside the dense regions of the target [148].

2.3.1.1 Radial thermal transport

Magnetic field is generated when the electric field has not vanishing curl:

$$\nabla \times \vec{E} = -\frac{\partial \vec{B}}{\partial t}. \tag{2.12}$$

The fluid equation of the momentum conservation for electrons is following [13]:

$$\rho \frac{\partial \vec{u}}{\partial t} + \rho(\vec{u} \cdot \nabla)\vec{u} = -\nabla P + \vec{F_L}, \tag{2.13}$$

where Lorentz force $\vec{F_L}$ satisfies $\vec{F_L} = q(\vec{E} + \vec{u} \times \vec{B})$, $\vec{u}$ is the electron velocity and ρ is the electron mass density.
Then, if two assumptions are taken: (i) the electric field keeps the quasinetrality on a large scales (i.e., much larger than Debye length) and over a long time (i.e., much longer than the laser pulse duration) and (ii) the volume force is given in the plasma mainly by the electric field; the inertia of electrons can be neglected (assuming the steady state) together with the magnetic field in Lorentz force and we can rewrite (2.13) as [13]:

$$0 = -\nabla P - e n_e \vec{E}. \tag{2.14}$$

Furthermore, with the use of ideal gas equation of state $P_e = n_e k_B T_e$, it can be shown, that the magnetic field originates from *a thermoelectric* source term, when the electron temperature and density gradients are not parallel [13], [100]:

$$\frac{\partial \vec{B}}{\partial t} = \frac{k_B}{e n_e}(\nabla T_e \times \nabla n_e), \tag{2.15}$$

where the equation was derived by substituting the electric field from (2.14) into (2.12) and then by using the mentioned ideal gas state relation for P.

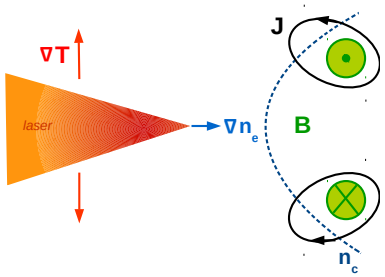

Figure 2.4: Geometry of thermoelectric magnetic field generation $\nabla T_e \times \nabla n_e$.

If the density gradient is directed along the target normal, i.e., $\nabla n_e / n_e \approx (L_{||})^{-1}$ and the temperature gradient is perpendicular, i.e., $\nabla T_e / T_e \approx (L_{\perp})^{-1}$, the magnitude of the magnetic field can be approximated as follows [13], [149]:

$$B \text{ [MGauss]} \quad \approx \quad 10 \left(\frac{\tau}{1 \text{ ns}}\right) \left(\frac{k_b T_e}{1 \text{ keV}}\right) \left(\frac{30\ \mu\text{m}}{L_{||}}\right) \left(\frac{30\ \mu\text{m}}{L_{\perp}}\right), \tag{2.16}$$

where τ is the laser pulse duration or the charasteristic loss time due to an ablation and a diffusion.

The corresponding magnetic field generation is schematically depicted in Fig. 2.4. In this scenario, the underdense plasma is expanding from the target, because the magnetic field pressure becomes comparable to the plasma pressure. Plasma plumes were observed in the experiments [112], [149] as well as in fully self-consistent MHD simulations [150]. In addition, an axial magnetic field can be generated by the electron currents in the preplasma by Inverse Faraday effect.

2.3.1.2 Direct currents (DC) in steep density gradients

A gradient in the time-averaged laser intensity drives Ponderomotive force F_p which pushes the electrons away from the high field, i.e., away from the focal spot. The electric field originating from the charge separation arises and the affected electrons acquire the velocity [100]:

$$v_p \propto m_e^{-1} F_p \propto \nabla E^2. \tag{2.17}$$

A nonlinear ponderomotive current of electrons creates the loops and satisfies $J = e n_e v_p \sim n_e \nabla I$. Hence, as schematically depicted in Fig. 2.5, Ampere's law gives the proof that a gradient in the laser intensity (i.e., the radial intensity profile) perpendicular to a gradient in the density drives a generation of the magnetic field:

$$\nabla^2 B \sim \nabla \times J \sim \nabla n_e \times \nabla I. \tag{2.18}$$

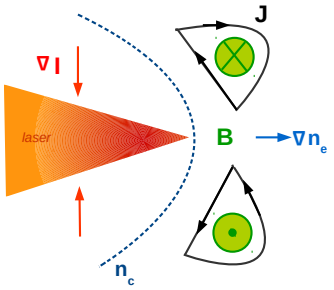

Figure 2.5: Geometry of ponderomotively generated magnetic field $\nabla n_e \times \nabla I$.

The orientation of such generated magnetic field has the opposite polarity than that created by $\nabla T_e \times \nabla n_e$ term in the previous case, see Fig. 2.4. However, the predictions of the magnitude of ponderomotively generated magnetic field vary depending on the theoretical model used [100]. For example, the case derived in [13] gives the magnetic field of 1 MG for the electron temperature of 1 keV and the pressure scale length of 30 μm according to the relation:

$$B\ [\text{MGauss}] \quad \approx \quad \left(\frac{m_i}{m_p}\right)^{1/2} \left(\frac{T_e}{1\ \text{keV}}\right)^{1/2} \left(\frac{30\ \mu\text{m}}{L_{||}}\right), \tag{2.19}$$

where m_i and m_p are the ion and the proton masses, respectively.

2.3.1.3 Hot electron currents

Hot electron current, both directed into the target or flowing along the target surface, is able to generate magnetic field similarly to previous two mechanisms. In contrast to ponderomotively generated electron flows, hot electron current is a natural consequence of collective absorption mechanisms described in the section Electron heating/accelerating mechanisms at the critical surface. As already discussed, the hot electron flow is usually partially balanced by the cold electron flow, which is the reason why the magnetic field generated this way is much lower than that originated from the previous scenarios driven at the target surface [100]. Specifically particle-in-cell simulations [151] give the values in the region of 100 MG for the laser intensity of 10^{20} W/cm^2.

2.3.2 Generation of magnetic field in underdense plasma

In underdense plasma, a stationary (DC) magnetic field is generated in the plasma wake behind the laser pulse. Magnetic fields results from the high order nonlinearities, such as the relativistic drag effect or mass increase. Similarly, the fields can be induced by nonlinear behavior in electrostatic waves due to geometrical effect – e.g. steepening and frequency shifts [152]. The quantitative analysis of the magnetic field is based on various 3D fluid models, which agree on the fact, that the field has both oscillatory and static components and that the amplitude scaling depends on the laser intensity as [100]:

$$B \sim \begin{cases} \frac{a_0^4}{\sigma_L} & a_0 \ll 0 \\ \frac{a_0^2}{\sigma_L} & a_0 \gg 0 \end{cases} \tag{2.20}$$

where σ_L is the laser spot size in units of c/ω_p.

2.3.2.1 Inverse Faraday effect in cold plasmas

The axial magnetic field can be also created in a medium due to the rotation of the electromagnetic field. This phenomenon is called Inverse Faraday effect and is usually observed in the case of a plasma interaction with circularly polarized laser pulses. In fact, when the laser light is *circularly* polarized, the electrons quiver with the oscillating electric field of the incoming laser light and they undergo a *circular* motion [13]. Correspondingly, a current loop at the edge of the plasma creates the magnetic field observed in the experiments [42] and schematically depicted in Fig. 2.6.
The estimation of the amplitude of such generated magnetic field is following [41]:

$$B\ [\text{Gauss}] \quad \sim \quad 6.5 \times 10^5 \left(\frac{n_e}{n_c}\right)^{1/2} \left(\frac{I}{10^{14}\ \text{W/cm}^2}\right)^{1/2}. \tag{2.21}$$

The equation (2.21) was derived from the experimental results [41] for the laser intensities between 10^{10} W/cm^2 and 10^{13} W/cm^2. For instance, according to this relation, the magnetic field of 150 kGauss are generated when the laser pulse having the intensity of 10^{13} W/cm^2 interacts with 0.5 n_c dense plasma. However, in the case of the higher laser intensity (e.g., 10^{14} W/cm^2), the experimental values are larger than those estimated by the equation (2.21) [13].

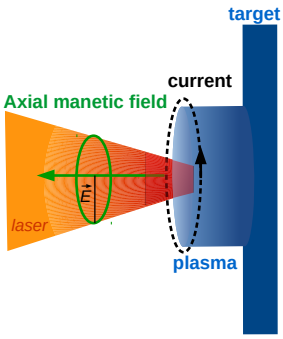

Figure 2.6: A schematic presentation of the Inverse Faraday effect.

2.4 Multipole magnets

The results from Particle-in-cell simulations performed within this work show the similarities in the magnetic field formation and its consequences with magnets used in accelerator physics. Generally, multipole magnets are often used in conventional accelerators and both conventional and laser-driven beamlines in order to, for instance, select the exact energy of particles, to tune the parameters of accelerated particle beam (e.g., divergence, emittance, spatial uniformity) or in order to assure the smooth beam handling and its propagation through a beamline. In following sections ideal multipoles as well as the examples of realistic magnets and their usage will be discussed from the point of view of particle accelerator physics [153], [154].

2.4.1 Ideal multipole magnetic field

An exactly shaped magnetic field can be created by the set of multipoles in the sense of a superposition principle. If we consider a cross section of an infinitely long magnet in 2D planar geometry $(y-z)$, the complex Fourier series expressing the vertical and the horizontal magnetic field components B_y and B_z are [155]:

$$B_y + iB_z = \sum_{n=1}^{\infty} C_n \cdot re^{i\theta(n-1)} = \sum_{n=1}^{\infty} (B_n + iA_n) \cdot (z+iy)^{n-1}, \tag{2.22}$$

where θ is the angle formed by the position vector r representing the number in complex plane and C_n is the Fourier coefficient; B_n and A_n are multipoles of the field, that determine the shape of the field lines. In fact, all multipoles can be obtained in their *normal* or *skew* versions. Whereas *normal* magnets have their poles separated by $360°/2n$, their *skew* equivalents are rotated by $180°/2n$, where n is the order of the multipole, see Fig. 2.7.
For example, the first order multipole has the only non-zero component in (2.22) either the term B_1:

$$B_z = 0, \qquad B_y = B_1, \tag{2.23}$$

or the term A_1:

$$B_z = A_1, \qquad B_y = 0. \tag{2.24}$$

In the first case, the magnetic field is oriented in the y-direction and a perfect *normal dipole* occurs. In the second case, the magnetic field is oriented in the z-direction and a perfect *skew dipole* occurs. A normal dipole magnet is therefore usually oriented perpendicularly to the plane of accelerator, whilst a skew notation means parallel to or in the plane of accelerator. Similarly, the second terms of Fourier series B_2 and A_2 correspond to the normal and skew quadrupoles (i.e., magnets having four poles), B_3 and A_3 to the normal and skew sextupoles (i.e., magnets having six poles) and so on. Therefore, the magnetic field amplitude, in the case of pure normal multipoles, scales as:

$$|B| = B_n r^{n-1}, \tag{2.25}$$

where r is the distance from the center and n is the order of the multipole. In fact, some literature defines also zeroth order multipole in the form of helix, so-called *solenoid*. This special case is not included in the (2.22), because the magnetic field inside the solenoid is parallel to the longitudinal axis and its magnitude follows $B = \mu_0 NI/l$, where NI is the total number of ampereturns and l is the coil length. In contrast to other multipole magnets, the field in the middle of solenoids and dipoles is not equal to zero [155], see also Fig. 2.7. The rest of multipole magnets imparts a force proportional to the distance from the center r as derived in (2.25). Therefore, the equipotential lines of the field are denser near the edges of the magnet which indicates that the field is stronger there.

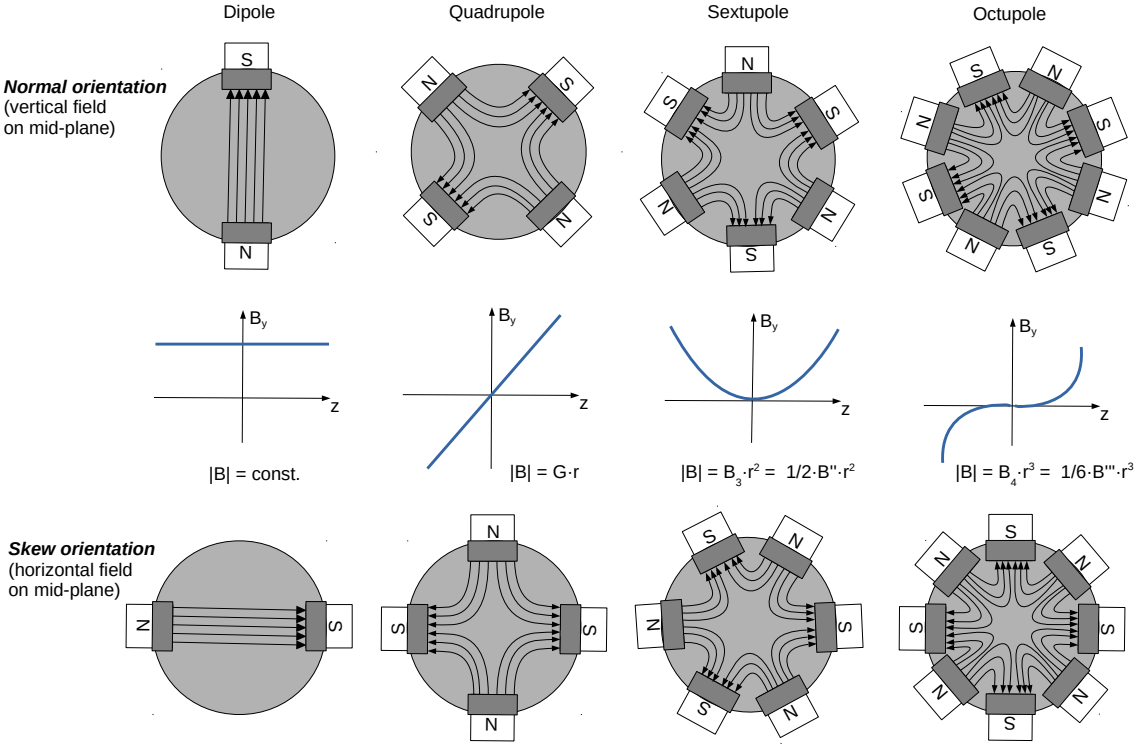

Figure 2.7: Magnetic multipoles of the order $n = 1, 2, 3, 4$ presented in their normal and skew orientations. The magnetic field lines are depicted in 2D plane $(y - z)$ and the field dependence is shown below each normal multipole.

According to the multipole order, we can distinguish:

- *dipole* having two poles and the uniform magnetic field with the amplitude $|B| = B_1$. Dipoles are used to bend particle beams [6], [153].

- *quadrupole* having four poles; the magnetic field amplitude increases linearly with the distance from the center, i.e., $|B| = B_2 r$. The parameter called the quadrupole strength k is introduced as a ratio between the quadrupole gradient G ($G \equiv B_2$) and the beam rigidity $B\rho$, i.e., $k = G/B\rho$. The parameter ρ is the radius of the trajectory curvature of a particle passing through the magnetic field where it is deflected. Consequently, quadrupoles are used to focus particle beams.
  A normal quadrupole field naturally focuses particles in one plane only, because in the another it has a defocusing effect [153], [154], see Fig. 2.8. Transverse motion of particles can be treated separately in vertical and horizontal plane according to linear beam dynamics, which results in so-called focusing and defocusing planes [153]. In other words, a perfect normal quadrupolar symmetric field will produce an asymmetric particle beam. Normal quadrupoles act as a chromatic lens, which means that the focusing effect depends on the energy of passing radiation [156]. In contrast to this, in the case of skew quadrupoles, the perturbation in field causes a coupling of both horizontal and vertical oscillation and an independent treatment of these planes is not possible anymore [153]. Skew quadrupoles are used, e.g., for correction of betatron coupling [157] (i.e., the coupling between transverse and longitudinal electron oscillations in betatron motion which are usually desired to be minimized).

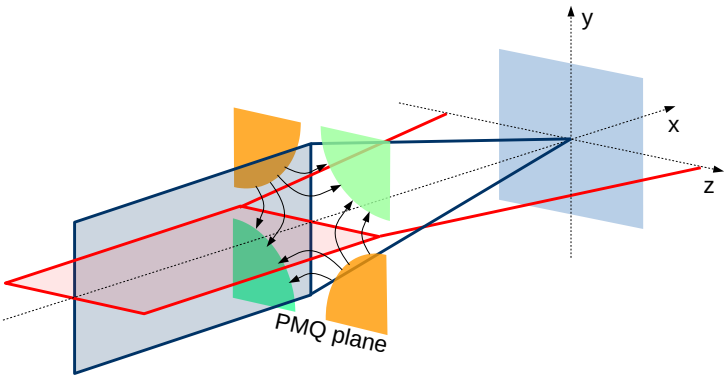

Figure 2.8: Sketch demonstrating focusing and defocusing plane for particle beam passing through normal quadrupole field.

- *sextupole* having six poles; the magnetic field amplitude increases with the distance from the center as $|B| = B_3 r^2$. Usually, the corresponding third order Fourier term is often described as the second derivative of the field, i.e., $B'' = 2B_3$. Sextupoles are used to correct beam chromaticity [158], [159] (particles in the beam are not monochromatic as they have an energy spread). Therefore, sextupoles are usually placed behind quadrupoles which focus differently particles with different energy.

- *octupole* having eight poles; the magnetic field amplitude increases with the distance from the center as $|B| = B_4 r^3$. Usually, the corresponding fourth order Fourier term is often described as the third derivative of the field, i.e., $B''' = 6B_4$. Octupoles are used to enhance particle beam spatial uniformity [153], [160].

- decapole, dodecatpole,... etc.

2.4.2 Realistic unideal multipole magnets

In reality, there is nothing like an ideal n-pole magnet, because all magnets have various contributions showing up in the higher harmonics of their Fourier spectrum. In other words, besides the strongest main multipole, also other orders of magnetic field occur in a realistic multipole magnet. In fact, two types of *error higher harmonics* can be distinguished: so-called *allowed* and *non-allowed* [153], [154]. The allowed harmonics are the additional multipole fields, usually much lower than the main multipole, nevertheless always present in every multipole magnet. Allowed harmonics can be only suppressed, but never removed. The probability and the strength of exact allowed multipole contributions depend on their order, i.e., on their position in the Fourier spectrum. For example, in the case of a quadrupole magnet, the third harmonic, i.e., a sextupole field, would appear first. On the contrary, not-allowed harmonics are magnetic field orders classified as an *errors*, when the optimal situation is somehow violated. High non-allowed orders can result from assembly asymmetries, not optimal proportions, material non-homogeneities, manufacturation errors, not precise geometry/positioning or/and from magnet's finite dimensions [153], [161]. The complete analysis of allowed and non-allowed harmonics of real accelerator magnets has to be provided and the components carefully suppressed or balanced, see the example for the case of ELIMAIA beamline in [162]. Sometimes magnets are designed to have more than one multipole component in purpose, because it can be beneficial or even required in accelerator beamlines. One of the most common type of these *combined function* magnets is a dipole with quadrupole component which is being used to steer and focus a particle beam simultaneously [155] or a quadrupole with sextupole component which is being used to compensate the natural chromaticity and in order to save space in experimental setups [159]. Octupole magnets are usually used in combination with quadrupoles for correction of spherical aberrations [163]. Also solenoids can be combined with quadrupole magnets in order to achieve rotated focusing magnetic fields to cancel an emittance growth [164].
Besides combined function magnets, more multipoles having the same order can be placed behind each other in order to ensure the required effect on the particle beam propagating through. The example is here demonstrated on the 4−pole magnet case. Quadrupoles are widely used in accelerator beamlines as already mentioned – *normal* quadrupoles for particle beam focusing, whilst their *skew* orientation for correction of betatron coupling [157] (both conventional accelerators [158], [166], [167], [168], [169] and laser-driven ones [6], [170] are included). In fact, focusing in both directions can be done by placing more quadrupoles behind each other with the separating distance smaller than their focal length and with an exact rotation of each magnet in respect to the previous one. Such focusing system is built on the FODO principle from optics, where FODO stands for focus-drift-defocus-drift. In principle, the first element of the FODO lattice from quadrupole magnets focuses the beam, e.g., in $x-y$ plane and defocuses it in $x-z$ plane. The following element is rotated by 90° and does the opposite, which creates focusing effect in both planes. Of course, the positioning must be

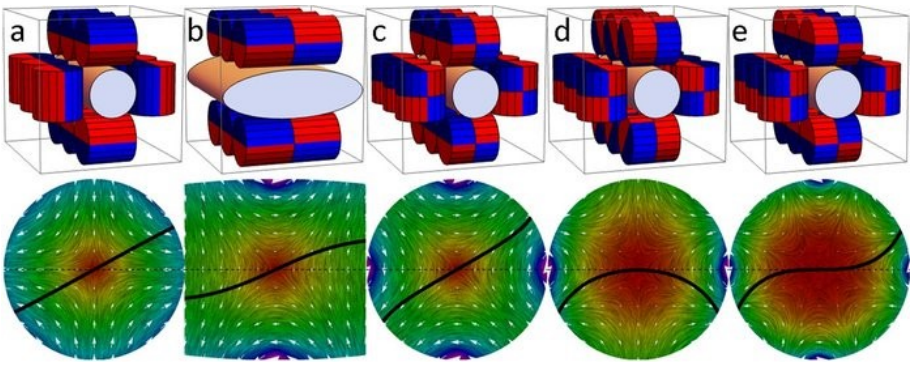

Figure 2.9: Variable period undulator magnet structure configured as multipole lenses (top) and corresponding field profile in the aperture (bottom): (a) skew quadrupole, (b) APPLE-II quadrupole, (c) quadrupole, (d) sextupole, (e) octupole [165].

very accurate [158], [171]. Sometimes, three quadrupoles are used in a sequence to have both vertical and horizontal focal points in the same position [153], [154]. Furthermore, a single skew quadrupole is often placed after a few normal quadrupoles, in order to correct tilting of the particle beam by rotating its plane [167], [169].
Multipole magnetic field used in accelerators is usually a result of the various multipoles placed in the exact geometry. For this reason, a standard multipole field can differ not only in the amplitude, but also in the shape and the slope of the field characteristics even within the same multipole order, see Fig. 2.9.
The magnetic field strength represented by the *magnetic flux density* corresponds to the number of the field lines penetrating a given area. The magnet is considered as an *open circuit* and its strength is directly related to the material (specifically to the material relative permeability) and the length to diameter ratio [153], [154], [172]. For example, magnets with small poles and long lengths have much higher open circuit flux density than short magnets with relatively large diameters, even when they are manufactured from the same grade of magnetic material [173]. Therefore, when a specific magnet measuring, e.g., 1 T on the poles is cut in its half, the result is definitely NOT the two smaller length magnets of the same Gauss reading in open circuit. Usually, magnets are designed to be at least two times longer than their thickness in order to let the field properly develop. In fact, the right geometry and shape of magnets are crucial in order to predict and to optimize the resulting field as well as in order to tune the amplitude of high order harmonics. For example, to compensate the non-infinite poles, the shims are added at their edges. The area and the shape of the shims are crucial for the strength of the field error amplitudes. In fact, the tapering of the poles may be necessary when high magnetic fields are present in order to provide small chamfer angles [174].

Chapter 3

Methods: Particle-in-cell simulations

Plasma is a partially or a fully ionized system of particles (free electrons, ions and possibly also neutral atoms) which shows collective behavior. In other words, particles interact with each other due to self-consistently induced electric and magnetic fields.
So-called *Particle-in-cell* (PIC) is one of the most favorite algorithms in plasma physics dating back to 1950's, i.e., even before the first usage of fortran language [175]. PIC code merges a high number of real particles into virtual macroparticles, which can move freely in the simulation box and interact with each other due to EM fields discretized on a finite mesh.
Simulations based on PIC numerical approach are used for the systems in which the force on any particle dominates by the sum of its interactions with distant particles, rather than by the contributions from its nearest neighbors. Such system is called collisionless or uncorrelated, i.e., Coulomb collisions are ignored. In fact, many plasmas showing collective behavior can be described in this way sufficiently. Also simulations presented in this work are collisionless, because high electron temperatures (and corresponding velocities) are expected in high-intensity laser-plasma interactions. Therefore, the collision frequency ν_{ie} is low; $\nu_{ie} \sim 1/T_e^{2/3} \sim 1/v^3$. Nevertheless, collisions can be added in PIC codes by various models based on Monte Carlo simulations [176].

3.0.1 Various approaches to plasma modeling

Before a brief description of Particle-in-cell method itself will be discussed, it is beneficial to summarize the approaches, which are usually used for plasma modeling. In general, plasma can be described from the *microscopic* (i.e., by using the exact values for individual particles or by the particle distribution function) or from the *macroscopic* point of view (i.e., by using the measurable variables of the system, such as temperature, pressure etc.). Therefore, we can distinguish Kinetic and Fluid (Hydrodynamic) descriptions of plasma, respectively. If the possibility of a combined description is needed, the Hybrid codes lying between discrete and continuous approaches are used [100], [177], [178], [179].

- **Kinetic models** employ either (macro)particles or the general distribution function $f_\alpha(t, x_\alpha, v_\alpha)$, where the index α represents particle species. The firstly mentioned is used for Particle methods (i.e., Particle-Particle Methods; Particle-Mesh methods (PIC) and

Mesh-Free Methods (Tree codes)), whilst the second mentioned is utilized in the statistical methods solving Boltzmann transport equation (3.4) for the distribution function. When the detailed knowledge of all involved physical processes on a single particle is crucial, plasma is usually described as a **particle-particle** system, i.e., the system of charged (macro)particles, which interact with each other and move freely in a space under the influence of electric $\vec{E}$ and magnetic $\vec{B}$ fields described via Maxwell's equations:

$$\nabla \times \vec{E} + \frac{\partial \vec{B}}{\partial t} = 0, \qquad \nabla \cdot \vec{B} = 0, \tag{3.1}$$

$$\nabla \times \vec{B} - \varepsilon_0 \mu_0 \frac{\partial \vec{E}}{\partial t} = \mu_0 \vec{j}, \qquad \nabla \cdot \vec{E} = \frac{\rho}{\varepsilon_0}, \tag{3.2}$$

where $\vec{j}$ is the current density, ε_0 is vacuum permittivity, μ_0 is vacuum permeability and ρ is the charge density.
In fact, the particle-particle approach is the most numerically challenging scenario used in plasma modeling. Dealing with a large number of real particles (e.g., in laser plasma, astrophysics, ...) is often too computationally demanding even for supercomputer clusters having hundreds of CPU cores. Therefore, a statistical approach, using the average macroscopic properties, is applied instead.
In fact, the biggest advantage of a **statistical description** lies in the fact, that any knowledge about the individual particle trajectories is required in order to describe observed phenomena. Of course, the precision is worse than that in the particle-particle approaches. On the other hand, much larger scale systems can be simulated [180], [181]. Consequently, kinetic methods introduce a *macroparticle* containing a large number of real particles. However, decreasing the number of particles leads to the increase of noise. Therefore, the user should be very careful when choosing numerical approaches to describe the real situation. Macroparticle description is used, for instance, in Particle-in-cell simulations (Particle-Mesh method). There, macroparticles are basically an approximation of distribution function by a set of finite phase-fluid elements (FPEE).
The time evolution of the general distribution function $f_\alpha(t, \vec{x}, \vec{v_\alpha})$ is described by Boltzmann transport equation (BTE). For example, when α-particles collide with a target made from β-particles, BTE has the following form [15]:

$$\frac{\mathrm{d}f_\alpha(t, \vec{x}, \vec{v_\alpha})}{\mathrm{d}t} = \sum_\beta S_{\alpha\beta}, \tag{3.3}$$

$$\frac{\partial f_\alpha}{\partial t} + \left(\vec{v_\alpha} \cdot \vec{\nabla}_x\right) f_\alpha + \frac{1}{m_\alpha}\left(\vec{F_\alpha} \cdot \vec{\nabla}_v\right) f_\alpha = \sum_\beta S_{\alpha\beta}, \tag{3.4}$$

where the right hand side is called Boltzmann collision integral expressing the collisional (or collisionless) term whose specific form varies depending on the various approaches to the collisions. The various evaluation of the Boltzmann collision integral leads to Fokker-Planck, Landau, Boltzmann, BGK (Bhatnagar-Gross-Krook) or to Vlasov equation(s) [15]. The lastly mentioned, i.e., Vlasov's equivalent of BTE, is used for collisionless systems corresponding to the Boltzmann integral equal to zero. Vlasov equation is used for high temperature plasmas, including laser-target interactions, where collisions are negligible:

$$\frac{\partial f_\alpha}{\partial t} + \left(\vec{v_\alpha} \cdot \vec{\nabla}_x\right) f_\alpha + \frac{1}{m_\alpha}\left(\vec{F_\alpha} \cdot \vec{\nabla}_v\right) f_\alpha = 0. \tag{3.5}$$

- **Fluid (Hydrodynamic) description** is other possible approach used in plasma modeling [14], [182] and it covers Magnetohydrodynamic (MHD) simulations, One fluid hydrodynamics or Two fluid hydrodynamics simulations [100], [178], [179]. In this case, not only Maxwell equations and conservation laws, but also equations of state, are required. Generally, plasma is described via macroscopic parameters whereas the equations for the system are obtained with the use of velocity moments evaluated from Boltzmann transport equation [14], [179]. That makes this modeling optimal to be compared with real experiments because it uses variables which can be measured (e.g., temperature, pressure etc.). Furthermore, even though fluid simulations have often high numerical demands, they are faster and more cost-effective than the previously described kinetic models. On the other hand, the results are less accurate. Unfortunately, hydrodynamic simulations can be used only when the local thermodynamic equilibrium is fulfilled, because both temperature and pressure (which macroscopically describe the system) can be defined only in LTE. Moreover, the simulation results strongly depend on the applied physical model and on the used assumptions. In fact, taking the laser plasma as a fluid is a good approximation for the interactions with relatively low laser intensities ($\leq 10^{15}$ W/cm^2) and long pulses (ns) [100].

- Another possibility is to use hybrid modeling [100], [178], [179] (generally, where more numerical approaches are needed together) or gyrokinetic description [180], [181] (i.e., modeling of plasma behavior of frequencies much lower than the particle cyclotron frequencies and on spatial scales comparable to the gyroradius), which is crucial for modeling of, for example, plasma turbulence.

3.1 Particle-in-cell (PIC) method

Particle-in-cell is a numerical method of a kinetic particle simulation approach, where a certain amount of real particles is represented by a virtual macroparticle. This macroparticle behaves like a cloud of real particles (electrons or ions) and propagates in electromagnetic fields freely according to the movement equation (Lorentz force). The electromagnetic fields are solved on the finite mesh from the charge and the current of the macroparticles evaluated at the grid points.
In fact, there are various models dealing with the strategy how the real particles should be merged together and how many of them is acceptable to be represented by a single macroparticle in order to reach high physical accuracy but also numerical efficiency. Generally, the model implementing a too low number of real particles merged together (i.e., too much macroparticles) would suffer from high computational demands, whereas the larger value (i.e., a low number of macroparticles) would suffer from insufficient statistics. Nevertheless, plasma physics is full of non-linear effects like instabilities and resonances where a small number of particles might be more important or even crucial for the examined phenomenon than the rest. In context of this, different numerical weights can be assigned to various macroparticles. Therefore, numerical weighting is used in order to lower the total particle number without loosing the reasonable statistics (or sometimes even enhancing it).
The equation of motion is solved using, e.g., Leap-Frog or Boris-Buneman schemes [177]. The EM fields are known only in the predefined grid junctions and they are calculated by solving Maxwell's equations by Finite Difference Time Domain (FDTD) method [177], [183] on a spatial grid and interpolated back to the particle positions. Thus, the particles do not

interact with all other particles but with the mean field generated by the particle ensemble. Particle-in-cell method is then a naturally closed 4-step scheme containing the procedures of *Particle pusher* and of *Field solver*, together with the weighting of variables from the particles positions to the grid and vice versa, see Fig. 3.1. Originally, the collisions are neglected in PIC codes, but if needed, they can be added by Monte Carlo modules [176], [184].

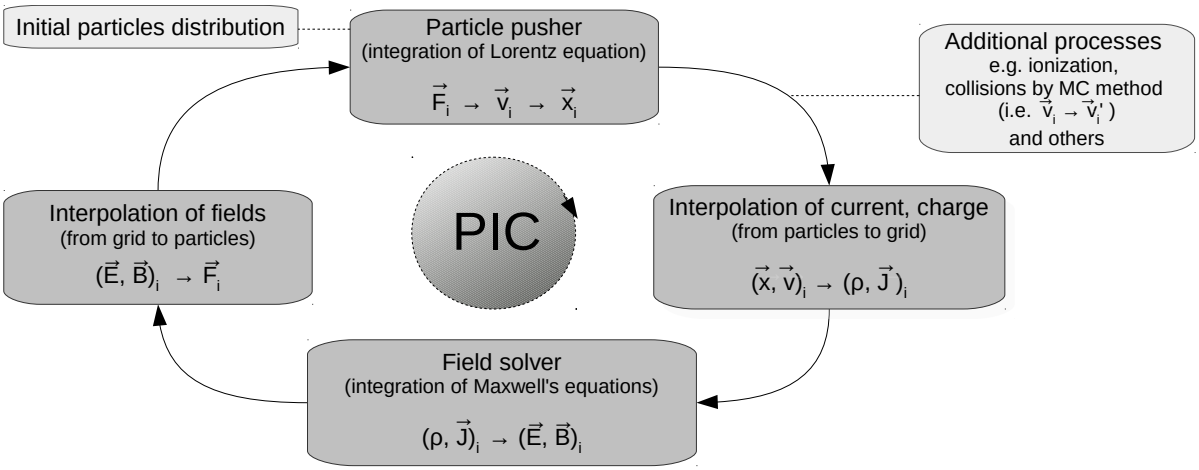

Figure 3.1: Basic four-step cyclic scheme of Particle-in-cell method.

3.1.1 The first step: Integration of equations of motion

The equation of motion, represented by Lorentz force $\vec{F}_i$ for each i-th macroparticle, is integrated in order to get the i-th macroparticle velocity $\vec{v}_i$ and its position $\vec{x}_i$:

$$\vec{F}_i = \frac{\mathrm{d}(\gamma \vec{v}_i)}{\mathrm{d}t} = \frac{q}{m_i}\left(\vec{E}_i + \vec{v}_i \times \vec{B}_i\right), \tag{3.6}$$

where γ is the relativistic factor, q is the particle charge, m_i is the particle mass and $\vec{E}_i$, $\vec{B}_i$ are the electric and the magnetic fields, respectively. In order to ensure better accuracy, the leap-frog scheme, as an improvement of numeric Euler method, is usually used to perform the integration. The advantage lies in replacing a forward time difference in Euler method by a central difference. Therefore, the velocities are evaluated at the time $t = (n + 1/2)\Delta t$, whereas the positions are calculated at the time $t = n\Delta t$, where n denotes n-th step.
Other option to solve the equations (3.7)–(3.8) is to employ Boris scheme, the widely used second-order Lorentz force integrator based on velocity-Verlet scheme [177], [185]:

$$\vec{x}_{n+1} = \vec{x}_n + \Delta t\left(\vec{v}_n + \frac{\Delta t}{2}\vec{F}(\vec{x}_n, \vec{v}_n)\right), \tag{3.7}$$

$$\vec{v}_{n+1} = \vec{v}_n + \frac{\Delta t}{2}\left(\vec{F}(\vec{x}_n, \vec{v}_n) + \vec{F}(\vec{x}_{n+1}, \vec{v}_{n+1})\right). \tag{3.8}$$

This method provides a smart way to evaluate (3.8) without any need to solve an implicit system [186]. In a nutshell, it is done by three steps: the first half of the electric push is followed by the rotation and the second half of the electric push. The detailed explanation of

multi-step Boris scheme can be found in [187] as well as in author's previous work [188]. Generally, the algorithm used for integration of equations of motion should be convergent, stable, efficient and accurate. In fact, the proper choice of the method ensures that any dissipation of physical quantities or any deviation of the conservation laws, both caused by the truncation error (originating from the approximation of derivatives with finite differences), would be minimized and they would not grow in time [177].

3.1.2 The second step: Interpolation of charge and current source terms to the field mesh

Since the macroparticles move freely in both space and time, the new charge and current densities have to be computed and assigned to the grid to advance the fields in the third step. In fact, the assignment is done by the means of interpolation functions being typically products of splines. According to these functions, the values of the current and the charge densities are assigned to the grid nodes. In fact, one macroparticle can contributes to more than one node, which is nearby. In other words, several neighboring macroparticles can be partly weighted to the same node. The continuity equation (3.9) must be satisfied:

$$\frac{\partial \rho}{\partial t} + \nabla \cdot \vec{J} = 0, \tag{3.9}$$

where ρ is the charge density and $\vec{J}$ is the current density.

3.1.3 The third step: Integration of electric and magnetic fields on mesh points

The electric and the magnetic fields are usually defined on Yee's FDTD mesh, where they are offset one-half time step, see Fig. 3.2. The staggered Yee's field algorithm has the accuracy of the second-order both in space and in time [189].

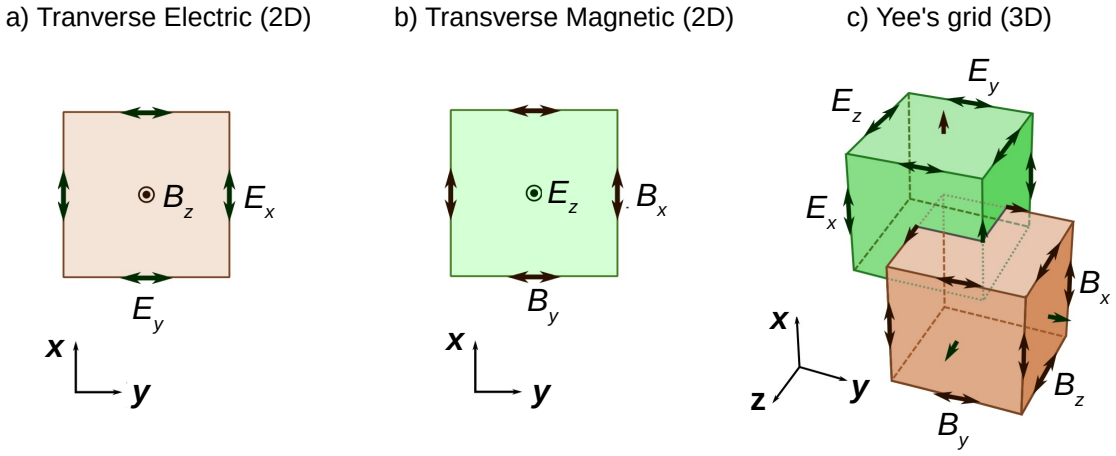

Figure 3.2: Illustration of FDTD space discretization for electric and magnetic fields: a) 2D case with the magnetic field along the $z-$axis (i.e., the axis perpendicular to the screen); b) 2D case with the electric field along $z-$axis; c) 3D case with so-called Yee's grid.

Taking the current and the charge densities from the previous step, both the magnetic and the electric fields ($\vec{B}$, $\vec{E}$) can be advanced in time in agreement with Maxwell's equations on the grid:

$$\nabla \times \vec{E} = -\frac{\partial \vec{B}}{t}, \tag{3.10}$$

$$\nabla \times \vec{B} = \mu_0 \vec{J} + \frac{1}{c^2}\frac{\partial \vec{E}}{\partial t}, \tag{3.11}$$

$$\nabla \cdot \vec{E} = \frac{\rho}{\epsilon_0}, \tag{3.12}$$

$$\nabla \cdot \vec{B} = 0, \tag{3.13}$$

where μ_0 is the vacuum permittivity, ϵ_0 is the permeability constant and c is the speed of light.

3.1.4 The fourth step: Interpolation of fields from the mesh to particle positions

The electric and the magnetic fields defined on the finite space grid are interpolated to the macroparticle positions by the means of interpolation functions. This step is thus the opposite to the second step, where the current and the charge densities were weighted from the macroparticle positions to the grid points. With the knowledge of the fields at the macroparticles' locations, Lorentz force can be computed and the cycle starts again.

3.1.5 Particle-in cell code EPOCH

The free full-source Particle-in-cell code EPOCH is used in the case of all simulations presented in this dissertation. EPOCH is MPI parallelised, explicit, second-order, relativistic PIC code developed at the University of Warwick and it is based on an older PSC code by Hartmut Ruhlby [9]. The EPOCH code is written in SI units and, as a solver, it implements 2^{nd} order Finite Difference Time Domain (FDTD) integration of the Maxwell's equations on a staggered Yee's grid [190]. The grid stagger means that some variables are defined on the domain boundaries, whereas others are defined on either side of the domain boundary. A particle pusher is done via Boris-Buneman scheme [177] for integrating the equations of particle motion, whilst the current weighting is performed with the help of a charge-conserving scheme by Villasenor-Buneman [191].

3.2 Computational demands

3.2.1 Comparison of Vlasov method with PIC

Vlasov equation (3.5) is a collisionless version of differential BTE. It is usually used in order to describe hot plasma by a single-particle density function $f(\vec{r}, \vec{p})$, where $\vec{r}$ and $\vec{p}$ are position vectors of the particle in a six-dimensional phase space. Naturally, this approach is very computationally demanding even for 1D, where there is still the need to retain two or three velocity components in order to properly cover the electron motion and its coupling to Maxwell's equations [12]. Therefore, even 1D situation grows towards 3- or 4-dimensional code. Usually, finite differences on the Eulerian grid is used for solving the partial differential

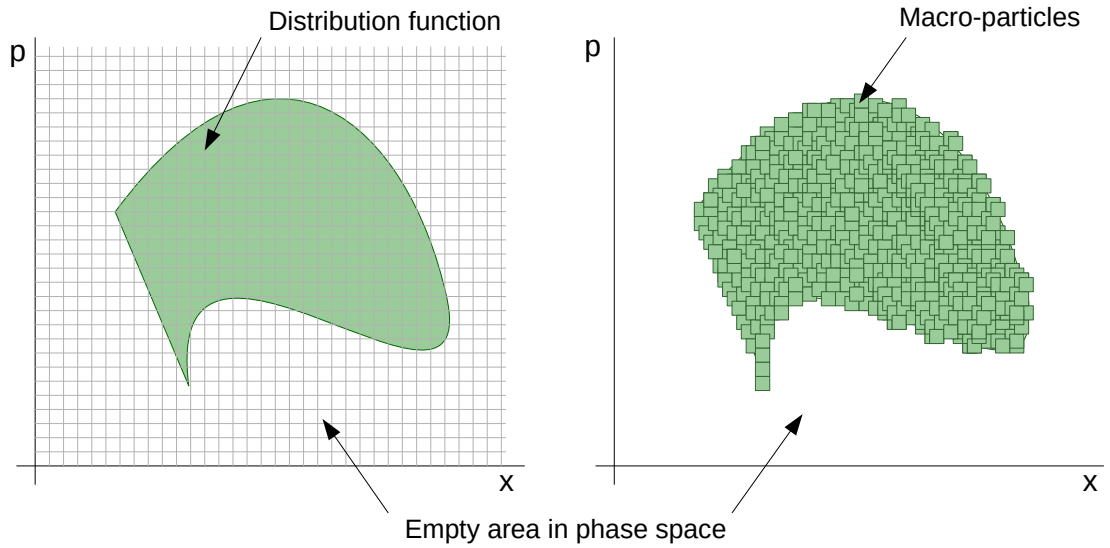

Figure 3.3: Illustrative representation of Vlasov method (left): distribution function on Eulerian grid in 2D phase space; or of Particle-in-cell (PIC) method (right): numerical macroparticles sample the distribution function.

equation of Vlasov.
In a nutshell, Vlasov approach is such computationally demanding, because, regardless whether the particles are in the region or not, all cells of the grid are included in numerical solving. Let's demonstrate this claim on a simple example depicted in Fig. 3.3, where one plane of phase space together with a distribution function are shown. The distribution function is positive in a green cloud representing the phase space occupied by a plasma. Conversely, the function has a zero value in a clear white surrounding space, where any particle is present. Obviously, the numerical cost rises quickly with each additional dimension. Consequently, solving the full 6D Vlasov equation becomes nearly impossible. In fact, the method is used in low dimensions, when extremely smooth results are needed.
In contrast to Vlasov equation, there is Particle-in-cell (PIC) method which can solve the problem more efficiently. The difference is clearly demonstrated in Fig. 3.3, where the distribution function on the left side (Vlasov method) is approximated by a set of finite phase-fluid elements (FPEE) on the right side (PIC method). Then, the equation for the distribution function f_s is [12]:

$$f_s(\vec{r},\vec{p}) = \sum_k W_k S(\vec{r}-\vec{r}_k, \vec{p}-\vec{p}_k), \tag{3.14}$$

where W_k is the weight of k-th particle of species s and $S(\vec{r}-\vec{r}_k, \vec{p}-\vec{p}_k)$ is the function describing the effective shape of the particle in the phase space; $\vec{r}$ is the observation point in phase space and $\vec{r}_k$ is the coordinate of the particle. In the case of the momentum $\vec{p}$, the same notation is valid.
In order to define the *shape* of a cloud of real particles merged to a single macroparticle, the shape function is introduced. Usually, there are various shape functions implemented in PIC codes, which can be chosen by the user. Nevertheless, all of them have to satisfy the conditions of space isotropy, charge conservation and of increasing accuracy (convergence) for

higher-order terms [192]. Furthermore, the shape function is related to the weighting function as they are usually the products of various splines. The most common weightings & shapes are NGP (Nearest Grid Point, i.e., the zeroth order weighting), LS (Linear Spline called also Cloud-in-cell), QS (Quadratic Spline) and CS (Cubic Spline) [193].

3.2.2 Reducing computational demands by PIC in comparison to Particle-Particle approaches

The crucial advantage of PIC method is that it significantly decreases the computational cost in comparison to Particle-Particle (PP) approaches or to Vlasov method. In fact, the macroparticle in PIC does not interact with each other as in PP models, but with a finite mesh and the values are not computed in the phase space regions where no (macro)particle is present. Generally, such methods are known as Particle-Mesh (PM) approaches [177], [194], [195].
Denoting N as the number of macroparticles in the simulation and N_g as the number of grid points of the mesh, PIC method decreases computational cost from N^2 (being valid for PP algorithms) to [195]:

$$\alpha N + \beta(N_g), \tag{3.15}$$

where the constants α, β depend on the PM scheme being used. The first term αN in (3.15) arises from the fact, that each macroparticle in the simulation is treated typically once in a single cycle (in fact, it could be also two or four times, but asymptotically it converges to αN steps). In other words, the steps $1, 2$ and 4 in the PIC scheme (see Fig. 3.1) are proportional to the number of particles N, whilst the operation count for the step 3 depends on the number of grid points N_g (which is asymptotically the same as the number of cells). The field solver therefore affects the term $\beta(N_g)$ in (3.15). For example, rapid elliptic solvers (such as Buneman algorithm or multiple Fourier Transform) need $\sim N_g \log_2 N_g$ operations [195].

There are also so-called Particle-Particle-Particle-Mesh codes (PPPM or simply P^3M) which combine PM and PM approaches and treat the slowly (by PM) and the rapidly (by PP) varying forces separately. Hence, such codes represent close encounters as accurately as the PP methods and they calculate long-range forces as rapidly as PM methods. The required number of operation is modified from (3.15) to $\alpha N + \beta(N_g) + \gamma N_g N_n$, where N_n is the number of neighbors (given generally by $N_n = Vn$, where n is the density of particles and V is the volume of the cell) [195].

3.2.3 Computational resources

Various computer clusters were used to perform the simulations presented in the chapter PIC simulations: affecting beam parameters by advanced target designs. The majority of cases were simulated on ECLIPSE cluster at ELI-Beamlines [196], although, SALOMON cluster at IT4Innovations (IT4I) [197] was used as well. Moreover, single nodes belonging to MetaCentrum VO [198] were sporadically used for MATLAB analysis scripts, but the rest of data was analyzed on site (i.e., on ECLIPSE/Salomon clusters). IT4I and MetaCentrum are virtual organizations operating and managing the computing infrastructure consisting of computing and storage resources. These resources are offered to researchers and students in the Czech

Republic for free (MetaCentrum VO) or are accessible by awarding the project through open-calls, being available several times per year (IT4Innovations). Within this work, two IT4I projects have been granted – *Multidimensional simulations of advanced target designs with the aim of improving parameters of laser-accelerated particle beams* (id OPEN-10-9, in total 567.000 core hours) and *Effects of advanced target designs on laser-accelerated ion beams parameters* (id OPEN-19-21, in total 308.000 core hours).
When performing huge 2D or 3D simulations, the data containing particle momenta in each direction, particle densities and positions for all species, laser absorption or electric and magnetic fields are saved into separate data files at particular time steps. These steps are not necessarily the same for each physical variable (due to the various needs when analyzing slowly or quickly varying processes), but they should have the common multiples in order to provide a proper analysis at the mutual time step. The produced files are huge, having from hundreds of MB to ones or even tens of GB (usually restart dumps), because approximately ten of double-precision numbers are stored for each particle and each cell.
In order to minimize any wasting of CPU hours, restart dump files are saved down regularly. The restart dumps are the data files containing all necessary info needed to restart the simulation from the time corresponding to the dump file. In fact, this can be crucial when an already running, but too time-consuming, simulation had been put in a short computing queue. Moreover, the restart is beneficial in the case of an unexpected crash or when a possibility to change the frequency of saving the data files down, if finer resolution is requested, is needed. This approach also allows to do the brief analysis in early stages of the simulation process and thus do not waste much time and resources if there is the need to change the input file. In the case of the simulations shown here, the restartable file(s) were not transferred somewhere else, but stayed on the cluster, where usually only the newest restart dump remains. This was done automatically by *rolling restart* option implemented in EPOCH code.

3.2.3.1 Estimation of requested cluster nodes for 2D and 3D EPOCH simulation

The right planning of the requested number of CPU cores for the simulation is crucial. In fact, the proper estimation of the node number can reduce the waiting time in cluster queues or prevent the job from crushing or freezing because of unadequate resources requested. The exact procedure, showing how to compute the needed resources, depends on the way how the PIC code is written (e.g., for EPOCH code this information can be found in *shared* file in *src* folder). Here, a very brief plan how to estimate the requested number of cores/nodes, when using EPOCH PIC code, is present. The procedure is valid for 3D simulation, and can be thus modified to 2D case very easily by reducing one dimension.
Let assume, that each number has a double precision (8 bytes); the requirement for the memory allocation can be divided into three parts:

1. the number of bytes requested per particle
   (a) momentum $\vec{p}$: 3 numbers needed $\rightarrow$ 24 bytes
   (b) space coordinate $\vec{r}$: 3 numbers needed $\rightarrow$ 24 bytes
   (c) weight w: 1 number needed $\rightarrow$ 8 bytes
   (d) pointer(s): 2 numbers needed $\rightarrow$ 16 bytes
2. the number of bytes requested per cell

(a) electric field $\vec{E}$: 3 numbers needed $\rightarrow$ 24 bytes

(b) magnetic field $\vec{B}$: 3 numbers needed $\rightarrow$ 24 bytes

(c) electric current $\vec{j}$: 3 numbers needed $\rightarrow$ 24 bytes

(d) charge density ρ: 1 number needed $\rightarrow$ 8 bytes

(e) electron density n_e: 1 number needed $\rightarrow$ 8 bytes

3. for any other information bounded to a cell: 1 number needed $\rightarrow$ 8 bytes (this value is overwritten regularly, thus 1 number is enough for the whole process).

Altogether, the relation estimating the total amount of nodes N_{nodes}, which should be requested for the simulation, is following:

$$N_{nodes} = \frac{(C \cdot (72 \cdot N + 88 \cdot N_g + 8 \cdot N))}{M_{node}}, \tag{3.16}$$

where N is the number of macroparticles, N_g is the number of grids/cells (which is asymptotically the same) and C is the safety constant ($C > 1$), which gives an operational space to ensure smooth running, when the simulation is not well-balanced at the very beginning (e.g., a thin small target is placed in a big empty area). Finally, M_{node} is the usable memory of the node in bytes. For instance, ECLIPSE cluster at ELI-Beamlines has $115 \cdot 10^9$ bytes per node [196].

3.3 Numerical stability of PIC codes

Numerical instabilities are, among others, driven by the fact, that particles are distributed across a computational grid, whereas fields are evaluated at discrete grid points. This means, for instance, that particles support higher wavenumbers than fields do and that the particle pusher is Lagrangian, whilst the field solver is Eulerian [189].
A sufficient choice of both cell dimensions and macroparticle parameters (the number, weighting etc.) is crucial for obtaining reliable and numerically stable results. There are a few factors we should consider and take care about before the start of the simulation. Fundamentally, the appropriate time step and the grid dimensions should be chosen.
Firstly, the so-called Courant limit (usually shortened as CFL condition) [177] has to be satisfied (here presented in 3D):

$$(c\Delta t)^2 \left(\frac{1}{(\Delta x)^2} + \frac{1}{(\Delta y)^2} + \frac{1}{(\Delta z)^2} \right) \leq 1. \tag{3.17}$$

In short, this condition ensures that no particle moves further than a single cell length (in each direction) during one time step and also that the time step is sufficiently short to enable a proper calculation of EM (light) waves propagation. Courant condition limits the simulation how fast it can advance in time for a given spatial resolution. Since standard EM-PIC codes are unstable for $c\Delta t > \Delta \vec{r}$, any practical use of such codes is restricted to $\Delta t \leq \Delta \vec{r}/c$.
Secondly, the attention should be payed on other condition limiting the choice of the time step in order to ensure that an electrostatic (Langmuir) waves propagation is calculated properly [199], [177]:

$$\omega_{pe} \Delta t \leq 2. \tag{3.18}$$

In other words, the time step should be significantly shorter than a period corresponding to the electron plasma frequency ω_{pe}, otherwise the processes in plasma, e.g., plasma oscillations of electrons, would be unresolved [15], [17]. Even though the condition (3.18) is required, the practical reasons related to energy conservation suggest to use, instead of the factor 2, a number one order of magnitude smaller [199], [200]:

$$\omega_{pe}\Delta t \leq 0.1. \tag{3.19}$$

Similarly as it is not possible to analyze too fast processes because of time discretion (i.e., the processes faster than the time step), it is not possible to study the phenomena, which take place in the spatial scale smaller than the cell dimensions. Therefore, not only the right choice of the time step, but also of the single cell dimension (i.e., the spatial step), is crucial for performing stable and sufficient PIC simulations. The spatial discretization of the simulation area should have the order comparable to the Debye length λ_{De} of the simulated plasma system. Within this length particles see each other as individuals. Furthermore, in the case of collisionless plasma, the collective modes exist only for $\lambda > \lambda_{De}$. It is because the electrons thermal motion damps strongly the modes having lower λ than Debye length λ_{De} by Landau damping [201], [202]. Consequently, in the literature [177], [203], [204], there is usually mentioned that the single cell dimension should resolve the Debye length, i.e., $\Delta x \approx \lambda_{De}$, in order to ensure numerical stability of PIC simulations. Nevertheless, in modern PIC codes, which use smooth high order shape functions, this condition is not such strict. In fact, for third order splines, the instability growth rates are more than one thousand times lower than the plasma frequency when the cell has $\Delta x = 10\lambda_{De}$ instead of $\Delta x = \lambda_{De}$ [205]. This is the reason, why in practice the cell dimension is chosen to be multiples of the Debye length because the finer resolution is usually too computationally demanded.
The basic considerations moreover indicate, that both the wavelengths of the plasma and of the laser should be sampled at least by the low tens of cells (i.e., $\lambda \sim 10\text{'s} \cdot \Delta x$), otherwise the reconstruction of the proper shape cannot be guaranteed, as illustrated in Fig. 3.4. For example, the PIC stability study [206] considering laser wakefield acceleration of electrons demonstrated that the dimension of the cell should be at least 24x (better 36x) smaller than the laser wavelength otherwise the non-physical self-heating (in the terms of the non-physically enhanced momentum spread) will occur.

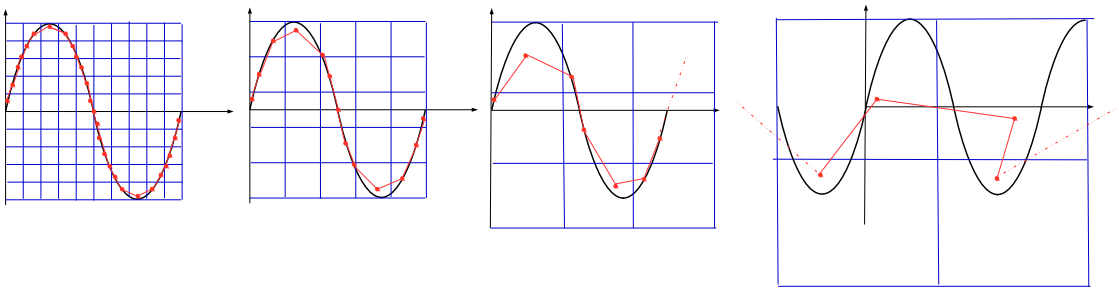

Figure 3.4: Illustrative sketch of a problematic shape reconstruction when too low number of cells was used to sample the plasma wave: the single wavelength is sampled, from left to right, by $27, 13, 7$ or by 4 cells.

Apart from this, the density of the spatial grid should be chosen accordingly to the number of particles. In fact, when Δx is too large, the spatial resolution of local fields is calculated

too roughly. On the contrary, when the too fine grid (compared to the number of particles) is chosen, the fluctuations in field intensities between each cell grow rapidly. Therefore, the empirical estimation advises to have only tens of macroparticles in one cell and to choose the step size Δx appropriately [178].
Among the already mentioned issues, also many other aspects can affect PIC simulations, such as a proper choice of boundary conditions both for fields and for particles [193].
The Yee FDTD scheme, similarly to other FDTD schemes, is stable as long as the Courant condition (3.17) is satisfied, as already discussed earlier. On the other hand, even with the Courant limit fulfilled, explicit PIC codes are unstable due to the field-particle interpolation coupled with disparities between the Eulerian field solver and the Lagrangian particle pusher – *Finite grid* and *Cherenkov numerical instability* are studied the most often in the case of relativistic beams (e.g., in so-called boosted frames, where the plasma length is Lorentz contracted while the plasma wake wavelength and the laser pulse length are Lorentz expanded, which saves computational cost) [189], [207], [208].
To summarize, numerical instabilities lead to unphysical simulation results or are even able to crash the simulation. The occurrence of numerical instabilities is dependent not only on the grid size, the time step size and the number of real particles per macroparticle, but also on the detailed particle phase space distribution through each step in the PIC computation loop. In other words, it means that different particle distributions used in the code would suffer from different numerical instabilities [208].

3.4 Combining PIC and (M)HD simulations

Usually, the investigation of a number of different phenomena is needed to understand the whole physical situation properly. Unfortunately, it is complicated or sometimes even impossible to simulate such processes by one numerical approach only, typically because of long time scales, a huge number of particles, a low statistical occurrence of the studied phenomenon or due to various computational needs in different stages of the simulated problem. Therefore, the investigated phenomenon is divided into parts, which are treated separately by different numerical approaches or by the means of hybrid simulations.
For example, kinetic and fluid plasma modeling, represented by Particle-in-cell (PIC) and (Magneto)hydrodynamics ((M)HD) codes, respectively, are combined together in order to study Earth's and other planets' magnetosphere [209], [210], magnetic reconnection [211], Cosmic ray transport in MHD turbulence in the interstellar medium or Astrophysical shocks [212]. Specifically, PIC results are used as the source terms in MHD equations or equivalently, the fields in PIC scheme are computed according to MHD equations.
In the frame of this dissertation, MHD and PIC simulations will be combined together in order to describe the effect of the laser prepulse on the proton beam accelerated from the channel-like target (i.e., the optimal step-like density target design studied and described in detail in the following chapter). MHD simulations will be used to simulate the target expansion by the laser prepulse. Then the resulting preplasma, represented by the electron density profile, will be taken as the input for PIC simulation, where only the main laser pulse, interacting with the created preplasma attached to the main target, will be performed. The results as well as the complete description of the parameters used in this study are described in the subchapter Expanded density profile: The effect of preplasma on ion beam parameters.

Chapter 4

PIC simulations: affecting beam parameters by advanced target designs

The increasing interest in laser-acceleration technique has been pushing the efforts made in studying and manufacturing micro/nano-structured targets forward in order to improve ion beam parameters. This covers for example decreasing or modifying beam divergence [213], increasing maximum energy of protons/ions, reaching narrow energy spread, enhancing the number of accelerated particles [214] or increasing the spatial uniformity and homogeneity of the accelerated beam. In fact, although maximum proton energies approaching the 100-MeV level have been experimentally achieved with a relatively high yield ($10^{10}-10^{12}$ protons/pulse) [1], [48], laser-accelerated particle beams are still not mature for applications. Particle-in-cell simulations become a great tool to test various ideas how to improve particle beam parameters in order to meet the strong requirements of foreseen applications with wide socioeconomic impact such as laser-driven hadrontherapy, 'fast ignition' of ICF targets, laser triggering and control of nuclear reactions, material science, chemistry (e.g. proton pulsed radiolysis of water), non-destructive heritage testing etc. [1], [2], see the chapter Possible applications of laser-driven ion beams.

Generally, particle divergence, which is one of the key beam feature which will be discussed within this work, is a crucial parameter for effectiveness of the beam handling, for the particle transport through beamlines and often also for the fulfillment of various applications' requirements. It was shown, both numerically and experimentally, that whereas micro/nano-structures on the target front surface increase the maximum proton energy and enhance the number of accelerated particles significantly, rear-placed periodical structures affect rather angular spread of accelerated ion/proton beam. Specifically, the higher number and proton energy were obtained experimentally when the monolayer of polystyrene nanospheres has been placed on the target front side [214], [215]. On the contrary, block structures present at the rear target side (separated by a gap smaller than the laser focal spot size) result in proton divergence reduction in one direction and simultaneously in proton divergence increase in the another, depending on the structures orientation [213]. Other divergence studies performing various target materials together [216] or employing laser-excited electromagnetic pulses directed along a helical path from wire attached to the target rear side and thus surrounding the laser-accelerated ion beams [217] were already published. The post-collimation

of laser-driven protons accelerated from a single flat foil was demonstrated experimentally already in 2006 when a separated metallic cylinder irradiated by the 2^{nd} laser pulse (in order to generate electrons along cylinder walls) was placed as a guiding channel in the accelerated beam trajectory [218]. This clearly illustrates the promising potential of the guiding-channel geometry studied in this dissertation, even though the cylinder structure from [218] was not a part of the target and has much larger dimensions than those chosen here (i.e., mm- instead of μm-scale). Various kinds of straight or tapering metal channels (Au, Cu, ...) attached to or encircling fully ionized hydrogen flat target were investigated also numerically because of their promising impact on proton beam parameters [219], [220]. The results are relevant mainly in terms of the target shape corresponding to the design of tapering channel target presented here. To summarize, various designs of targets have been already proposed and investigated in order to decrease ion beam divergence, but they have not been compared to each other and no study of the possible effect of multipole magnetic field on ion beam parameters (including divergence) has been performed.

In this dissertation, 2D and 3D Particle-in cell simulations of advanced target designs are performed in order to improve laser-driven particle beam in various ways. The target designs include structurally modified plastic targets, i.e., flat or curved targets with micro structures in the form of straight or tapering channels attached to the target rear surface and they are studied primarily for a step-like density profile. In the real experiments, this represents the situation when the laser pulse contrast is as high as possible, i.e., the target is not disintegrated or expanded significantly by the prepulse before the main pulse comes. Therefore, besides the foils with step-like density profile, the optimal target design with preplasma created by a laser prepulse is studied. In fact, the laser prepulse is usually an peculiar feature of ultra-short and ultra-intense pulses having an insufficient laser contrast and it is therefore important to include such study in this theoretical work. The overall desired output is the creation of a proton/ion beam showing a strong divergence reduction and improved spatial uniformity, but having as high energy as possible. Such laser-accelerated particles would better meet the strong requirements of foreseen applications with high socioeconomic impact [1], [2].

4.1 Simulation parameters

In order to improve ion beam parameters, particularly the proton beam divergence, various designs of advanced plastic targets were performed by the use of collisionless 2D and 3D PIC code EPOCH [9], see the summary of various target types in Fig. 4.1. Specifically, different target shapes were formed by flat or curved foils with flat or tapering microstructures forming a *channel* attached to their rear side. A single flat foil having the same thickness as the channel targets was used as a reference for a comparison. In 3D, a cylindrical geometry of the channel instead of a block one was chosen because of high-level of symmetry. In other words, the channel transverse cut is a circle and not a square. The thickness both of the target itself (the part perpendicular to the laser pulse) and of the structures is set to 1 μm and the distance between the channel arms is 7 μm, which corresponds to the target lateral dimension of 9 μm. The thickness was chosen with respect to well-manufacturable limits of mylar targets already used in experiments [214] and in order to be relevant for widely used TNSA mechanism of laser-driven ion acceleration [1], [50]. Transverse target dimensions were

chosen in agreement with actual experimental conditions of L3 HAPLS laser (decribed in detail below) [6], [7], [221] in terms of fitting the laser focal spot size between the rear-placed channel structures and in terms of reasonable limits of laser pointing stability. As a result, the target width is three times larger than the size of the laser focus having 3 μm which is close to optimal laser beam width in order to reach the highest laser-driven ion acceleration efficiency [222].

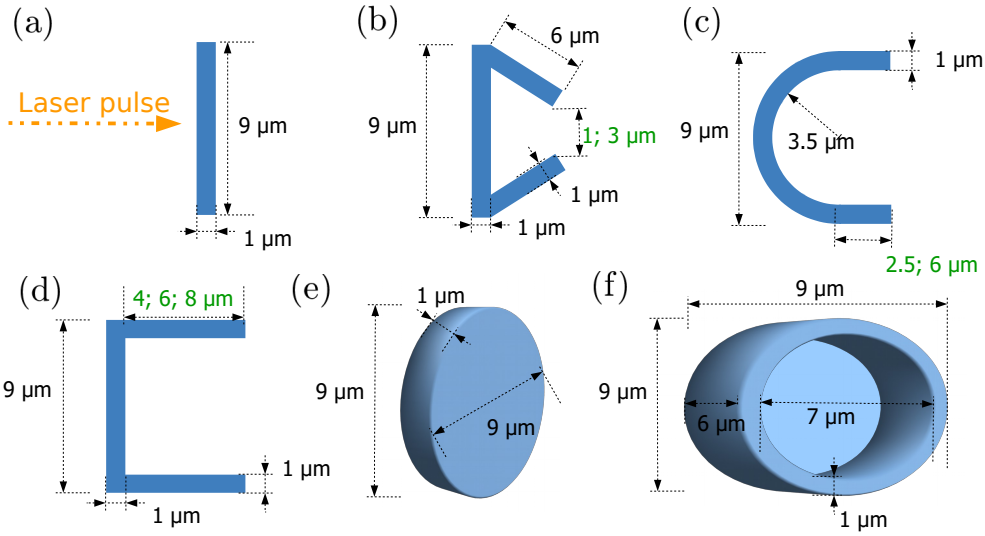

Figure 4.1: Simulated plastic targets: (a) flat target, (b) flat target with tapering 6 μm long arms forming a hole between them being 1 or 3 μm wide; (c) curved target with straight arms forming 6 μm channel of two types – firstly measured from the target rear side, i.e., from the rear side of the curved part, secondly measured from the beginning of the straight part only; (d) flat target with a straight channel having various length: $4, 6$ or 8 μm; all targets were simulated by 2D PIC code EPOCH. The single flat foil and the flat target with 6 μm channel having cylindrical shape were simulated in 3D PIC as well – case (e) and (f), respectively.

The straight channels vary in lengths between 4 μm, 6 μm and 8 μm. The rising channel length is studied in order to demonstrate proper formation of generated quasistatic EM fields, to establish a higher field integral and also in order to reach more optimal ratio between the transverse and longitudinal dimensions widely used when designing magnets [153], [154], [161]. In the case of the flat target with tapering channel, the arms length is set to 6 μm and the dimension of the hole between these arms is changed as depicted in Fig. 4.1 (b) in green (i.e., the angle between the flat part and the arms varies). Curved foils have a radius of curvature of 3.5 μm (the distance between parallel arms is the same as in the case of flat foils with straight channels, i.e., 7 μm) whilst the length of the attached channel varies because of two possible views what the *length of the channel* in reality is. The case of 2.5 μm straight arms represents the situation where the 6 μm channel is measured already from the rear side of the curvature, whilst the case of 6 μm arms represents the situation where only the straight part is considered to be a *channel*. The possibility of targets manufacturing is discussed in the section Discussion: Towards future experiments.
All simulations were performed with a linearly polarized laser pulse along $y-$axis (the polarization plane corresponds to the simulation area in 2D) having wavelength $\lambda = 800$ nm and intensity $I = 5 \cdot 10^{21}$ W/cm^2 which corresponds to dimensionless laser amplitude of $a_0 = 48$.

The laser beam has the focal spot size of 3 μm (FWHM) and propagates along the $x-$axis in the positive direction, i.e., has 0° angle of incidence on the target. The spatial profile of the laser pulse is Gaussian, whilst the time profile has $\sin^2$ shape in intensity both in 2D and 3D. The full duration of the pulse is 60 fs which approximately corresponds to 30 fs at FWHM for a Gaussian profile. The used laser parameters are in good agreement with the L3 HAPLS laser at ELI-Beamlines [7], which is the 1 PW laser system with high repetition rate capability (up to 10 Hz), which will be available at the ELIMAIA beamline [6] and TERESA target area [221], both dedicated to various user experiments. Both 2D and 3D simulations were run for additional 270 fs after the beginning of the laser-target interaction and the simulation area has dimensions of 50 μm × 30 μm (one cell is a square having the edge of 8 nm) in 2D and of 32.0 μm × 13.2 μm × 13.2 μm (one cell is a cube with the edge length of 16 nm) in 3D. Targets are made of plastic having the density of 200 n_c, $n_c = 1.73 \cdot 10^{27}$ m^{-3}. Three particle species are used in the simulation (electrons, protons and carbon ions C^{6+}), while quasineutrality stays conserved.
In each simulation, the third order b-spline shape function was used, which corresponds to the 5^{th} order of particle weighting [9] (i.e., each macroparticle represents a different number of real particles, which was taken into account in analysis). The stability is ensured by fulfilling the corresponding conditions (see the section Numerical stability of PIC codes). Specifically, Debye length is ~ 0.7 nm which is enough for the cell dimension of 8 nm as well as of 16 nm (with the high order particle weighting) in the case of 2D and of 3D simulations, respectively. The plasma skin depth is about 9 nm and the time step was chosen automatically by the EPOCH code in order to reach a good numerical stability.
For all presented simulations (both 2D and 3D), a *simple laser* and a *simple outflow* boundary conditions were applied in the direction of the laser propagation, i.e., at the boundary in front of and behind the target (x_{min} and x_{max}), respectively [9]. Consequently, EM waves are transmitted with as little reflection as possible. At the left simulation box border, the outflowing characteristics propagate through the boundary unchanged whereas the inflowing characteristics are specified by attached laser. At the right simulation box border, the boundary condition again allows outflowing characteristics to flow unchanged, but this time the inflowing characteristics are set to zero. The particles are fully transmitted at both borders in laser propagation direction, i.e., they are simply removed from the simulation when they reach the boundary. The boundary conditions at the transverse axes (i.e., y and z) are set to be *thermal*. In EPOCH Particle-in-cell code, these boundaries imitate the existence of a thermal bath of particles in the vicinity of the boundary. When a particle leaves the simulation area it is replaced randomly near the boundary with an incoming particle sampled from a Maxwellian velocity distribution of a temperature corresponding to that of the initial conditions [9], [223]. Therefore, the heat flux is effectively absorbed by the boundary.
Three dimensional simulations were performed in order to compare the optimal target design chosen from 2D study (i.e., the flat target with 6 μm long straight channel) with a reference single flat foil. Adding another spatial dimension gave us the opportunity to understand deeper physics behind the acceleration process, e.g. the creation of EM fields responsible for the proton divergence reduction feature in the case of the channel target.
In all simulations, the full ionization of targets has been assumed. Since the relatively light and thin/tiny plastic targets are investigated, the approximation of fully ionized dielectric material is sufficient [224] and often assumed because of an efficient propagation of generated hot electrons through such thin target material [225], [226], [227]. Moreover, ionization by laser pulse typically occurs already for values of $a_0 \ll 1$.

Simulation area and time parameters	
area dimensions in 2D and in 3D	(50.0×32.0) μm; $(32.192 \times 13.392 \times 13.392)$ μm
cell size	(8×8) nm or $(16 \times 16 \times 16)$ nm
boundary conditions for particles	thermal
boundary conditions for fields	simple outflow
simulation time	270 fs after the start of laser-target interaction
Laser pulse parameters	
Propagation	along $x-$axis with given angle of incidence
Incidence angle	$0°$
Spatial profile	Gaussian
Time profile	$\sin^2$ in intensity
Wavelength	800 nm
Laser dimensionless amplitude	48
Peak intensity	$5 \cdot 10^{21}$ W/cm^2
Laser pulse beam width FWHM	3 μm
Laser pulse duration FWHM	30 fs
Full-time $\cos^2$ pulse duration	60 fs
Polarization	linear along $y-$axis
Target(s)	
Particles	p^+, e^-, C^{6+}
Electron density	200 n_c, $n_c = 1.73 \cdot 10^{27}$ m^{-3}
Density profile	homogeneous
Weighting of particle	yes, for all simulations
Initial temperature of particles	3000 eV
Target $x-$dimension	various, see Fig. 4.1
Target $y-$dimension	various, see Fig. 4.1
Target $z-$dimension	as in $y-$direction in 2D case, see Fig. 4.1 (e) and (f)
2D MHD + 2D PIC study, full description in 4.8	
Prepulse intensity and shape	$I_p = 10^{11}$ W/cm^2, square shape
Prepulse duration	0.5 ns
Target	plastic 6 μm-long target (d), Fig. 4.1
MHD preplasma used in PIC	analytical fit of electron density was used (details will be provided in the corresponding section 4.8)

Table 4.1: Simulations parameters of microstructured targets study: 2D and 3D PIC (if any differences from 2D case are applied in 3D case, they are highlighted in green color); combination of 2D MHD with 2D PIC.

Also hot electrons are generated before the main laser peak, because the intensities above 10^{14-15} W/cm^2 [100] are sufficient for their production. In fact, the generation occurs near the laser-target interaction point only, but hot electrons can spread to the whole target area, which is, in the presented cases, relatively compact. The full ionization will not affect the created EM fields significantly, since they are established because of hot electrons, not because of the electrons originated from the ionization.
Taking into account the complex profile of the realistic laser pulse, also 2D MHD simulation of the optimal target design was performed in order to study the effects of the preplasma on laser-driven ion and proton acceleration. The 2D MHD output (i.e., the analytical fit of plasma density) was used as the input in a new 2D PIC simulation. Detailed parameters of MHD simulation will be described directly in the subchapter Expanded density profile: The effect of preplasma on ion beam parameters.
The PIC simulation(s) parameters are summarized in Tab. 4.1. Nevertheless, additionally to the simulations mentioned here, two more cases were performed in order to support theories. Firstly, the 3D simulation of the flat foil interacting with $z-$linearly polarized pulse instead of $y-$polarized one was performed in order to study its effect on the produced particle beam (the results are presented in the chapter The role of laser polarization direction in beam cross-section shape and divergence). Secondly, the extension of the flat target in its transverse dimension was performed in order to study the infinite-target effect on accelerating electric field (the results are presented in the section Dependence of the sheath field shape in transverse direction on the target design). All other parameters in these simulations are kept the same and results are referred in the text.

4.2 Divergence

Half-angle proton and carbon ion divergence was measured at FWHM at the end of both 2D and 3D simulations, i.e., at 270 fs after the start of laser-target interaction. In 2D cases, all target designs (see Fig. 4.1) were simulated and only particles moving forward in ± 3.5 μm cut or in ± 0.5 μm cut in transverse direction around the laser propagation axis were analyzed, see the results in Tab. 4.2. The first space interval corresponds to the inner diameter of the channel(s) and it was used in order to analyze the whole particle beam coming from the channel and not from the disintegrated arm-structures. On the contrary, the second space cut was used in order to analyze only the narrow on-axis-particle beam filament. In 3D cases, only the wider space cut, i.e., the cylinder having radius of ± 3.5 μm around the laser propagation axis, was used and the analysis in various energy intervals were added.

4.2.1 Flat targets with straight channel

The strongest decrease of 2D half-angle proton divergence was observed for the flat target with 8 μm long channel, no matter if only on-axis protons or the whole proton beam propagating through the channel were analyzed. Specifically, when taking the wide transverse space cut of ± 3.5 μm around the laser axis, the divergence reduction for this design reaches 34% in comparison to the flat foil. Moreover, significant divergence improvements were recorded as well for the flat target with 6 μm and 4 μm long channel where the half-angle angular spread at FWHM dropped by 29% and by 2%, respectively, see Tab. 4.2. The values of divergence decrease obtained for carbon ions were comparable for all channel lengths, numerically by $\sim 45\%$ compared to the flat foil, because of their higher mass corresponding to weaker and

Protons							
Target type	Half-angle divergence in FWHM [°]						
	2D*				3D**		
	±3.5 μm		±0.5 μm		Interval	x-y	x-z
Flat foil (=FF)	11.2	100%	4.6	100%	>0.5 MeV	15.4	17.7
					>10 MeV	10.3	12.4
					>30 MeV	9.3	9.8
FF with straight 4 μm channel	11.0	98%	2.5	54%	-		
FF with straight 6 μm channel	8.0	71%	1.8	39%	>0.5 MeV	6.8	8.6
					>10 MeV	3.1	5.5
					>30 MeV	3.0	7.2
FF with straight 8 μm channel	7.4	66%	1.5	33%	-		
FF with tapering ch. (1 μm hole)	18.1	162%	4.6	100%	-		
FF with tapering ch. (3 μm hole)	12.6	113%	2.8	61%	-		
CF with straight 6 μm channel	14.8	132%	3.3	72%	-		
CF with straight 2.5 μm channel	20.0	179%	3.7	80%	-		
Carbon ions C^{6+}							
Target type	Half-angle divergence in FWHM [°]						
	2D*				3D**		
	±3.5 μm		±0.5 μm		Interval	x-y	x-z
Flat foil (=FF)	14.5	100%	3.5	100%	>0.5 MeV/amu	8.7	8.9
					>5 MeV/amu	7.1	5.4
					>10 MeV/amu	6.4	6.5
FF with straight 4 μm channel	8.0	55%	2.8	80%	-		
FF with straight 6 μm channel	7.8	54%	2.2	63%	>0.5 MeV/amu	7.2	8.2
					>5 MeV/amu	2.2	3.1
					>10 MeV/amu	3.1	3.9
FF with straight 8 μm channel	7.8	54%	2.5	71%	-		
FF with tapering ch.(1 μm hole)	4.7	32%	3.1	89%	-		
FF with tapering ch. (3 μm hole)	5.9	41%	2.5	71%	-		
CF with straight 6 μm channel	12.4	86%	9.4	266%	-		
CF with straight 2.5 μm channel	13.6	94%	9.3	269%	-		

Table 4.2: Summary of half-angle protons and carbon ions divergence measured at FWHM for different target designs when only particles which are moving forward were taken into account. The analysis was done at the end of each 2D or 3D simulations. Two-dimensional study includes all simulated flat foil (FF) and curved foil (CF) target types (according to Fig. 4.1), in 3D only the optimal target design and the flat foil (as a reference) were simulated.

* in 2D only particles within specified space cut around the laser propagation axis and having above 0.5 MeV/amu were analyzed. The percentage reduction of the divergence in comparison to the flat foil is given.

** in 3D only particles inside the cylinder of radius 3.5 μm around the laser propagation axis (i.e., the channel inner dimension) and exceeding various energy thresholds were analyzed; two divergence planes are investigated.

slower response to differences in EM fields.
The tighter 2D transverse space cut presented in Tab. 4.2. (i.e., ±0.5 μm) was done in order to analyze the narrow on-axis-proton beam only (see the analyzed filament in figures of Density profiles section) and in order to investigate if the targets' ability to modify the proton divergence strongly depends on the analyzed space interval. Particularly, protons located transversely ±0.5 μm from the laser axis show even stronger divergence reduction – namely by 67% or by 61% for the flat target with 8 μm or with 6 μm channel in comparison to the flat foil, respectively. Nevertheless, in spite of diverse nominal values depending on transverse space interval, flat targets with channels show a clear ability to decrease the divergence as well as the dependence on the channel length.
Although the longer channel proved to provide a better proton focusing capability because of the higher electric field integral (which quantifies the total field strength produced and will be discussed in Focusing by the transverse electric field section), the effectiveness of decreasing the particle divergence does not increase linearly with the extension of the channel length. In fact, this effectiveness would be developed to its full potential (and does not rise much more) for a specific value, see Tab. 4.2. Moreover, the length of the arms has natural limits regarding a fabrication of such targets which has to be taken into account (i.e., the arms cannot be too long and too thin to ensure the mechanical stability of the channel), see chapter 4.9.
In general, protons form more populations during the acceleration stage, for instance, the high-energy narrow beam propagating along the laser axis or the more wide particle bunch with the bubble-shaped front. Contrarily, carbon ions are accelerated behind the narrow proton filament as a thick beam having the same transverse dimension as the channel itself, see Density profiles and Energy-resolved spatial distributions of the proton beam sections. Therefore, protons show a higher reduction of the angular spread in the tighter transverse space cut, but carbon ions act differently. In fact, the carbon ion divergence drop was higher in the wider space cut and what is more, it was stable for all simulated channel lengths. Contrarily, carbons propagating in the vicinity of the laser axis (i.e., in the tighter space cut) show the same divergence trend as protons, i.e., the decreasing tendency with the increasing channel length, nonetheless the spread is higher than that along guiding channel walls. In different words, light protons have been focused with the dependence on the channel length no matter the space cut analyzed. In contrast to this, carbon ions respond to the same field less (because of their higher mass compared to protons), therefore, the focusing fields (or the differences between them) have to be stronger to see the comparable effect as in the case of protons. In fact, such stronger fields are located along the guiding channel (and not around the laser axis), which is the reason, why the focusing of ions is more effective there. The ion divergence lowering in the wide space cut is the same for each channel length, simply because the differences between the field amplitudes along the channel walls and the field integrals are too small to have a significant impact on carbons (nevertheless, it is enough to see the differences in the proton angular spread). We also have to keep in mind, that carbon ions and protons feel repulsive force from each other, thus their divergence is affected also by that accordingly.
The divergence features observed in 2D simulations are in great correspondence with 3D simulated cases (i.e., with the comparison of the flat target with 6 μm straight channel and the reference flat foil). In particular, the middle-length channel was chosen to be simulated in 3D, because it provides a significant divergence decrease together with higher beam spatial uniformity accompanied by a small drop in maximum energies and a conservation of particle number in contrast to the target with 8 μm channel, where the energy drop was too big to

be acceptable for the benefit of a few percents of additional divergence drop. All mentioned features will be discussed further in following sections.

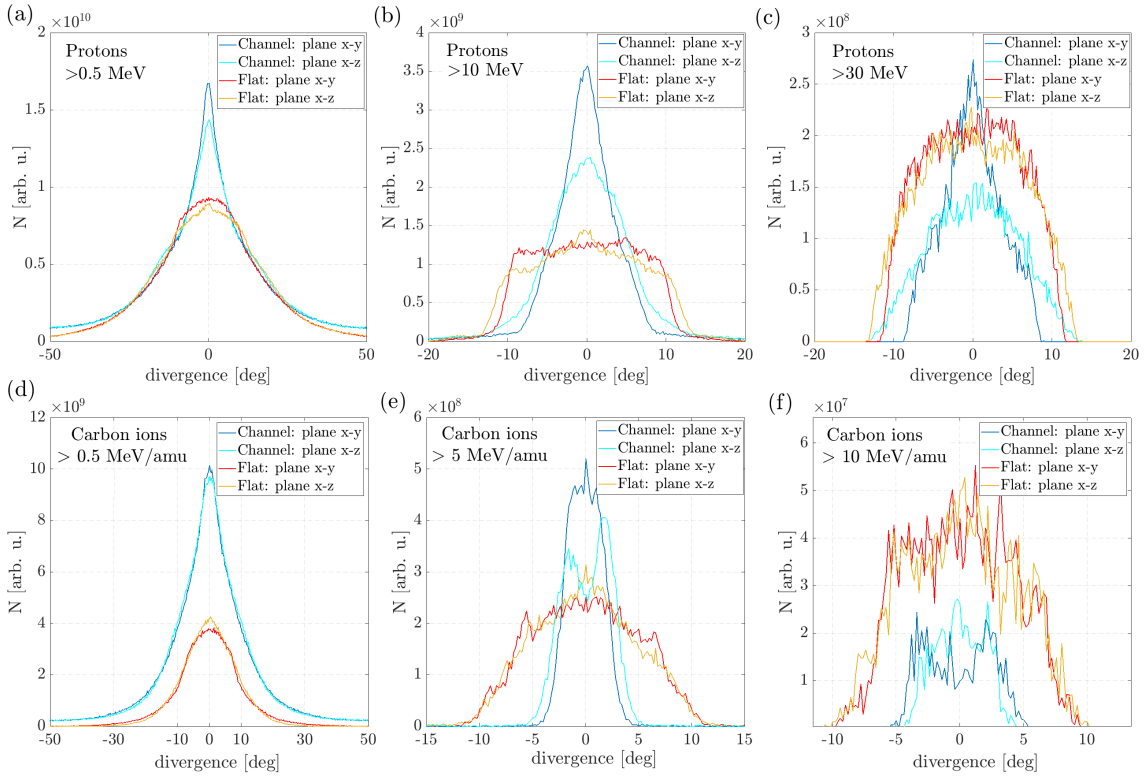

Figure 4.2: Comparison of proton and carbon ions angular distributions in $x-y$ and $x-z$ planes between the flat target and the flat target with 6 μm long channel at the end of 3D simulations. Only particles moving forward within the cylinder of radius 3.5 μm (i.e., the channel inner dimension) and having energy (a)+(d) above 0.5 MeV/amu, (b)+(f) above 10 MeV/amu or (c) above 30 MeV for protons and (f) above 5 MeV/amu for carbon ions were taken for the analysis.

The comparison in Fig. 4.2 presents particle distributions shown in various planes in the laser propagation direction (i.e., in $x-y$ and in $x-z$) and in various energy intervals, which were analyzed separately for each ion species. Protons and carbon ions are shown in the energy interval above 0.5 MeV/amu or above 10 MeV/amu, whilst the interval above 30 MeV was chosen only for protons and above 5 MeV/amu only for carbon ions, see Tab. 4.2 and Fig. 4.2. The analysis for carbon ions above 30 MeV/amu is not present, since they reached their maximum at $E^{C6+}_{maxCHANNEL} = 14.2$ MeV/amu in the case of the channel target and $E^{C6+}_{maxFLAT} = 16.6$ MeV/amu in the case of the flat foil, see section Energy spectra & Number of particles section. Besides the very low energy particles have naturally the larger divergence than those one with high energy from the beginning of the acceleration [228], [229], [230], they are also focused the least efficiently, as can be concluded from three rough energy intervals analyzed. The detailed analysis showing the dependence of half-angle proton divergence reduction on energy is discussed in detail in Comparison of the magnetic and electric field effectiveness section. The analysis is not properly done here, because the exact explanation strongly needs the detailed knowledge of electric and magnetic field effectiveness in various

energy intervals. In this work, proton beam is prioritized over carbon one in order to sufficiently implement the future laser-driven proton beam applications, which gives the reason why detailed study showing effectiveness of divergence reduction with dependence on energy interval is given only for protons.
From the results presented in Tab. 4.2 and in Fig. 4.2, it is clearly observable that both protons and carbon ions are focused slightly better in $x-y$ than in $x-z$ plane of the channel target and this feature does not change with time, only the focusing efficiency varies with the energy interval. In fact, the reason of different focusing efficiency in various planes is bounded with the establishment of magnetic multipoles inside the channel (a quadrupole focusing in $x-y$ plane and an octupole making the particle beam more uniform), as discussed in Generation of multipole magnetic field section.
With careful look, the angular plots are (in a minority of cases) not exactly centralized around zero by a few degrees (i.e., a small deviation from the laser propagation axis is present), see Fig. 4.2. This rarely occurred deviation is caused by non-ideally homogeneous particle beam, non-ideal hot electron transport and by fluctuations of the field(s). Generally, any real magnetic or electrostatic lens, which is a good approximation of our channel target, suffers from geometrical aberration (including the astigmatism in this sense) and from chromatic aberration (which is here strong due to the large energy spread). Geometrical aberration is present due to the field imperfections which are contained as well in accelerator beamlines [154], [153], [231]. Moreover, in the present case it is discussed that the magnetic field has a strong octupole component, which is called as a non allowed high order harmonics for a quadrupole and it contributes also to geometrical aberration [153], [162].
The small differences in focusing planes in the case of the flat foil (nevertheless, much smaller than in the channel target case) can be assigned to the combination of a few reasons. Firstly, the preferable $x-y$ plane providing the lower divergence results is caused by the establishment of the multipole magnetic field (quadrupole). Although the quadrupole field is present mainly at the beginning of the laser interaction with the reference foil, it is not well-confined and nearly no visible in macroscopic figures, we saw its evidence in 1D plots, see Generation of multipole magnetic field section. The second feature is connected with the direction of linear laser polarization [232], see The role of laser polarization direction in beam cross-section shape and divergence section.
Furthermore, in. Fig. 4.2 we can also notice, that whereas the higher number of particles is reached for the channel target in the first two low-energy intervals, the flat foil dominates in the number of high-energy particles. It is natural, because the channel target contains more particles as a target itself and because higher maximum energies were reached for the flat foil, see Number of particles section for more details.

4.2.1.1 Delivery system: the importance of divergence reduction by targets shape

In real experiments, the reduction of particle beam divergence already by shaping the target itself is important due to the optimal injection into transport beamline section. In other words, divergence of accelerated particle beam can be reduced by accelerator magnets, nevertheless, when the beam has too angular spread and consequently too large diameter a few cm behind the target, it simply cannot enter into shaping magnets and some particles would be clipped by the entrance aperture. For example, ELIMED transport section of ELIMAIA

beamline will be positioned approximately 7 cm behind the target and the entrance slit of magnets has 3 cm in diameter. Therefore, the maximum acceptance angle for the particle beam is around 12°. Applying these particular condition on the results of 3D simulated flat and the channel target, ∼ 36% of protons accelerated from the reference flat foil having energy above 10 MeV would be clipped when entering the transport system in comparison to the high-energy main proton beam accelerated from the channel target, where only 9% of protons have higher divergence than the maximum acceptance angle. Moreover, the distance of 7 cm used in this simple estimation is rather too short in comparison to other accelerator beamlines where this distance can be even one meter. Therefore, the clear benefit of reducing divergence by channel-like targets would be even stronger with comparison to flat foils with increasing distance between the target and the transport section.

4.2.2 Curved targets with straight channel

The biggest growth of both proton and carbon ion divergences is associated with the design of curved targets with straight channel. This rise is caused by the TNSA mechanism [1], i.e., by the fact that ions are accelerated perpendicularly to the target rear surface having the concave shape, see Fig. 4.1 (c). Consequently, protons are focused into a small area corresponding to the geometrical center of the curvature (located at 3.5 μm behind the target back side in the laser propagation direction). Unfortunately, the focusing field is not strong enough to sustain the particles in a narrow beam when they reach this point and the beam is defocused again in a short time, because particles follow their original trajectory, as visible also in Density profiles section, particularly in Fig. 4.22. This feature is suppressed by the growing channel length, see Tab. 4.2, due to the bigger electric field integral, i.e., a stronger particle focusing when the field acts over a longer distance.

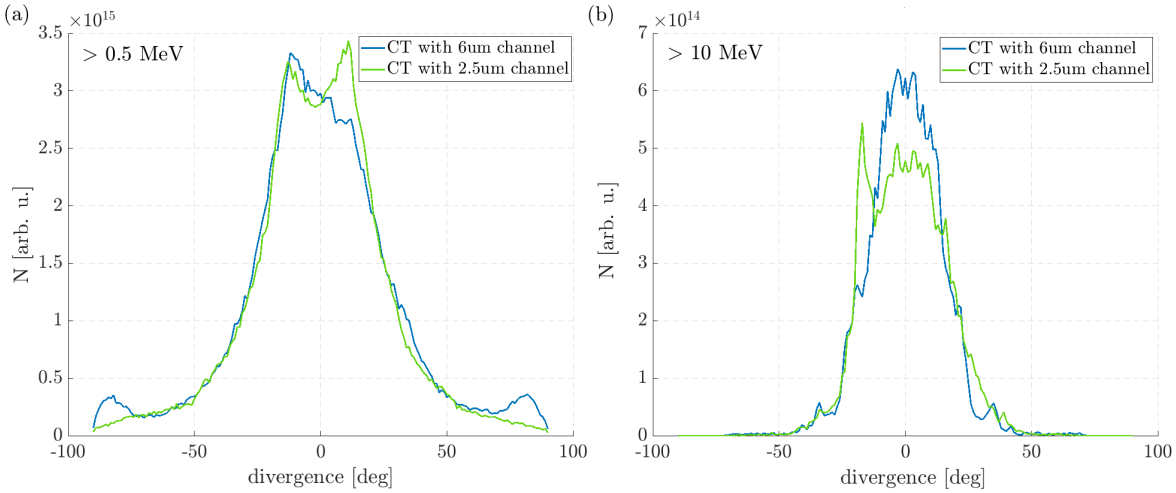

Figure 4.3: Comparison of proton angular plots for a curved target (CT) with two various lengths of straight channel attached to its rear side. Only protons moving forward within ±3.5 μm around the laser axis and having energy (a) above 0.5 MeV and (b) above 10 MeV were taken into account. The divergence was analyzed at 270 fs after the start of laser target interaction.

As demonstrated on the example of proton angular plots in Fig. 4.3, the formation of two beams (peaked at $-14°$ and at $11°$ for protons above 0.5 MeV) is visible in the case of shorter channel no matter the energy interval, whereas only one thick beam was formed in the case of longer channel. However, it is not centralized around the laser axis anymore, when also low energy particles are taken for analysis (only protons (a) above 0.5 MeV and (b) above 10 MeV were taken into account). In fact, the formation of these two proton beams is visible in proton density plots Fig. 4.22 as well. In contrast to this, no comparable beam filamentation connected with other target types was observed.
In the case of carbon ions, the divergence was reduced only by a few percents in comparison to the flat foil (specifically, by 6% and by 14%, for shorter and longer channel, respectively, when ± 3.5 μm transverse space cut was applied). The moderate divergence decrease is caused by a favorable orientation of EM fields which are stronger near the channel walls. On the other hand, carbon ions are pushed out from the geometrical center of the curvature (i.e., from the tight focus of protons) by repulsive forces, which results in strong divergence growth (by $\sim 170\%$) in the tight ± 0.5 μm space cut around the laser axis, see Tab. 4.2.

4.2.3 Flat targets with tapering channel

The on-axis proton beam produced from the flat target with tapering channel forming a 3 μm hole between arms shows the divergence decrease by 39% in comparison to the flat foil (± 0.5 μm transverse cut applied). As we can see in Tab. 4.2, any angular reduction was observed for on-axis proton beam in the case of 1 μm aperture, nor in the case of larger space cut (i.e., ± 3.5 μm) where, for both tapering-channel cases, the divergence was even higher. Such result was expected, because even the tighter transverse cut contains the highly divergent particles originated from disintegrated channel arms (especially from their endings) which do not in reality contribute to the on-axis accelerated beam due to their relatively low energy. On the contrary, carbon ions show divergence reduction in both transverse space cuts, because heavier ions are harder to be deflected from their trajectory by defocusing fields which are present at the outer surface of the tapering arms. In fact, these fields are present in all channel target designs, but only in the case of tapering ones they are spatially able to affect particles having lower divergence than $\sim 90°$. Moreover, the smaller amount of highly divergent ions are accelerated from the channel endings in comparison to the protons.
However, the true advantage of flat targets with tapering channels lies in their conceptual behavior of collimators. In fact, sloping arms are able to stop the particles accelerated from the flat part of the target with low energy and corresponding high divergence, see Collimating feature of tapering channels section for more information.

4.3 Particle divergence reduction affected by favorable establishment of EM fields

The principle of the decreasing divergence phenomenon in the case of the channel target in comparison to the flat foil stems from the combination of two things: i) the change in transverse E_y field in the case of the channel target due to different hot electrons motion (E_y and E_z in 3D) and ii) the formation of multipole magnetic field.

4.3.1 Focusing by the transverse electric field

The origin of the focusing phenomenon in the case of targets with channel is connected to the establishment of transverse electric fields (E_y and E_z). Whereas in the case of the channel target the transverse electric field components (E_y and E_z) are positive for negative transverse positions (y and z, respectively) and vice versa, in the case of the flat foil the situation is radically changed to opposite orientation after a few tens of fs after the laser-target interaction. In other words, electric force components affecting divergence are established in focusing direction for both foil designs at the very beginning, but the field orientation lasts during the whole simulation (i.e., $\sim$ 270 fs) only in the case of the channel target. On the contrary, in the case of the flat foil, the focusing field is attenuated quickly (i.e., $\sim$ 20 fs) and it is switched to the defocusing orientation, see Fig. 4.4. Consequently, the forces push positively charged particles produced from the flat target from the laser axis which increases proton beam divergence.

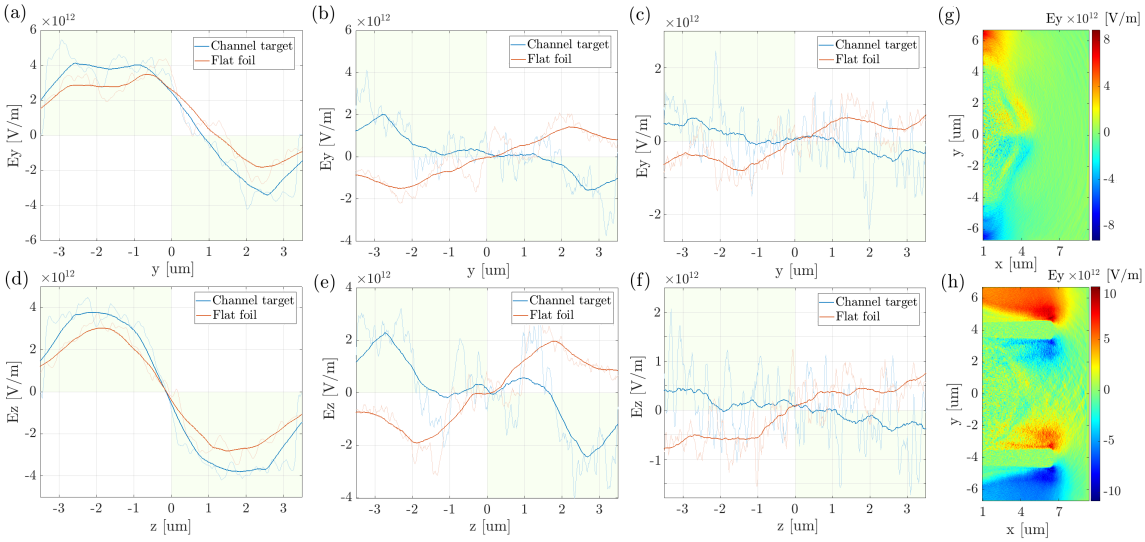

Figure 4.4: Demonstration of the opposite orientation establishment of electric field components affecting particle density: (a) – (f) Transverse electric field components E_y and E_z are plotted along their corresponding axis for the flat foil (red curve) and the flat foil with 6 μm channel (blue curve) at different times – at 30 fs ((a), (d)), at 90 fs ((b), (e)) and at 120 fs ((c), (f)) after the start of laser-target interaction. Focusing regions for ions are highlighted in green, defocusing regions in white. The analysis was done 3 μm behind the rear side of the flat part of the both foils, i.e., in the middle of the channel length in the case of the target with guiding arms. Graphs (g) and (h) show transverse electric field E_y in the plane $x-y$ at 90 fs after the start of laser-target interaction for the flat foil and the channel target, respectively.

Such big difference in electric field formation is caused by the target shape and by the corresponding spatial density and the movement of hot electrons in the region where protons are accelerated. In the case of the flat foil without any additional structure, hot electrons escape the target at its rear side, which temporarily leads to the focusing electric field formation (Fig. 4.4 (a) and (d)), since the area, where the ions are accelerated, is filled with negative electrons. Nevertheless, such electrons are spread to the sides quickly (few tens of fs), which

results in uncompensated transverse density gradient of the accelerated ions bounded with the establishment of transverse electric field with opposite, i.e., defocusing, direction as visible in Fig. 4.4 (b), (e) and (c), (f).
In the case of the flat foil with channel, the situation is different. Firstly, electrons are accelerated from the flat part of the target, however in contrast to the flat foil, they are confined by the channel afterwards. In particular, they do not spread to the sides, but propagate along the channel walls, recirculate in the target and/or bounce within the guiding cylinder walls. Originally focusing electric field is thus confined in its orientation longer in contrast to the flat foil, because electrons do not spread away from the laser axis quickly, but they stay in the vicinity of the guiding channel walls where the quasineutrality is consequently violated. Therefore these electrons are attracted back to the center which causes the presented focusing electric field. Such feature is the same for both electric fields affecting the divergence, i.e., for E_y as well as for E_z as shown in Fig. 4.4. The electrons motion inside the channel and their corresponding formation of current loops will be discussed later in 4.3.2 section.
The difference between electric field orientation of the flat target and the channel target is also demonstrated in Fig. 4.4 (g) and (h), where E_y component is shown in side view, i.e., in $x - y$ plane at 90 fs after the start of laser-target interaction, which corresponds to the situation depicted in Fig. 4.4 (b). This is the clear demonstration of one reason leading to the divergence reduction in the case of flat targets with channels.
The formation of transverse electric field having reversed sign inside the channel in comparison to that of the flat foil has been already reported in 2D [219], [233] as well as electrons propagation along the channel walls with strong return current [219]. Although the simulation parameters were different, it clearly demonstrates the ability of rear-placed structures to keep electric focusing field for longer time due to the electron confinement and motion along the channel walls.

4.3.2 Generation of multipole magnetic field

Strong magnetic fields driven by nonparallel gradients of electron temperature and density are generated at the back side of a target flat-part (i.e., the part perpendicular to the laser beam axis direction) by radial thermal transport mechanism as described in [13], [100] and experimentally seen in [144]. In fact, the orientation of transverse magnetic fields schematically depicted in Fig. 4.5 (a) corresponds to the laser-generated hot electron transport along channel arms forming loops from the return current. The situation is demonstrated by plots showing current densities in the laser axis direction for both target designs, see Fig. 4.5 (b) and (c). In the case of the channel target, electron forward and return flows are visible along the arms, whereas in the case of the flat foil, electrons do not undergo any preferable motion. Consequently, well-organized magnetic field structure inside the guiding channel is expected and will be proved. From a divergence point of view, both B_y magnetic field (in $x - z$ plane) and B_z field (in $x - y$ plane) have defocusing effect on a proton beam passing through the cylinder. Nevertheless, if these symmetric magnetic fields are combined together into the radial one $B_r = (B_y \cdot y)/r + (B_z \cdot z)/r$ (where r represents the radius measured from the channel center), a quadrupole as well as an octupole magnetic fields are obtained. The order of prevailing multipole depends on the time and the exact position along the channel, see Fig. 4.6 (g) and (h), where both 4- and 8-pole multipoles are visible.

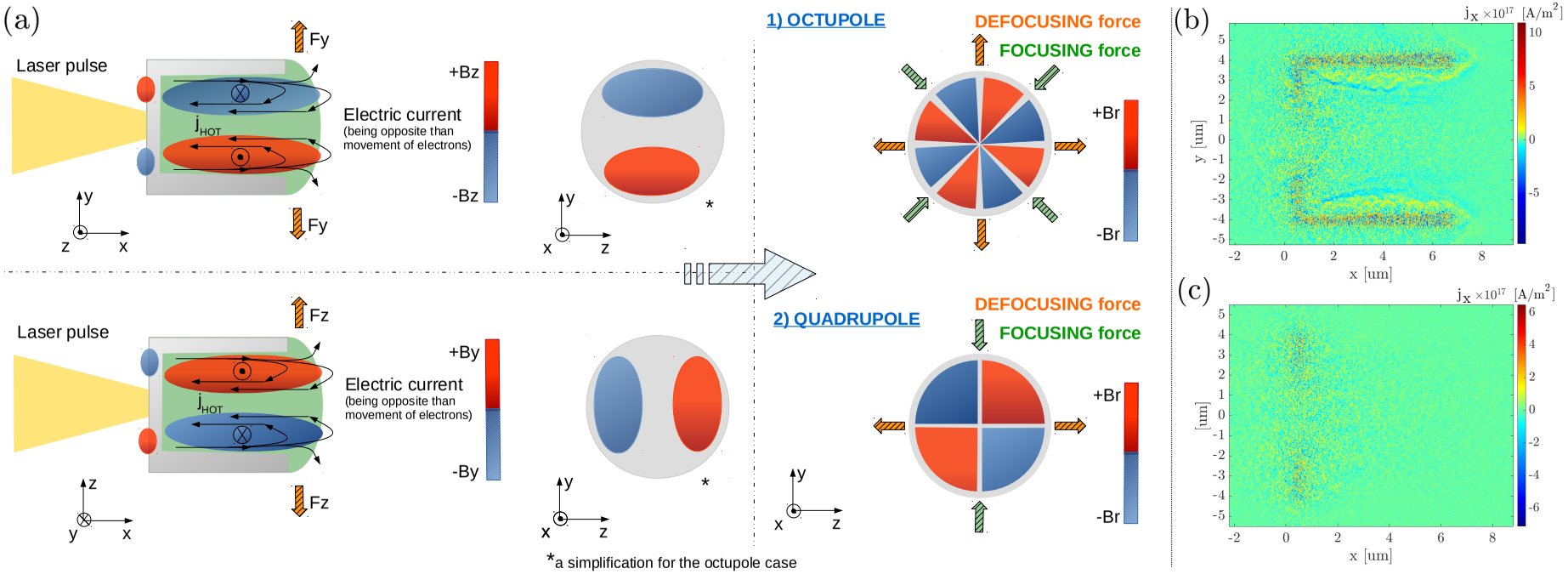

Figure 4.5: (a) Schematic sketch of the establishment of magnetic field components driven by electron motion, i.e., by the formation of current loops, and of the magnetic multipoles creation in all planes of Cartesian coordinate system. Both magnetic octupole and quadrupole were observed inside the channel, depending on the time and the position along the channel length. Electron current density j_x showing prevailing electron motion in the laser axis direction for (b) the channel target and for (c) the flat foil is presented at the end of 2D simulations.

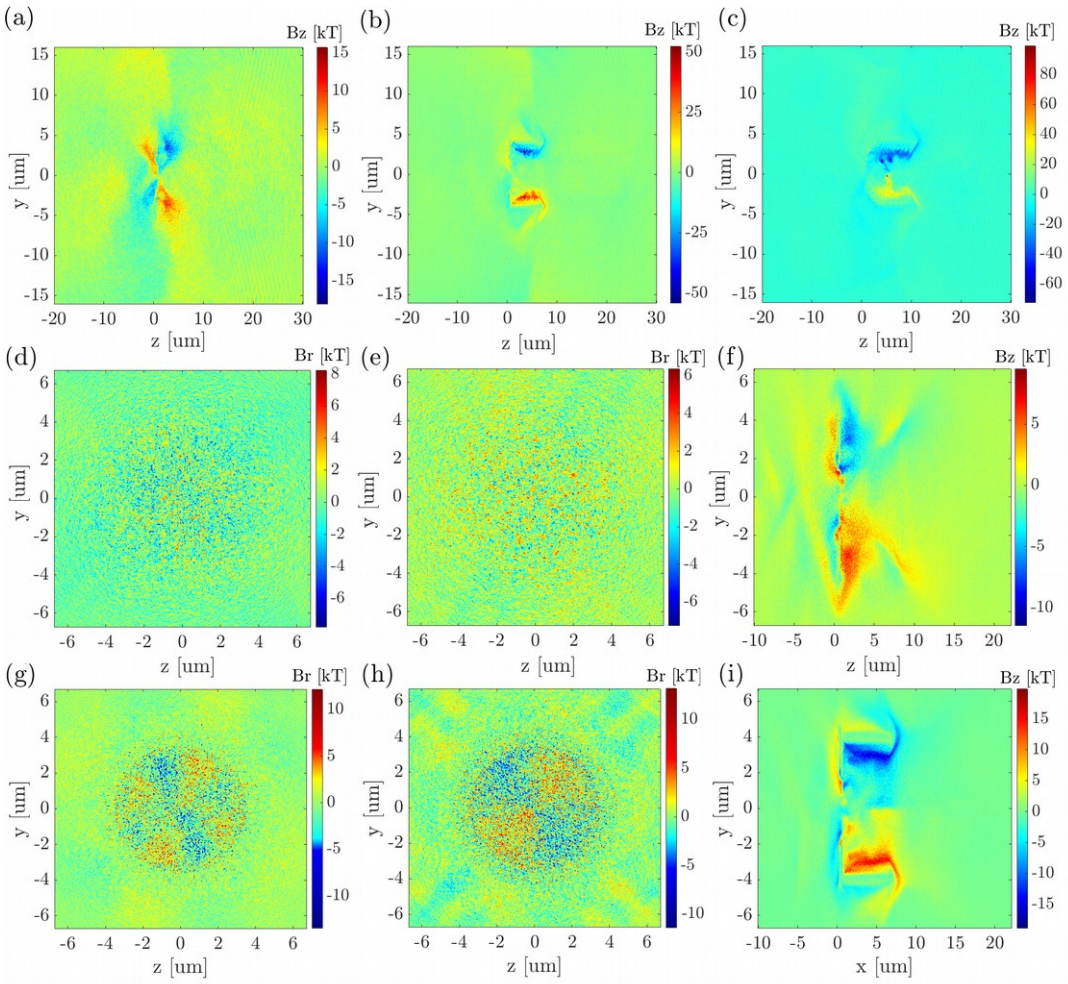

Figure 4.6: Magnetic field comparison; *2D case:* magnetic field component B_z for various target types at the end of the simulation: (a) the flat foil; (b) the flat target with straight 6 μm long channel; (c) the curved foil with straight 6 μm long channel. *3D case:* Magnetic field components B_r and B_z in various 2D planes of (d) - (f) the flat foil and of (g) - (i) the channel target (i.e., the case corresponding to (b) in 2D). Radial magnetic field B_r in $y-z$ plane is taken at 160 fs after the start of laser-target interaction (d) + (g) at 3 μm (*the channel case (g) shows the octupole (i.e., the quadrupole with strong octupole component)*) and (e) + (h) at 5.85 μm (*the channel case (h) shows the quadrupole*) behind the rear side of the flat target parts. At the presented time scan, the acceleration process is fully developed and the majority of protons are still in the channel. (f) + (i) show B_z field at the end of the simulation.

4.3.2.1 Quadrupole field with strong octupole component

The combination of quadrupole and octupole magnetic fields is natural, since an octupole is the first and the strongest not allowed high order harmonics of a quadrupole [161], [162]. In reality, the so-called not allowed harmonics become present when the magnet symmetry is somehow violated, which is exactly the case of disintegrated target by the laser pulse. On the contrary, allowed harmonics are always present in real multipoles and can be only suppressed but not removed.
In fact, octupole magnets are usually used in combination with quadrupoles for correction of spherical aberrations in accelerator physics [163] and they make particle beam spatially uniform [160]; for more information see also the section Multipole magnets.
As depicted in Fig. 4.5 (a), if a simple analysis of magnetic Lorentz force is made for an octupole, we can see defocusing forces along the Cartesian coordinate system and focusing forces along the axes rotated by 45°. The space differences between these forces are small and uniformity of the produced particle beam is achieved (which can be justified from the beam optics formulation for an octupole [153]) instead of setting any preferable focusing or defocusing transverse directions. In contrast, quadrupoles are usually used for focusing particles in one plane only, because in the second plane they cause defocusing [153], [154]. The position of positive and negative poles determines their focusing and defocusing plane, see Fig. 4.5 (a). This means that a perfect quadrupolar symmetric field (which arose from symmetric magnetic field components) will produce an asymmetric particle beam. Since this effect is widely known in accelerator physics, two quadrupoles are usually used in a so-called FODO cell, to have a net focusing effect, and three quadrupoles to have both vertical and horizontal focal points in the same position [153], [154]. Both divergence reduction in preferable plane and higher spatial uniformity of accelerated proton beam from the channel target were observed in the simulation.
Furthermore, any real magnetic or electrostatic lens, which is a good approximation of our channel target, suffers from geometrical aberration and from chromatic aberration (which is here strong due to the large energy spread). Whereas the various focusing in different planes is caused by magnetic quadrupole, the minor decentralization of some angular distributions is caused by the combination of non-ideally homogeneous particle beam, non-ideal hot electron transport and the field imperfections, see Fig. 4.2. All these features occur also in accelerator beamlines [153], [154].

4.3.2.2 Strength of generated multipole and its time&space evolution

Produced multipole magnetic field inside the guiding channel has a strong gradient, namely 5.7 kT/μm (i.e., 5.7 GT/m over 7 μm (the total length of the channel target)) in the case of both B_z field along $y-$axis and B_y field along $z-$axis. This corresponds to a relatively high field integral of 0.368 T·m (the maximum reached at 90 fs after the start of the interaction). The values of the field integral vary with time although they remain comparatively strong during the whole simulation. Specifically, the magnetic field integral starts at the value of 0.217 T·m at the beginning of the acceleration, whereas it drops down gradually from the maximum of 0.368 T·m to 0.098 T·m till the end of the simulation. For comparison, quadrupole electromagnets being used for beam focusing implemented at ELIMAIA beamline (implemented with L3 HAPLS laser of relevant parameters) have gradients up to 10 T/m over 70 mm (field integral 0.084 T·m) and PMQ magnets being also installed there have 100 T/m

over 36 mm (field integral 0.291 T·m) [6], [231]. Therefore, the field produced inside the channel target shows a higher field integral than that of quadrupole electromagnets of ELIMAIA during the whole acceleration process. The field integral value gives a proper insight and a comparison of the magnetic field effectiveness for different magnetic lenses, since it is reflecting both the field strength and the distance at which it affects the particles directly. On the other hand, strong fluctuations were observed in $B_y - y$ and $B_z - z$ characteristics, which should be zero in ideal quadrupoles or octupoles. The amplitude of these fluctuations reaches at maximum 25% of B_y (along $z-$axis) and of B_z (along $y-$axis) field amplitudes, see Fig. 4.7 (a) and (d). In real quadrupole/octupole well-designed magnets it would be a few tenths of percent. These oscillations are caused by the combination of the additionally generated fields by the moving particles, which are not present in standard magnets, and by limited number of numerical macroparticles in computationally demanding 3D simulation. Nevertheless, a quadrupole/octupole structure of the field is definitely present as demonstrated in Fig. 4.7 and participates in the proton focusing effect, even though the data suffer from relatively high fluctuations. Particularly, magnetic quadrupole with strong *octupole* component is visible in Fig. 4.7 (e) where radial magnetic field B_r is plotted over the angle (be aware of four positive and four negative "poles" indicating the octupole) as well as in in Fig. 4.7 (b) and (c) showing $B_y - z$ and $B_z - y$ characteristics. These characteristics should have a linear spatial profile for ideal quadrupole or a cubic profile for ideal octupole as shown in Fig. 2.7 (see the section 2.4), therefore it is visible that the field recorded in PIC simulation is due to the high fluctuations somewhere in between. The pure *quadrupole*, having only two positive and two negative "poles", is demonstrated in Fig. 4.7 (f). The difference between obtaining strong octupolar or quadrupolar magnetic field is only the various positions along the channel where the field was taken; the time scan remained the same.

The creation of magnetic multipoles was verified via COMSOL and Opera Simulation Software[1] [234] by Dr. Francesco Schillaci being responsible for ELIMAIA/ELIMED magnetic system [6], [231]. Two codes were used, because the modelling of magnetic field in COMSOL is straightforward, nevertheless it systematically overestimates the magnetic field of permanent magnets by $\sim 6\%$. This value comes from magnetic measurements on real systems and from simulations performed in Opera 3D (which is the reference code for magnets in accelerators). Consequently, the correcting factor of 0.94 has been applied in COMSOL, where the octupole magnet (having the same ratio between its dimensions as the channel target) was modeled. The obtained magnetic field characteristics are presented in Fig. 4.8 and can be compared with corresponding plots for the target with 6 μm long cylindrical channel in Fig. 4.7.

Multipole magnetic field produces different strength (gradient) from the central axis to the channel walls because of various density of current loops. Moreover, if we took the channel target as a magnet, the field would not be established properly because of insufficient target's dimensions. In fact, the magnet mechanical length should be at least two times longer than its diameter in order to let the magnetic field develop to its full power [153], [154]. This fact corresponds well to the decreasing divergence tendency associated with the channel length extension as visible in 2D simulations (where the channel lengths of 4, 6 and 8 μm were studied). When the described dimension rule is applied on our expanded channel target (where the similar magnetic field as that of a multipole magnet has been created), the optimal ratio

[1] Opera Simulation Software is a Finite Element Analysis software which allows users to perform simulations of electromagnetic (EM) and electromechanical systems in both 2D and 3D. Opera complements the existing SIMULIA EM portfolio with its strength in low frequency simulation, which is extremely useful for optimizing the design of magnets, electric motors and other electrical machines [234].

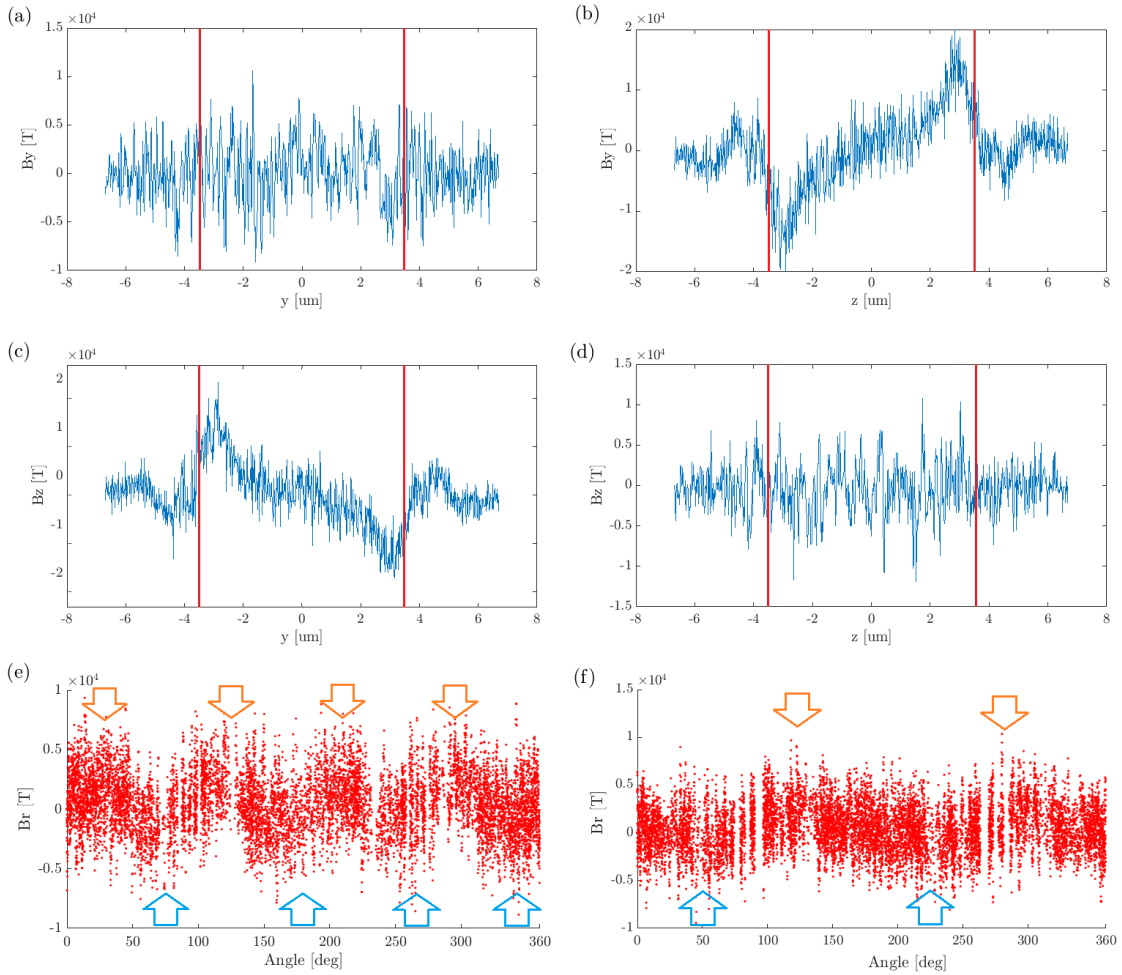

Figure 4.7: Graphs showing magnetic quadrupole and octupole characteristics B_y or B_z plotted against two transverse axes: (b) and (c) demonstrate the magnetic octupole field, whilst (a) and (d) indicate high fluctuations present in the multipole ($\sim$ 25% of the $B_y - z$ field characteristics). The magnetic field is recorded at 270 fs after the start of laser-target interaction and it is taken in the middle of the channel length along $x-$axis. The red lines illustrate the inner walls of the cylindrical channel. The radial magnetic field B_r taken within 0.32 μm thick annulus inside the channel plotted against the angle shows (e) an octupole in the middle of the channel (i.e., at 3 μm from the flat rear along the laser propagation axis) and (f) a quadrupole at the end of the channel (i.e., at 5.85 μm) at 160 fs after the start of laser-target interaction. Fig. 4.6 (g) and (h) showing the octupole and the quadrupole field corresponds to the graphs (e) and (f) here, respectively.

between the channel length and its inner gap implies the optimal channel length equal or larger than 14 μm, when the internal diameter of the cylinder remains the same. Similarly, when the ratio is evaluated between the overall longitudinal and transverse dimensions of the channel, even the cylinder longer than 17 μm would be required. If such mechanical length of the magnet/target is reached, the amplitude of the magnetic field would, according to this rule, rise and the magnetic field integral would develop to the required shape. Therefore, we can expect that the features of established multipole would be stronger and more stable. Nevertheless, such target design has been never studied because of high numerical demands of 3D PIC simulations and future problematic manufacturing due to the long and thin channel. Moreover, it is also important to point out that in the case of longer channel, the particle energy drop is expected since the trend of decreasing maximum energy with increasing channel length will be demonstrated in Energy spectra & Number of particles section. Consequently, the simulated flat target with straight 6 μm channel seems to be still the best option in order to reach a compromise among the high energy, low divergence of accelerated ion beam and reasonable fabrication efforts, which is the reason why 3D simulation of this design was performed.

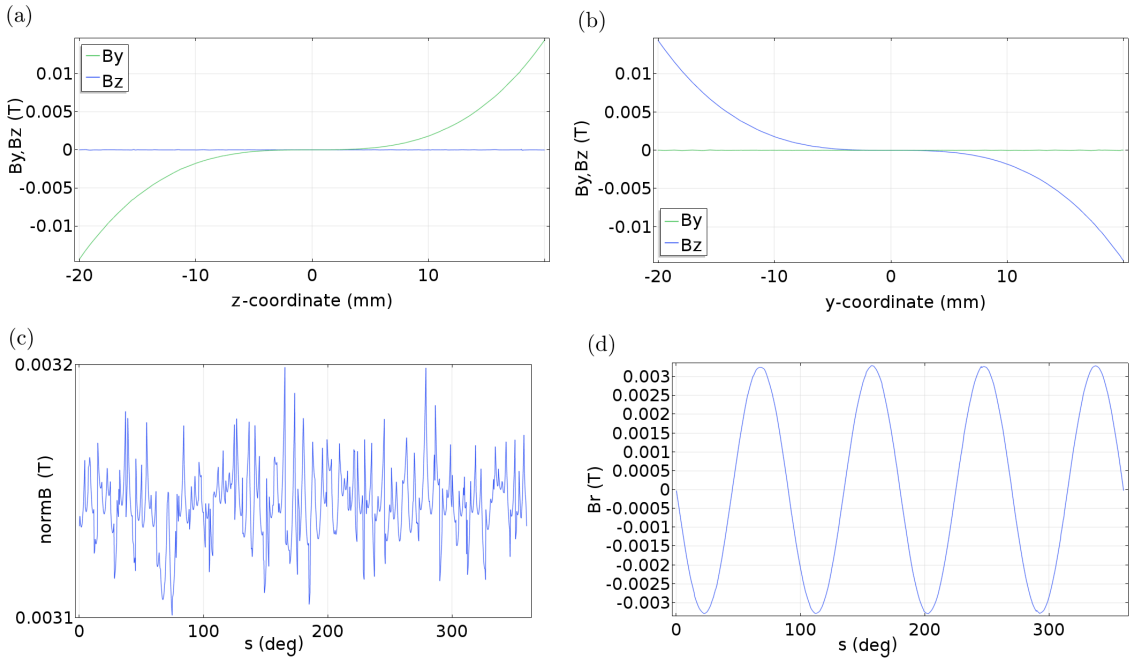

Figure 4.8: Magnetic characteristics of octupole magnet modeled in COMSOL by Dr. Francesco Schillaci with corrections obtained from Opera Simulation Software [234]. The magnet has the same ratio between dimensions as the plastic channel target simulated in PIC. The presented characteristics obtained in COMSOL correspond to the magnetic field profiles Fig. 4.7 obtained by PIC simulation.

The radial magnetic field varies also along the channel length and with time, because the quadrupole has the strong octupole error (as discussed in the section 4.3.2.1). Despite of that, the magnetic multipole remains relatively strong inside the channel during the whole acceleration process (few hundreds of fs), it has relatively well-defined shape and high field integral in contrast to the flat foil. In fact, in the case of the reference flat target, magnetic

field components drop in amplitudes quickly (in 10 fs after the end of laser-target interaction) and the field spreads to the sides, which, in later times, results in a creation of only a week magnetic multipole with no specific order and low field integral, see Fig. 4.6 (d) and (e). The difference between these two scenarios lies in already discussed organized or disorganized electron motion (see Fig. 4.5 (b) and (c)) and in spatial confinement of the field structure. To summarize, although the general magnetic multipole creation was seen in both target cases, it was formed and confined well only for the channel one.

4.3.2.3 Comparison between 2D and 3D

The magnetic field amplitude was suppressed in 3D for each target case compared to 2D, similarly as the electric field amplitude was, since the magnetic field is generated by the current loops of electrons. With an extra added dimension, electrons can expand in two transverse axes, not only in one, which limits their current in each direction over the same distance. Magnetic field amplitude is then reduced accordingly. Nevertheless, the orientation of transverse magnetic field is not affected by the target design as it is in the case of transverse electric field. Higher values of magnetic field were observed in 2D for all structured targets in comparison to the flat foil, see Fig. 4.6.

4.3.2.4 Summary

A quadrupolar magnetic field with strong octupole component was observed in our 3D simulation of the channel target. Two effects on passing particle beam can be observed. Firstly, the formation of quadrupole magnetic field contributes to the establishment of the preferable focusing plane $x - y$ (as discussed earlier, see Divergence section, particularly Fig. 4.2 and Tab. 4.2). Secondly, octupole field makes the beam more uniform, see Spatial uniformity of the proton beam section.

4.3.3 Comparison of the magnetic and electric field effectiveness

In fact, the ability of divergence modification can be assigned both to electric and to magnetic fields as already demonstrated, although their effectiveness depends on the proton energy. In Fig. 4.9 (a) the comparison of electric and magnetic curvature radii in $x-y$ plane (taken from the electric and the magnetic rigidity) of a reference proton having particular energy are shown for the flat and the channel target simulated in 3D. The reference proton moves only along the $x-$axis and the values of magnetic and of electric fields were taken as an average from 3D PIC simulation at its end for both targets. In other words, the graph shows how strongly a trajectory of the reference proton (moving along the laser axis with particular energy) would be affected by EM fields (3D PIC simulated values) while the particle propagates through. Even though the amplitudes of both fields fluctuate in time during the simulation, the average values are sufficiently stable. It was verified that the proton energy value, dividing the areas where electric and magnetic fields become more efficient, does not change substantially (i.e., quantitatively by a few MeV on the overall scale of tens MeV). In general, this analysis provides only an approximate information, because the assumption of a reference proton propagating only along the laser axis was used. In reality, particles move with a non-zero momentum also in the $y-$ and $z-$directions. Consequently, the energetic boundary between electric and magnetic field effectiveness will vary, but the tendency will remain the same.
One can notice that the electric field affects the low energetic particles more than those

with high energies for both targets (i.e., the radius of curvature (the bending of the particle trajectory) is smaller for the low energy particles). Nevertheless, this fact alone gives no information whether the effect is focusing or defocusing, which is why the additional knowledge of the bending direction is crucial. Therefore, the green legend was added at the top of Fig. 4.9 (a) in order to highlight that the electric field causes a focusing effect on protons in the case of the channel target, whereas it generates defocusing effect in the case of the flat foil (see Focusing by the transverse electric field section and Fig. 4.4). The proton beam parameters, including not only the divergence but also the uniformity of the beam, are mostly affected by magnetic fields for proton energies above 3.5 MeV and above 8.5 MeV for the flat and the channel target, respectively. In contrast to the electric field, the magnetic field is well-defined for the channel target only and disorganized for the flat one. Thus, the magnetic multipole is focusing (quadrupole) in $y-$direction and/or makes the beam more uniform (octupole) in the case of the channel target, but it has no specific order in the case of the flat foil, i.e., no specific effect on protons.

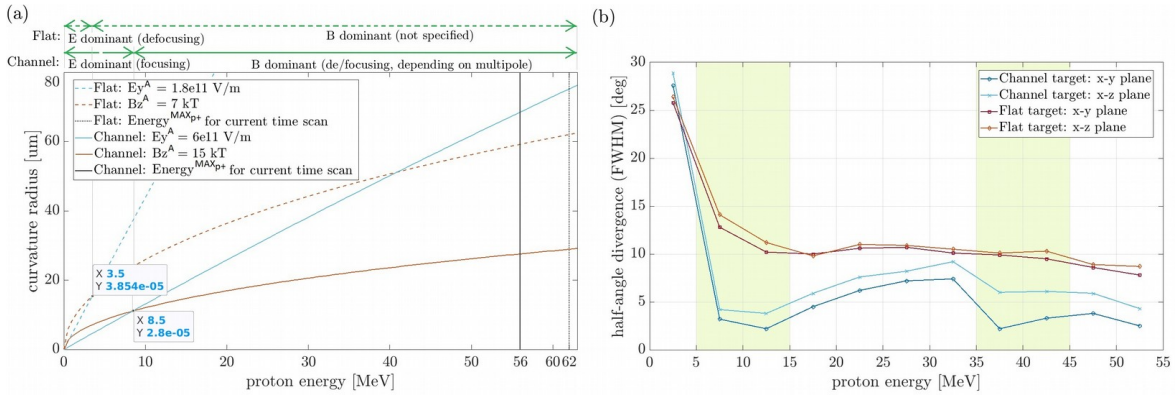

Figure 4.9: Comparison of electric and of magnetic field impact on the proton beam divergence for the channel and the flat target at the end of 3D simulations: (a) the dependence of electric and magnetic curvature radius in $x-y$ plane (taken from electric and magnetic rigidity) on a particular energy of the reference proton (moving along $x-$axis); the nature of the radius (de/focusing) is shown above the graph for both fields; (b) half-angle proton beam divergence (FWHM) in both $x-y$ and $x-z$ planes inferred from 3D PIC simulations and analyzed separately for energy intervals of 5 MeV width up to 55 MeV.

The effect of the electric and the magnetic fields is depicted in Fig. 4.9 (b) where the values of half-angle divergence (FWHM) in $x-y$ plane (studied in Fig. 4.9 (a)) as well as in $x-z$ plane are shown for the flat and the channel target with dependence on proton energy. Here, the proton divergence values are taken at the end of 3D PIC simulations, i.e., no reference proton strictly moving only in $x-$direction was used as in the case of Fig. 4.9 (a). Consequently, this analysis indirectly covers various field conditions (e.g. various orders of the magnetic multipoles and various field strengths along and across the whole channel), because the resulting proton divergences were affected by them. In reality it means that, whereas, e.g. the 40 MeV protons experienced the quadrupole field in the middle of the channel, the 20 MeV protons did not, because the order of the multipole had been already changed when they arrived to that place. This is the difference from Fig. 4.9 (a) which is more static in this meaning and it serves as a model situation.

The energy intervals analyzed in Fig. 4.9 (b) were sampled from 0 MeV to 55 MeV with the width of 5 MeV. Although the maximum energies were slightly higher than 55 MeV (56 MeV and 62 MeV for the channel and the flat target, respectively), the statistics was low in these intervals, thus they are not included in the analysis. The results indicating a reduction in ion beam divergence by magnetic field depend on specific particle energy and they are in good agreement with the fact that a quadrupole and an octupole act as a chromatic lens [153]. We can clearly observe two regions of proton divergence reduction in the case of the channel target in comparison to the flat one (marked in green, being stronger in $y-$direction).
The first region is located approximately in the energy interval of $\langle 5, 15 \rangle$ MeV and is caused by the combination of focusing electric field and well-defined magnetic field in the case of the channel target where both terms have significantly lower curvature radius (in Fig. 4.9 (a)) than those for the flat foil. Moreover, in the case of the flat foil, the electric field has defocusing effect and the magnetic field does not form a proper multipole as discussed earlier, thus it has no specific effect on protons. The divergence of protons moving inside the cylinder with the radius of 3.5 μm was reduced in this energy interval by 78% and by 69% for $x - y$ and $x - z$ planes in comparison to the flat foil, respectively (the overall divergence drop of protons above 0.5 MeV was 56% and 51% for various planes, see Tab. 4.2 and Fig. 4.2).
The second region, where the proton divergence was effectively reduced, is located in the energy interval of $\langle 35, 45 \rangle$ MeV and is caused by the favorable establishment of the magnetic quadrupole focusing in the y-direction and appearing at the position where the protons of corresponding energy were located at that time. In this case, the divergence of protons moving inside a cylinder with the radius of 3.5 μm was reduced by 73% and by 46% in $x - y$ and $x - z$ planes in comparison to the flat foil, respectively (the overall divergence drop of protons above 30 MeV was 68% and 27% for various planes, see Tab. 4.2 and Fig. 4.2).
Naturally, the difference between divergence values in various planes is greater in the channel target case than in the case of the flat foil where both planes show more similar results since no proper quadrupole was formed. Nevertheless, a moderate drop with respect to the flat foil was recorded in $x - z$ quadrupole defocusing plane as well because the focusing electric field was still present. It is the reason why the difference between the channel target planes are bigger in the high-energy interval, where the electric field is less efficient, than in the low-energy interval. Furthermore, the small differences between flat foil divergence in various planes are discussed from the point of view of the linear polarization direction in the section 4.4.3.

4.4 Additional features of generated fields

4.4.1 The inversion in focusing components of electric and magnetic fields

The phenomenon of a field inversion has been observed in plasma physics in various fields. For instance, the heliospheric magnetic field suffers from field inversions regularly as they are the consequences of various processes connected with magnetic reconnection [235], [236], [237] and corresponding loops opening or with coronal effects driven by superthermal electron beams propagating predominantly in atypical direction than the rest of electrons [238], [239]. Moreover, plasma waves and fluctuations may deflect magnetic field as well. Therefore, they are able to drive the field inversion similarly as in space physics [240], [241]. The magnetic field inversion is perceived as a field error when designing magnets and it is caused by the manufacturing inaccuracies resulting in the distorted geometry [242]. To summarize, the field

inversions are connected either to an atypical motion of electrons (in comparison to the rest) or to an anomalous magnetic field establishment due to some discontinuities.
The small field inversion was observed also in the presented simulations, explicitly around the laser propagation axis both in transverse magnetic and transverse electric fields (even though the orientation of the prevailing transverse magnetic field inside the channel is stable and established properly). The inverted field structure propagates slowly from the channel interior towards the vacuum behind the target and loses its strength gradually for approximately ~ 100 fs. Specifically, the spatially determined electric inverted field (highlighted by the red areas in Fig. 4.10 (a)) is caused by the ponderomotive expulsion of electrons from the laser axis at the flat rear side of the target. In fact, electrons were pushed from the high field region (i.e., from the transmitted laser pulse visible in Fig. 4.10 (b) to the sides, see also the section 4.4.1.1), which, together with the fact that the narrow proton filament is accelerated on-axis resulted in the reversed sign of the electric field on the laser axis, similarly as in the flat target case, see Focusing by the transverse electric field. The spatial cut along $x-$axis, where the 1D analysis of the electric field inversion is presented (Fig. 4.10 (a)), corresponds to the position of the magnetic field inversion at the same time. The inverted magnetic field movement is demonstrated by the various time scans presented in Fig. 4.10 (b)–(d), where the propagation of the transverse magnetic field is clearly observable. Naturally, the electric field inversion is moving together with the inverted magnetic field.

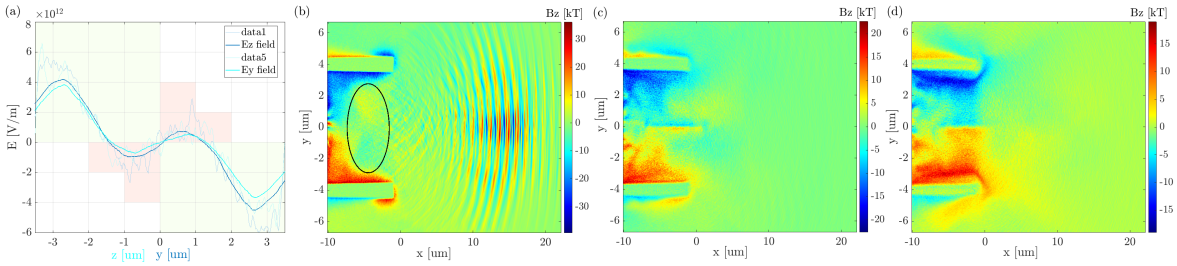

Figure 4.10: Field inversion in EM fields of the channel target: (a) electric field components E_y and E_z affecting focusing of ions at 80 fs after the start of laser-target interaction at $x = 0$ μm, the field inversion is highlighted by red regions; transverse magnetic field B_z showing gradual movement and continuous disappearing of the magnetic field inversion (marked in black oval in (b)) at (b) 90 fs, (c) 170 fs and 240 fs after the start of laser-target interaction.

The phenomenon of EM fields inversion in our case can be justified from the magnetic point of view (i.e., from the theory of standard magnets) as well as from the electric one (i.e., by the movement of electrons):

- *Movement of electrons - current loops:* As already presented in the electron current densities plot Fig. 4.5 in Generation of multipole magnetic field section, electrons form current loops along the guiding channel arms. In fact, a strong return current was already reported in similar case [219]. Nevertheless, some electrons around the laser propagation axis form a loop in opposite direction, when they are attracted back to the channel center towards the accelerated ions more than towards the guiding arms. The electron movement forms a well-known fountain shape [51], [84] originating from a kinetic force $E \times B_\theta$ described, e.g., in the Target Normal Sheath Acceleration (TNSA) section. See the schematic sketch of the current

flow in Fig. 4.11 which is, from the definition, opposite than the real electrons movement. In fact, such current loops generate accordingly oriented magnetic field B_z, which has the opposite orientation than the prevailing field structure. With increasing time, the turning point of electrons shifts further from the target, which results in the motion of inverted field along the laser axis. The inversion disappears when the majority of electrons are not attracted back to the target.

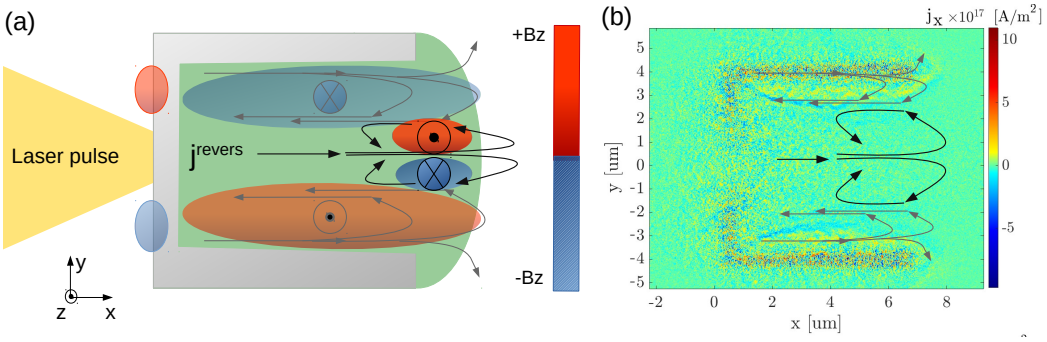

Figure 4.11: Schematic sketch of the generation of the field inversion driven by electrons: (a) Current loops of presented orientation generate the transverse magnetic field observed in the simulations of the channel targets. The current loops responsible for the inverted field are demonstrated schematically by bold black arrows (from the definition of a current, electrons move in opposite direction than the loop orientation); (b) Simulated electron current density j_x showing prevailing electron motion in the laser axis direction for the channel target; the simplified current loop orientation is shown.

- *Similarity with features of real magnets:* The magnetic field inversion effect is well known also in magnet designing & production. The phenomenon occurs when the dimensions of the magnet are not in the optimal ratio, i.e., when the longitudinal dimension is not at least two times longer than the transverse dimension of the magnet [154], [157] or when the manufacturing suffers from inaccuracies resulting in the distorted geometry of the magnet [242]. In fact, both of these features are present also in the channel target case, which has not the optimal ratio between its dimensions and it undergoes an expansion/shape violation during the acceleration process. The presence of the magnetic field inversion in the case of a non-optimal octupole magnet, having the same dimensions as the simulated channel target, was also demonstrated in COMSOL, see Fig. 4.12.

As demonstrated, the structure of the fields inversion is moving inside the channel along the laser axis, hence, it influences the on-axis proton filament predominantly. From the divergence point of view, the electric field inversion has defocusing effect on protons and ions. From the magnetic point of view, a week multipole with opposite orientation than the already described one is generated (e.g., the quadrupole has its focusing and defocusing planes switched). Although the inversion field is more disorganized than the field present in the stable multipole described before, the clear evidence of the inverted radial magnetic field was observed at 5.85 μm behind the target flat rear side (i.e., nearly at the end of the channel) at 210 fs after the start of laser target interaction. See the comparison of the reversed and

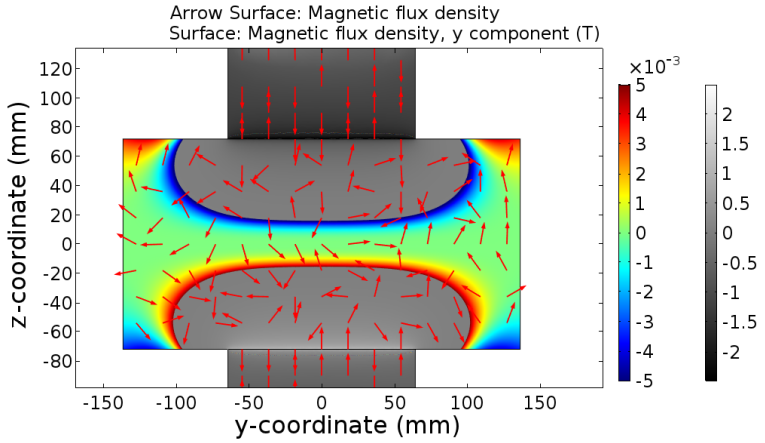

Figure 4.12: Magnetic field simulation of a non-optimal octupole magnet, having the same dimensions as the simulated channel target. The case was treated in COMSOL and shows the field inversions at both sides of the magnet; courtesy of Dr. Francesco Schillaci.

the standard octupole in Fig. 4.13.
The field inversion was very limitedly observed also in the case of the flat foil, but only in magnetic field B_z. The inverted field shows up at 90 fs after the start of laser-target interaction along the laser propagation axis, in agreement with the channel target case. Then, it starts spreading to the sides and vanishes quickly in next 40 fs. In addition, the inverted field is also weaker in comparison to that in the channel target, because electrons are not confined inside the cylinder, but they are spread into vacuum, which suppresses the density of current loops and the magnetic field correspondingly. Anyway, no true electric field inversion was observed in the case of the flat foil, since the orientation of transverse electric fields is already defocusing, see the section Focusing by the transverse electric field.

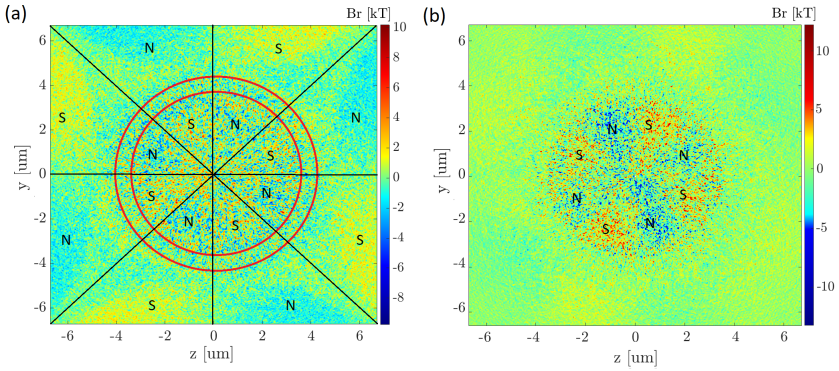

Figure 4.13: Comparison of standard and inverted radial magnetic fields in $y-z$ plane inside the channel: (a) inverted octupole generated at 5.85 μm behind the target flat rear side, i.e., at the cylinder end (the channel walls are depicted by red circles) at 210 fs; (b) standard octupole at 3 μm behind the target flat rear side at 160 fs after the start of laser-target interaction.

4.4.1.1 Partially-transmitted laser pulse

The radiation visible behind the channel target in Fig. 4.10 (b) was moving with the speed of light, had the reduced intensity and the two times shorter full-duration than the originally incident laser pulse. Moreover, the same partially-transmitted light was observed in the case of the reference flat foil (and, hence, in all 3D simulations presented within this work). Therefore, it has been identified as the partially-transmitted original laser pulse, even though the evidence is not straightforward. The scope of this subchapter is to suggest possible scenario(s) how the part of the laser pulse might penetrate through the foil, even though no clearly visible leak (i.e., an undeniable perforation) through the target material has been found. Nevertheless, the author is aware that the observed phenomenon is likely more complex, therefore the following explanation is rather the basic background for the extended study in the future. In fact, strong similarities with already published & described phenomena discussed below were observed.

Firstly, it has been already proved that femtosecond nearly single-cycle ultraintense light pulses can be produced from the laser pulses interaction with ultrathin foils [243]. When the laser light interacts with an adequately thin overdense plasma, both are self-consistently (nonlinearly) modulated. The optimal foil parameters depend on the specific laser pulse and the skin depth of the plasma; the example used in the article [243] covers the 4-periods-long laser pulse having $a_0 = 20$ and $\lambda = 1$ μm which interacts with the 0.7 μm thick target having the density of $n_e/n_c = 8$. In a nutshell, ponderomotive force initiated by the laser pulse has to compress electron layer inside the target to a slab thinner than the skin depth. Then, the target is transparent only to the highest intensity part of the laser pulse, which can be partially transmitted through the foil. In other words, when the target thickness is reduced to the value, which is still larger than the skin depth, the laser pulse can be still significantly transmitted because of the compression of the electron layer only. As a result, the transmitted pulse has a much shorter duration than the incident pulse. This duration depends primarily on the laser-light intensity gradient and foil conditions. The similar process is usually used for the generation of single attosecond pulses [244].

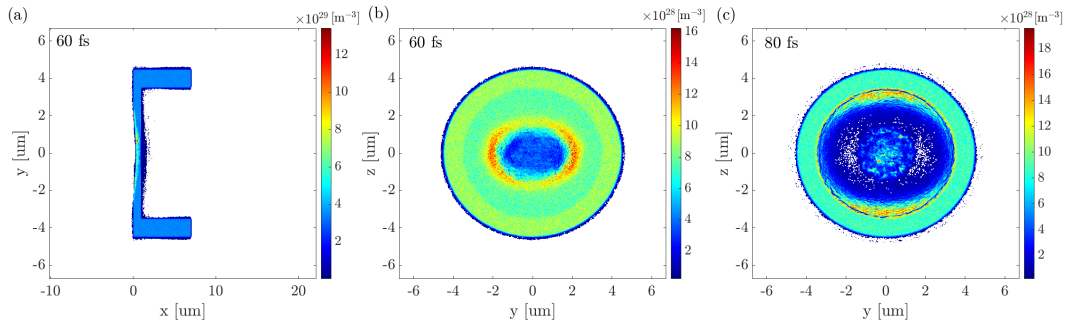

Figure 4.14: Electron density plots showing only above critical values at (a) + (b) 60 fs or at (c) 80 fs after the start of laser target interaction. The side view cuts the target in the middle of the second transverse axis and the densities in the transverse plane $y - z$ are plotted at $\sim$ 10 nm inside the target from its rear side (i.e., nearly behind the flat target part, inside the channel).

In the case of PIC simulation presented within this work, such scenario is not excluded, because the theoretical skin depth reaches $\sim$ 10 nm for unexpanded target and the laser pulse

was observed further than 0.9 μm behind the front side of the foil (the overall thickness was 1 μm). Although only the situation at 0.5 μm (and not at 0.9 μm) from the target front is shown in Fig. 4.15 due to better visibility, the field of the laser pulse was present also further inside the target, i.e., with the same spatial profile and without any shrinking in size. In other words, the laser pulse propagated in the material as a whole, because the electric fields had the same pattern in front of the target as well as inside it. Electron plots demonstrating only above critical densities at 60 fs or at 80 fs are shown in Fig. 4.14 from the side view (laterally in the middle of the target) and in the transverse plane $y - z$ at $\sim$ 10 nm inside the target from its rear side (i.e., at 0.99 μm along $x-$axis from the target front side). The cases (b) and (c) demonstrate the compressed circularly-shaped electron layer as well as the undercritical density areas (in white) in later time.According to the equation (9) in the article [243], the *significant* transmission would occur when the electron layer would be compressed to the ones of nm for the target & laser parameters used in the presented PIC simulations. Unfortunately, even though the compressed layer has been observed in the simulation, its overall thickness was higher. On the other hand, the EM radiation present behind the target had the same wavelength as the original laser pulse, the reduced intensity of $\sim 10^{19}$ W/cm^2 (from originally $5 \cdot 10^{21}$ W/cm^2), the speed of light and two times shorter full-duration (i.e., $\sim$ 30 fs) than the incident pulse. These parameters correspond well with the above described scenario.

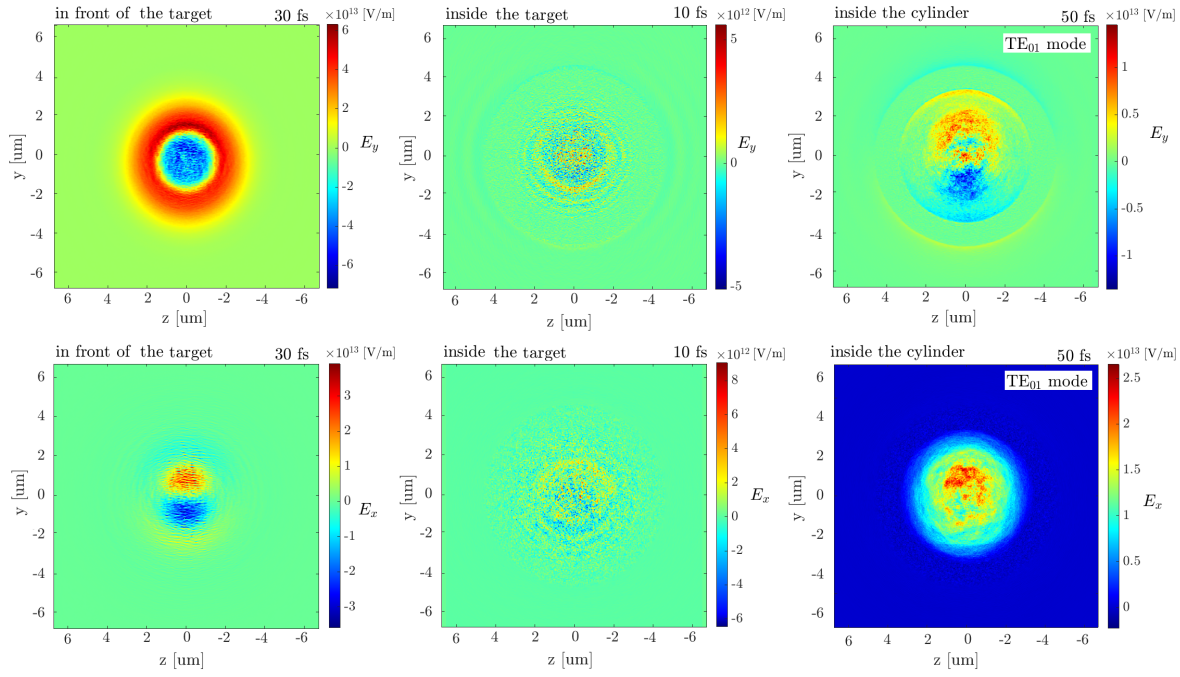

Figure 4.15: Spatial distributions of electric field components of the laser pulse radiation in front of the channel target, inside the flat-part target material (specifically, 0.5 μm from the target front) and inside the cylindrical channel (at 0.5 μm from the target rear side), where the part of the laser pulse is transmitted. The components E_x (the component in the direction of propagation) and E_y (the component in the direction of laser polarization) are shown in the plane $y - z$. The time scans are chosen in order to demonstrate clear examples and their values (written above the each plot) are given after the start of laser-target interaction.

Furthermore, the spatial distribution of each electric field component of the EM radiation inside the channel has been changed behind the target (i.e., *switched* in comparison to the original incident pulse) – compare the first and the last figure of each row in Fig. 4.15. This brings us to the additional theory of waveguides.
In general, the only way how a Gaussian pulse can propagate through a smaller area than its own dimension is the establishment of the exact modes in so-called waveguide [245], [246]. Similarly, when the part of the laser pulse propagates through a 1 μm-thick part of the channel target or of the flat target, it can be taken, from the optical point of view, as a radiation which propagates through the self-established channel inside the target material forming a waveguide. The work [247] investigates the modes of the THz linearly polarized laser pulse (i.e., the wavelengths ranging from hundreds of μm to hundreds of nm, which fits the L3 HAPLS laser used here having $\lambda = 800$ nm) propagating through a pinhole and then guided in the cylinder coated with polystyrene. The spatial distributions of electric field components presented there are the same as those ones which has been observed behind the both targets simulated by 3D PIC here. See the electric fields E_x and E_y in the plane $y-z$ (i.e., the plane perpendicular to the laser propagation direction) in front of the channel target, inside its flat target part (the space cut 0.5 μm from the channel target front side is shown, nevertheless the similar results were obtained also for 0.9 μm) and inside the guiding channel itself in Fig. 4.15. The results were verified in optical design software VirtualLab Fusion [248], where the electrical field components E_x, E_y and E_z of a linearly $y-$polarized laser pulse as well as of the TE_{01} mode described in [247] have been displayed and compared to the plots obtained from PIC simulations, see Fig. 4.15. All these results (i.e., PIC, VirtualLab and the citted article) show the same spatial distribution of electric field components in all directions which supports the hypothesis of TE_{01} mode formation.

To summarize, the light observed behind the targets in 3D has two orders lower intensity than the original pulse, two times shorter duration, but the same wavelength and it propagates with the speed of light. Moreover, the spatial distributions of all electric field components were the same inside the target material (in the part perpendicular to the laser propagation direction) as in front of the target. Further behind the target rear sides, i.e., when the part of the laser pulse has been transmitted through, the space distributions of electric field components changed. In fact, these changes were in a great agreement with the establishment of TE_{01} mode as demonstrated in [247], when the pulse propagates in the dielectric cylindrical waveguide. These results were verified also in VirtualLab Fusion software. Therefore, the observed light in Fig. 4.10 (b) proclaimed to be a partially-transmitted laser pulse, even thought the obvious leak through the target material has not been found.

4.4.2 Magnetic field strength and shape with dependence on target designs

In order to provide full information about magnetic fields, their orientation, shape and magnitude were studied for each target design separately, see Tab. 4.3. Naturally, the orientation of B_z field is the same for all targets (see a few representatives in Fig. 4.6 (a) – (c)) because it is the result of radial thermal transport mechanism described in Magnetic field generation section and of the hot electrons motion, their recirculation and corresponding formation of loops from return current.
In 3D, the maximal values of the magnetic field magnitude were reduced by approximately $\sim 50\%$ for both simulated targets, see Tab. 4.3. The magnetic field is higher in 2D cases,

because it is generated by the current loops formed by electrons, which can expand in two transverse axes when an extra dimension is added. This limits their current in each direction over the same distance in comparison to 2D situation. On the other hand, it is important to point out, that the differences between magnitudes for various 3D target designs, presented in Tab. 4.3, are partially caused by the choice of the spatial position behind the target where the analysis was taken. In fact, the data corresponds to the distance of 5.85 μm behind the back side of the flat target part (i.e., in the case of the channel target it is nearly at the end of the guiding cylinder), but the magnitudes of B_z were comparable for both target types in the immediate vicinity of the target rear side (i.e., at 0.5 μm). Numerically, these *on target* values reach $\langle -24; 22 \rangle_{channel}$ kT for the channel target and $\langle 22; 19 \rangle_{flat}$ kT in the case of the flat one. In other words, the field strengths are comparable on targets rear sides, whereas a few micrometers further they are not. In fact, this is natural observation, because electrons can spread into a larger area in the case of the flat foil compared to the channel design, thus the density of electron current loops is reduced significantly in a few μm behind the target. Therefore, it was demonstrated, that the generation of magnetic field is similar no matter the target design, but the crucial difference lies in its confinement.

Target type	B_z^{2D} [kT]	B_z^{3D} [kT]
flat target	$\langle -18; 16 \rangle$	$\langle -9; 9 \rangle$
flat target with a 4-μm-straight channel	$\langle -49; 47 \rangle$	–
flat target with a 6-μm-straight channel	$\langle -54; 52 \rangle$	$\langle -24; 22 \rangle$
flat target with a 8-μm-straight channel	$\langle -46; 51 \rangle$	–
curved target with a 2.5-μm-straight channel	$\langle -65; 62 \rangle$	–
curved target with a 6-μm-straight channel	$\langle -72; 99 \rangle$	–
flat target with a tapering channel (a 1-μm hole)	$\langle -76; 70 \rangle$	–
flat target with a tapering channel (a 3-μm hole)	$\langle -66; 60 \rangle$	–

Table 4.3: Values of B_z field affecting particle beam divergence for all simulated target designs in 2D and in 3D. The analysis was done at the end of the simulations, i.e., at 270 fs after the start of laser-target interaction. In 3D simulations, the values were taken at 5.85 μm behind the rear side of the target flat part. The values fluctuate with time, nevertheless the tendency remains the same.

The stronger magnetic field B_z was observed for all structured targets in comparison to the flat foil. Among studied target designs, the highest B_z magnitude was observed in the case of the curved foil with 6 μm long straight channel arms – nearly 100 kT in 2D, which is the increase of 550% in comparison to the flat foil, see values in Tab. 4.3. Nevertheless, this magnitude was reached for a very limited spot only, corresponding to the geometrical center of the curvature, where the majority of accelerated particles meet together (see the high-field area in Fig. 4.6 (c)). On the other hand, the amplitude of B_z field *along the guiding arms* of the curved channel target was comparable to that observed in the flat channel targets. This implies that both the curved and the flat channel target have similar impact on particles located far from the channel center, but not on the on-laser-axis ones. In addition, the position of the high-field magnetic spot corresponds to a de-accelerating peak in E_x field, which will be discussed in Electric sheath field section, specifically Fig. 4.27.

Even though the lowest amplitude of B_z field was observed from all simulated target designs for the flat foils with straight channel, such design proved to be the optimal for decreasing proton and ion beam divergence. In fact, the establishment and mainly the confinement of magnetic multipole, which was properly generated specially in the case of flat targets with straight channel, play the crucial role in divergence reduction (see Generation of multipole magnetic field section). Moreover, these targets are the most symmetrical solution without any strong violation (e.g. no focusing to a single point, as in the case of the curved channel targets, or any blockage of the particle beam by target outer parts, as in the case of the flat tapering channel targets), which results in the stable confinement of the magnetic multipole. Although the magnitude of the field varies depending on the channel length, it does not increase linearly as maybe primarily expected. In fact, it is natural, since the channel forms not ideal magnet which can be better developed for longer arms as already discussed. Even though the magnetic field amplitude is higher for 6 μm long channel than for 8 μm one, the field integral is stronger for the longer channel which is together the reason why the effect on particle divergence is only slightly higher for the longer channel.

4.4.3 The role of laser polarization direction in beam cross-section shape and divergence

It was shown, both numerically and experimentally, that the degree of ellipticity in the laser pulse polarization can be used to control the collective plasma electron response which strongly affects the proton beam profile if the target is relativistically transparent (RT) [232]. This effect is driven by the diffraction structure of the laser light created inside the aperture of RT target. In the case of linearly polarized pulse, the double lobe profile oriented perpendicularly to the polarization direction is formed [249]. Consequently, electrons are pushed from the high field regions, preferably from the polarization axis, by transverse ponderomotive force and they subsequently form two areas with concentrated density. The electron beam structure is propagated into a proton beam via transverse modulation of the electrostatic field that is produced by the charge displacement [232]. Naturally, the effect on proton density profile is energy-dependent, because of various electric field efficiency on particles of different energy. In fact, the high energy protons form the beam cross-section profile elongated in the direction perpendicular to the polarization axis, whereas the low-energy protons form a halo structure. The polarization of the laser pulse moreover affects both the front and the rear accelerated protons (i.e., RPA and TNSA) even though the structures observed in these two proton populations slightly vary [232].
In PIC simulations presented within this work, the laser dimensionless amplitude reaches $a_0 = 48$, which is not enough for $200n_c-$dense plastic target to undergo relativistic transparency. Nevertheless, a partially-transmitted laser pulse was observed at the rear side of the target as reported in Partially-transmitted laser pulse section. Therefore, the pulse reached the target rear side, similarly as it does when RT occurs. In other words, a similar, but definitely not optimal, situation in respect to the one described in [232], occurs. To summarize, in the cited works [232], [249], the key feature was to obtain a diffraction structure of the laser pulse inside relativistically transparent target, but in the case of the simulated targets presented here, it was not clearly observed.

Anyway, because of the described similarities, an additional 3D simulation of the reference flat foil was performed with *the linearly polarized laser pulse in $z-$direction* (and not $y-$ as

the original one) in order to see if the elongation of the proton beam cross section observed in both 3D simulated targets (the flat and the channel target) as well as energy-dependent divergence is anyhow affected not only by generated magnetic multipoles (no matter if well or unsuccessfully confined) and by transverse electric fields, but also by the direction of linear laser polarization. All other simulation parameters stayed unchanged.
Even though the 200 n_c target was not relativistically transparent for given laser parameters, the elongation of proton beam density cross sections was observed, but in contrast to [232] *along the direction of laser linear polarization*, see Fig. 4.16. This is assigned to the fact, that no diffraction structure had been observed inside the target and that the transmitted laser pulse propagates in mode TE_{01}. Since the mode has diverse structure of electric field components than the original pulse (see the section Partially-transmitted laser pulse and specifically Fig. 4.15 for $y-$polarization), the part of electrons are directly affected by the "new" pulse. The structure of E_y and E_z fields in TE_{01} mode for $y-$ and $z-$polarized transmitted pulse (i.e., behind the target) is just the opposite.

protons	linear polarization	div θ_{x-y} [°]	div θ_{x-z} [°]
> 0.5 MeV	y-polarized	15.4	17.7
	z-polarized	17.7	15.1
> 10 MeV	y-polarized	10.3	12.4
	z-polarized	11.2	10.1
> 30 MeV	y-polarized	9.3	9.8
	z-polarized	10.5	9.7

Table 4.4: Summary of half-angle proton divergence measured in FWHM in various energy intervals and diverse planes of 3D simulated flat foils interacting with linearly polarized laser pulses in various directions: along $y-$ or $z-$axis. Only protons moving forward and located inside the cylinder with the radius of 3.5 μm around the laser propagation axis were taken into account.

The results of proton beam half-angle divergence (FWHM) in various planes and energy intervals for both $z-$ and $y-$polarized laser pulse are summarized in Tab. 4.4. From this comparison, a relatively small (compared to the channel target) difference between proton divergences in various transverse planes can be assigned to the direction of linear polarization of the laser light, no matter the analyzed energy interval. Overall, the divergences of low-energy protons in various planes differ the most. This energy dependence is natural, since the laser polarization affects electrons quiver motion, therefore the corresponding electric field (as will be discussed further in this text and particularly in Fig. 4.17). This electric field acts on protons of various energy differently. In fact, the low energy particles are affected the most (as shown already in Comparison of the magnetic and electric field effectiveness), which is in great correspondence with the strongest differences in divergence between $x-y$ and $x-z$ planes for protons above 0.5 MeV. Generally, the linearly polarized laser pulse in $z-$axis leads to the lower divergence in $x-z$ plane and vice versa. Furthermore, the values of angular spread were switched in transverse planes for $90°-$rotated linearly polarized pulse in comparison to the original one. The discrepancy in these "switched" divergences between various polarization was very small, i.e., low ones of percent. Therefore, linearly polarized pulse causes, for our set of parameters, the decrease in proton divergence in the transverse plane parallel to the polarization direction.

Furthermore, laser polarization affects predominantly the angular spread of the wide bulk of protons, whereas the central narrow filament reported before stays unchanged. In fact, the divergence of this filament was analyzed within the tighter space cut around the laser axis, i.e., ± 0.5 μm (not ± 3.5 μm), in the same three energy intervals as in Tab. 4.4, but the values were identical for both directions of linear laser polarization.

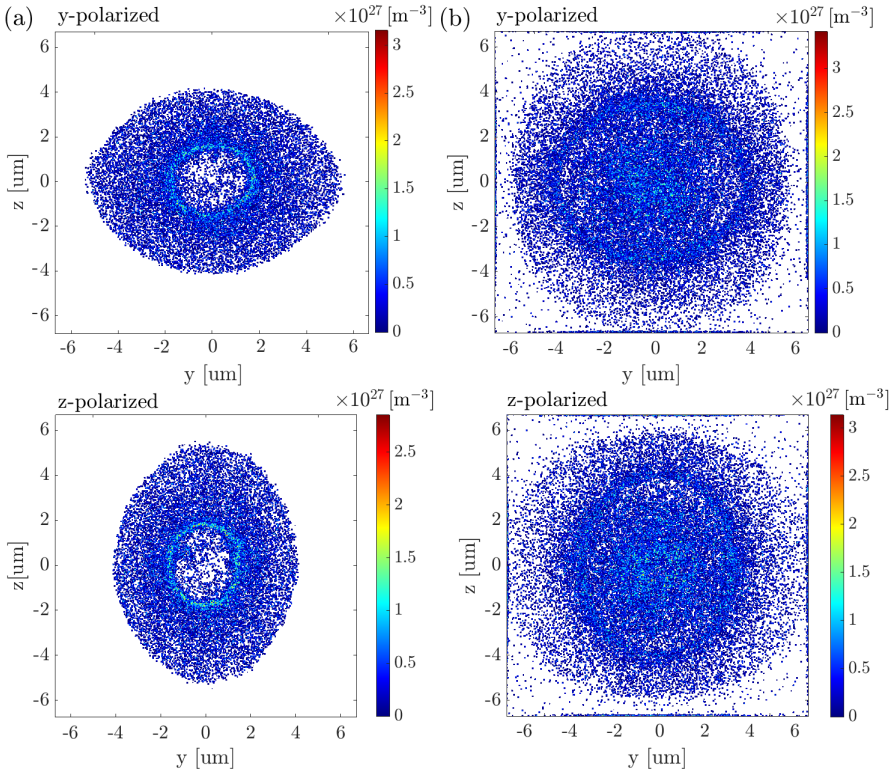

Figure 4.16: Density plots comparison of the proton beam cross sections in the case of the reference flat target interacting with $y-$linearly or with $z-$linearly polarized laser pulse. The beam cross sections are shown at ~ 6.5 μm behind the target rear surface at (a) 180 fs or at (b) 270 fs after the start of laser-target interaction.

As demonstrated on the example of the flat reference foils, the various directions of linear laser polarization affect the efficiency of focusing planes. In fact, the direction in which electric field oscillates in the laser wave directly forces electrons to periodically move in the same direction. Transverse components of the electric field are therefore modified accordingly to $y-$ or $z-$ linearly polarized light in the sense that, for example, electrons are forced to oscillate in $z-$axis in the case of $z-$polarized lase pulse, which straightens E_z field over E_y. In the previous simulations, the polarization was set along $y-$axis. The transverse electric field along corresponding direction (i.e., $E_y - y$ for $y-$polarization) are summarized in Focusing by the transverse electric field section, specifically in Fig. 4.4. It is worth reminding, that in the case of the flat foils discussed here, the field has focusing direction only at the beginning of acceleration. However, because of the spread of electrons, it changes its orientation to defocusing after low tens of fs. Whereas focusing E_y shows slightly higher values along $y-$axis than along $z-$axis in the case of $y-$polarized laser pulse, the situation is opposite in the case of linearly polarized pulse along z (i.e., the focusing E_z field has higher values in z for

$z-$polarized laser pulse), see the comparison at 50 fs in Fig. 4.17. Similarly, after a few tens of fs, when the fields change their orientation from focusing to defocusing, the defocusing E_y field shows slightly lower values along $y-$axis than along $z-$axis in the case of $y-$polarized laser pulse and vice versa (nevertheless, these differences are even smaller than those in the focusing fields). In other words, the linearly polarized laser pulse contributes to the stronger focusing in the direction identical to its linear polarization.
Even though these field differences (i) are not huge (average $< 10\%$, spatially up to $\sim 50\%$ (i.e., limited to a small area in space)), (ii) they strongly depend on the distance behind the target and (iii) their fluctuations (both in space and in time) are significant, they definitely contribute to the establishment of *focusing* and *defocusing* planes.

To summarize recent results with those obtained in previous chapters, the particle divergence variations in transverse planes in 3D can be assigned to the combination of more factors: firstly, to the transverse electric fields and their different strengths in various directions (affected both by the confinement of electrons (which is important difference between the channel and the flat targets) and by the direction of linear polarization of the laser pulse) and secondly, to the magnetic fields (i.e., the establishment of magnetic multipoles (being strong in the channel target case, but weak in the case of reference flat foils)).

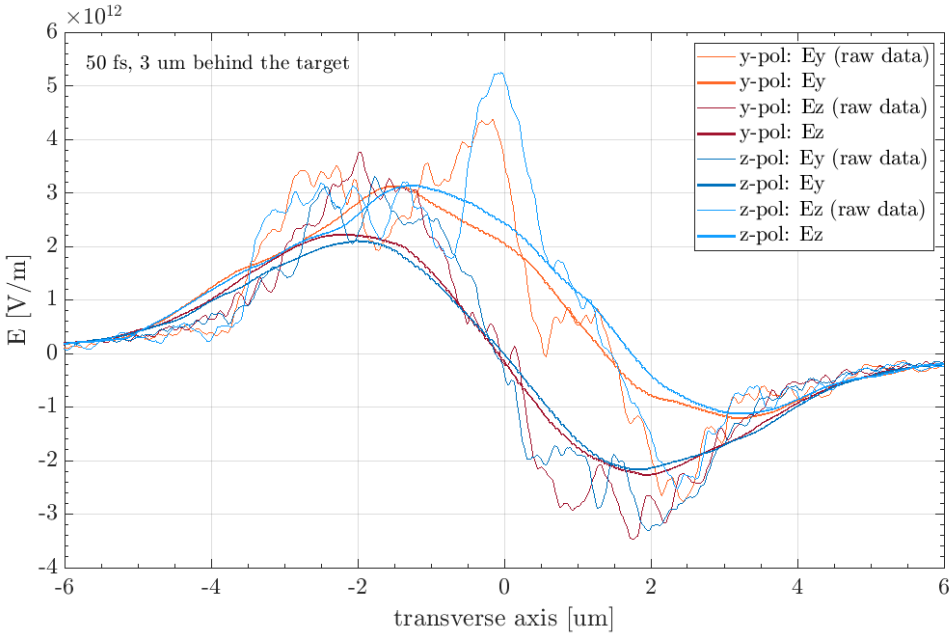

Figure 4.17: Comparison of 1D profiles of transverse focusing electric field components plotted along corresponding axes, i.e., $E_y - y$ and $E_z - z$, for linearly $y-$ and $z-$polarized laser pulses. The field is analyzed 3 μm behind the rear side of the reference flat target at 50 fs after the start of laser-target interaction.

4.5 Energy spectra & Number of particles

4.5.1 Maximum energy & Shape of energetic spectra

As investigated in the previous sections, the target design strongly affects the produced particle beam divergence, but in fact, it influences other beam parameters as well. The studies reporting the particle energy dependence on the target structured shape have been already published. Generally, if the structures are placed on the *rear side* of the target, proton and carbon ion energies are reduced, because the accelerating field is lowered when hot electrons are spread to the additional target material (in this case, to the structures). Since the hot electrons are generated at the foil front side in the vicinity of the laser-target interaction point, their number is comparable, no matter if the target contains the rear-attached structures or not. On the other hand, when nano/microstructures are placed on the target *front side*, the absorption of the laser pulse is enhanced. When the laser beam is not everywhere perpendicular to the target surface anymore, the additional Brunel vacuum heating of electrons takes its place. Consequently, the hot electron temperature rises as well as the strength of electric sheath field and consequently the energy of accelerated protons and ions is higher [214], [250], [251], [252], [253].
In accordance with that, all our simulated targets with channels (no matter if flat or curved ones with straight or tapering arms) decrease the maximum obtained proton and carbon ion energy by ones or low tens of percents in comparison with the reference flat foil of the same thickness, see Tab. 4.5. The energy reduction strongly depends on the strength, the shape and the duration of accelerating sheath field E_x, which scales with hot electron temperature and density [254], [255].

target type	E_{max}^{p+} [MeV]				E_{max}^{C6+} [MeV/amu]			
	2D		3D		2D		3D	
Flat target	108.4	100%	62	100%	23.8	100%	16.6	100%
FT with a 4-μm-straight channel	97.0	89%	-	-	22.0	92%	-	-
FT with a 6-μm-straight channel	95.7	88%	56	90%	21.6	91%	14.2	86%
FT with a 8-μm-straight channel	88.1	81%	-	-	21.0	88%	-	-
CT with a 2.5-μm-straight channel	102.6	95%	-	-	19.7	83%	-	-
CT with a 6-μm-straight channel	92.2	85%	-	-	17.5	74%	-	-
FT with a tap. ch. (a 1-μm hole)	77.6	72%	-	-	18.0	76%	-	-
FT with a tap. ch. (a 3-μm hole)	94.3	87%	-	-	21.7	92%	-	-

Table 4.5: Maximum protons and carbon ions energy recorded at the end of 2D and of 3D simulations (270 fs) for all target types; only particles moving forward were taken into account; FT= flat target, CT = curved target.

In performed 2D simulations, the maximum particle energy decreases with the increasing length of the channel for both flat and curved targets. Although the dependence of energy reduction on the channel length is not that strong for carbon ions as it is for protons, the tendency is the same. Particularly, the energy drops in the case of flat targets with straight channels by $11-19\%$ for protons and by $8-12\%$ for carbon ions. The exact numbers vary with the specific channel length, see Tab. 4.5. In fact, the energy decrease is not massive, because the differences between channel targets and the reference flat foil in the accelerating

field magnitude, shape and duration are not very large; see the Electric sheath field section. For the majority of simulated target designs, the similar reduction of maximum particle energy in comparison to the reference flat foil was observed for both protons and carbon ions. However, *curved* foils with straight channel are the exception, because a significantly higher energy decrease was observed in the case of carbon ions in comparison to protons. Specifically, the energy reduction reaches 5% or 15% in the case of protons and 17% or 26% in the case of carbon ions depending if the channel has the length of 2.5 μm or of 6 μm. In other words, the carbon energy reduction was approximately doubled over protons in the case of curved targets with straight arms. The result is assigned to the fact, that this target design, as the only type, has a spatially fixed decelerating E_x field located in the geometrical center of the target curved part; see the section Electric sheath field, specifically the Fig. 4.27. In fact, the negative E_x field is limited in space, i.e., it forms a relatively thin and spatially stable decelerating slab perpendicular to the laser-axis as visible in Fig. 4.18. In general, to accelerate carbons to the energy of 1 MeV/amu higher than the original value, the higher field would be needed than in the case of protons, because of the carbons higher mass-to-charge ratio. The energy lowering (in the comparison to the reference flat foil) is more significant in the case of carbons than in the case of protons, because the high-energy proton population is already located behind the decelerating field, when it is established to its full power. On the contrary, the carbon beam front is just entering it, see Fig. 4.18 where this phenomenon is highlighted by the grey line over the plots. Then, the accelerating field located behind the decelerating slab is not strong enough to accelerate the already slowed-down carbons sufficiently.
To summarize, no matter the differences in values, the tendency of energy lowering has been observed for both ion species. In other words, the list of targets sorted from the best to the worst design according to the maximum energy reached stays unchanged.
In 3D, the energy drop between the channel target and the flat foil was weaker – only 10% for protons and 14% for carbon ions, i.e., numerically, the energies decreased from $E^{FLAT}_{3Dmaxp+} = 62$ MeV and $E^{FLAT}_{3DmaxC6+} = 16.6$ MeV/amu to $E^{CHANNEL6}_{3DmaxC6+} = 56$ MeV and $E^{CHANNEL6}_{3DmaxC6+} = 14.2$ MeV/amu, see Tab. 4.5. The energy reduction between 3D and 2D was around 40% for both target designs and both ion species. Such difference between maximum particle energy observed in 2D and 3D simulations is caused by the fact that electrons can spread in $y-$axis and $z-$axis in the case of 3D geometry in comparison to 2D where only one direction is possible. This results in a lower electron density and temperature in the 3D case, which then leads to a weaker proton and ion acceleration than in the 1D and 2D cases [254], [255], [256]. Discussing this matter a little further, the observed results are in good correspondence with an already demonstrated phenomenon, that 2D simulations generally overestimate the particle energy over 3D simulations. Nevertheless, the dramatic differences between 2D simulations implementing p-polarized (2D-P) or s-polarized (2D-S) laser pulses were reported [256]. In particular, 2D-P simulations show a significantly higher electron heating in the simulation plane, whereas 2D-S simulations demonstrate a more isotropic energy distribution. The reason is connected with the overall amount of light energy that is converted into the particles which have only a limited number of degrees of freedom in the case of 2D-P compared to 2D-S and 3D PIC modeling. Therefore, the higher temperature of electrons is reached in 2D-P simulations, which leads to the stronger sheath field formation at the target rear side and to the correspondingly higher particle energies than those observed in 3D (and also 2D-S). In our 2D performed cases, only p-polarized laser pulse was used (i.e., linear polarization along $y-$axis), therefore, the larger heating of electrons as well as the enhanced

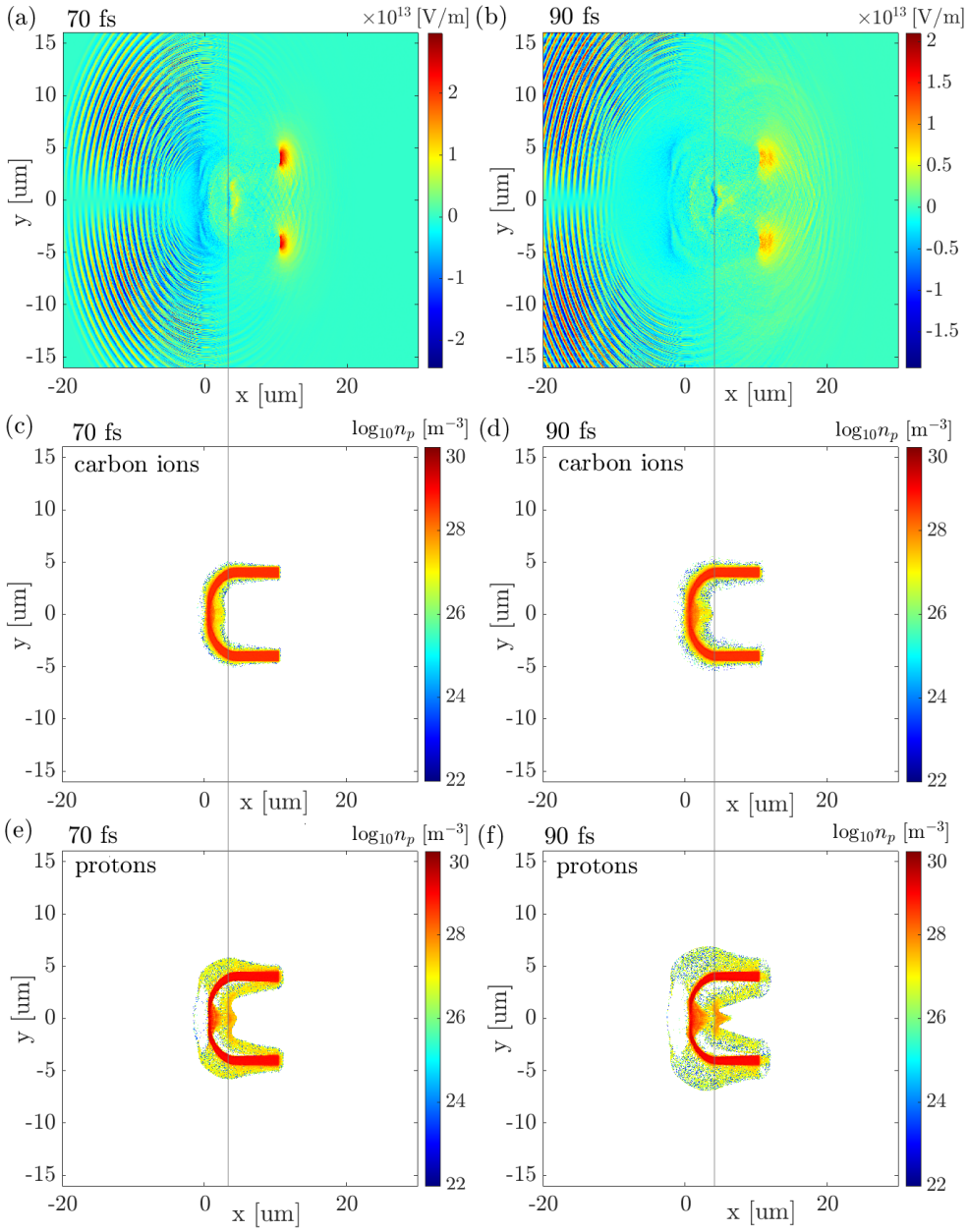

Figure 4.18: 2D simulation of curved channel target with 6 μm long straight channel: The plots demonstrating accelerating and decelerating electric field E_x (a), (b) are shown together with protons and carbon ions density plots (c), (d) and (e), (f) at 70 fs and 90 fs after the start of laser-target interaction, respectively. The grey line indicating the position of decelerating electric field is present in order to show the corresponding location of the beam front of carbons and protons at particular time scan.

expansion rate in comparison to 3D simulations were observed.

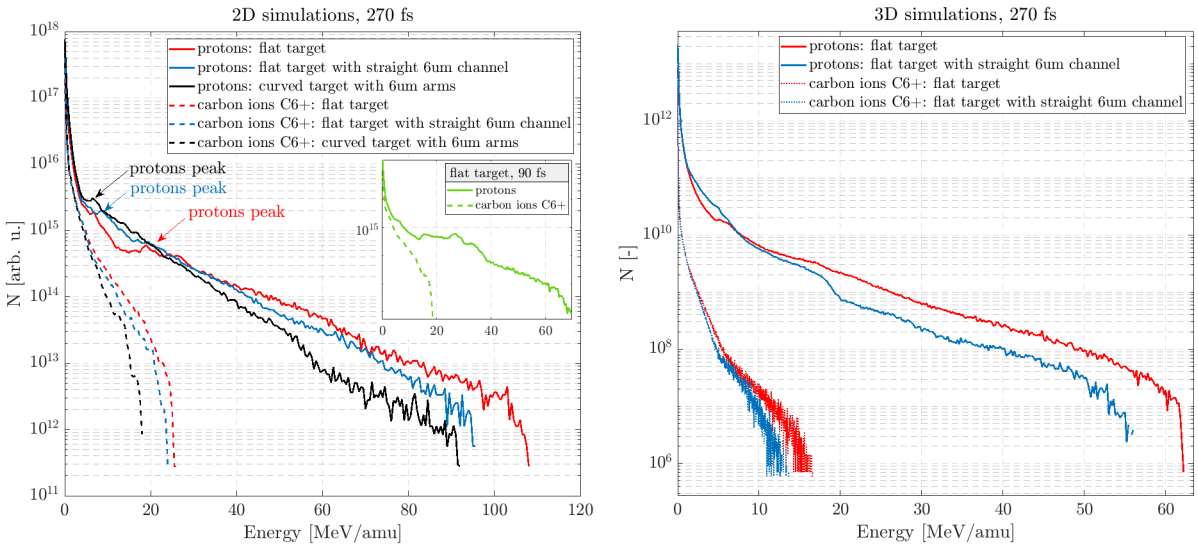

Figure 4.19: Comparison of energy spectra of protons and carbon ions recorded at the end of 2D (left) and 3D (right) simulations, i.e., at 270 fs after the start of laser-target interaction. Three representative targets were chosen for 2D comparison – the flat target (the red color), the flat target with 6 μm straight channel (the blue color) and the curved target with 6 μm straight channel (the black color), whereas the first two mentioned designs were compared in 3D. The small green plot in the left figure show the particle energy spectra of the reference flat target (2D) presented additionally at 90 fs in order to see the clearer example of the proton peak formation.

For all simulated target types in both 2D and 3D geometry, the shape of proton energy spectra shows a moderate valley followed by a peak at low energy, see Fig. 4.19. Such peaked shape is caused by the accelerated carbon ion cloud which pushes the protons of corresponding energies in front of itself. The affected protons are further accelerated by the carbon ion push. That results in the number lowering of protons with lower energies and to the corresponding number increase of protons with slightly higher energies, which leads to the peak formation in energy spectra. Consequently, this peak is located before the ending of carbon energy spectrum at the time when such pushing happened, see the example in Fig. 4.19 for the reference flat target at 90 fs (the small plot in green). Due to the various time evolution of the accelerating field and the diverse energy distribution across the particle beam, the low-energy proton peak is observable well in different times depending on the target design. Moreover, the carbon pushing force is more efficient in earlier time scans, when the particles are closer to each other. Hence, at the end of the simulations, the characteristic profile of the proton spectra is still present, but the proton peak is slightly weaker and its positioning with the ending of carbon spectrum is shifted, because both protons and carbons were further accelerated with ongoing time, see Fig. 4.19 for both 2D and 3D cases. The drop in the electric accelerating field caused by the front of carbon ion cloud is correlated with the protons and carbon ions densities as visible in Fig. 4.19 and it is discussed further in the Dependence of the sheath field shape along the laser propagation axis on the target design section, particularly in Fig. 4.27.

4.5.2 Energy-resolved spatial distributions of the proton beam

The analysis of energy-resolved spatial distributions of accelerated protons gives us the indirect insight to both the time and the space evolution of the acceleration. Proton populations, accelerated both from the target front and from its rear side, were observed for 2D simulated cases, see the example in Fig. 4.20 (a) for the channel target design. In fact, these populations have been observed also in 3D, specifically in phase space graphs presented in Phase spaces section and particularly in Fig. 4.32.

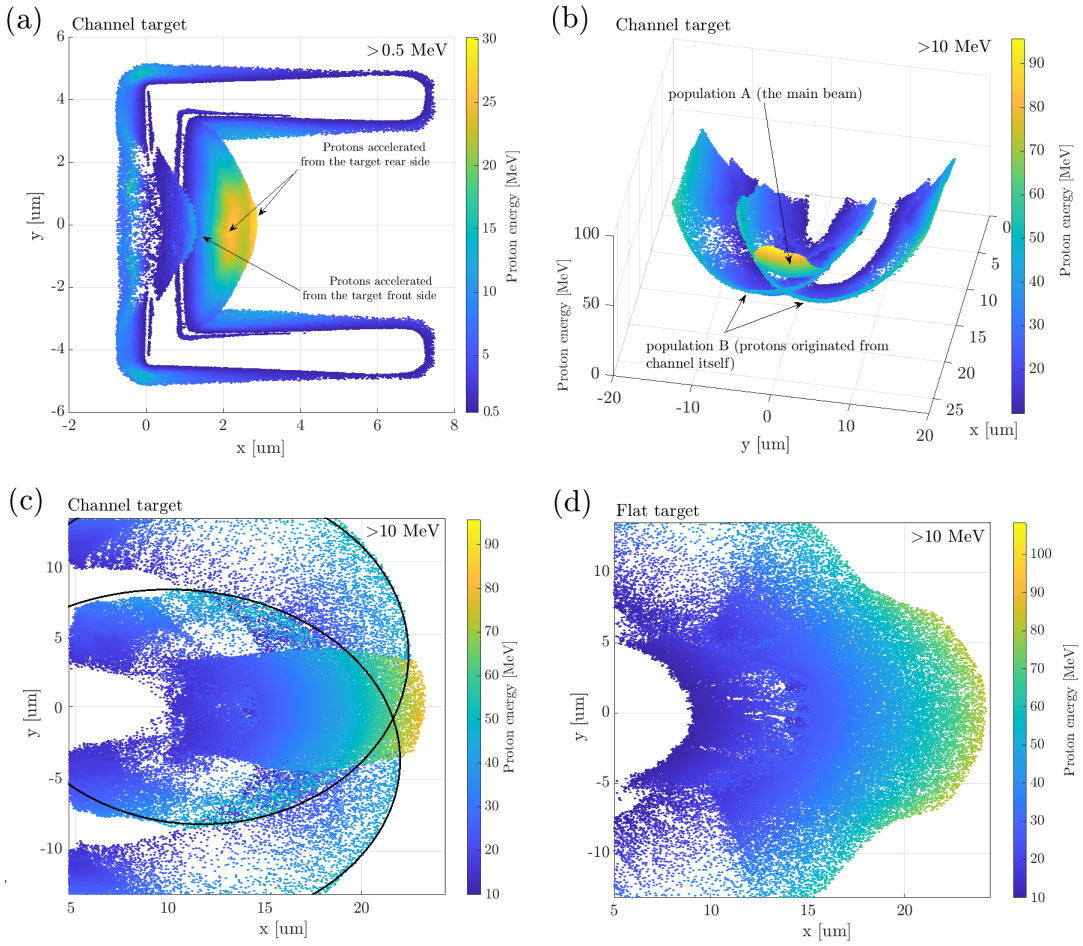

Figure 4.20: Energy resolved spatial distribution of protons accelerated from (a)–(c) the flat 6 μm-long channel target and from (d) the reference flat foil. The data were taken from 2D simulations and show only protons moving forward and having energy above (a) 0.5 MeV or (b)–(d) above 10 MeV. Graph (a) corresponds to 50 fs and graphs (b)–(d) to the end of the simulation, i.e., to 270 fs after the start of laser-target interaction. The channel target is located from 0 μm to 7 μm ($x-$direction) and from -4.5 μm to 4.5 μm ($y-$direction); the flat target is located from 0 μm to 1 μm in x, the transverse dimension is the same as in the case of the channel target.

The group of the most energetic protons are accelerated from the rear side of each target. At early simulation times, the proton beam has two epicenters of high energies (see the yellow areas in Fig. 4.20 (a)), which are separated by high-energy carbons. These two high-energy

areas gradually fuse together with protons accelerated from the target front side to one main proton beam (see Fig. 4.20 (b) and (c), where the major beam (population A) has no visible discontinuation and it is composed from three small populations depicted in (a)). Besides the protons accelerated from the target part perpendicular to the laser pulse (i.e., the main proton beam), another proton population rises from the channel material, i.e., from the surface of the arms. This channel-originated proton population is represented by two low-energy arches in Fig. 4.20 (b). Gradually, the protons accelerated from the channel walls gain relatively high energy, because accelerating electric field is sufficiently strong also behind the channel itself. On the other hand, the divergence of such particles is higher than the divergence observed in the case of the main beam passing through the unique combination of EM fields containing the well-established magnetic multipole.
The 2D comparison between the flat and the 6 μm-long channel targets shows, that the main high-energy proton beam produced from the channel target is thinner and narrower than that produced from the flat foil, see Fig. 4.20 (c) and (d). Naturally, the high energy particles are located at the front of the main accelerated beam, no matter the target design. The fronts of each *side beam*, originated from the channel and forming two arches in Fig. 4.20 (b), are highlighted by black lines in (c).

4.5.3 Number of particles

The evaluation of the realistic particle number from 2D simulations is complicated, but the comparison between each simulated case can provide valuable results showing the overall trend (e.g. the fraction of particles being accelerated). Naturally, targets with channel produce a higher number of particles because they have extra material (additional guiding arms) in comparison to the reference flat foil. In fact, the particles are accelerated not only from the target flat part perpendicular to the laser propagation axis, but also from the channel itself. For example, in 2D simulations, the absolute number of protons accelerated above the energy of 10 MeV was increased by $\sim 20\%$ (depending on the length and the type of the channel) in comparison to the flat foil although the maximum obtained energy was slightly reduced. Nevertheless, this effect was not observed in 3D, where the reduction of maximum energies was naturally followed by the lowering of absolute number of protons above 10 MeV. It was verified, that carbon ions follow the similar trend as protons, even though the numbers were slightly different.
Considering that both the overall proton number and the maximum proton energy are strongly dependent on the target design (e.g. due to the amount of used material and the formation of the fields), the ratio between the number of forwardly accelerated (i.e., $p_x > 0$) protons above 10 MeV and above 0.5 MeV (i.e., $N_{0.5}^{10} \equiv N_{10}/N_{0.5}$) will provide clearer information whether any reducing or enhancing of mid- and high-energy proton amount can be expected. In 2D, the fraction $N_{0.5}^{10}$ was evaluated to $\sim 20\%$ in the case of the reference flat foil and to $\sim 15-19\%$ in the case of channel targets, see the exact values in Tab. 4.6. That corresponds to $< 10\%$ reduction in the relative amount $N_{0.5}^{10}$ in the case of channel targets in comparison to the reference flat foil. To conclude: from 2D simulations, any significant reduction in the relative number of high-energy protons is expected for none of simulated channel designs.
However, the comparison was done also for two targets simulated in 3D, where the reducing trend of the proton number was spotted. The ratio $N_{0.5}^{10}$ was evaluated to 12% for the flat foil and to only 7% for the channel target. The drop can be caused by the higher amount of protons originating from the cylinder material (above 0.5 MeV) in 3D simulations in comparison to

2D simulations	$N_{10}/N_{0.5}$			
	protons		carbon ions	
	value [-]	relative to FT	value [-]	relative to FT
Flat target (=FT)	0.195	100%	0.052	100%
FT with 4 um straight CH	0.186	95%	0.036	69%
FT with 6 um straight CH	0.178	91%	0.034	65%
FT with 8 um straight CH	0.177	91%	0.029	56%
CT with 2.5 um straight CH	0.170	87%	0.022	42%
CT with 6 um straight CH	0.159	82%	0.015	29%
FT + tapering CH – 1um hole	0.149	76%	0.030	58%
FT + tapering CH – 3 um hole	0.172	88 %	0.037	71%
3D simulations	$N_{10}/N_{0.5}$			
	protons		carbon ions	
	value [-]	relative to FT	value [-]	relative to FT
Flat target	0.118	100%	0.005	100%
Channel target	0.065	55%	0.002	40 %

Table 4.6: Comparison of proton and carbon ion number ratio obtained from 2D and 3D simulations. N_{10} is the number of protons/carbon ions moving forward ($p_x > 0$) and having energy above 10 MeV/amu; $N_{0.5}$ is the number of protons/carbon ions moving forward ($p_x > 0$) and having energy above 0.5 MeV/amu. The ratio between these numbers is shown as the dimensionless value as well as the relative number in comparison to the reference flat target (FT). The comparison contains all simulated designs, i.e., the reference flat target (FT), the flat targets with straight channels, the curved targets (CT) with straight channels and the flat foils with tappering channels (TCH) forming a hole between their arms. The abbreviation CH is used for the "channel". All data are taken at the end of simulations, i.e., at 270 fs after the start of laser-target interaction. Particle weighting was used.

2D. Nevertheless, the absolute number N_{10} of protons above 10 MeV reached for the channel target only $\sim 70\%$ of the value obtained for the reference flat foil. This trend is visible also in proton energy spectra comparison in Fig. 4.19. It is also important to point out, that the number of protons above certain high energy level is naturally higher in the flat foil case, because its maximum energy is higher compared to that for the channel target. This confirms also the fact, that the ratio $N_{0.5}^{5} \equiv N_5/N_{0.5}$ for the channel target is higher than $N_{0.5}^{10}$ and it reaches nearly 90% of the flat target's one (26.1% and 29.5%, respectively).

4.5.4 Collimating feature of tapering channels

It was investigated that flat foils with tapering channel (see Fig. 4.1 (b)) can conceptually act as a collimator. In fact, sloping arms are able to provide electrostatic field which is strong enough to catch the protons with low energy and high divergence. In other words, this channel is able to "cut" the particle beam accelerated from the target flat part and thus to select the maximum divergence angle being accepted (i.e., it filters out a relatively large amount of the low energy particles). For example, the foil with a 3-μm hole between its 6 μm-long tapering arms can reduce the number of protons having $0 - 5$ MeV by 49%, whilst the target with

a 1-μm-wide hole between its tapering arms by 58%. Since the less energetic protons have bigger divergence [228], [229], [230], the energy interval of the stopped ones naturally depends on the size of the hole, i.e., a smaller hole stops more energetic particles. In our collisionless simulations, the effect is caused purely by electrostatic field. The produced narrow beam can be observed in proton density plots in Density profile section, Fig. 4.21.

4.6 Density profiles, uniformity of the beam

4.6.1 Two dimensional study of target designs

The laser-driven particle acceleration resulted in a more narrow ion beam when the targets with guiding arms were used. The comparison of proton and carbon ion density plots between channel designs and the reference flat foil can be seen in Fig. 4.21. It is well observable that carbon ions do not spread to as large area as protons do, because of their higher mass leading to the lower energies in MeV/amu. Nevertheless, a relatively high amount of particles is accelerated from the channel arms, nearly perpendicularly to the laser pulse direction. Such acceleration is the result of hot electrons motion inside the channel material. The produced particles have typically lower energy compared to the main narrow beam because of the insufficient conditions for TNSA acceleration [1], [50]. Moreover, it is complicated to guide these particles through a beamline and thus to produce any useful beam for foreseen applications. Therefore, these ions are not taken for divergence analysis, where the space cut of ± 3.5 μm (fitting the channel inner dimensions) together with the condition of $p_x > 0$ are applied.

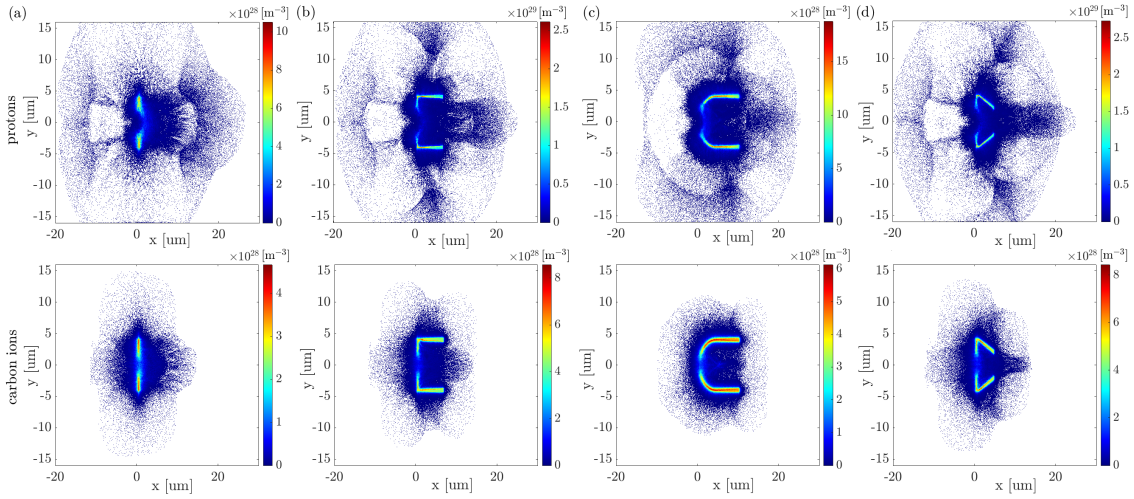

Figure 4.21: Density plots of protons (the first row) and of C^{6+} carbon ions (the second row) at the end of 2D simulations, i.e., at 270 fs after the start of laser-target interaction: (a) the reference flat foil, (b) the flat foil with straight 6 μm long channel, (c) the curved target with straight 6 μm long channel, (d) the flat target with 6 μm long tapering channel arms forming a 3 μm hole between them.

An interesting feature of multiple beam formation is visible in proton density plots of curved targets with straight channel, see Fig. 4.22. In fact, this target design is associated with the growth of proton beam divergence caused by the TNSA mechanism [50], i.e., by the fact

that ions are accelerated perpendicularly to the target rear surface. As already discussed in Divergence section, protons thus primarily move towards the geometrical center of the target curved part. Because the fields are not strong enough to sustain the proton beam in a tight focus, the protons continue in their trajectories, have relatively high divergence (compared to the rest of advanced target designs) and they form multiple beams. This feature is suppressed with increasing length of the straight channel attached to the curved part, see divergence values in Tab. 4.2. That was caused by the bigger electric field integral, i.e., the stronger particle focusing since the field acts over a longer distance. In presented simulations, even the channel prolongation by additional 3.5 μm was enough to visibly suppress the proton beam filamentation, see density plots in Fig. 4.22 and compare mainly the effect of the long channel (a) with the short one (b).

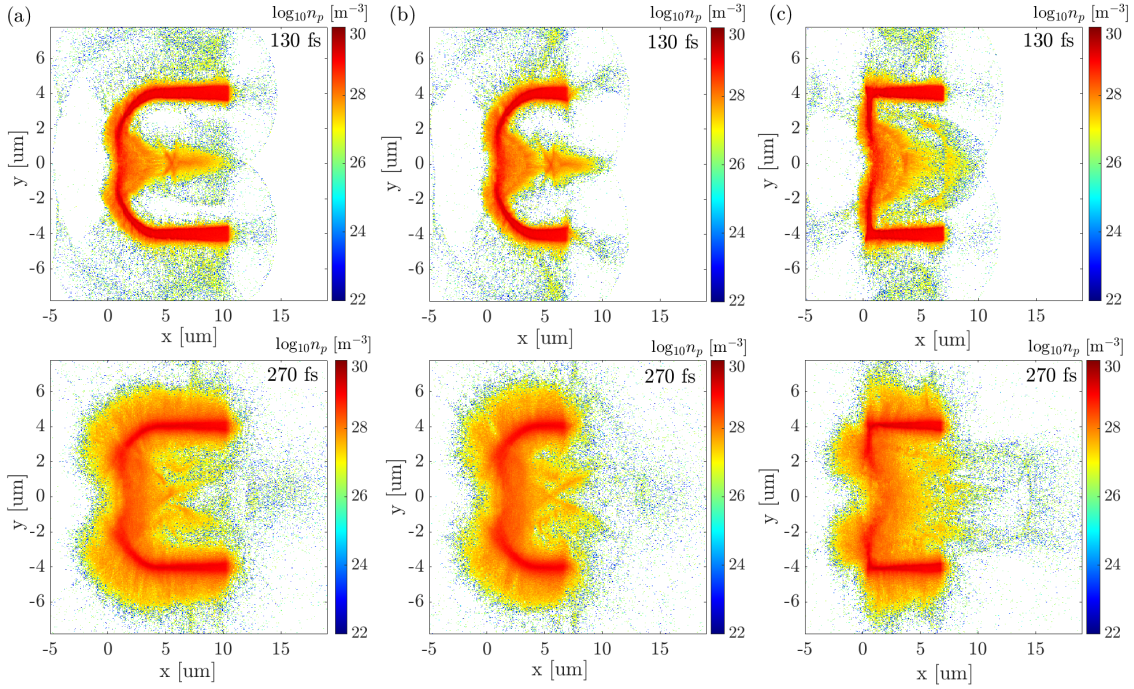

Figure 4.22: Comparison of logarithmic-scaled proton densities of (a) the curved target with straight 6 μm long channel, (b) the curved target with 2.5 μm long channel and of (c) the flat target with straight 6 μm long channel at 130 fs (the first row) or at 270 fs (the second row) after the start of laser-target interaction.

4.6.2 Three dimensional features

The proton density plots of both the flat and the channel targets simulated in 3D are presented in Fig 4.24 and Fig. 4.23, respectively. The particle densities are displayed at diverse times from the beginning of laser-target interaction and at different space cuts along the laser propagation axis: namely at 3 μm (i.e., in the middle of the channel length), at 6.5 μm (i.e., directly behind the channel), at 7.6 μm (i.e., at 1.6 μm behind the channel) and at 16.9 μm (i.e., $\sim$ 10.9 μm behind the channel) behind the rear surface of the flat target part being perpendicular to the laser pulse. In addition, the side view of the target density cut in the middle of $z-$axis is provided as well.

Firstly, the elliptical shape of the proton beam cross sections (slightly elongated in $y-$direction or nearly symmetrical) is formed for both target cases. Such shape has been evolving with ongoing time and with rising distance from the target flat rear side. In fact, the gradual change to more symmetrical cross section or even that one elongated in $z-$direction in later stages/ further from the target flat rear side was observed in the case of the channel target as the result of fully developed EM fields acting on the passing proton beam. This time development progressively shows the lower divergence in $x - y$ plane (i.e., the originally $y-$elongated beam evolves to the symmetrical or the $z-$elongated one) recorded at the end of the simulations, see specific values in Tab. 4.2 in Divergence section. Because of the less efficient EM field formation in the case of the reference flat foil, the shape of the proton beam was affected less than in the case of the channel. Moreover, a higher spatial uniformity of the main proton beam accelerated from the channel is visible even from the presented density plots (compare beam cross sections in Fig. 4.24 with those in Fig. 4.23), nevertheless this feature will be demonstrated properly in Spatial uniformity of the proton beam section. In fact, the establishment of the magnetic quadrupole contributes to the elliptical elongation in $z-$direction (the preferable focusing plane was $x - y$) whilst the magnetic octupole is responsible for making the beam more spatially uniform. Thus it is natural that both the more significant changes in the beam cross section outline and the more spatially uniform proton beam were obtained in the case of the channel target whose fields are stronger and better-developed than those of the reference flat foil. Since the quadrupole focusing has various efficiency in different energy intervals, each specific proton population (having different energy at the current time scan and the cut along the laser axis) forms a various shape of the proton beam cross section, see e.g. Fig. 4.23 (a) for 180 fs, where two different ellipses corresponding to two proton populations are visible inside the channel. For more details about EM fields see the section Particle divergence reduction affected by favorable establishment of EM fields.

The *particle halo* formed around the main beam was observed both in the flat and the channel target cases and it was much stronger for protons, see Fig. 4.24 and Fig. 4.23. Generally, the denser center with a concentric circle corresponds to the display of various proton populations – the first population propagates as a "bubble front" and the second one forms more localized narrow beam. In the case of the channel target, the proton halo around the main beam is nearly not apparent (since the proton beam is more uniform due to the octupole magnetic field effect) and the "fake halo" comes from the channel material. The main proton beam and both halos in the case of channel target (i.e., the first one from the various proton populations accelerated from the target flat part and the second one from the cylinder material (which is stronger)) are visible in Fig. 4.23 (a) and (b) for 180 fs. In the case of the flat foil, the proton halo comes truly from the various proton populations (observable also in side views of Fig. 4.24) and indicates strongly inhomogeneous beam. That is influenced also by the shape of accelerating electric field along transverse axes, visible, for instance, in Fig. 4.29 (b) + (c) for 2D case and (e) for 3D geometry (the red curve). In short, this field has two "epicenters" – the first one accelerates particles along the laser axis whilst the second one is peaked ± 4 μm from the center which corresponds to the halo formation. On the contrary, the accelerating electric field present in the case of the channel target forms only the on-axis structure. Spatial uniformity of the beams will be discussed separately in the section Spatial uniformity of the proton beam.

Carbon ions act similarly, although their response to EM fields is not as strong as in the case of protons, thus the elongation of the beam cross sections is nearly not observable, see Fig.

4.25. On the other hand, the non-symmetrical divergences are present for carbon beam as well (see divergence values in Tab. 4.2), but the longer simulation time would be needed to let the effect develop significantly to observe it clearly also in the density plots.

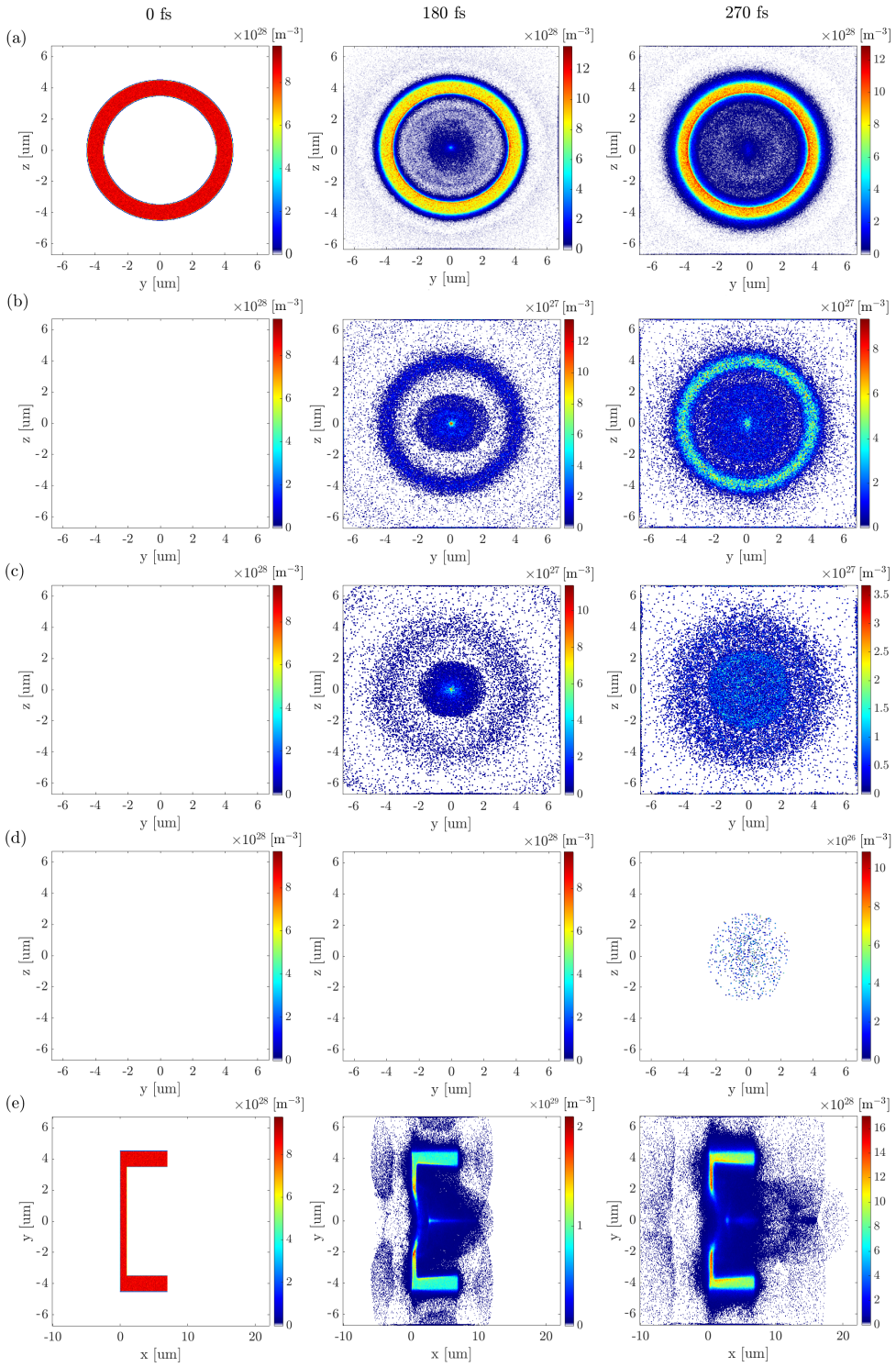

Figure 4.23: Channel target: Proton density plots are shown in various times (0 fs, 180 fs and 270 fs; corresponding to three columns) after the start of laser-target interaction and at various spatial cuts along the laser propagation axis: (a) at 3 μm (i.e., in the middle of the channel), (b) at 6.5 μm (i.e., directly behind the channel), (c) at 7.6 μm (i.e., at 1.6 μm behind the channel) and (d) at 16.9 μm (i.e., $\sim$ 10.9 μm behind the channel) behind the rear surface of the flat target part. The last set (e) corresponds to the side view of the target density cut in the middle of $z-$axis.

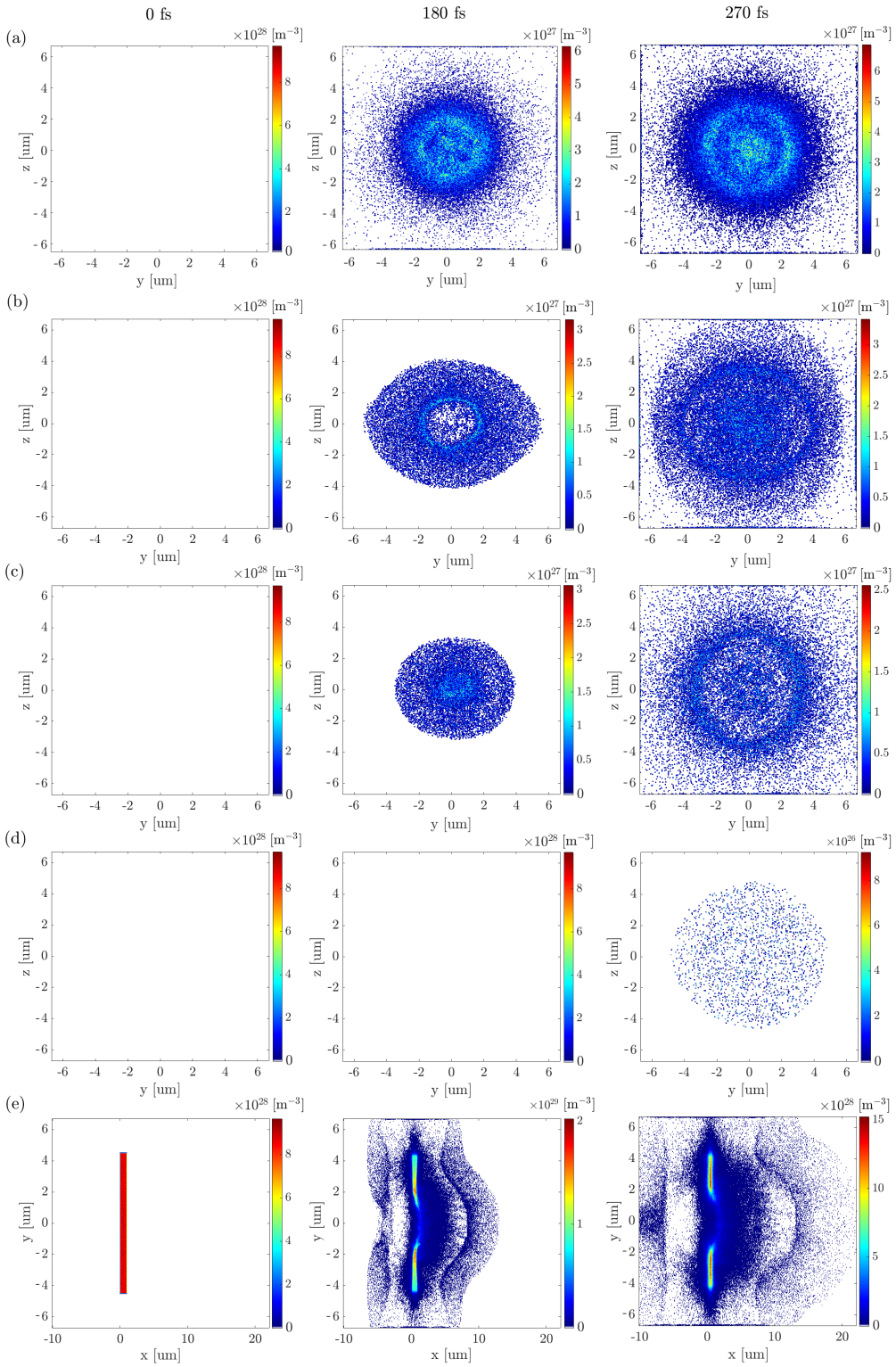

Figure 4.24: Flat target (reference): Proton density plots are shown in various times (0 fs, 180 fs and 270 fs; corresponding to three columns) after the start of laser-target interaction and at various spatial cuts along the laser propagation axis: (a) at 3 μm, (b) at 6.5 μm, (c) at 7.6 μm and (d) at 16.9 μm behind the target rear surface. The last set (e) corresponds to the side view ($x-y$) of the target density cut in the middle of $z-$axis.

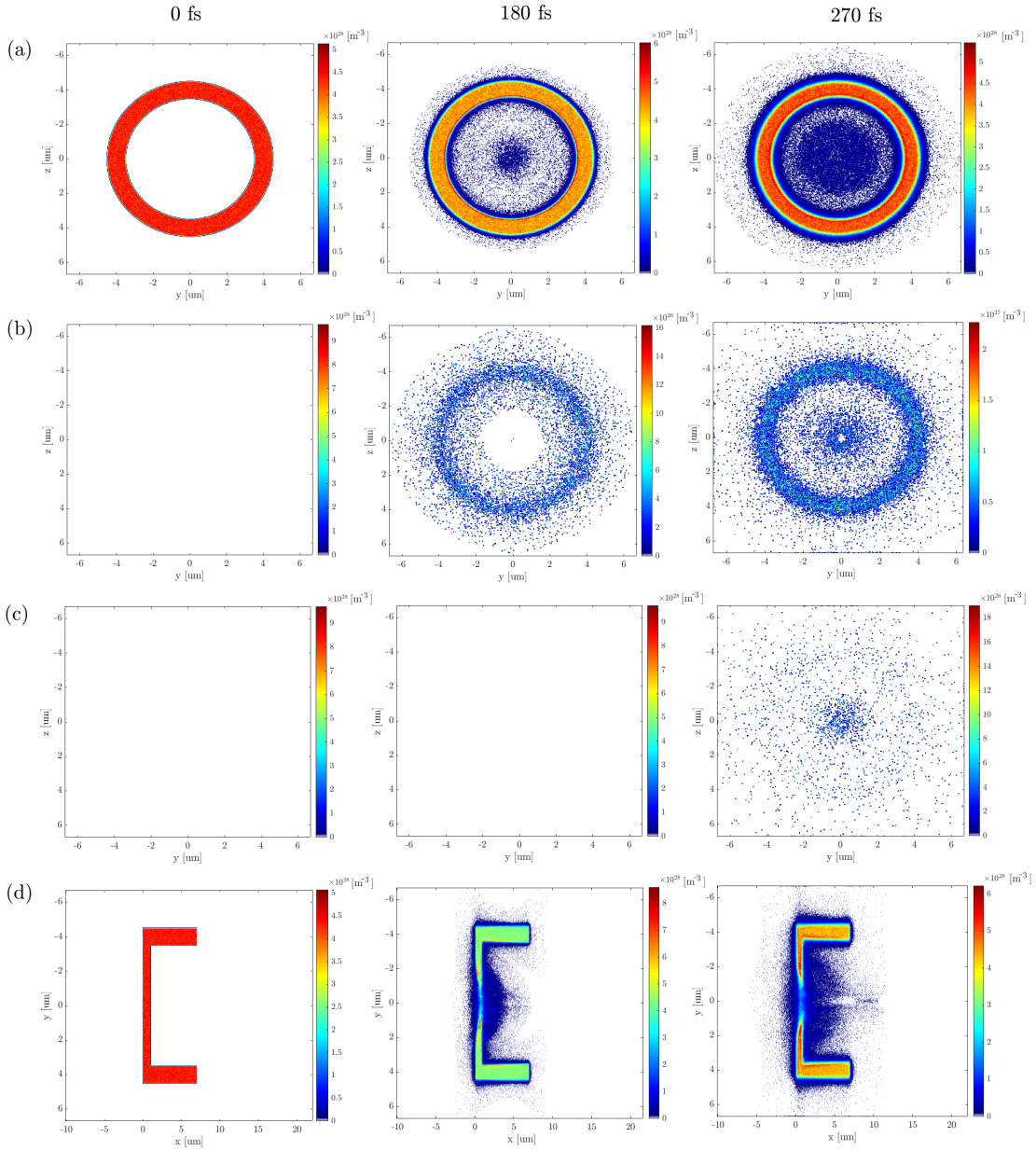

Figure 4.25: Channel target: Carbon ions (C^{6+}) density plots are shown in various times (0 fs, 180 fs and 270 fs; corresponding to three columns) after the start of laser-target interaction and at various spatial cuts along the laser propagation axis: (a) at 3 μm (i.e., in the middle of the channel length), (b) at 6.5 μm (i.e., directly behind the channel), (c) at 8.9 μm (i.e., at $\sim$ 2.9 μm behind the channel) behind the rear surface of the flat target part being perpendicular to the laser pulse. The last set (d) corresponds to the side view ($x-y$) of the target density cut in the middle of $z-$axis. None of the cuts correspond to the proton plots in Fig. 4.23 (c) or (d), because carbons do not propagate so far as protons do during the same time, thus the different space reference was chosen.

4.6.3 Spatial uniformity of the proton beam

Attempts in improving spatial beam uniformity have been extensively investigated in the field of conventional particle accelerators [157], [257] as well as in the field of surface modifications of various materials, such as ion implantation and film deposition by accelerated particle beams from laser-plasma [258], [259], [260]. The supporting effect of external magnetic field on the flux uniformity of laser-driven proton beams was reported [260]. Similarly, the multipole magnets, specifically magnetic octupoles, are used in particle accelerators in order to improve a spatial uniformity of ion beam [160] as already discussed in previous sections.

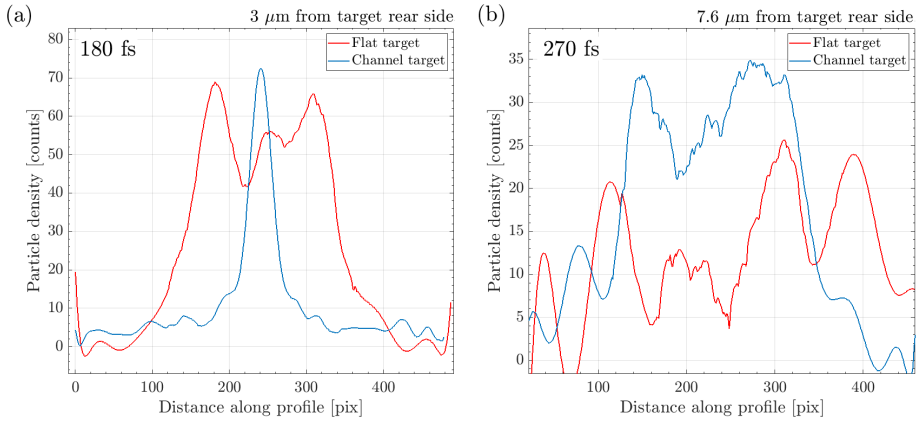

Figure 4.26: Spatial uniformity of the proton beam accelerated from the flat target (red curve) and from the channel target (blue curve); 3D simulations. The curves show 1D smoothed proton density profile in the plane perpendicular to the laser propagation direction, i.e., along $y-$axis in the middle of $z-$axis (the targets are centralized around 0). The profiles are shown at different positions along the laser propagation axis: (a) at 3 μm behind the rear side of the targets flat part (i.e., in the case of the channel target, it corresponds to the half of the channel) at 180 fs; (b) at 7.6 μm behind the rear side of the targets flat part (i.e., 1.6 μm behind the channel) at 270 fs after the start of laser-target interaction.

Within 3D simulated designs, a significantly higher spatial uniformity of the proton beam was observed in the case of the channel target. In the comparison demonstrated in Fig. 4.26, two graphs showing smoothed proton density profiles are presented for both 3D simulated targets at diverse times and positions along the laser propagation axis. All density profiles were taken in the middle of the proton beam ($z = 0$) along $y-$axis (a) at 3 μm behind the target flat rear side (i.e., in the case of the channel target, it corresponds to the half of the channel) at 180 fs or (b) at 7.6 μm behind the target flat rear side (i.e., 1.6 μm behind the channel) at 270 fs after the start of laser-target interaction. The red curve represents the reference flat target, whilst the blue curve depicts the channel one. These spatial-uniformity plots correspond to the 2D maps of the proton beam density in Fig. 4.23 and in 4.24, particularly to the cases (a) at 180 fs and (c) at 270 fs, for the channel and the flat target, respectively. At both the space and the time cuts, the proton beam produced from the channel target shows significantly higher spatial uniformity than the beam produced from the reference flat foil. The biggest difference between the flat and the channel profiles was observed naturally inside the channel, i.e., closer to the targets flat rear side (see Fig. 4.26), where the magnetic octupole, responsible for making the beam more uniform, is directly present. For more information about the octupole

formation see the section Particle divergence reduction affected by favorable establishment of EM fields. Even at the end of the simulation and simultaneously further from the target rear, the channel-produced proton beam sustains undoubtedly more spatially uniform than that produced from the reference target. Moreover, the demonstrated feature of generally higher proton beam spatial uniformity in the case of the channel target does not change with time or with various position along the laser propagation direction. The 1D density profiles taken along another transverse axis, i.e., in the middle of the beam ($y = 0$) but along $z-$axis (and not along $y-$axis), were studied as well, but no significant difference in comparison to the presented case was observed.
These results are in a great agreement with the calculated standard deviations of the proton density evaluated from the beam cross-sections which are presented in Tab. 4.7 for various target designs. The standard deviation is a measure of the amount of variation or dispersion of a set of values. Therefore, the closer the standard deviation is to zero, the more values tend to be close to the mean of the set (also called the *expected value*), which indicates the high uniformity of the beam. On the contrary, the large standard deviation indicates that the values are spread over a wider range and the uniformity of the particle beam is poor. The values of the standard deviation of the whole proton beam cross section were evaluated at 3 μm or at 7.6 μm behind the rear side of the targets flat part at 180 fs or at 270 fs after the start of laser-target interaction, respectively, see Tab. 4.7. Such parameters correspond with those used in plotting of Fig. 4.26. At both evaluated space and time scans, the proton beam produced from the channel target shows the higher beam uniformity, particularly by $\sim 15-30\%$ in comparison to the flat foil. Naturally, the higher spatial uniformity was reached inside the channel (as already seen in Fig. 4.26) where the magnetic octupole directly acts on the passing particles.

σ_{SD} at:	3 μm at 180 fs		7.6 μm at 270 fs	
Flat target	0.3914	100%	0.4147	100%
Channel target	0.2742	70%	0.3553	86 %

Table 4.7: Standard deviation values σ_{SD} measured at proton beam density cross sections along two various positions on the laser-axis (i.e., at 3 μm and at 7.6 μm behind the flat rear side of targets) are shown at diverse time scans – at 180 and 270 fs after the start of laser-target interaction.

Finally, but not less importantly, the transverse profile of the accelerating electric field E_x affects the spatial density of the particle beam as well. In fact, this profile significantly differs between the flat and the channel target due to the various electrons confinement inside the channel or in the vacuum behind the flat target. Generally, the accelerating field of the flat foil is peaked not only on the laser axis, as in the case of the channel target, but also transversely further from the axis to the sides (symmetrically), which contributes to a halo in the particle beam cross section resulting in the lower uniformity of the produced beam, see the section 4.7.1.2, particularly Fig. 4.29 (b) and (e) (the comparison of accelerating field profiles) and Fig. 4.24 (the example of the particle halo).

4.7 Particle beams acceleration

4.7.1 Electric sheath field

The electric sheath field formation is essential for laser-driven ion acceleration, especially in the case of TNSA mechanism [1], [50], [52]. The detailed knowledge of its evolution, both in time and space, is crucial for understanding of the acceleration stages. In addition, spatial analysis of E_x field has to be treated separately for transverse and longitudinal (i.e., along the laser-axis) directions. Generally, the electric sheath field is strongly dependent on the hot electrons generation, their motion and confinement. In fact, the profile of electric sheath field along the laser propagation axis is formed by the hot electrons accelerated from the vicinity of the laser-target interaction point, whilst the profile of the sheath field along the transverse direction is modified according to the electrons confinement behind the target (in the means of, for instance, angular spread of the hot electron beam). In other words, whereas the shape of E_x field along the laser-axis is affected mainly by the the shape of the target part perpendicular to the laser pulse, the shape of E_x field along the transverse axes (i.e., y or z) is more influenced by the structures attached to the target back side.

4.7.1.1 Dependence of the sheath field shape along the laser propagation axis on the target design

The space & time evolution of the electric sheath field E_x along the laser propagation axis was compared between all simulated target types in 2D and correlated with corresponding proton and carbon ion charge densities for chosen designs. This comparison is presented in Fig. 4.27, namely for the reference flat foil and for the flat or the curved targets with 6 μm long channel. Other target designs do no show any additional differences than those already observed for the described set.

As can be observed in Fig. 4.27 (a), carbon ions are accelerated after the firstly generated proton bunch and they drag behind themselves the second proton population, which corresponds to the deceleration valley between two positive peaks in $E_x - x$ plot. Furthermore, the negative spike in the electric field corresponds to the beam-front position of the carbon cloud and thus it is connected with the sudden rise in proton charge density. The presented plots are shown with the modified range of density axis in order to see the exact correlation between the sudden change of the charge densities and the sheath field. Moreover, the sheath field in Fig. 4.27 (a) is plotted as a raw data whereas in (b) – (d) the curves are already smoothed in order to see the overall trend. In fact, the carbon ions drag effect is connected not only with the sudden rise in proton densities, but also with the proton energy bump observed in the energy spectra and discussed further in Energy spectra & Number of particles section.

The only variation from the typical shape and the time evolution of accelerating electric field was observed for the curved foils with straight channel, see the green curve in Fig. 4.27 (b) – (d). Whereas the flat foils (no matter if plain or with channels) experience two stages of positive acceleration separated by the deceleration part, the curved foils additionally produce a relatively strong sheath-field-structure inside their channel. This structure consists of firstly negative and then positive E_x spikes, both having the comparable amplitude. Furthermore, the negative peak is located in the geometrical center of the curvature whilst the positive peak at the end of the channel, see Fig. 4.27. In contrast to other target designs, the field-structure produced from the channel target does not move with the time or with any accelerated particle bunch, but stays on place and vanishes gradually. Naturally, this leads to the conclusion

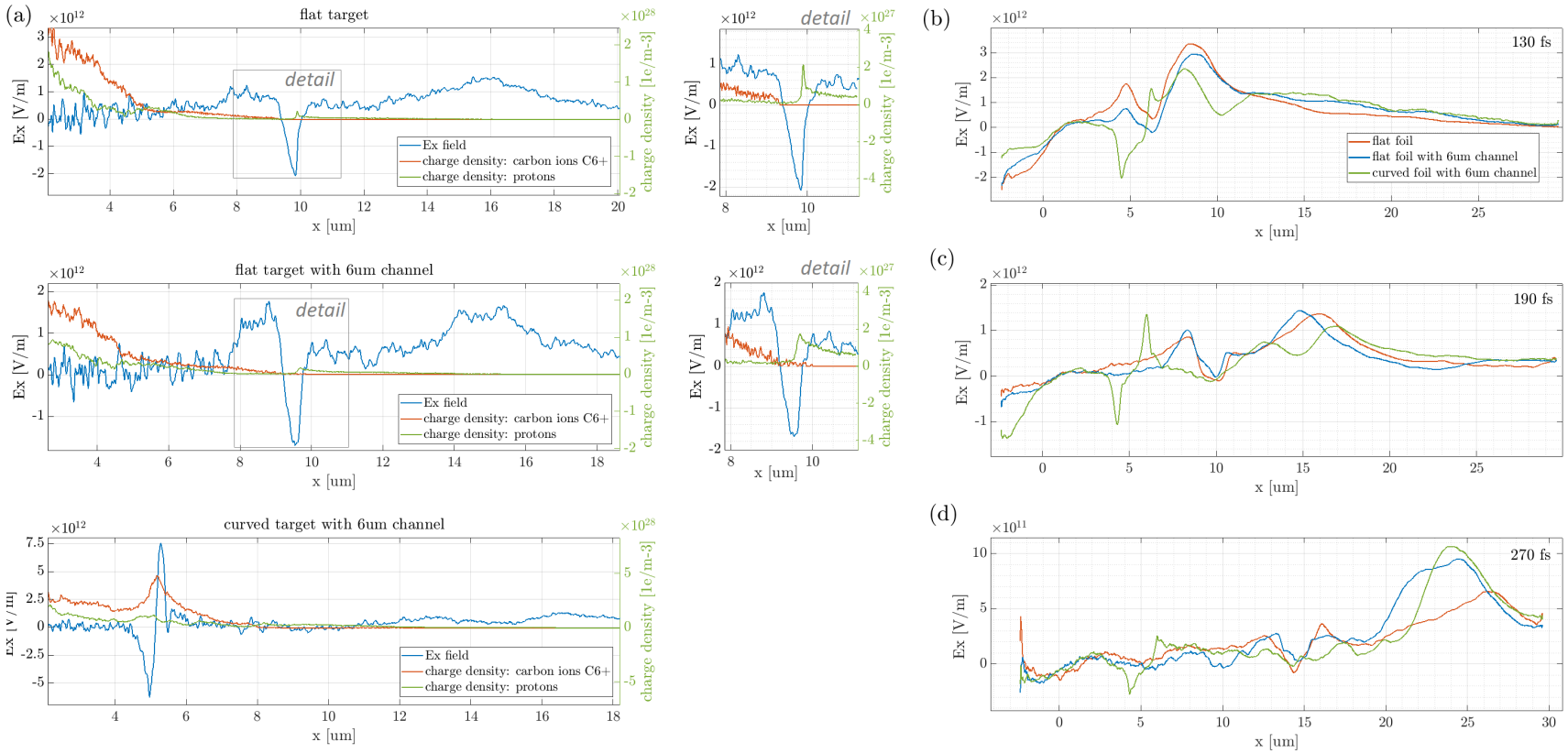

Figure 4.27: Study of accelerating sheath field E_x along the laser propagation axis of three chosen target designs simulated in 2D: the flat target and the flat/curved target with 6 μm long straight channel. (a) E_x field is compared with proton and carbon ion charge densities at 190 fs after the start of the laser-target interaction (the data were not smoothed); Graphs (b) – (d) show the time and the space evolution (along the laser propagation axis) of the smoothed accelerating electric sheath field E_x at 130 fs, at 190 fs and at 270 fs after the start of laser-target interaction, respectively.

that such field-structure is caused by the curved target shape primarily.
In 3D, the field formation was compared between the flat and the channel target. The situation is demonstrated in Fig. 4.28, where the chosen time scans of accelerating E_x field in $x-y$ plane are shown for both designs of 3D-simulated targets. Firstly, the high positive E_x field is formed nearly immediately at the rear side of targets flat part, i.e., at $\sim$ 10 fs after the start of the laser-target interaction, and it rapidly grows in the next 50 fs. No matter the target design, the produced field moves with the first bunch of protons and it is followed by the creation of the second positive spike in E_x. This second spike occurs approximately at 70 fs after the start of laser-target interaction and it results in another proton population (visible, for example, in density plot Fig. 4.20 (a) showing the early stage of acceleration). The time of the second field-peak creation corresponds to the time when the whole laser pulse (having the full time duration of 60 fs) had already interacted with the target. The positive areas of accelerating sheath field are visibly separated by a gap which spatially corresponds to the carbon ion cloud between two proton populations as already discussed in 2D part. Moreover, these two accelerating field areas are gradually becoming more distant from each other, because the first one co-moves with the main proton bunch of high energies, whilst the second one with the less-energetic proton population. In the case of the channel target, another accelerating field area is naturally present at the end of the channel (because of hot electrons escaping from the cylinder material), but no significant kick in proton energies was observed in corresponding phase spaces, when the main proton bunch exits the channel.

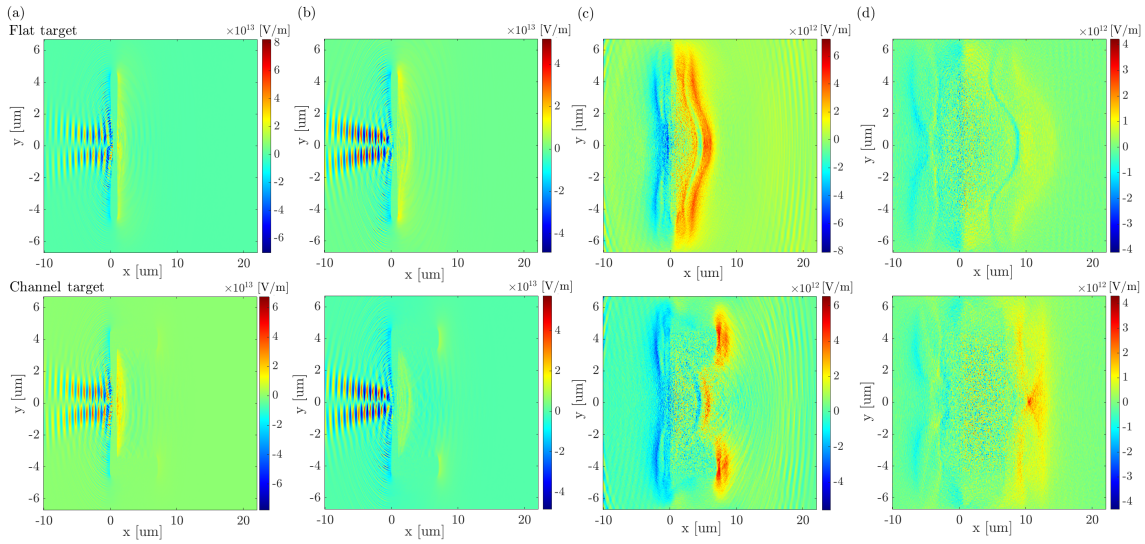

Figure 4.28: 3D simulations: Time evolution of accelerating E_x field in $x-y$ plane in the middle (i.e., $z=0$) of the flat target (the first row) and of the channel target (the second row) at (a) 60 fs, (b) 70 fs, (c) 110 fs, (d) 190 fs after the start of laser-target interaction.

In conclusion, obtained results from 2D and 3D simulations are in a good agreement. The rear-placed mictrostructures, i.e., channels, do not change the tendency of accelerating field E_x along the laser axis direction significantly, in contrast to the shape of the target part perpendicular to the laser pulse direction. On the other hand, as will be demonstrated in the following section, microstructures can change the shape of sheath field significantly, but in the *transverse*, not the laser-axis, direction.

4.7.1.2 Dependence of the sheath field shape in transverse direction on the target design

As already mentioned, the shape of the electric sheath field *along transverse direction(s)* is affected by the confinement of electrons. Hence, from the target design point of view, the formation of $E_x - y$ and of $E_x - z$ profiles is modified according to the presence/the shape of the channel (or any structure on the target rear side), not by the shape of the foil to which this cylinder is attached (i.e., the flat or the curved one). This is, in fact, well demonstrated in Fig. 4.30 (a) at 30 fs, where the field shape at the rear side of the targets flat part is comparable at the beginning of acceleration for all 3D simulated target designs, but it starts to differ with time. In order to demonstrate the trend both in 2D and 3D, only the reference flat foil and the channel target are presented in this comparative study. Three-dimensional data provide the opportunity to investigate the possible difference between transverse directions (y and z) as well as the changes in amplitudes or the field-shape variations compared to 2D cases.

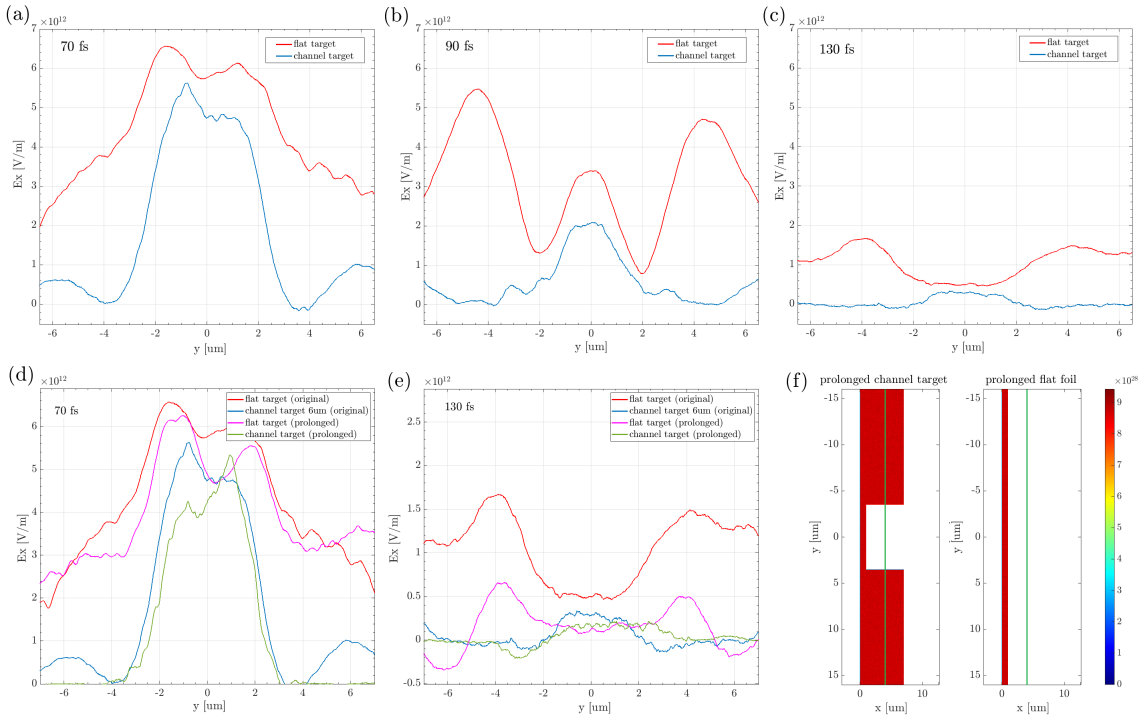

Figure 4.29: 2D simulations: (a) – (c) comparison of sheath electric field E_x over the transverse axis between the flat foil (the red curve) and the flat target with 6 μm channel (the blue curve). The analysis was done at 3 μm behind the rear side of the flat part of the both foils (i.e., in the middle of the channel length in the case of the target with guiding arms) at 70 fs, 90 fs and at 130 fs after the start of the laser-target interaction. Graphs (c) – (d) show the comparison of limited and unlimited versions of the flat and the channel target designs as shown in (f), at 70 fs and 130 fs, respectively. The green lines in (f) indicate the space cut along which the electric field profiles are presented (i.e., at 3 μm behind the rear side of the targets flat part).

Generally, transversely limited targets simulated here are a widely used simplification of larger

foils which would be more likely used in a real experiment than a single μm–scale target. Since the electric sheath field establishment is bounded with the hot electrons production, spreading and confinement, the transversely *unlimited versions of the flat and the channel targets* were **additionally simulated, primarily in 2D**, see Fig. 4.29 (d) and (e). The main aim was to verify if the edge-peaked field structure in the case of the transversely limited flat foil (visible, for example, in Fig. 4.29 (b)) is strongly influenced by the hot electrons reflected from the foil edges (in our case 1 μm thick) or if this field-structure is even their direct result. If so, these field-structures vanish when the flat foil is prolonged transversely and no big advantage of the channel target over the flat one would be observed.
The electric sheath profiles in Fig. 4.29 were taken along the direction perpendicular to the laser propagation axis, 3 μm behind the flat rear side of the targets, at various time scans for limited and unlimited versions of both the flat and the channel targets. As demonstrated by this comparison, the transversely limited and unlimited versions of the channel target do not differ much in the electric sheath field from each other, both in their amplitudes and the shape of the profile, in comparison to the flat target designs. The negligible difference between accelerating field profiles of channel target versions is caused by the target geometry. Whereas electrons escaping the outer edges of the channel (when the target is transversely limited) do not contribute to the main accelerating field (which is located inside the channel), the electrons escaping the edges of the transversely limited flat foil do, since they are mixed with the electrons originating from the flat foil rear side. Therefore, the prolonging of the reference flat foil prevents the production of electrons from the foil edges (in our case 1 μm thick), but the prolonging of the channel target does not have any significant effect on the accelerating field. Consequently, only the *transversely unlimited flat target* was **additionally simulated in 3D** and added to the comparison of various target designs in Fig. 4.30.

Time & Shape evolution in 3D
The time and the space evolution of accelerating field E_x along transverse axis is presented in Fig. 4.29 for all 3D simulated target designs. The sheath field is shown along $y-$axis at three various space cuts along the laser propagation direction – (a) *cut 1* shows the field at ~ 0.3 μm behind the targets flat side, (b) *cut 2* shows the field at ~ 3 μm behind the targets flat side (i.e., in the case of the channel target in the half of the cylinder) and finally, (c) *cut 3* shows the field at ~ 6.3 μm behind the targets rear flat side (i.e., in the case of the channel target at 0.3 μm behind the cylinder). The spatial positions of the cuts are visible for all target designs in the blue border of Fig. 4.30 (d). The spatial cut in the another transverse direction (in this case in $z-$direction) was done in the middle of the target. All values presented in the graphs (called *raw data* in the legend) were obtained by averaging the values from 10 cells centralized around the chosen spatial cut in order to suppress the effect of high fluctuations of the field. Nevertheless, in some cases the field fluctuations are so significant, that the averaging lines (called *average* in the legend) were added additionally to guide the eyes smoothly. The raw data were left in the figures in order to see that, for instance, even though the averaging line for the channel target in (a) has the lower amplitude than that in the case of the flat target, the positive spikes of the field itself reach the comparable values for both target designs. The fields were analyzed at various times (i.e., at 30, 70, 90, 130 or at 150 fs, depending on the target type) after the start of laser-target interaction.
At the beginning of the acceleration process, the originally bell-shaped E_x field is distributed and peaked around the laser propagation axis for all presented target designs. In later times of acceleration, the high-field amplitude stays centralized in the case of the channel target,

because the hot electrons are confined inside the cylinder and they move along its inner walls. On the contrary, in the case of the flat foil, the field profile diverges towards the edges of the simulation box, starts to grow there and finally surmounts the field in the center. Such evolution is the consequence of the movement of hot electrons, which do not circulate along the guiding arms as in the case of the channel target (demonstrated in Fig. 4.5 (b)), but spread freely into the vacuum. Compared to 2D simulations, the field evolution is faster in 3D, because of the additional transverse direction where electrons can spread. The shape of accelerating field along $y-$axis in 3D follows the same trend as that obtained from 2D simulations in Fig. 4.29. Depending on the space cut where the analysis was done, the field of the channel target has preferably a bell-shaped or a flat-like profile, slightly peaked at the cylinder center and decreasing towards the channel walls. The only exception is (c) at 70 fs where the high-amplitude field structures located around $x = 3.5$ μm originate from the cylinder endings, since the field profile is taken directly behind the channel and simultaneously at the time when the main TNSA accelerating field has not reached the area yet. Contrarily, the sheath field of the flat foils (no matter if the reference's one or the prolonged's one) has, with ongoing time, the lowest values in the center and it rises to the sides, i.e., perpendicularly to the laser-axis. Therefore, the acceleration field is moving away from the laser-axis and it does not contribute to the formation of the narrow on-axis particle filament which is a clear disadvantage in contrast to the channel target, compare the field profiles in, e.g., Fig. 4.30 (c) at 150 fs. In the case of the prolonged flat foil, the field diverges less to the transverse boundaries of the simulation area than in the case of the original limited flat foil at later times, but the trend is still there (compare, for instance, the time evolution in Fig. 4.30 *cut 1* (a)). Therefore, the clearly observable differences in the shape of the field profiles (moreover of the comparable amplitudes) are demonstrated even between the channel target (blue) and the prolonged flat foil (green).

To summarize, from the comparison of the electric sheath field along the axis perpendicular to the laser propagation direction between transversely limited and unlimited flat foils, nearly no differences in the time evolution and the comparable shapes of the electric sheath field were observed. On the other hand, the E_x amplitude was reduced with the target prolongation, because the limited flat foil reflects more hot electrons escaping from its edges which strengthen the accelerating electric field. In the realistic flat foil scenario, an energy decrease connected with the sheath field amplitude drop is therefore expected. In comparison to the channel target, the amplitude of prolonged flat foil sheath field is similar or even lower, but the opposite shapes of the field profiles between various target designs are still well-observable. Therefore, the clear advantage of channel target over the both limited and unlimited reference foils was demonstrated. In real experiments, this could suppress the maximum energy difference between the particles accelerated from the channel target and from the flat foil. In fact, a similar observation of the field structures (bell-shaped or peaked at edges) has been already reported in the case of hydrogen foil with aluminum ramparts (2D only) [261].

Field maximal values

From the point of view of the field strength, the highest values were reached for the limited flat foil, but the amplitudes around the laser axis (i.e., approximately within $y = \pm 2$ μm and $z = \pm 2$ μm) were comparable for all three simulated cases in 3D. As already mentioned, the averaging lines (called *average* in the legend) were added to some plots in 4.30 due to the high fluctuations of the raw data. Note, that even though some average curve has the low amplitude, its raw-field spikes sometimes reach the comparable values as those related

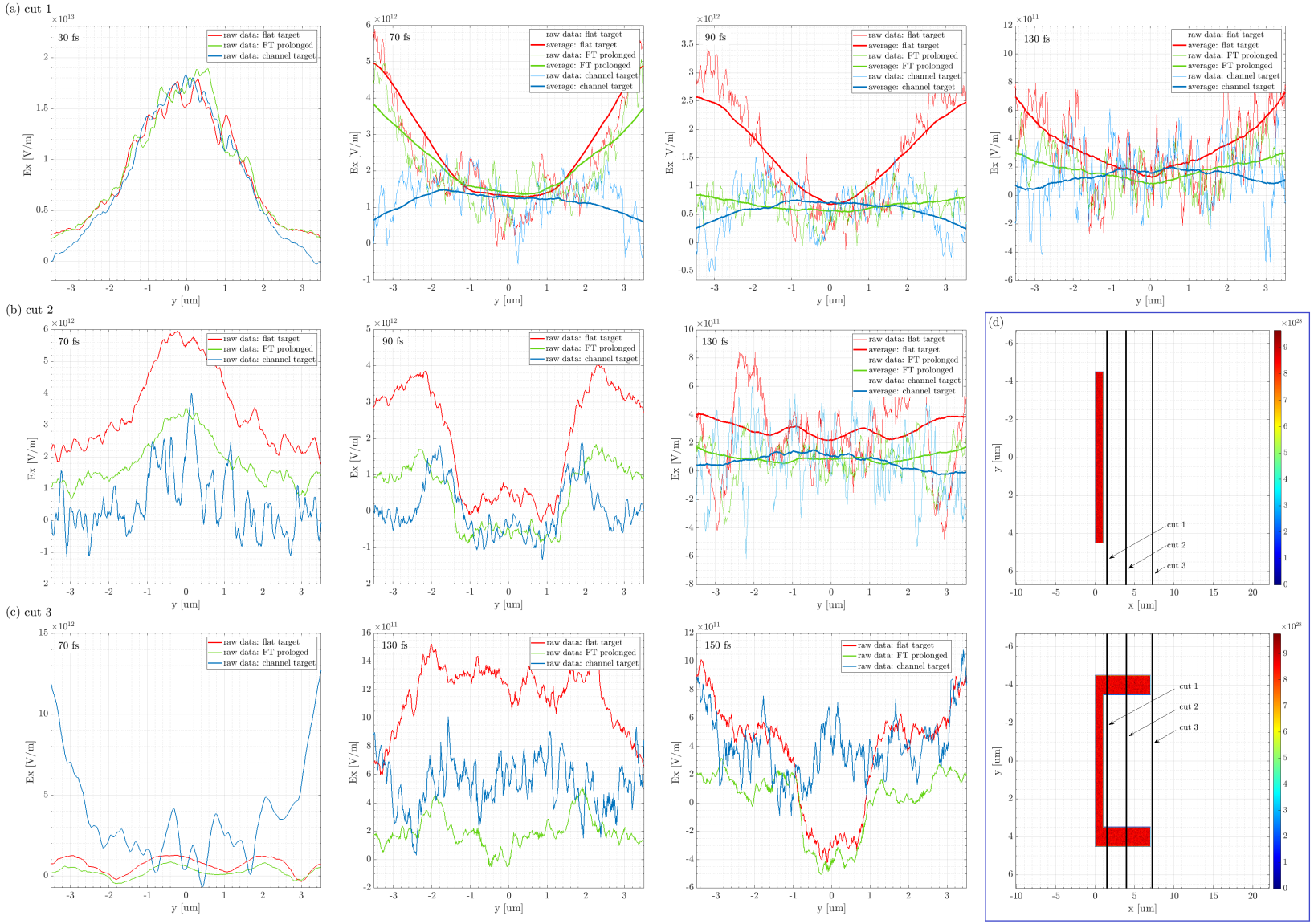

Figure 4.30: Comparison of the sheath electric field E_x along the transverse $y-$axis between the flat foil (red curve) of lateral dimension 9 μm (i.e., Fig. 4.1 (a) case), the flat foil filling laterally the whole simulation area from boundary to boundary (green curve) is given at (a) cut 1 showing the field at ~ 0.3 μm behind the targets flat side, (b) cut 2 showing the field at ~ 3 μm behind the targets flat side and (c) cut 3 showing the field at ~ 6.3 μm behind the targets rear flat side. The spatial cuts are visible for both target designs in figures (d) presented in the blue border. The fields are analyzed at various times (i.e., at $30, 70, 90, 130$ or 150 fs) after the start of laser-target interaction, the info is present in the left upper corner of each figure.

to much stronger average line (see, for instance, Fig. 4.30 (a)). Around the laser axis & with ongoing time, the average field profile of the channel target even exceeds in values that of the prolonged flat target. Comparing the field amplitudes originating from 2D and 3D simulations, the higher values were naturally observed in the case of 2D simulated targets, because the additional dimension allows the hot electrons spread to another direction, which suppress the field in 3D.
Even though the field suffers from fluctuations, it has the same tendency and comparable shape along $z-$axis as along $y-$axis for all target designs in 3D, thus only the representative $y-$direction is shown in Fig. 4.30. Nevertheless, the maximum values were slightly lowered in $z-$direction, maximally by 10%. This is caused by the linear laser polarization along $y-$axis as discussed earlier in the section 4.4.3.

Effect on particle beam parameters
The shape of the electric sheath field in the direction perpendicular to the laser propagation axis can affect the divergence of the accelerated proton beam and its uniformity.

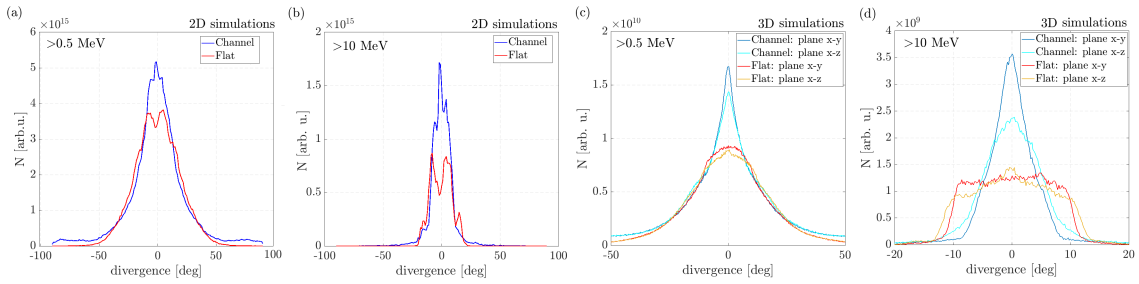

Figure 4.31: Comparison of proton angular distributions between the reference flat target and the flat target with 6 μm long channel at the end of 2D and 3D simulations. Only protons moving forward ($p_x > 0$) within the cylinder of radius 3.5 μm (i.e., the channel inner dimensions) and having energy (a) + (c) above 0.5 MeV or (b) + (d) above 10 MeV were taken for the analysis.

In the case of the flat foil, the edge-peaked sheath field contributes to the higher proton angular spread, because electrons are more accelerated in the marginal regions which in turn increases the proton beam divergence. In fact, this sheath field is continuously changing from the centralized bell shape to the edge-peaked structure, i.e., the high-field epicenter gradually moves from the center to the sides as shown and described earlier in this section. That causes also the halo in proton density cross sections (see Fig. 4.24) and worse spatial uniformity of the flat-foil-produced beam in comparison to the one produced from the channel target, see sections 4.6 and 4.6.3. In fact, the flat target field evolution does not contribute to the formation of the narrow on-axis particle filament which is a clear disadvantage in comparison to the channel target. Moreover, the generation of double-splitted (in 2D) or more realistic plateau-like (in 3D) proton angular profiles were observed for the reference target in comparison to the channel one for which the angular spectra were peaked on the laser axis for both 2D and 3D simulations, see Fig. 4.31 or Divergence section. The moderate beam filamentation in the case of the flat target is visible also in the phase spaces in Fig. 4.33 (discussed in Phase spaces section).
In the case of the channel target, the sheath field has a flat-like profile, which results in a uniform acceleration of particles along transverse direction and corresponding lower divergence.

4.7.2 Phase spaces

The occurrence of various proton acceleration epicenters, as already seen from the electric sheath field and from the particle densities, were confirmed also by analyzing phase spaces – see Fig. 4.32, where the time-evolved proton phase spaces $v_x - x$ between various 2D simulated target designs and their equivalents in 3D are compared; and Fig. 4.33, where phase spaces $v_y - v_x$ and $v_z - v_x$ of 3D-simulated targets are shown.

The first acceleration epicenter is located at the front target side, where the protons are accelerated by Hole-Boring (HB) mechanism, no matter the specific target design. The target surface is then strongly pushed inwards by the pressure of incident laser light. Nevertheless, HB scenario is not efficient for the used laser parameters. In fact, according to the analytical approximation (1.39) – (1.40) (discussed in the section RPA acceleration – Hole Boring [74] and suitable also for linearly polarized pulses [262]), the maximum energy of protons accelerated only by HB-RPA mechanism is below 5 MeV/amu and the energy of carbon ions is even lower. Because of the low particle energy and their limited number in comparison to those originated from Target Normal Sheath Acceleration, HB-accelerated particles affect the overall divergence only slightly.

Secondly, the multiple epicenters are assigned to Target Normal Sheath Acceleration (TNSA) mechanism and they are located at the target rear side as well as at the structure endings if the channel target design had been used. The acceleration from *the target flat rear side* undergoes two phases corresponding to two positive spikes in E_x field discussed in the section Dependence of the sheath field shape along the laser propagation axis on the target design and also visible in the proton energy-resolved density plots Fig. 4.20 or in the side-view proton densities Fig. 4.23. In fact, the first E_x spike forms the proton population with the highest energy. The protons accelerated by TNSA from *the channel material* (i.e., from the channel endings or its outer surface) gain only a low momenta in the laser propagation direction, see Fig. 4.32. Moreover, the proton population accelerated from the target front side by HB reaches the area of the sufficiently high TNSA field in the time when the strength is still significant and it is consequently post-accelerated (although it was not enough to obtain higher energy than the main TNSA-beam). In fact, such protons reach the energy < 20 MeV (HB+TNSA) from the original < 5 MeV (HB), see the front-side generated proton fillament reaching nearly 0.2 v_x/c in Fig. 4.32.

In the phase spaces in Fig. 4.32 (c) or (e), the protons having a low momenta in the laser-axis direction (but the higher velocity in the transverse axes connected to their high divergence) are visible. These protons originate from the channels inner or outer walls due to the target expansion. In fact, the design of the channel itself strongly influences the shape of this low $x-$momenta particles in phase spaces. In other words, the reason why the low energy protons form only one group along the straight channel, whereas they form two groups in the case of the tapering channel, is the design of the guiding arms. Particularly, the particles originated from the channel material are accelerated by TNSA mechanism perpendicularly to the channel surface, which results in two directions in the case of the straight channel target – firstly, from the inner cylinder surface to the channel central axis and secondly, from the outer cylinder surface towards the horizontal boundaries of the simulation area. Both these options result in the negligible velocity in $x-$direction (both positive and negative, but without significant differences) and in some cases also in the high transverse velocity. On the contrary, in the case of the target with tapering channel, the direction of perpendicular propagation from the channel surface is changed because of the arms slope. The protons moving

perpendicularly from the outer surface of the channel gain currently the higher velocity in $x-$direction (positive) than those accelerated from the straight channel surface, even though the overall energy is the same. Similarly, the protons, which move perpendicularly from the inner tapering channel surface, gain also higher v_x than those accelerated from the straight cylinder, but with negative sign.
From the comparison between 2D target designs with their 3D-simulated equivalents, it was investigated that the proton momentum in $x-$direction was slightly reduced with the second transverse dimension. In fact, an extra dimension lowers the accelerating electric field (due to the additional axis where hot electrons can spread) as well as the corresponding maximum particle energies as had been already reported. Nevertheless, no significant differences in the shape of phase spaces, their evolution or the overall trend were observed, see Fig. 4.32.
Because the part of the laser pulse has been observed at the rear side of the targets (see, for example, Fig. 4.10 (b) and the section Partially-transmitted laser pulse), the presence of Magnetic Vortex Acceleration (MVA) has been investigated. No jump in the particle energy spectra/phase spaces was observed when the particle beam exits the channel, which should be one of the distinguishing signs of efficient MVA acceleration. Although a gradual rise in the energy of HB-protons was observed at the time when they reached the rear side of the target flat part (i.e., when they entered the channel), this enhancement was assigned to the TNSA field present in the area rather than to the weak MVA. Moreover, magnetic field was confined inside the channel, therefore, it could not spread to the sides and generate longitudinal electric field as in MVA scenario. In fact, the B_z magnitudes having tens of kT in the case of the channel targets were observed (see Tab. 4.3). Nevertheless, such values are higher than ones of kT predicted by MVA regime [85], [86], [263], [264]. In conclusion, even though the narrow proton filament having high energy was observed in the case of the channel target, the presence of MVA acceleration is not likely or it was not significant in this case. It is possible, that if the optimal parameters for MVA had been fulfilled (e.g. significantly lower target density or RT occurrence), the enhanced Magnetic vortex scenario would have occurred. The electron fountain would be developed fully at the end of the cylinder and not at the rear side of target flat part. In other words, it is possible that the guiding arms of the channel target would mechanically prolong the self-established channel described in MVA, if the scenario is sufficiently reached.
Graphs showing $v_y - v_x$ and $v_z - v_x$ phase spaces at different times during the acceleration phase are beneficial for demonstrating the divergence/filaments evolution in various planes. In Fig. 4.33, such phase spaces from 3D simulations of the flat and of the channel targets, are shown both for the protons and the carbons ions having energy above 0.5 MeV/amu. The originally narrow proton beam generated from the flat target diverges to the sides rapidly with ongoing time, which is in a great agreement with the time evolution of accelerating $E_x - y$ field observed for this target type, see Fig. 4.29. In the case of the channel target, the particle beam stays significantly more compact, although the beam broadening occurred as well, see Fig. 4.33 and Fig. 4.31. In contrast to the reference flat foil, the higher amount of particles having low momenta in $x-$direction, but high velocities in the transverse one (y or z) was observed in the channel target case. These particles originate from the cylinder material. The unsymmetrical particle divergence in transverse planes, already reported in Divergence section, is observable in Fig. 4.33 as well. In fact, the v_z velocity component reaches the larger value than v_y does for both foil designs although the difference is much stronger in the channel target case.

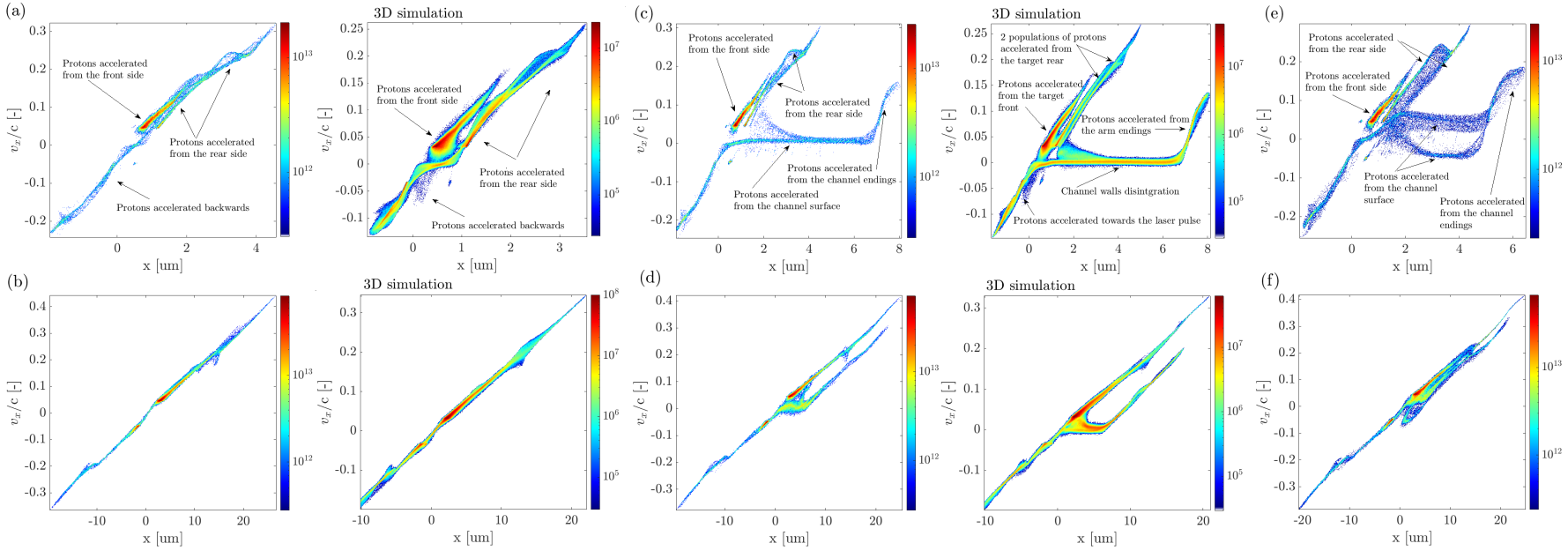

Figure 4.32: Comparison of the time-evolved proton phase spaces $v_x - x$ between various 2D simulated target designs and their equivalents in 3D. Graphs showing the flat target ((a), (b), both in 2D and 3D), the flat target with 6 μm long straight channel ((c), (d), both in 2D and 3D) or the flat target with tapering channel forming the 3 μm-wide hole between arms ((e), (f), only 2D) are plotted at two various times – at 90 fs (the first row, i.e., (a), (c) and (e)) and at 270 fs (the second row, i.e., (b), (d) and (f)) after the start of laser-target interaction. The logarithmic scale of color bars showing the particle density was applied.

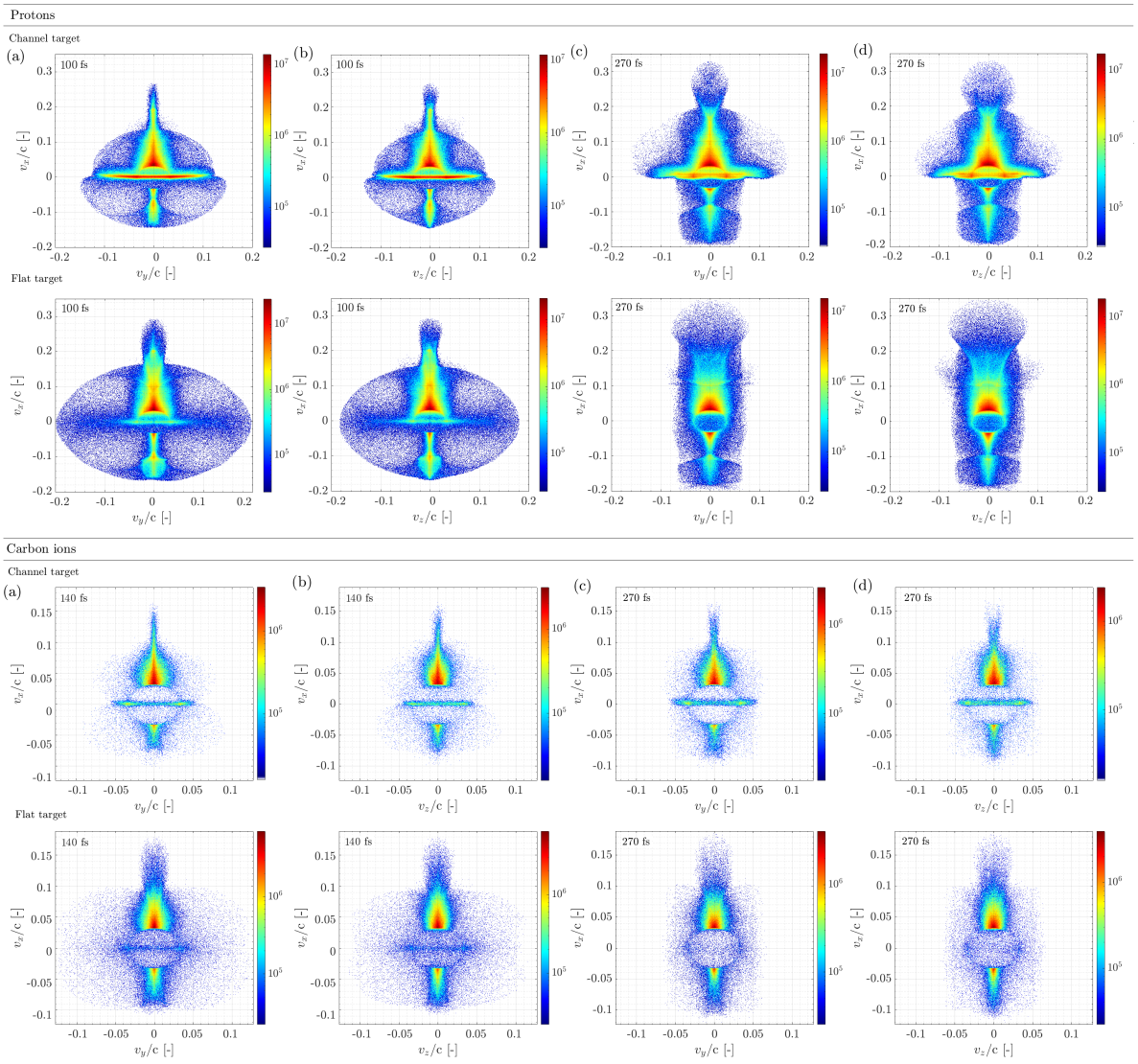

Figure 4.33: Phase spaces $v_y - v_x$ and $v_z - v_x$ of the flat and of the channel target showing the protons having the energy above 0.5 MeV at (a) + (b) 100 fs or at (c) + (d) 270 fs after the start of laser-target interaction. Phase spaces showing the carbons ions having the energy above 0.5 MeV/amu are plotted at later time scan due, particularly at (a) + (b) 140 fs or at (c)+(d) 270 fs after the start of laser-target interaction. The logarithmic scale of color bars showing the particle density was applied.

4.8 Expanded density profile: The effect of preplasma on ion beam parameters

Current petawatt laser technologies can produce pulses having duration of only a few tens of femtoseconds in FWHM. Such short-pulse production suffers from a relatively low-energy (nevertheless still significant) femtosecond or nanosecond prepulses which accompany the main pulse. In fact, the realistic laser pulse profile contains, among the main pulse and these prepulses (having typically the second highest peak intensity), also a picosecond ramp and nanosecond amplified spontaneous emission (ASE) discussed in the section Realistic laser profile including prepulse and pedestal. Moreover, the exact shape of the realistic pulse is complicated to be fully predicted.

Generally, the laser prepulse is usually taken as an unwanted feature because it ionizes and evaporates the material at the target front side and sometimes even at the rear side. The main pulse then interacts with the preplasma before it can reach the solid density region of the original target (if it is still present) which would cause a significant difference not only in the interaction itself, but also in the corresponding accelerated particle beam parameters. When the laser contrast is low, the prepulse may destroy also various structures made on target front and even back surface [129], [130]. Laser prepulses can therefore lead to a fast depletion of the main pulse and it can diminish the ion acceleration efficiency, which is definitely an unfavorable situation for ion acceleration. Furthermore, the expansion of the target at the rear side decreases the TNSA accelerating field, whereas the possible destruction of target shapes is connected to, e.g., a higher divergence of accelerated proton beam. On the other hand, in some occasional cases the prepulse could be an advantage as discussed further in The impact of generated preplasma on laser-driven particle acceleration. For example, the laser pulse typically undergoes self-focusing during its propagation through the preplasma, which increases its intensity connected to the lower volume of the laser field immediate interaction [139]. The prepulse energy is absorbed mainly in the region close to the critical density surface. When the target is as thin as possible to form the preplasma at the target front side but at the same time keep the step-like density profile at the rear side, it results in the strengthen electron heating leading to the heat transport because of the thermal conductivity towards the overcritical density region and finally to the ion energy enhancement [129], [142]. The exact parameters of generated preplasma (e.g. its length, density gradient and profile) are important for laser-driven acceleration efficiency as well [72], [138], [265], [266], [267].
In the previous subchapters, the targets with step-like density profile were studied. In real experiments, the relatively sharp density boundary with nearly no preplasma at the target front can be reached by implementing so-called plasma mirrors [128], which are the targets undergoing ionization when interacting with a laser prepulse. Then, the prepulse-affected plasma mirrors turn to be opaque for the main laser pulse which is reflected from their surface. Therefore, these components allow to filter-out laser prepulse(s) without significant lowering of the laser main pulse intensity. Even though this idea is elegant, the experimental set-up is relatively expensive and demanding to be implemented in small vacuum chambers. Therefore, the investigation of laser-driven proton acceleration from targets with preplasma is truly interesting. For the purpose of this work, the effects of preplasma on laser-driven proton and ion acceleration will be studied in 2D for the channel target design.
Firstly, the interaction of the specific laser prepulse with the channel target having a step-

like density profile (i.e., the design shown in Fig. 4.1 (d)) was modeled by our colleagues [2] from The Keldysh Institute of Applied Mathematics (Russian Academy of Sciences). The simulation was performed by the 2D MHD code 3DLINE, [268], [269] and the physical model includes equations of one-fluid one-temperature hydrodynamics taking into account thermoconductivity and radiation transport. The thermodynamic functions as well as optical transport coefficient for the laser pulse were calculated in THERMOS code [270]. Secondly, the resulting 2D output in the form of electron density was fitted along the laser propagation axis by the combination of exponential functions (see the section 4.8.1) and then used as an input in a new 2D PIC simulation, where the interaction of the main laser pulse with the already modified channel target was performed afterwards.
In the following chapters, the comparison of the particle beams accelerated by the same main laser pulse from the identically shaped channel target having (i) a step-like density profile or (ii) preplasma (generated by the laser pulse) on its front side is presented.

4.8.1 Preplasma created by simplified laser prepulse: MHD input

The laser prepulse used in MHD simulation had a square shape, the duration $t_0 = 0.5$ ns and a transverse Gaussian profile. The peak intensity on target was $I_p = 10^{11}$ W/cm^2 (see the bottom part of Fig. 4.34), which would, in the case of L3 HAPLS laser, give the laser contrast between $\sim 10^{10} - 10^{11}$. Such value is in a good agreement with the real situation. The following radial intensity profile of the pedestal was used:

$$I_p(r, t < t_0) = I_p \exp(-\frac{4r^2}{D^2} \ln 2), \tag{4.1}$$

where r is the radial coordinate used in the simulation and $D = 5$ μm is the laser beam diameter (FWHM).
In order to simplify the input for 2D PIC simulation, 2D electron density obtained after the interaction with the laser prepulse (see Fig. 4.34) was fitted along the laser propagation axis (i.e., vertically in the middle of the channel target) with a linear combination of exponential functions. Specifically, the fit consists of one exponential (the prevailing overall trend) and two Gaussian functions (two fluctuations at low electron densities), see Fig. 4.35 (a). In fact, this shape corresponds to experimentally observed preplasma density profile [271] which cannot be generally described by one exponential function only (even though it corresponds to the fast drop near the target surface) and it contains the fluctuations at low densities further from the target front surface as well. The preplasma satisfying the fit was added at the front side of the original target and loaded into PIC, see the proton density of such target before the interaction in Fig. 4.35 (b). Since the preplasma was attached to the unperturbed target, the number of numerical macroparticles were artificially enhanced, specifically by 60%. Particle weighting is implemented as well as in the previous simulations. The scale length of the preplasma [19], [132] varies along the fit, but it is always lower than 1 μm. Moreover, low density preplasma below 0.1 n_c was cut out, which results in the overall preplasma length of ~ 6 μm. The boundary of one tenth of critical density ($n_c = 1.73 \cdot 10^{27}$ m^{-3}) was chosen in order to assure proper conditions for the electron heating mechanisms.

[2] Gennadiy Bagdasarov, Pavel Sasorov, Vladimir Gasilov, Olga Olkhovskaya, Alexey Boldarev, Ilia Tsygvintsev

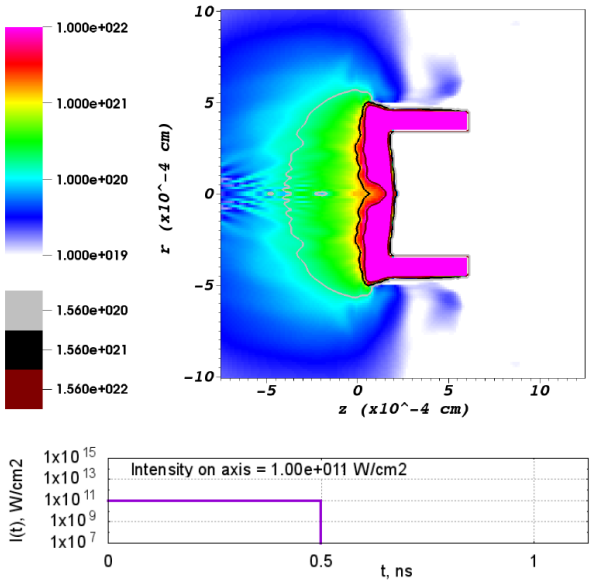

Figure 4.34: 2D electron density output from MHD simulation of the channel target interaction with the square laser prepulse (having the intensity of $I_p = 10^{11}$ W/cm^2 and the duration of $t_0 = 0.5$ ns).

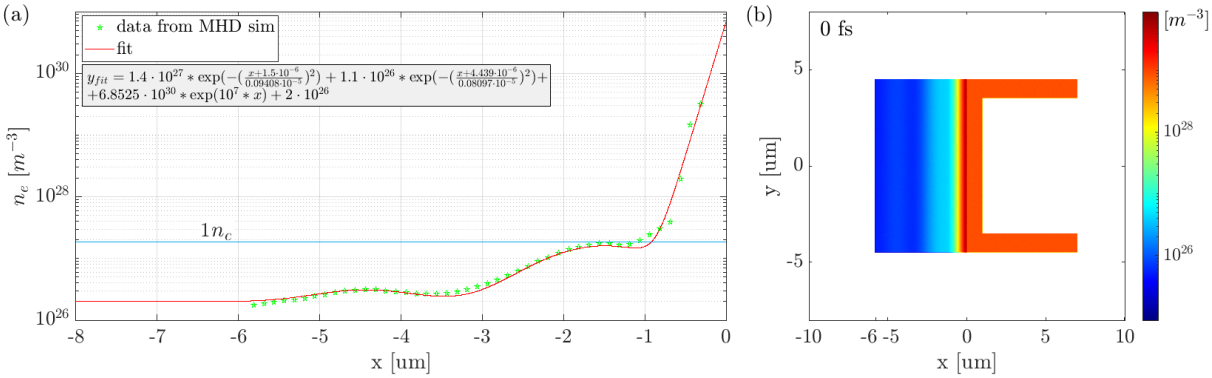

Figure 4.35: (a) Electron density profile originated from the interaction of the laser prepulse with the channel-target plotted along the laser propagation direction; green stars corresponds to the electron density values simulated by MHD, the analytical fit (used as the input in PIC simulation) is plotted in red. The blue line indicates the critical density; (b) 2D PIC simulation area showing the proton density of the channel target with preplasma implemented by the fit (b) before the laser-target interaction.

4.8.2 2D PIC simulation of laser interaction with already expanded channel target

As specified in the previous section, the electron density output from MHD simulation visible in Fig. 4.34 was fitted along the laser propagation axis and the resulting analytical function were used as the input for initial preplasma densities in the new 2D PIC simulation. Since the preplasma was attached to the unexpanded target front side, the number of particles was artificially enhanced. Therefore, when referring to the proton number in the following results, the relative ratio (i.e., the ratio between the numbers of particles having particular parameters, for example, the energy above specific values) is presented instead of absolute values. All other simulation parameters remain the same as in previous studies and they are summarized earlier in Tab. 4.1.
When referring to the specific time scan, the number of femtoseconds *after the start of laser-target interaction* is used, as in all previous sections. Nevertheless, this value corresponds to the case when only vacuum was present at the target front side. Due to the presence of preplasma, the laser pulse interaction with the overdense front side of the target is slightly retarded ($\sim$ 10 fs) as it was slowed down during the propagation through mainly underdense plasma and moreover the reflection point is slightly shifted due to the overdense preplasma slab. Nevertheless, in order to compare the results easily, the same time notation was used for the preplasma target case (i.e., no time shift in the case of preplasma was taken into account), even thought it does not refer to "the start of laser-target interaction" anymore.

4.8.2.1 Energy & Number of particles

When the preplasma was present at the front side of the channel target, the maximum proton energy slightly increased in comparison to the case without preplasma. Particularly, it rose from 95.7 MeV to 102.2 MeV, i.e., by less than 10%. The carbon ions energy stayed nearly unchanged, i.e., $\sim$ 21.5 MeV/amu (with the difference below 2%). In fact, the increase of maximum proton energy is in correspondence with previously published results, where the ion energy was enhanced when the optimal target thickness (meaning a relatively thin target with a sufficiently long preplasma at the front and a step-like density profile at the back side) was implemented [129], see the section 2.2.2.
In the performed PIC simulation, the "optimal" situation was caused slightly artificially, because the preplasma was attached at the front side of the unexpanded original target. In fact, this simplification is tolerable, because the MHD-simulated electron density at the rear side of the target was orders of magnitude lower than that present on the front side. This supports the correctness of the obtained trend of the results. Nevertheless, the maximum energy was not enhanced significantly, because, for instance, the laser main pulse has not been self-focused in the relatively short preplasma sufficiently (as discussed later), see Fig. 4.39. Therefore, the pulse intensity was increased only slightly as well as the maximum proton energy. Furthermore, the artificial choice of placing the original target (i.e., anyhow modified by the laser prepulse) behind the preplasma further limited the ion energy enhancement, because of the overall higher thickness of the target.
Corresponding particle energy spectra are shown at the end of the simulations (i.e., at 270 fs after the start of laser-target interaction) in Fig. 4.36, where also the flat target was added as a reference. All plots show a similar shape with a *bump* in the proton spectrum located around the maximum energies of carbon ions. The origin of this phenomenon was already

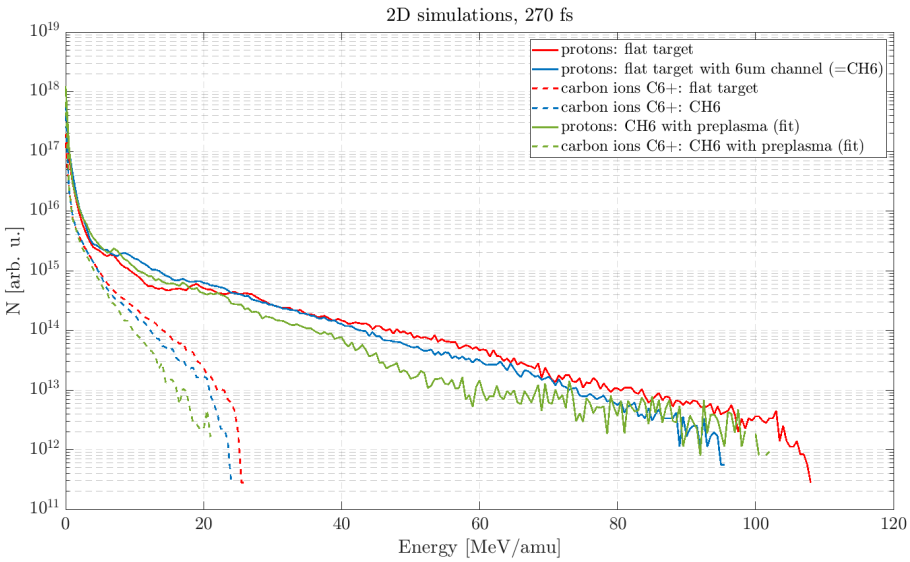

Figure 4.36: Energy spectra of protons (solid lines) and carbon ions (dashed lines) taken at the end of of 2D PIC simulations, i.e., at 270 fs after the start of laser-target interaction. Three target designs are included in the comparison: the original step-like density channel target with 6 μm long channel (blue spectra), the same channel target with preplasma on its front side (green spectra) and the reference flat foil (red spectra).

described in the section 4.5. In short, it is connected to the repulsive forces between the proton and the carbon ion clouds, thus it is natural, that the presence of preplasma does not make a big difference.

2D simulations	protons				carbon ions			
	$N_{10}/N_{0.5}$		N_{10}/N		$N_{10}/N_{0.5}$		N_{10}/N	
	[-]	relative to CHT	[-]	relative to CHT	[-]	relative to CHT	[-]	relative to CHT
channel target (=CHT)	0.178	100%	0.037	100%	0.034	100%	0.003	100%
preplasma + channel target	0.144	81 %	0.016	42 %	0.016	46 %	0.0007	23 %
flat target	0.195	110 %	0.071	192 %	0.052	153 %	0.011	367 %

Table 4.8: Comparison of particle numbers obtained from 2D simulations of the channel target with or without preplasma and of the reference flat foil. N_{10} is the number of protons/carbon ions moving forward ($p_x > 0$) and having energy above 10 MeV/amu; $N_{0.5}$ is the number of protons/carbon ions moving forward ($p_x > 0$) and having energy above 0.5 MeV/amu; N is the total number of protons/carbons present in the simulation area. The ratios between these numbers are shown as dimensionless values as well as relative numbers in comparison to the channel target having the step-like density profile. All data are taken at the end of simulations, i.e., at 270 fs after the start of laser-target interaction, and the particle weighting are taken into account.

It is expected that the energy enhancement in the case of preplasma target compared to the intact one will be lower in 3D because of the additional dimension where hot electrons, responsible for the establishment of accelerating electric field, can spread. This would lower the electric sheath field and consequently also particle energies, which is in agreement with the results already obtained from previous comparisons of 2D and 3D simulations presented earlier in this work.
Even though that all energy spectra in Fig. 4.36 have a similar shape, the clear tendency of decreasing particle number with preplasma (as well as with overall rising area occupied by the target) is evident. That is attributed to the changes in the laser interaction with underdense or slightly above critical preplasma. In fact, the laser pulse accelerates electrons from a larger volume and to the higher temperatures in the case of preplasma in contrast to the highly overdense step-like density targets. On the other hand, these preplasma electrons are worse confined and their recirculation is more chaotic [142] and not as efficient when the density profile is not sharp. Depending on the particular parameters of the preplasma, both the lower [72], [135], [265], [272] and the higher [137], [138], [266], [267], [273] laser absorption efficiency resulting in suppressed or enhanced proton acceleration have been reported. The basic difference lies in the reaching optimal or non-optimal plasma density gradients and the overall preplasma length which can leads, for example, to the self-focusing of the laser pulse as well as to its filamentation. In the simulation presented here, the laser pulse gains a slightly higher intensity due to self-focusing phenomenon and, therefore, it heats electrons to the higher temperature (as discussed later in subsection 4.8.2.3 and 4.8.2.2), but their recirculation is not optimal. This results in only a small increase of proton energy, which is accompanied with the particle number lowering.
The relative numbers of particles accelerated from the preplasma and from the intact targets are compared in Tab. 4.8. There, the ratio $N_{10}/N_{0.5}$ evaluating the number of protons moving forward ($p_x > 0$) and having the energy above 10 MeV to the number of protons moving forward and having the energy above 0.5 MeV is used. The value of this ratio for the channel target with preplasma reached only 80% of the value for the original channel target with the step-like density profile. When the protons above 10 MeV are compared to the overall number of protons N present in the simulation area (noted as the ratio N_{10}/N), the value was further reduced to its half (i.e., $\sim 40\%$), because of the larger amount of the material in the case of preplasma target. The same trend has been observed for carbon ions. For comparison, the reference values of the flat foil are presented in Tab. 4.8 as well.
In fact, the proton energy spectrum form a flat-like shape around mid-high energies above 50 MeV, see Fig. 4.36. This is caused by the protons accelerated from the target front side which gain slightly higher energy when the preplasma was present, see phase space section, specifically Fig. 4.43. In other words, the front-side originated proton population enhances the number of protons with relatively high energy which results in the more flat-like spectrum than in the case of the step-like density profile target. This is connected to the shape of accelerating field (having higher values in front of the overdense target in the preplasma case) discussed in the following section.

4.8.2.2 Accelerating field and hot electron temperature

The tendency of forming flat-like energy spectrum profile in the case of preplasma target originates from the formation of higher accelerating field at the target front side, i.e., inside the preplasma, accompanied with the lower field at the target back side. That was caused

by the higher amount of electrons accelerated from the preplasma/front side of the overdense target. The shape of accelerating field profile is visible in Fig. 4.37 (particularly at 30 fs), where the extended time evolution of E_x along the laser propagation axis is shown for the reference flat foil (red), for the channel target with step-like density profile (blue) and with preplasma at its front side (green).

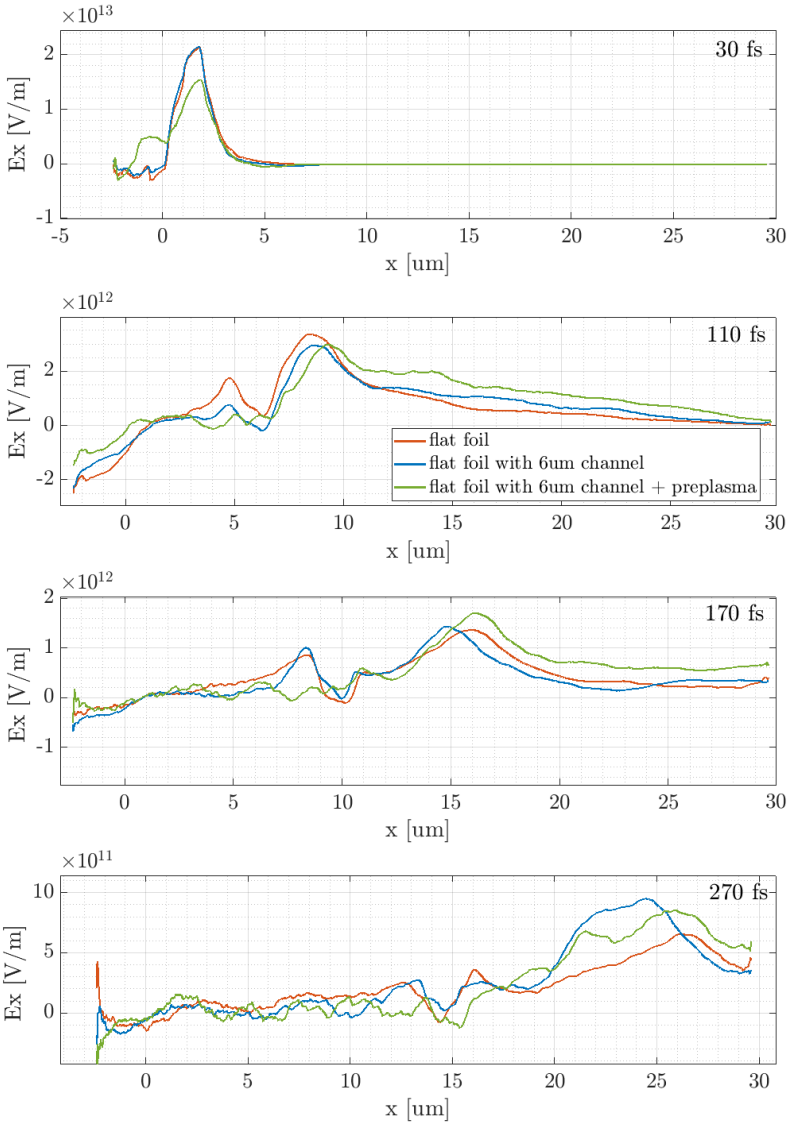

Figure 4.37: Time evolution of accelerating electric field E_x along the laser propagation axis. The field profiles are presented for the reference flat foil (red), the channel target with step-like density profile (blue) and the channel target with preplasma on its front side (green) at various time scans: $30, 110, 170$ and 270 fs after the start of laser-target interaction.

As visible, adding the preplasma at the channel target front does not change the evolution of the field shape significantly, nevertheless the slight tendency of higher values can be observed on the laser axis at 110 and 170 fs. Moreover, as already demonstrated earlier (see the section 4.7.1.1 and Fig. 4.27), the accelerating field of channel targets is stronger further from the

target back side than the accelerating field of the reference flat foil at the same place, see Fig. 4.37 for 270 fs. Preplasma did not change this tendency. Generally, accelerating field is crucially affected by the hot electron component, whose parameters differ depending whether the preplasma is present on the target front side or not. In Fig. 4.38, both energy spectra of hot electron populations accelerated from the intact (red) and from the preplasma channel (blue) targets are present and they form a typical bi-Maxwell electron distribution as described in the section 1.3.2. Since the scope of the less steep part of the spectrum characterizes the hot electron temperature, we can clearly observe that it is higher for the preplasma case, particularly $\sim$ 17.6 MeV. The temperature of hot electrons accelerated from the step-like density target was evaluated to 11.3 MeV, which corresponds to approximately 55% rise in the electron temperature when the preplasma is present on the target front side. This result should be taken rather like a tendency, since the estimation of exact numbers is not easy due to the high fluctuations. The spectra were analyzed at 50 fs, i.e., at the time when the peak pulse has already interacted with the target, and only electrons spatially located at the target rear side or further were taken into account.

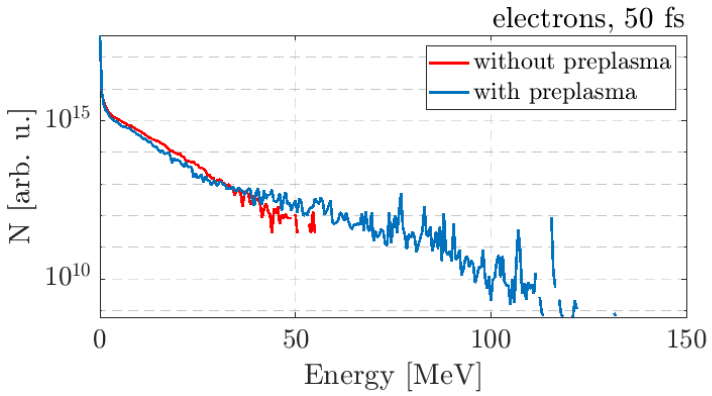

Figure 4.38: Comparison of electron energy spectra for the channel target with preplasma (blue spectrum) and without preplasma (red spectrum) at 50 fs after the start of laser-target interaction. Only electrons located at the rear side of the targets and further were taken into account.

4.8.2.3 Changes in laser pulse interaction with target due to preplasma

The interaction of the main laser pulse with the channel target naturally differs whether the target has already interacted with the laser prepulse or not (i.e., whether the preplasma is present). For example, the critical power condition (2.1) for optical channeling and self-focusing is fulfilled for the used laser parameters, hence, the main pulse undergoes self-focusing when it enters the preplasma on the target front side. In fact, the simulated preplasma was relatively short, having only 6 μm in total (because the electron densities below 0.1 n_c were cut out), therefore the self-focusing was not massive. Nevertheless, as far as it can be estimated from the limited time resolution (20 fs time step), the laser focus was reduced from originally 3 μm to less than 2 μm in diameter, see Fig. 4.39 (a), where the self-focused laser pulse is shown in detail at 10 fs for both density profile cases. The mesh is added into the figures in order to simply approximate the dimension of the laser self-focus by eye. In fact, due to the shrink in focal spot size, the temporal and spatial growth in the laser intensity was observed

in the simulation, specifically from originally $I = 5 \cdot 10^{21}$ W/cm^2 (i.e., the electric field of $\sim 1.95 \cdot 10^{14}$ V/m) to $I_{SF} = 8 \cdot 10^{21}$ W/cm^2 (i.e., the electric field of $\sim 2.5 \cdot 10^{14}$ V/m). That is the enhancement by 160% in the temporal growth of the laser pulse intensity corresponding to the factor of $\beta = 1.6$. It is worth mentioning, that the numbers were carefully taken from the 2D PIC simulations before the incident and the reflected light of the laser pulse started interfering, i.e., before the intensity was increased further due to the created standing wave, but not because of self-focusing. Nevertheless, it is expected that in 3D geometry the self-focusing and corresponding growth in the laser intensity will be even stronger (by the factor of $\beta^2 \sim 2.5$, i.e., up to the intensity of $1.25 \cdot 10^{22}$ W/cm^2), due to the additional dimension in which the laser pulse has to be self-focused; see more about the self-focusing phenomenon in the section Relativistic self-focusing of laser pulse. That is in great correspondence with the simple theoretical calculation: Since the parameters of the laser pulse stayed unchanged for both the simulations (i.e., with the intact and with the expanded channel targets), the power of the *original* and the *self-focused* main pulse is the same, when no filamentation of the incoming light, and thus no depletion of the laser energy, occurs, i.e., $P_{SF} = P_{orig}$. Under this assumption, the relation for comparing the intensities of the standard and the self-focused pulses having the same power but various focal spots in 3D geometry is following:

$$I = P/S = P/(4\pi r^2) \qquad \rightarrow \qquad \frac{I_{SF}}{I_{orig}} = \left(\frac{r_{orig}}{r_{SF}}\right)^2,$$
$$I_{SF}^{3Dtheory} = 4 \cdot I_{orig} \approx 1.125 \cdot 10^{22} \text{ W/cm}^2,$$

where $2 \cdot r_{orig} = 3$ μm and $2 \cdot r_{SF} = 2$ μm. It is worth mentioning that $\left(\frac{r_{orig}}{r_{SF}}\right)^2 \approx \beta^2$.
Naturally, the self-focusing of the pulse can be beneficial for acceleration of particles. Even thought the preplasma was relatively short in our case and it was attached to the overdense target with no pre-expansion (which would be there in reality), the small increase in the maximum energies of protons was observed in correspondence with theory, as discussed earlier in the sections 4.8.2.1 (PIC+MHD results) and in The impact of generated preplasma on laser-driven particle acceleration (theory).
The backscattering of the laser pulse is affected by the shape modification of the front target surface, which was slightly more concave in the preplasma case. That led, together with the rest of preplasma, to the smaller "focal spot" of the backscattered light and correspondingly stronger defocusing, see Fig. 4.39 (b) and (c) showing the backscattering and the interference of the incident and the reflected light at 30 fs and 50 fs, respectively. In fact, the interference of the laser light results in a standing wave which is important for acceleration of electrons. These electrons can moreover gain higher energy when the preplasma has a longer scale length [142]. This is in good correspondence with the results in Fig. 4.38 (see also the previous section 4.8.2.2), where the tendency of the higher energy of hot electrons was obtained for the preplasma target case, even though the scale length was relatively low (less than 1 μm).
As already mentioned in the beginning of this section, the information about the time scan is always given after the start of laser-target interaction when the preplasma was NOT present. In fact, the pulse was slightly retarded when it had to propagate through the preplasma, which consists from both underdense and overdense parts. For example, the retardation of the propagating radiation is well noticeable in Fig. 4.39 (a), where the laser pulse propagating in the preplasma has not reached the front side of the overdense layer, even though the pulse propagating through the vacuum already has. Furthermore, the location of the main reflection point, where the majority of the laser light has been backscattered, differs by low hundreds

of nm between the preplasma and the step-like density channel targets. In the case of the step-like density profile, the light is naturally backscattered at the front side of the inwardly-pushed target surface (≈ 0.2 μm), whereas in the case of preplasma, the reflection point was shifted towards the laser pulse (≈ -0.2 μm). The overdense region of the preplasma was relatively thick (~ 1 μm, see Fig. 4.35 (a) where $n_c = 1.73 \cdot 10^{27}$ m^{-3}), but the temporal rise in the laser intensity due to the self-focusing let the laser pulse penetrate further. That is partly illustrated in the comparison of detailed electron density plots between the preplasma and the step-like density profiles at early stages of acceleration in Fig. 4.42 in the following section 4.8.2.5.

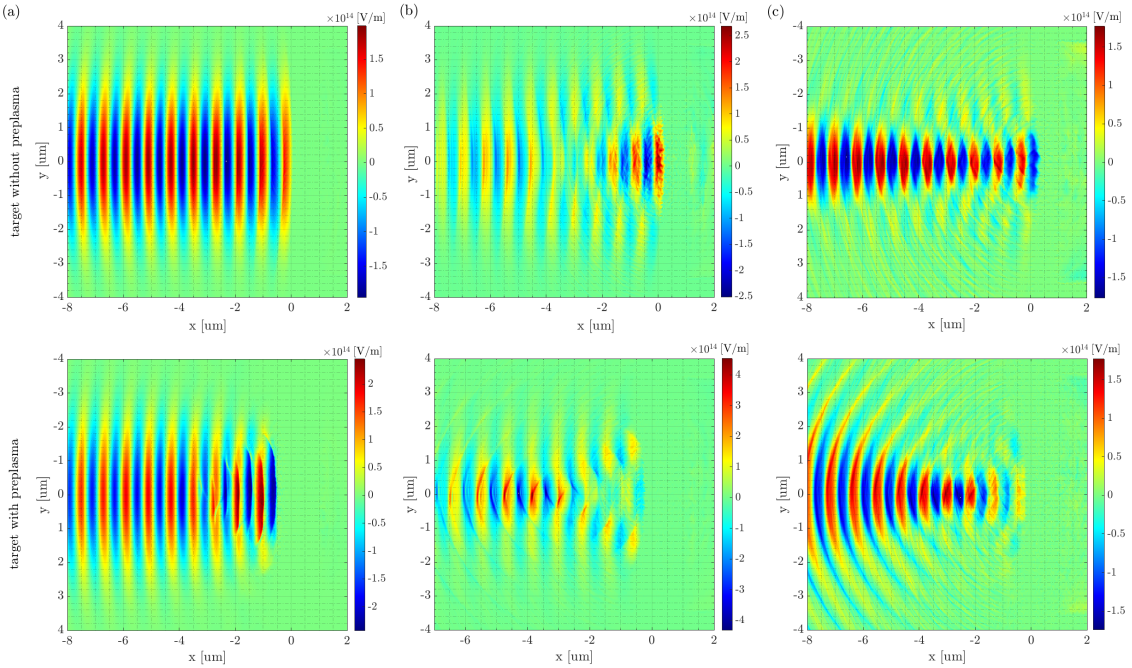

Figure 4.39: Electric field E_y showing the time evolution of laser pulse propagation without and with preplasma on the channel target front side – the self-focusing, the backscattering of the pulse as well as the interference of the incident and reflected light can be observed. The front side of the target is located at 0 μm, whilst the preplasma (if it is present) starts at ≈ -6 μm (electron densities below 0.1 n_c were cut out). The case (a) shows the situation at 10 fs, (b) at 30 fs and (c) at 50 fs after the start of laser-target interaction when the time of interaction is related to the pulse propagation in vacuum.

4.8.2.4 Particle divergence

The presence of preplasma naturally affects the angular spread of accelerated protons as well. Obtained proton half-angle divergences (measured in FWHM) are summarized in Tab. 4.9; only particles moving forward ($p_x > 0$) in the various space cuts around the laser propagation axis (i.e., within $y \pm 0.5$ μm or no space cut in y) and having the energy above 0.5 MeV were analyzed. In fact, the space cuts were applied in order to distinguish the behavior of the large particle cloud and of the protons propagating along the laser axis only, similarly as in the previous simulations. It was found, that the proton divergences in both spatial

cuts were slightly increased when the preplasma was present at the target front side, see the comparison in Tab. 4.9 and the angular plots in Fig. 4.40. The more significant change in angular profiles was observed in the case of on-axis proton beam (i.e., ± 0.5 μm), which is assigned to the higher angular spread of hot electrons generated in the preplasma compared to the spread of electrons generated in the vicinity of the focal spot at the front side of the step-like density target. The works [132], [133], [134] demonstrate that the laser-generated hot electron divergence increases approximately linearly with the preplasma scale length for a fixed laser intensity. This can be explained by a larger interaction volume being available for longer scale lengths. Nevertheless, the combined profile of relatively short preplasma (~ 6 μm) simulated here is characterized with the relatively short scale length lower than 1 μm, which is the reason why particle divergence did not increase more. It was also demonstrated [132], that the various laser intensities between 10^{18-21} W/cm^2 had nearly no effect on the electron divergence. Therefore, the temporal rise of the laser intensity observed in the preplasma due to self-focusing does not affect the hot electron spread significantly.

Half-angle *protons* divergence in FWHM [°]		
Channel target having:	no space cut in y	cut in $y \in \langle -0.5; 0.5 \rangle$ μm
step-like density profile	8.4	1.8
preplasma on its front	8.6	2.5

Table 4.9: Half-angle divergences (measured in FWHM) of protons accelerated from the flat channel target (6 μm long straight channel) with the step-like density profile or with preplasma generated due to the interaction with laser prepulse; 2D simulations. The different space cuts around the laser propagation axis were applied and only protons moving forward ($p_x > 0$) having the energy above 0.5 MeV were analyzed.

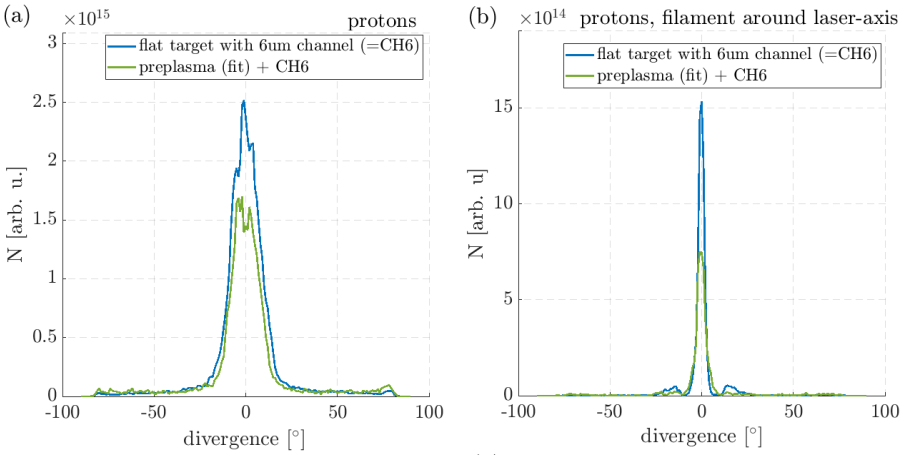

Figure 4.40: Comparison of proton divergences analyzed for the intact channel target (blue) and for the same target, but with preplasma on the front side caused by the laser prepulse (green). The angular plots show the spread of forwardly-moving protons ($p_x > 0$) above 0.5 MeV when (a) no space cut or (b) ± 0.5 μm cut around the laser propagation axis was used, respectively. The plots are presented at the end of the 2D simulations, i.e., at the 270 fs after the start of laser-target interaction.

On the other hand, the total number of accelerated particles is lower in the case of the target with preplasma compared to the target with step-like density profile. This was caused by the difference in electron heating between preplasma and step-like density cases. Whereas the electrons originated from the step-like density target were heated in the vicinity of laser focal spot by $\vec{j} \times \vec{B}$ mechanism; in the case of preplasma, hot electrons are accelerated at the front of the laser pulse and in the standing wave created by the incident and the reflected pulse. Their confinement is nevertheless weaker and the recirculation more chaotic [142] than in the case of step-like density profile. The corresponding preplasma particle number lowering is more significant in the case of on-axis filament, because the not optimal confinement of hot electrons is naturally visible the most on axis.

4.8.2.5 Particle densities and phase spaces

The proton density plots, presented in logarithmic scale in Fig. 4.41, nicely summarize the previously mentioned differences between the preplasma and the original channel target cases. For example, (i) the small deviations in inwardly-shaped front target surface due to the laser radiation or (ii) the higher divergence of the proton cloud and (iii) the formation of multiple particle filaments (visible in angular plots Fig. 4.40 (a)) can be observed in the case of the channel target with preplasma compared to the target with the step-like density profile. Also, the compressed electron slab at the preplasma/target boundary or more bell-shaped electron beam formation in the case of the original step-like density target are demonstrated in the detailed comparison of electron densities in Fig. 4.42 (particularly, in the case (c) at 30 fs or (b) at 90 fs after the start of laser-target interaction, respectively).
The proton phase spaces of the intact and the preplasma versions of the channel target can be compared in Fig. 4.43, where the early stage of the acceleration process (i.e., at 90 fs) as well as the situation at the end of the simulation (i.e., at 270 fs after the start of laser-target interaction) are shown. Plots (a), (b) demonstrate the proton acceleration along the laser propagation axis at various time scans. The overall structure of the phase spaces $v_x - x$ is the same, no matter if preplasma was present or not. One population of protons is accelerated from the front side of the target, two populations from the rear side (they merge together with time) and one from the channel endings. This had been already seen and reported from the energy-resolved proton densities (the section 4.5.2, e.g. Fig. 4.20) and from the electric field profile (the section 4.7.1.1, e.g. Fig. 4.27). The low energy protons located approximately between $1 - 7$ μm in Fig. 4.43 (a) originate from the channel surface and do not contribute much to the main accelerated beam. In fact, the biggest difference between the intact and the preplasma channel targets, which has been observed in phase spaces Fig. 4.43 (a), is connected to the energy increase of the protons accelerated mainly from the front side of the preplasma target, although the small enhancement is visible also in other proton populations. The enhanced front-proton population is the result of the higher accelerating field located in front of the preplasma target discussed earlier, see Fig. 4.37. It causes the more flat-like shape of the proton energy spectrum in comparison to the spectrum shape produced by the step-like density target, see Fig. 4.36. Nevertheless, the maximum energy was gained by the protons accelerated from the rear side for both target cases.
Naturally, the higher amount of backward-accelerated protons is visible in the phase spaces Fig. 4.43 when the preplasma is present at the target front side, even though their velocity in $-x$ direction is lower than that of protons accelerated from the step-like density target case. The difference lies in the area from which the hot electrons are accelerated. When the

laser pulse is propagating through the preplasma, the electrons are heated in front of the pulse as well as in the surrounding volume. On the other hand, when the target has the step-like density profile, hot electrons are generated only in the vicinity of the focal spot by $\vec{j} \times \vec{B}$ mechanism. Therefore, the accelerating field formed by the electrons escaping towards the laser pulse has wider spread in the case of preplasma, contrary to the accelerating field of the step-like density target. There, the electrons originate from the limited area which results in stronger, well-localized and well-developed electric sheath field [274]. This leads to the higher energy of backward-accelerated protons from the target without preplasma, which move preferably along $x-$axis in the negative direction. That is, for example, visible in the comparison Fig. 4.43 (a), (b) for various time scans. Furthermore, as observable in phase spaces $v_x - v_y$ in Fig. 4.43 (c), (d), the protons, which were backwardly accelerated from the step-like density target, have also lower velocity along the transverse $y-$axis in comparison to the preplasma case. The shorter expansion along $-x$ as well as the wider proton spread in the case of preplasma can be seen additionally in the proton density plots in Fig. 4.41.

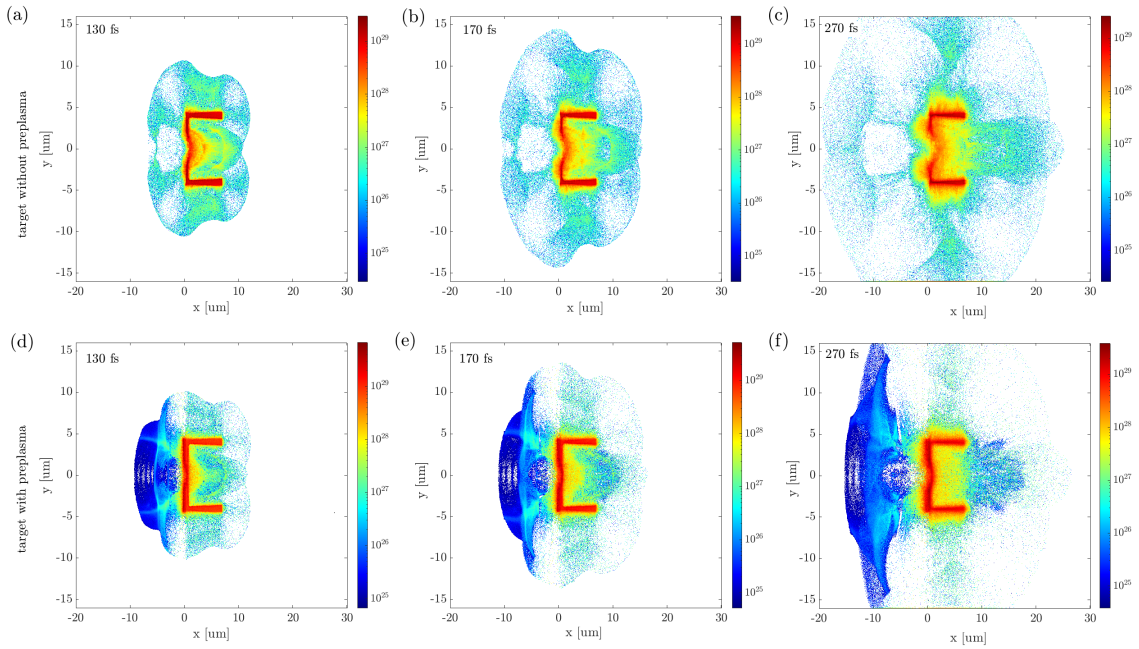

Figure 4.41: Time evolution of proton densities of the flat target with narrow 6 μm long channel having (a) – (c) step-like density profile (i.e., without preplasma) or (d) – (f) preplasma on its front side. The figures are plotted in logarithmic scale. Each column shows a different time scan: at 130 fs, 170 fs, and at 270 fs after the start of laser-target interaction (from left to right).

The mentioned $v_x - v_y$ phase spaces in Fig. 4.43 (c), (d) show the evolution of proton velocities in both horizontal and transverse axes during the acceleration process in the case of the intact and the preplasma targets (the first and the second row, respectively). Therefore, they provide the additional insight to the accelerated particle beam filamentation as well as to the evolution of particle beam divergence. In the case of the step-like density channel target, the protons are accelerated predominantly along the laser-axis and their velocity increases in the horizontal direction ($y-$axis) with ongoing time and the growing distance from the focusing

channel. In the case of preplasma target, the protons form preferably more beams moving away from the laser axis, see multiple *proton filaments* in phase spaces Fig. 4.43 (the cases (c), (d) in the second row) as well as in the angular plot Fig. 4.40 (a) or the density map Fig. 4.41. Although the on-axis protons are still present, their number is lower than in the case of target that was not affected by the laser prepulse. This has been already seen in the angular spread plot analyzed in the tight space cut along the laser axis, see 4.40 (b).

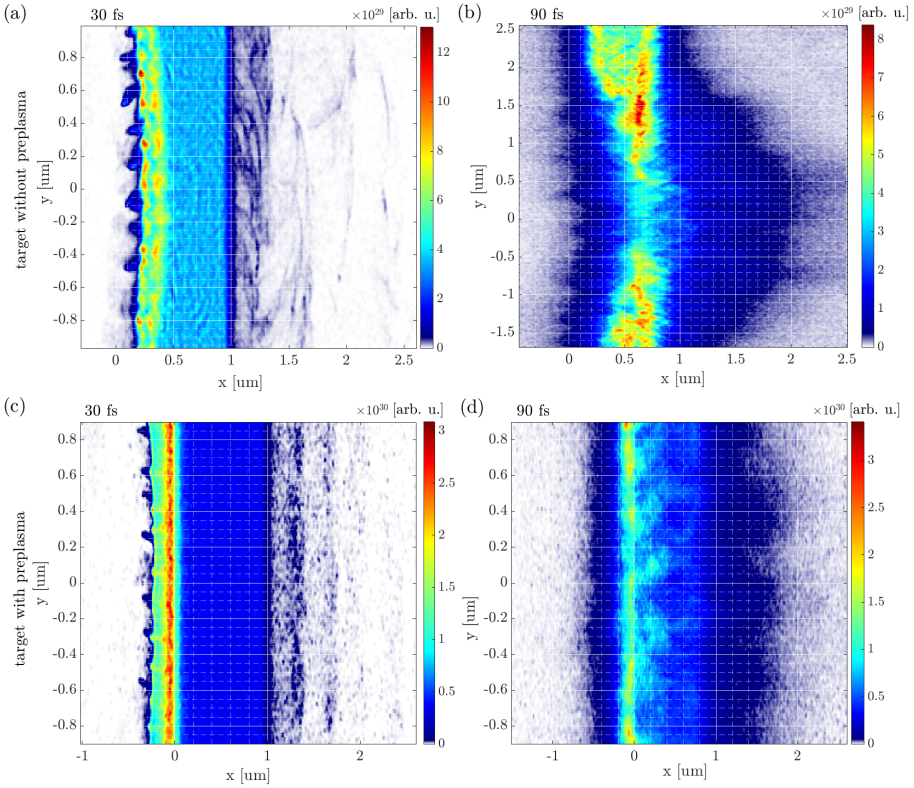

Figure 4.42: Comparison of detailed electron density plots between channel targets with step-like density profile (a) + (b) and with the preplasma on the target front side (c) + (d) at early stages of acceleration, specifically at 30 and 90 fs after the start of laser-target interaction.

To summarize, even though the difference between phase spaces of the intact and the preplasma channel target were observed, they partly blurred in time and no evidence about the presence of any different acceleration mechanism, than those already seen in the case of the step-like density target, was found in the preplasma case.

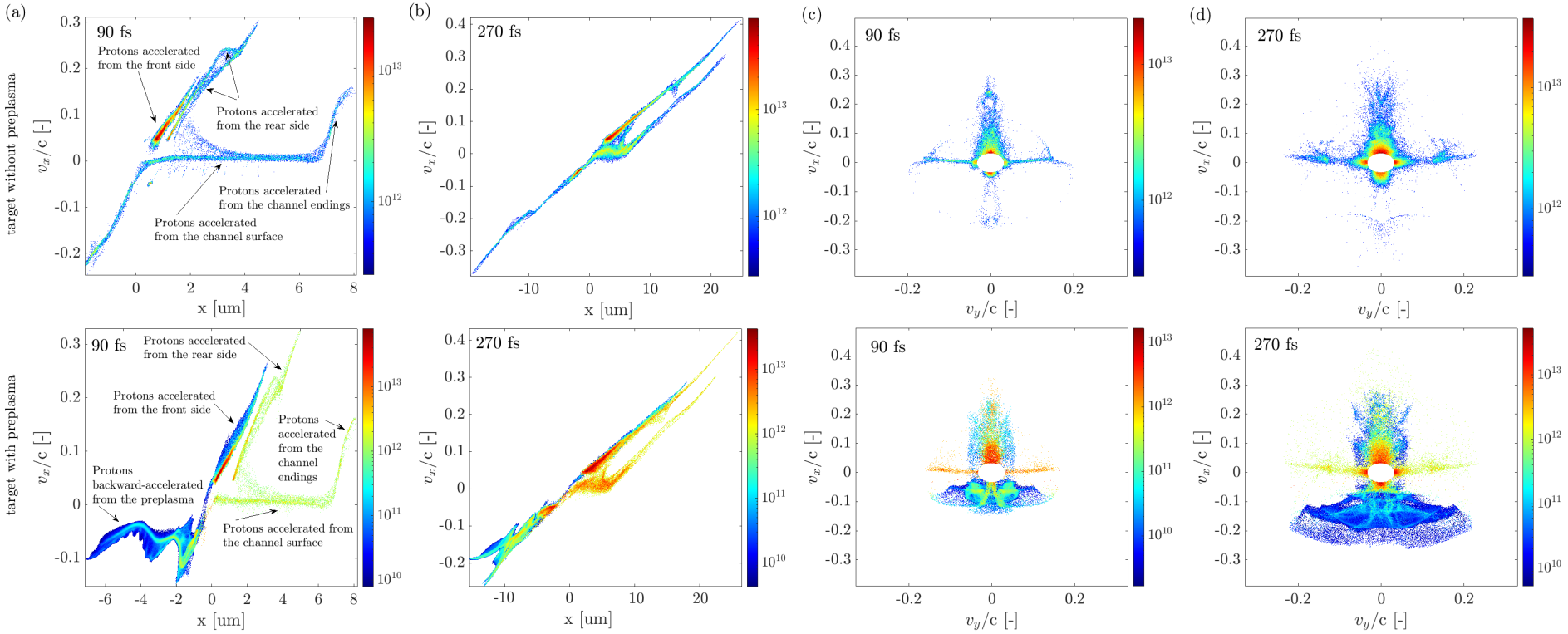

Figure 4.43: Comparison of proton phase spaces $v_x - x$ and $v_x - v_y$ from 2D simulations of the channel targets with step-like density profile, i.e., without preplasma, or with preplasma generated by the laser prepulse on the target front side. Two time scans, specifically, at 90 fs, i.e., (a) + (c), and at 270 fs, i.e., (b) + (d), after the start of laser-target interaction, are shown for both target cases. Only protons having energy above 0.5 MeV (both moving forward ($p_y < 0$) or backward ($p_x < 0$)) are taken into account for the analysis (the cutting of low energies out corresponds to the white circles in the middle of the phase spaces $v_x - v_y$).

4.9 Discussion: Towards future experiments

In order to provide theoretical results which are important and trusthworthy to motivate future experiments, general comments both on the laser parameters and on targets dimensions are provided. Furthermore, the possible manufacturing techniques are commented.

4.9.1 Discussion on the impact of various laser parameters

Although the parametric study on laser parameters is above the scope of this work, some tendencies can be predicted. For instance, if a significantly higher laser intensity is used, the bigger thickness of target plastic material would be needed to avoid full penetration of the laser pulse through the foil. If the laser pulse penetrates the target completely, different accelerating mechanisms as well as diverse establishment of EM fields are expected. The main changes will be connected to the breaking of symmetry, the target decomposing and to the corresponding change in the movement of hot electrons. Contrarily, if the lower laser intensity is used, the lower energy of protons and the weaker EM fields due to the lower temperature of electrons would be expected.
In performed simulations presented within this work, the parameters of L3 HAPLS laser were used. Therefore the results corresponds to the real laser system dedicated to laser-driven proton and ion acceleration user experiments with the possibility to operate at high-repetition rates (up to 10 Hz). Moreover, HAPLS laser system parameters (1 PW, 30 fs, 30 J, 10 Hz) [7] are comparable to other laser systems already used for proton acceleration, for example with GEMINI laser (15 J, 30 fs,) at RAL [275], VEGA-3 (1 PW, 30 fs, 30 J, 1 Hz) at CLPU [276] or J-KAREN-P (PW, 30 fs, 30 J, 0.1 Hz) at QST [11].

4.9.2 Feasibility of advanced channel-like target design

Besides laser parameters, both material and dimensions of the target itself can be discussed. The shape of the cylindrical channel target is crucial for the establishment of well-developed EM fields leading to the reduction of particle beam divergence and to the enhancement of beam spatial uniformity. Hence, it is truly important to keep the rear-placed channel design and also to preserve the similar dimension ratio(s). If the radius of the cylinder would be larger, but the channel length stays unchanged, the EM fields, mainly the magnetic multipole, would be worse confined because of a larger area where hot electrons can be spread. It would rise the difference in the field amplitude between the channel center and along the channel walls which results in less homogeneous EM field-effect on the accelerated particle beam. On the other hand, with longer channel arms and the same cylinder inner radius (which seems to be harder to manufacture), the higher beam collimation is expected because of the higher field integral (i.e., the longer path in the well-defined EM field for particles) and the more optimal ratio between the transverse and the longitudinal dimension of the self-produced *target-magnet* discussed earlier.
In previous works performing channel-like targets, usually two materials were used - a light low-Z material for the target part placed perpendicularly to the laser pulse, and a high-Z material for cylinder/arms/structures [219], [220]. The possible technologies able to fabricate variously structured targets include, for example, Focused Ion Beam (FIB) technique used for milling, deposition, implantation or imaging of various materials over a wide range of length scales. The FIB can produce targets having the thicknesses down to several tens of nm with

lateral dimensions up to ones of cm as well as to provide coating having ones of nm [277], [278], [279]. The example of a ten-by-ten array of holes with the diameter of 500 nm and the period of 1 μm fabricated into a silicon nitride membrane is reported in [280]. There is a possibility to stop milling of the holes before the foil is penetrated completely through, which could be the way how to fabricate the proposed target design, although from different material. Furthermore, the free-standing SiN membranes (hundreds of nm) have been already deposited by a plasma enhanced chemical vapor deposition (PECVD) reactor on a silicon substrate and then lithographically shaped into various gratings and structures by a chemical etching [213], [281]. This indicates possible ways how the suggested channel target design may be produced.

In principle, the single plastic channel target might be also 3D printed as a whole by advanced technologies, which are able to provide sub-micrometer scales resolutions and have been extended from metals to polymer materials lately [282], [283]. The single target is then suitable to be attached to the supporting foil having an aperture, similarly as in [127]. Such target arrangement can be placed repeatedly in the target tower [6], which is be able to switch the targets even at relatively high repetition rates enabled by ultrashort-pulsed laser systems.

Generally, each target material brings different advantages (e.g., higher energy of protons, suitability for high repetition rates experiments, vacuum compatibility, pure materials, debris free interaction) and suffers from various difficulties (e.g., hard possibility of shaping, handling and stabilizing, extra equipment present in a vacuum chamber). Therefore, the usage of plastic targets performed in our simulations is not the strict condition which has to be fulfilled in future experiments. In fact, the simulations should primarily demonstrate the physical principles, which are not strictly bounded to the plastic material only. Nevertheless, plastic targets provide the accelerated proton beam of satisfactory parameters in return for sufficient balance between the vacuum compatibility, material availability and target handling & stability (which is important, e.g., for positioning of the laser focus on a target front surface).

Chapter 5

Possible applications of laser-driven ion beams

Wide range of foreseen applications of laser-driven ion beams has been discussed over the years. For example, the list includes 'fast ignition' of ICF targets [151], [284], laser triggering and control of nuclear reactions [285], [286], [287], material science [1], [2], chemistry (e.g. proton pulsed radiolysis [288]) or non-destructive testing used in archaeological [3], [4], [289] and possibly also in botanical [290], enviromental [291], [292] and other fields of interests. Also, huge efforts have been made in investigation of various medical treatments performing laser-accelerated ions (e.g. hadrontherapy [293], [294], [295], [296], proton-boron capture therapy [297]) as well as in other medicine-related research such as radiographic and dosimetric studies [2], [298], [299], [300]. In the following chapter, a few representative examples of laser-driven ions beams applications, in which the author of this thesis has been partially involved, will be discussed.

5.1 Hadrontherapy

One of the most discussed application of laser-accelerated ion beams is laser-driven hadrontherapy. Hadrontherapy is already known radiological technique dealing with treatment of cancerous tumors using accelerated hadrons: protons (better dose distributions), neutrons (better tumor killing), pions and ions (α, C, B, Li). The clinical approach is the same for both conventional and laser based hadrontherapy, thus the "only" difference lies in the method how the accelerated hadrons will be obtained.
Generally, the great advantage of protons or ions is associated with their energy deposition property, i.e., with delivering the most of their energy at the end of their path during propagation through healthy tissue surrounding a tumor. In contrast to photons (X-rays), protons show an increasing energy deposition with the growth of the penetration distance. Therefore, it is mainly the tumor that is treated. Protons lose their energy in atomic or nuclear interactions and they slow down faster than photons, because of their non-zero mass. Consequently, the energy is deposited more sufficiently when protons are decelerated due to the more frequent interactions with material [301]. That is the reason why the end of the proton trajectory (and generally any hadrons trajectory) inside the body is followed by a sharp increase of energy deposit; this characteristic is called *Bragg peak* and it is schematically depicted in Fig. 5.1. Furthermore, there is a possibility to cover the whole tumor volume by

integrating more Bragg curves together, i.e., by using more proton beams of slightly different energies corresponding to slightly different positions of their Brag peaks, see Fig. 5.1. In other words, the proton beam can be precisely shaped ($\sim \mu$m accuracy [302]) in three dimensions in order to fit the tumor precisely.

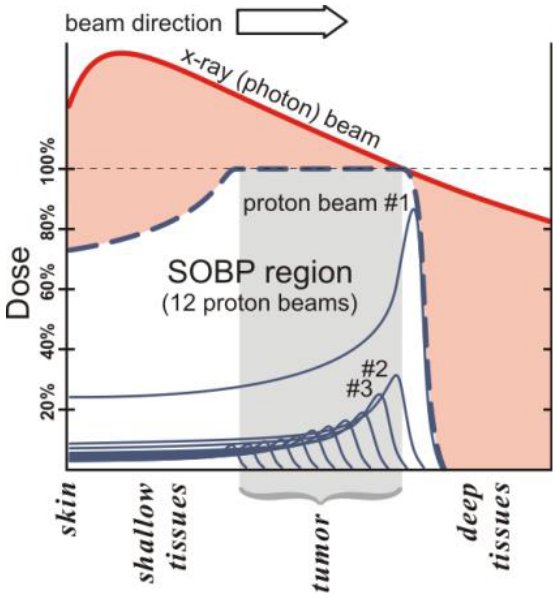

Figure 5.1: Dependence of typical dose deposition on a penetration depth for both proton (grey) and photon (red) beams. A proton beam can be precisely shaped (in three dimensions) to fit the tumor. Making the area of maximum relative dose in required depth wider consists of putting together more energy deposition curves with different space-position of their Bragg peaks. Compared to proton beams, photon beams have greater dose on healthy tissue in front of and behind the tumor [302].

Speaking about the laser-driven cancer treatment, the compact size of laser-based accelerating system in comparison to conventional accelerators is usually given as a huge advantage. In fact, that argument is little bit outdated, because it has been mentioned over long time ($\sim$ 30 years), but the size of conventional systems has been significantly reduced in meantime. The personal opinion of the author of this text is therefore that the advantage of using laser-driven beams lies rather in their variability in the terms of number of particle species which can be accelerated and in the typical exponential spectrum which gives a possibility to obtain various energies (which can be chosen by magnetic chicane [231], [303]) in one configuration. Additionally, no need of a big radiation shielding of bending magnets in the case of laser-driven beamlines are surely advantageous, especially in the hypothesis of an all-optical gantry. Furthermore, although compact conventional proton acceleration systems are currently commercially available, the size of heavier ion (e.g. carbon ions) treatment installations (accelerator, beam transport, shielding, and gantry) are still extremely large. The another often given argument about the reduced cost of future hadrontherapy centers over the conventional ones could be found in a number of papers [294], [304].
Nowadays, tens of hadrontherapy centers have been built worldwide [294], [305], but all of them are based on cyclotron/synchrotron concept, because laser-driven beams still do not fulfill all the physical, biological and clinical requirements. For example, the improvements

towards the higher maximum energy (i.e., reaching the upper range of $60-250$ MeV interval, because with the higher energies, the tumor deeper seated in human body could be treated), monoenergetic features of the beams, low divergence, ... and generally towards the reliability of the laser-driven ion sources have to be done.
To properly investigate *biological effects of ionizing radiation on living cells*, the detailed overview of the interaction between quanta of the radiation and the electron shell of atoms, rarely atomic nuclei, is required. In fact, the irradiation leads to the excitation and ionization of atoms leading to physical changes, chemical reactions and biochemical modifications, which can cause death of both healthy and tumor cells. Studies dedicated to the biological effect of laser-driven ions on living cells have already been abundantly performed [294], [306], [307], [308] and are planned at ELI Beamlines with Proton pulsed radiolysis of water experiments, firstly investigating the early time physical/chemical interactions in $\sim ns$ time scales. This work would be crucial for laser-acceleration community, because it would confirm if the laser-accelerated protons have the same impact on living cells as the conventionally accelerated ones or not. Generally, it is very probable that if an ultra high dose rate effect exists it must be bounded with specific early time physical interactions (e.g. ionization, excitation and generation of radicals). In fact, even though the first studies claimed, that the effect of laser-driven radiation at an ultra-high dose rate does not likely differ from that of radiation at moderate or low dose rates generated by conventional accelerators [294], the recent research of FLASH effect shows the opposite (i.e., normal tissue sparing effect of high dose rate radiation) [306], [307], [308]. Generally, radiobiology research with laser driven ion beams is still at its infancy, thus the availability of beamlines dedicated to such kinds of experiments (e.g. ELIMAIA at ELI Beamlines) will open new opportunities in this field.

5.2 Proton pulsed radiolysis of water

Generally, radiolysis is dissociation of molecules by ionizing radiation. In other words, it is the cleavage of one or several chemical bonds resulting from exposure to high-energy flux. The crucial advantage of the usage of protons in pulsed radiolysis experiments is their comparatively short range, but high energy [309]. Because the radiolysis process takes place also in molecules of water, it has been deeply studied in radiotherapy treatments [310], where the resulting reactive fragments may interacts further with biological cells and possibly damage them. That is one of the reasons why the effects of ionizing radiation on human body have to be carefully monitored. Nevertheless, water radiolysis occurs and are studied also in many other situations such as radiosterilization [311], sewage treatment [312], food irradiation [313], or when any effect on solid/liquid interfaces is crucial, for example, in water-cooled nuclear reactors [314]. Particularly, water radiolysis results in the production of electrons, $^{\bullet}H$ atoms, $^{\bullet}OH$ radicals, H_3O^+ ions and molecules (e.g. dihydrogen H_2 and hydrogen peroxide H_2O_2).

The complex description of different stages and corresponding reactions of water radiolysis is depicted in Fig. 5.2; the more detailed explanation, than that which will follow, can be found in [288]. Firstly, the *physical stage* was achieved nearly immediately after the initial protons-water ionizing interaction and lasts up to $\sim 10^{-15}$ s. The exposure to radiation results in energy deposition to the water followed by fast relaxation processes. Particularly, ionization of water molecules (H_2O^+), their excitation (H_2O^*) and corresponding formation of subexcitation electrons ($e-$) take place. The second *physico-chemical stage* arises at $10^{-15}-10^{-12}$ s

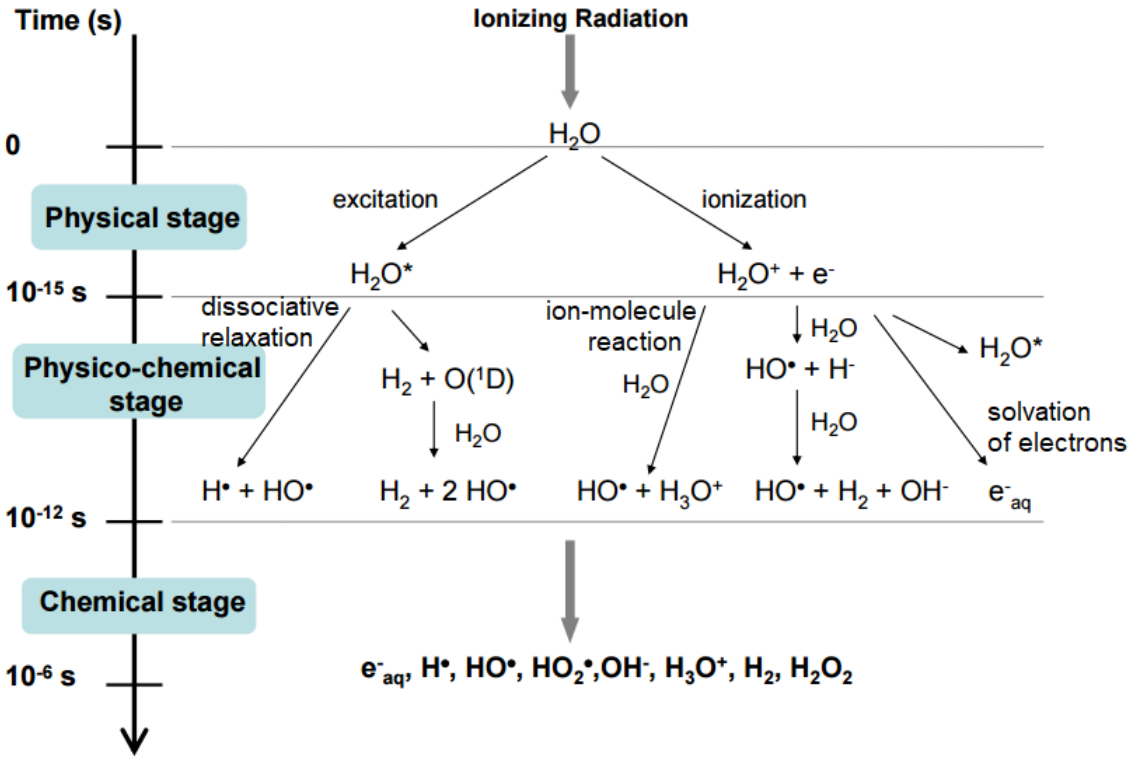

Figure 5.2: Main reactions occurring during the three stages of water radiolysis [288]; the dot notation emphasizes that there is a free radical that includes an unpaired electron.

after the interaction. Numerous processes occur, including ion-molecule reaction, dissociative relaxation, autoionization of excited states, thermalization of subexcitation electrons (solvation of electrons), hole diffusion, etc. The last non-homogeneous *chemical stage*, taking place between $10^{-12} - 10^{-6}$ s, pertains to particle tracks of various linear energy transfers (LET). Naturally, their reactions with surrounding molecules follow. As time passes, radicals diffuse and undergo chemical reactions. Consequently, the particle tracks expand. Recombination becomes unimportant after approximately 1 μs because particles are simply too distant from each other [288]. The processes may be simulated by the combination of Monte Carlo and a set of codes generating physical tracks of particles [315].
Laser-driven proton beams are interesting to be implemented in proton pulsed radiolysis studies due to their natural production of short bunches of relatively high charge ($\sim$nC) in related energy intervals leading to ultrahigh dose rates ($> 10^9$ Gy/s) [6]. The deep investigation of water decomposition processes is important for the basic chemical research as well as for laser-driven hadrontherapy and relevant dosimetric studies. In fact, the detailed knowledge of laser-driven proton radiolysis of water could answer the question if there are any significant differences between irradiation of living cells by conventionally accelerated or by laser-accelerated protons.

5.3 Non-destructive heritage testing

The characterization of cultural heritage material composition is usually made from small fragments which were removed from the examined subject. These techniques are very widely known as *destructive* testing. Contrarily, non-destructive heritage techniques providing analysis of chemical composition of wide range of materials are naturally considered to be a step forward. Non-invasive and non-destructive methods using laser-accelerated protons for testing and therefore for protecting cultural heritage are a novel approach and they enable accurate documentation and verification of ancient and historical artifacts. Their use serves to prove originality, detect forgeries, and to provide information about the original materials and artistic and manufacturing techniques used. Such facts are relevant for provenance studies (e.g. by determining trace elements present in native metals allowing information on trade routes) and indirect dating. Consequently, these techniques attract attention of archaeologists, historians, conservators, museum curators and collectors.

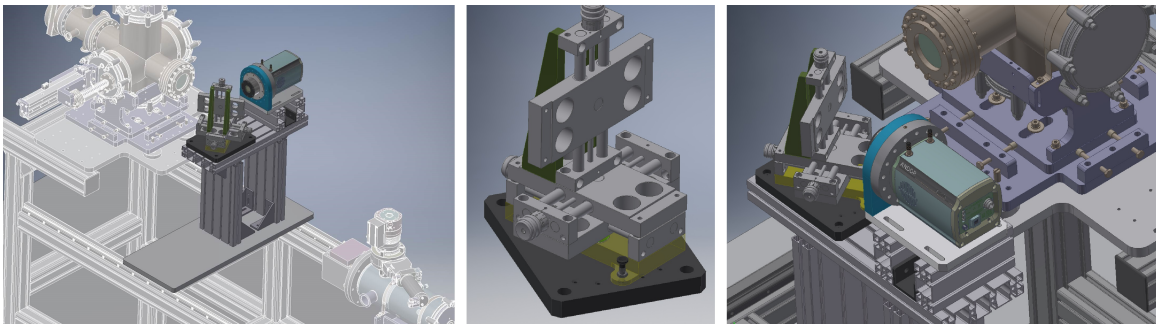

Figure 5.3: Design of the end-station dedicated to non-destructive heritage techniques at ELIMAIA beamline. The setup consists of energy dispersive X-ray CCD camera, polycapillary optics and various holders.

Generally, non-destructive methods may implement X-rays or other EM radiation and particles as well. The most used techniques are X-Ray Fluorescence (XRF), Energy dispersive X-ray fluorescence (EDXRF), X-ray Photoelectron Spectroscopy (XPS), Proton Induced X-ray Emission (PIXE), Proton Induced Gamma Emission (PIGE), AA techniques (Activation Analysis based on nuclear reactions induced in the sample by irradiating it either with ionizing or non-ionizing radiation) or Scanning Electron Microscope (SEM), Raman spectroscopy and others.
Current efforts at ELI Beamlines have been made to provide secondary laser-driven proton sources for (not only) non-destructive heritage testing at ELIMAIA [6] and TERESA [221] beamlines instead of using conventional accelerators (cyclotron, synchrotron, Van der Graaf, tandem etc.). The ongoing project *Non-destructive methods of monument testing* related to this topic (see 5.3.2) was granted by Prague City Hall and the cooperation with both physical and historical/archaeological science institutes was established (e.g. the Czech National Gallery, the Institute of Archaeology of the CAS, The city of Prague Museum and Istituto Nazionale di Fisica Nucleare - Laboratori Nazionali del Sud (INFN LNS)). Laser-driven proton beams of required parameters will be implemented in PIXE and (D)PAA (Deep Proton Activation Analysis) methods in order to provide non-destructive analysis of historical artifacts. These two supplementary techniques are able to recognize the elemental composition (ranging from sodium to uranium) even with low ppm concentrations and at different layers

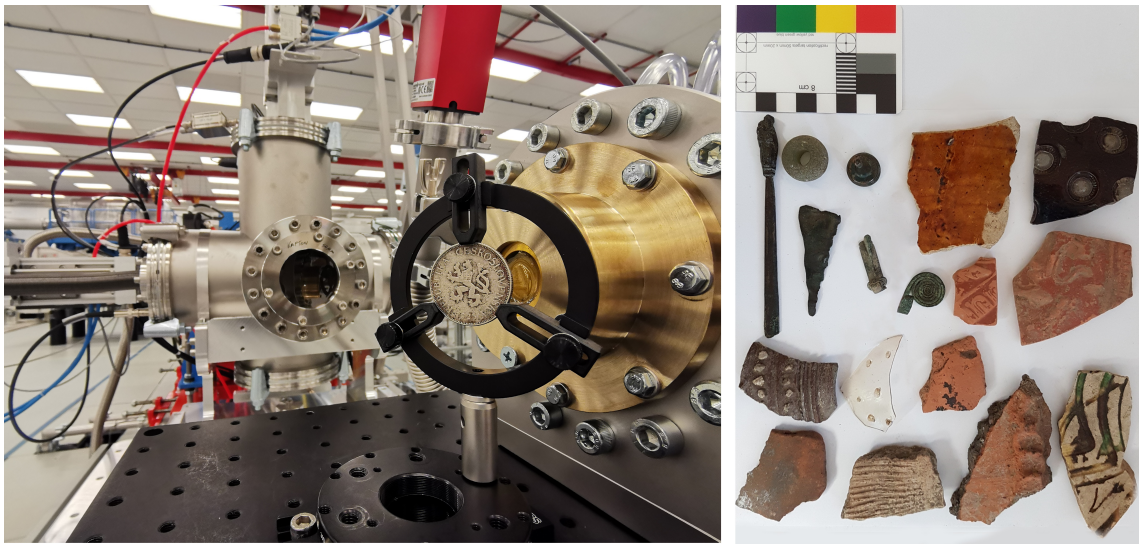

Figure 5.4: Left: Non-destructive end-station at ELIMAIA beamline with a sample coin; Right: samples lend from The city of Prague Museum to be tested at ELI Beamlines.

of the object. They are suitable for (but not limited to) painted and glazed ceramics, statues, glass, jewelry, paintings, inks, and icons. The developing technologies do not require vacuum for measurements and thus there is no risk of degradation caused by outgassing or dehydration of the tested items, and no limitation due to the dimensions or shape of the samples to be investigated. Of course, other benefit is no vacuum contamination inside the vacuum chamber coming from the dusty heritage objects, which makes this experimental application easy to perform and quickly replaceable to different experiment. The main advantage of laser-driven approaches would be the simple achieving of different energies of protons at one beamline, i.e., $2-5$ MeV for PIXE and $10-30$ MeV for (D)PAA (the exact required energy depends on the material itself and on its thickness which has to be analyzed, or thickness of another material which has to be penetrated). Therefore, the complex information about the material/layers will be reached, since PIXE can provide information about a surface ($5-10$ μm) and (D)PAA can go deeper and provides information about inner parts only ($300-400$ μm) which is crucial, for instance, when a corroded surface is treated. As the long term goal, foreseen table-top PIXE device is planned with compact laser system. Such apparatus could be bought by any museum/gallery or laboratory in the future.
The first pioneering study of laser-driven PIXE have been already performed at different facility [3], [4], [289] which demonstrates the proof of principle for this technique. The efforts made in implementation of laser-driven ion beams into (D)PAA method nevertheless stay purely novel.

5.3.1 PIXE

When the area of a sample is exposed to an ion beam, it induces the atoms emission of X-ray radiation with wavelengths corresponding to the specific element. PIXE method detects various elements ranging from Na to U at very low concentrations (ppm) and it is therefore suitable for the trace elements analysis as well. It provides the integrated information about the sample surface in a range of a few micrometers depending on a specific material. In

fact, conventional PIXE method have been already used from 1970s for elemental analysis of any kind [316], [317]. For instance, archaeological [318], [319], environmental [291], [292], geological [320], medical [321], [322], botanical [290] studies have been performed.

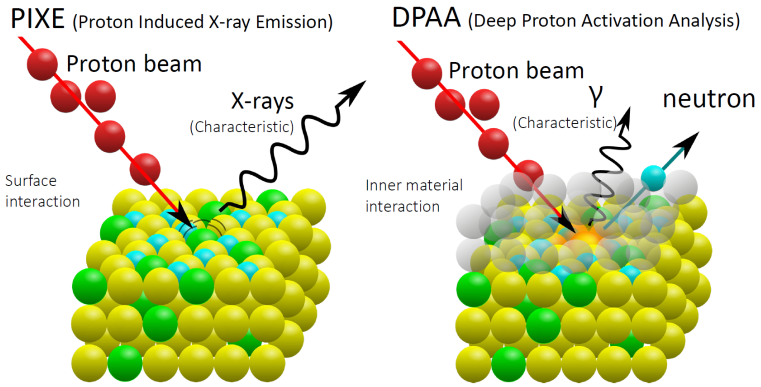

Figure 5.5: The schematic principles of non-destructive ion beam analysis: PIXE (Proton Induced X-ray Emission) providing elemental composition of the subject's surface by measuring characteristic X-rays (left) and complementary (D)PAA ((Deep) Proton Activation Analysis) providing info about the inner bulk of the material by measuring characteristic γ radiation (right).

5.3.2 DPAA

The non-destructive Deep Proton Activation Analysis method (DPAA) consists in the spatially controlled production of radioactive isotopes, through the absorption of protons by the stable atomic nuclei of interest that compose the samples [323]. By selecting the appropriate incoming proton energy and the suitable nuclear reaction, it is possible to restrict the analysis to the internal region only avoiding surface effects. Proton energy range lies usually between $10 - 30$ MeV (depending on the depth and the material) and in the case of Ag, Cu, Sn, Pb based materials, the (p, n) reactions can be selected for analysis. The sample material contains after proton beam irradiation an extra proton, which makes the molecule unstable and usually it decays by electronic capture according to the usual exponential law with the characteristic decay constant. After the decay, the stable element in its excited state is often produced followed by element de-excitation and corresponding gamma ray emission. Since this emission is characteristic of each element, it allows us to know the composition of the sample under examination. From the number of gamma rays detected, it is possible to trace a quantitative measurement of the atomic species inside the sample. Therefore DPAA provides information only about the interior part of the material, thus it eliminates any influence of the surface layers which made it optimal supplementary technique for PIXE. Consequently, DPAA technique is crucial for the analysis of corroded metals such as coins [324], [325].

Summary of the main results and Conclusions

The continuous progress in proton and heavier ion acceleration using ultra-intense laser pulses paves the way for many foreseen applications with a high socio-economic impact. Even though the extensive research was done within the field and is still ongoing, laser-driven particle beams are not ready to be widely utilized yet. The particular efforts in tuning parameters of these secondary sources are adjusted according to each application. Generally, endeavors may result in various parameter improvements, for example, a decrease in ion beam divergence, an increase in maximum energy, an improvement of homogeneity and spatial uniformity of the proton beam, or an adjustment in the charge of a whole ion bunch as well as only of a particular energy interval.

In order to improve laser-driven proton beam parameters, a set of 2D PIC simulations performing various target designs, including flat or curved foils with straight or tapering channels attached to their rear side, was compared with the reference flat foil. The flat channel target with a few microns long straight arms has been found to be an optimal target design, therefore, it was further investigated in 3D. Eventually, the 2D joint study of MHD and PIC simulations performing the preplasma (generated on the channel target front side by the laser prepulse) is discussed.

Within two-dimensional PIC comparative study, the flat targets with straight channels proved to be the apparent favorite for improved laser-driven ion acceleration, because they reduce significantly the beam divergence (up to 77% in the case of on-axis proton beam) and do not show any massive energy decrease or particle number lowering (up to 10%) in comparison to the reference flat foil. This is in a great correspondence with 3D results, even though the number of particles was reduced more than in 2D cases. In addition, various interesting features of other studied target designs have been discussed. For example, the targets with tapering channel conceptually act as collimators, and they can suppress the number of protons with low energy by more than 50%, depending on the size of the aperture between the arms. Curved foils with straight channel produce the highest, but very spatially localized, magnetic field in the center of their curvature. Nonetheless, this field was insufficient to sustain particles in a narrow beam, even though the prolonging of the arms had a positive effect. To summarize, flat targets with straight channel are the optimal solution in tuning parameters of accelerated proton beams due to the favorable establishment of EM fields. This triggered the efforts in studying the field formation in detail in 3D geometry.

Crucial differences between both the electric and the magnetic fields formation, their confinement and orientation were observed in 3D PIC simulations for the cylindrical channel target in comparison with the flat one. The long-lasting electric focusing field confined by

the guiding cylinder was shown in contrast to mostly defocusing field of the reference flat foil. Furthermore, the creation of a magnetic quadrupole with an extremely strong octupole component inside the cylindrical channel was described through the combination of well-confined transverse magnetic fields. In fact, the comparison of produced magnetic field strengths with standard electromagnets and with permanent magnets used in accelerator beamlines shows that the generated multipoles inside the channel target have comparable or even higher field integrals than those used in large-scale facilities for shaping accelerated ion beams. The magnetic multipoles inside the target cylinder were established by the electron motion along the guiding arms and subsequent formation of current loops. Contrarily, in the case of the flat target, no exact order of magnetic multipole was established, because electrons did not have any preferable flow and did not form desired current loops. In fact, the phenomenon of magnetic multipoles formed inside channel targets is original and it opens new possibilities in shaping particle beams magnetically already during the acceleration process by using ad-hoc designed targets. Moreover, the presence of octupole magnetic field led up to a 30% higher spatial uniformity of the proton beam produced from the channel target in comparison to the one produced from the reference foil. In addition, the favorable shape of the electric sheath field profile along the transverse axes supports this phenomenon. On the contrary, in the case of the flat foil, the electric sheath field profile in transverse direction was not only centralized around the laser axis, but it was also peaked "on sides". Consequently, the significant halo around the main beam was observed in particle densities, which results, together with the absence of octupole magnetic field, in the poorer spatial uniformity of the accelerated proton beam.

Since the particle divergence was influenced by the electric and magnetic fields, their effect and dominance have been studied with dependence on proton energy. The two most effective energy intervals ($\langle 5, 15\rangle$ MeV and $\langle 35, 45\rangle$ MeV) of divergence suppression, particularly up to $\sim$ 80% in a favorable plane, have been found. Naturally, the particle angular spread is plane and energy-dependent, because the fields act on ions with various energy differently and because, even though the individual symmetric elements of the magnetic field form a symmetric magnetic multipole, the multipole may have asymmetric impact on the divergence of passing particle beams (particularly, in the case of quadrupole).

In fact, one of the crucial advantages of reducing divergence already by target shaping, i.e., in front of the magnetic transport system of accelerator beamlines, is the optimal fitting of the accelerated particle beam in the entrance aperture. For example, even in the case of a very tight positioning of the ELIMED transport section of the ELIMAIA beamline, $\sim$ 36% of protons accelerated from the reference flat foil with energy above 10 MeV would be clipped when entering the transport system, in comparison to the high-energy main proton beam accelerated from the channel target, where only 9% of protons have higher divergence than the maximum acceptance angle.

In order to evaluate the practical utilization of channel targets in future experiments, sections dealing with a non-optimal laser contrast ratio as well as with discussion on target manufacturability have been added. Since the presence of preplasma affects the conditions of laser-driven ion acceleration and consequently also beam parameters, the main pulse interaction with the channel target already affected by the laser prepuse has been studied by additional PIC simulation. The preplasma profile was taken from MHD simulation dealing with prepulse of the intensity corresponding to the realistic contrast of current laser systems. The results show that the preplasma presence causes the temporal increase of laser pulse intensity leading to the slight enhancement of maximum proton energies, accompanied by the

flatter shape of the energy spectrum due to the strengthening of proton acceleration from the target front side. On the other hand, the modest divergence growth was observed and is expected in real experiments. To conclude, the channel target design studied within this doctoral thesis is reasonably resistant to the weak laser prepulses.

The presented work demonstrates the ability of straight channel targets to decrease proton beam divergence, which is additionally accompanied by improved spatial uniformity of the beam and only negligible reduction of maximum proton energy. Taking into account its manufacturability, such target design is suitable for real experiments in order to meet the challenging requirements of innovative applications of laser-driven ion beams.

Bibliography

[1] Andrea Macchi, Marco Borghesi, and Matteo Passoni. Ion acceleration by superintense laser-plasma interaction. *Reviews of Modern Physics*, 85(2):751, 2013.

[2] M Borghesi, A Bigongiari, S Kar, A Macchi, L Romagnani, P Audebert, J Fuchs, T Toncian, O Willi, SV Bulanov, et al. Laser-driven proton acceleration: source optimization and radiographic applications. *Plasma Physics and Controlled Fusion*, 50(12):124040, 2008.

[3] F Mirani, A Maffini, F Casamichiela, A Pazzaglia, A Formenti, D Dellasega, V Russo, D Vavassori, D Bortot, M Huault, et al. Integrated quantitative pixe analysis and edx spectroscopy using a laser-driven particle source. *Science advances*, 7(3):eabc8660, 2021.

[4] M Barberio and P Antici. Laser-pixe using laser-accelerated proton beams. *Scientific reports*, 9(1):1–9, 2019.

[5] Matteo Passoni, Luca Fedeli, and Francesco Mirani. Superintense laser-driven ion beam analysis. *Scientific reports*, 9(1):1–11, 2019.

[6] Daniele Margarone, GA Cirrone, Giacomo Cuttone, Antonio Amico, Lucio Andò, Marco Borghesi, Stepan S Bulanov, Sergei V Bulanov, Denis Chatain, Antonín Fajstavr, et al. Elimaia: A laser-driven ion accelerator for multidisciplinary applications. *Quantum Beam Science*, 2(2):8, 2018.

[7] E Sistrunk, T Spinka, A Bayramian, S Betts, R Bopp, S Buck, K Charron, J Cupal, R Deri, M Drouin, et al. All diode-pumped, high-repetition-rate advanced petawatt laser system (hapls). In *CLEO: Science and Innovations*, pages STh1L–2. Optical Society of America, 2017.

[8] B Rus, P Bakule, D Kramer, J Naylon, J Thoma, M Fibrich, JT Green, JC Lagron, R Antipenkov, J Bartoníček, et al. Eli-beamlines: progress in development of next generation short-pulse laser systems. In *Research Using Extreme Light: Entering New Frontiers with Petawatt-Class Lasers III*, volume 10241, page 102410J. International Society for Optics and Photonics, 2017.

[9] TD Arber, K Bennett, CS Brady, A Lawrence-Douglas, MG Ramsay, NJ Sircombe, P Gillies, RG Evans, H Schmitz, AR Bell, et al. Contemporary particle-in-cell approach to laser-plasma modelling. *Plasma Physics and Controlled Fusion*, 57(11):113001, 2015.

[10] N Jourdain, U Chaulagain, M Havlík, D Kramer, D Kumar, I Majerová, VT Tikhonchuk, G Korn, and S Weber. The l4n laser beamline of the p3-installation: Towards high-repetition rate high-energy density physics at eli-beamlines. *Matter and Radiation at Extremes*, 6(1):015401, 2021.

[11] H Kiriyama, M Nishiuchi, AS Pirozhkov, Y Fukuda, H Sakaki, A Sagisaka, NP Dover, K Kondo, K Nishitani, K Ogura, et al. J-karen-p laser facility at qst: High contrast, high intensity petawatt opcpa/ti: Sapphire hybrid laser system. In *The European Conference on Lasers and Electro-Optics*, page CF_3_5. Optical Society of America, 2017.

[12] Paul Gibbon. *Short pulse laser interactions with matter*. World Scientific Publishing Company Singapore, 2004.

[13] Shalom Eliezer. *The interaction of high-power lasers with plasmas*. CRC press, 2002.

[14] Francis F Chen. *Introduction to plasma physics*. Springer Science & Business Media, 2012.

[15] P Kulhánek. *Úvod do teorie plazmatu*. AGA, 2011.

[16] J Limpouch. Transparencies of lectures principles of plasma physics. http://kfe.fjfi.cvut.cz/~limpouch/plazma/lecplaz.html, 2012. online, accessed 01-09-2014.

[17] M Žáková. Optimization of laser-accelerated ion beam divergence. 2015.

[18] J Pšikal. *Ion Acceleration in Small-size Targets by Ultra-intense Short Laser Pulses (Simulation and Theory)*. PhD thesis, Czech Technical University, 2009.

[19] J Peebles, MS Wei, AV Arefiev, C McGuffey, RB Stephens, W Theobald, D Haberberger, LC Jarrott, A Link, H Chen, et al. Investigation of laser pulse length and pre-plasma scale length impact on hot electron generation on omega-ep. *New Journal of Physics*, 19(2):023008, 2017.

[20] MS Huzan, D Neely, and CD Armstrong. Plasma scale length effects on an imaging geometry. *world*, 2:4.

[21] K Wiesemann. A short introduction to plasma physics. *CAS - CERN Accelerator School : Ion Sources, pp.85-122*, 2014.

[22] Stanley Skupsky. Coulomb logarithm for inverse-bremsstrahlung laser absorption. *Physical Review A*, 36(12):5701, 1987.

[23] E Bésuelle, RRE Salomaa, and D Teychenné. Coulomb logarithm in femtosecond-laser–matter interaction. *Physical Review E*, 60(2):2260, 1999.

[24] Alexander Piel. *Plasma physics: an introduction to laboratory, space, and fusion plasmas*. Springer Science & Business Media, 2010.

[25] T Zh Esirkepov and SV Bulanov. Fundamental physics and relativistic laboratory astrophysics with extreme power lasers. *European Astronomical Society Publications Series*, 58:7–22, 2012.

[26] Christoph Thomas Baumann. *High intensity laser–plasma interactions and their potential for exploring strong-field QED*. PhD thesis, 2020.

[27] Sasi Palaniyappan, B Manuel Hegelich, Hui-Chun Wu, Daniel Jung, Donald C Gautier, Lin Yin, Brian J Albright, Randall P Johnson, Tsutomu Shimada, Samuel Letzring, et al. Dynamics of relativistic transparency and optical shuttering in expanding overdense plasmas. *Nature Physics*, 8(10):763–769, 2012.

[28] Marco Borghesi and Ulrich Schramm. Wg2 summary: Ion acceleration.

[29] Predhiman Kaw and John Dawson. Relativistic nonlinear propagation of laser beams in cold overdense plasmas. *The Physics of Fluids*, 13(2):472–481, 1970.

[30] Claire Max and Francis Perkins. Strong electromagnetic waves in overdense plasmas. *Physical Review Letters*, 27(20):1342, 1971.

[31] F Cattani, A Kim, D Anderson, and M Lisak. Threshold of induced transparency in the relativistic interaction of an electromagnetic wave with overdense plasmas. *Physical Review E*, 62(1):1234, 2000.

[32] Heinrich Hora. Self-focusing of laser beams in a plasma by ponderomotive forces. *Zeitschrift für Physik A Hadrons and nuclei*, 226(2):156–159, 1969.

[33] Heinrich Hora. Physics of laser driven plasmas. *New York*, 1981.

[34] B Arad, S Eliezer, S Jackel, A Krumbein, HM Loebenstein, D Salzmann, A Zigler, H Zmora, and S Zweigenbaum. Effect of pulse duration and polarization on momentum and energy transfer to laser-irradiated targets. *Physical Review Letters*, 44(5):326, 1980.

[35] P Kaw, G Schmidt, and T Wilcox. Filamentation and trapping of electromagnetic radiation in plasmas. *The Physics of Fluids*, 16(9):1522–1525, 1973.

[36] GJ Morales and YC Lee. Generation of density cavities and localized electric fields in a nonuniform plasma. *The Physics of Fluids*, 20(7):1135–1147, 1977.

[37] M Dâ€™Evelyn and GJ Morales. Properties of large amplitude langmuir solitons. *The Physics of Fluids*, 21(11):1997–2008, 1978.

[38] P Mulser and C Van Kessel. Profile modifications and plateau formation due to light pressure in laser-irradiated targets. *Physical Review Letters*, 38(16):902, 1977.

[39] JA Stamper and DA Tidman. Magnetic field generation due to radiation pressure in a laser-produced plasma. *The Physics of Fluids*, 16(11):2024–2025, 1973.

[40] Thierry Lehner. Intense magnetic field generation by relativistic ponderomotive force in an underdense plasma. *Physica Scripta*, 49(6):704, 1994.

[41] Y Horovitz, S Eliezer, Z Henis, Y Paiss, E Moshe, A Ludmirsky, M Werdiger, B Arad, and A Zigler. The inverse faraday effect in plasma produced by circularly polarized laser light in the range of intensities $10^9 - 1014$ w/cm^2. *Physics Letters A*, 246(3-4):329–334, 1998.

[42] Y Horovitz, S Eliezer, A Ludmirsky, Z Henis, E Moshe, R Shpitalnik, and B Arad. Measurements of inverse faraday effect and absorption of circularly polarized laser light in plasmas. *Physical review letters*, 78(9):1707, 1997.

[43] HH Chen and CS Liu. Soliton formation and saturation of decay instability of an electromagnetic wave into two plasma waves. *Physical Review Letters*, 39(14):881, 1977.

[44] S Jackel, S Eliezer, and A Zigler. Effect of ponderomotive forces on wave dispersion and second-harmonic light emissions in laser-produced plasmas. *Physical Review A*, 24(3):1601, 1981.

[45] A Yandow, T Toncian, and T Ditmire. Direct laser ion acceleration and above-threshold ionization at intensities from 10^21 w/cm^2 to 3×10^{23} w/cm^2. *Physical Review A*, 100(5):053406, 2019.

[46] SS Bulanov, E Esarey, CB Schroeder, SV Bulanov, T Zh Esirkepov, M Kando, F Pegoraro, and WP Leemans. Radiation pressure acceleration: The factors limiting maximum attainable ion energy. *Physics of plasmas*, 23(5):056703, 2016.

[47] SS Bulanov, A Brantov, V Yu Bychenkov, V Chvykov, G Kalinchenko, T Matsuoka, P Rousseau, S Reed, V Yanovsky, DW Litzenberg, et al. Accelerating monoenergetic protons from ultrathin foils by flat-top laser pulses in the directed-coulomb-explosion regime. *Physical Review E*, 78(2):026412, 2008.

[48] A Higginson, RJ Gray, M King, RJ Dance, SDR Williamson, NMH Butler, R Wilson, R Capdessus, C Armstrong, JS Green, et al. Near-100 mev protons via a laser-driven transparency-enhanced hybrid acceleration scheme. *Nature communications*, 9(1):1–9, 2018.

[49] TM Jeong and J Lee. Femtosecond petawatt laser. *Ann. Phys. (Berlin)*, 16, 2014.

[50] Matteo Passoni, Luca Bertagna, and Alessandro Zani. Target normal sheath acceleration: theory, comparison with experiments and future perspectives. *New Journal of Physics*, 12(4):045012, 2010.

[51] Christian Rödel, D an der Brügge, J Bierbach, M Yeung, T Hahn, B Dromey, S Herzer, S Fuchs, A Galestian Pour, E Eckner, et al. Harmonic generation from relativistic plasma surfaces in ultrasteep plasma density gradients. *Physical review letters*, 109(12):125002, 2012.

[52] M Roth and M Schollmeier. Ion acceleration - target normal sheath acceleration. *CERN Yellow Reports*, 1:231, 2016.

[53] BM Hegelich. *Acceleration of heavy ions to MeV/nucleon energies by ultrahigh-intensity lasers*. PhD thesis, lmu, 2002.

[54] J Fuchs, P Antici, E dâ€™Humières, E Lefebvre, Marco Borghesi, E Brambrink, CA Cecchetti, Malte Kaluza, Victor Malka, M Manclossi, et al. Laser-driven proton scaling laws and new paths towards energy increase. *Nature physics*, 2(1):48–54, 2006.

[55] J Fuchs, Y Sentoku, E dâ€™Humières, TE Cowan, J Cobble, P Audebert, A Kemp, A Nikroo, P Antici, E Brambrink, et al. Comparative spectra and efficiencies of ions laser-accelerated forward from the front and rear surfaces of thin solid foils. *Physics of plasmas*, 14(5):053105, 2007.

[56] P Mora. Collisionless expansion of a gaussian plasma into a vacuum. *Physics of plasmas*, 12(11):112102, 2005.

[57] Patrick Mora. Thin-foil expansion into a vacuum. *Physical Review E*, 72(5):056401, 2005.

[58] Patrick Mora. Plasma expansion into a vacuum. *Physical Review Letters*, 90(18):185002, 2003.

[59] K Flippo, BM Hegelich, BJ Albright, L Yin, DC Gautier, S Letzring, M Schollmeier, J Schreiber, R Schulze, and JC Fernandez. Laser-driven ion accelerators: Spectral control, monoenergetic ions and new acceleration mechanisms. *Laser and Particle Beams*, 25(01):3–8, 2007.

[60] T Esirkepov, M Yamagiwa, and T Tajima. Laser ion-acceleration scaling laws seen in multiparametric particle-in-cell simulations. *Physical Review Letters*, 96(10):105001, 2006.

[61] K Matsukado, T Esirkepov, K Kinoshita, H Daido, T Utsumi, Z Li, A Fukumi, Y Hayashi, S Orimo, M Nishiuchi, et al. Energetic protons from a few-micron metallic foil evaporated by an intense laser pulse. *Physical review letters*, 91(21):215001, 2003.

[62] XQ Yan, C Lin, Zheng-Ming Sheng, ZY Guo, BC Liu, YR Lu, JX Fang, JE Chen, et al. Generating high-current monoenergetic proton beams by a circularlypolarized laser pulse in the phase-stableacceleration regime. *Physical review letters*, 100(13):135003, 2008.

[63] T Tajima, K Nakajima, and G Mourou. Laser acceleration. *Nuovo Cimento Rivista Serie*, 40:33–133, 2017.

[64] M Passoni, VT Tikhonchuk, M Lontano, and V Yu Bychenkov. Charge separation effects in solid targets and ion acceleration with a two-temperature electron distribution. *Physical Review E*, 69(2):026411, 2004.

[65] Sylvain Fourmaux, Stéphane Payeur, Philippe Lassonde, Jean-Claude Kieffer, and François Martin. Laser pulse contrast ratio cleaning in 100 tw scale ti: Sapphire laser systems. *Laser Systems for Applications*, pages 139–154, 2011.

[66] T Esirkepov, M Borghesi, SV Bulanov, G Mourou, and T Tajima. Highly efficient relativistic-ion generation in the laser-piston regime. *Physical review letters*, 92(17):175003, 2004.

[67] S Kar, M Borghesi, SV Bulanov, MH Key, TV Liseykina, A Macchi, AJ Mackinnon, PK Patel, L Romagnani, Angelo Schiavi, et al. Plasma jets driven by ultraintense-laser interaction with thin foils. *Physical review letters*, 100(22):225004, 2008.

[68] Tatiana V Liseykina, Marco Borghesi, Andrea Macchi, and Sara Tuveri. Radiation pressure acceleration by ultraintense laser pulses. *Plasma Physics and Controlled Fusion*, 50(12):124033, 2008.

[69] Andrea Macchi, Federica Cattani, Tatiana V Liseykina, and Fulvio Cornolti. Laser acceleration of ion bunches at the front surface of overdense plasmas. *Physical review letters*, 94(16):165003, 2005.

[70] EV Stenson, J Horn-Stanja, MR Stoneking, and T Sunn Pedersen. Debye length and plasma skin depth: two length scales of interest in the creation and diagnosis of laboratory pair plasmas. *Journal of Plasma Physics*, 83(1), 2017.

[71] J Denavit. Absorption of high-intensity subpicosecond lasers on solid density targets. *Physical review letters*, 69(21):3052, 1992.

[72] SC Wilks, WL Kruer, M Tabak, and AB Langdon. Absorption of ultra-intense laser pulses. *Physical review letters*, 69(9):1383, 1992.

[73] T Schlegel, N Naumova, VT Tikhonchuk, C Labaune, IV Sokolov, and G Mourou. Relativistic laser piston model: Ponderomotive ion acceleration in dense plasmas using ultraintense laser pulses. *Physics of Plasmas*, 16(8):083103, 2009.

[74] APL Robinson, Paul Gibbon, M Zepf, S Kar, RG Evans, and C Bellei. Relativistically correct hole-boring and ion acceleration by circularly polarized laser pulses. *Plasma Physics and Controlled Fusion*, 51(2):024004, 2009.

[75] SV Bulanov, T Zh Esirkepov, M Kando, F Pegoraro, SS Bulanov, CGR Geddes, CB Schroeder, E Esarey, and WP Leemans. Ion acceleration from thin foil and extended plasma targets by slow electromagnetic wave and related ion-ion beam instability. *Physics of Plasmas*, 19(10):103105, 2012.

[76] L Yin, BJ Albright, BM Hegelich, and JC Fernández. Gev laser ion acceleration from ultrathin targets: The laser break-out afterburner. *Laser and Particle Beams*, 24(02):291–298, 2006.

[77] L Yin, BJ Albright, BM Hegelich, KJ Bowers, KA Flippo, TJT Kwan, and JC Fernández. Monoenergetic and gev ion acceleration from the laser breakout afterburner using ultrathin targetsa). *Physics of Plasmas (1994-present)*, 14(5):056706, 2007.

[78] BM Hegelich, I Pomerantz, L Yin, HC Wu, D Jung, BJ Albright, DC Gautier, S Letzring, S Palaniyappan, R Shah, et al. Laser-driven ion acceleration from relativistically transparent nanotargets. *New Journal of Physics*, 15(8):085015, 2013.

[79] D Jung, BJ Albright, L Yin, DC Gautier, R Shah, S Palaniyappan, S Letzring, B Dromey, HC Wu, T Shimada, et al. Beam profiles of proton and carbon ions in the relativistic transparency regime. *New Journal of Physics*, 15(12):123035, 2013.

[80] D Jung, BJ Albright, L Yin, DC Gautier, B Dromey, R Shah, S Palaniyappan, S Letzring, H-C Wu, T Shimada, et al. Scaling of ion energies in the relativistic-induced transparency regime. *Laser and Particle Beams*, 33(4):695–703, 2015.

[81] L Yin, BJ Albright, KJ Bowers, D Jung, JC Fernández, and BM Hegelich. Three-dimensional dynamics of breakout afterburner ion acceleration using high-contrast short-pulse laser and nanoscale targets. *Physical review letters*, 107(4):045003, 2011.

[82] L Willingale, SPD Mangles, PM Nilson, RJ Clarke, AE Dangor, MC Kaluza, S Karsch, KL Lancaster, WB Mori, Z Najmudin, et al. Collimated multi-mev ion beams from high-intensity laser interactions with underdense plasma. *Physical review letters*, 96(24):245002, 2006.

[83] L Willingale, SR Nagel, AGR Thomas, C Bellei, RJ Clarke, AE Dangor, R Heathcote, MC Kaluza, C Kamperidis, S Kneip, et al. Characterization of high-intensity laser propagation in the relativistic transparent regime through measurements of energetic proton beams. *Physical review letters*, 102(12):125002, 2009.

[84] Tatsufumi Nakamura, Sergei V Bulanov, Timur Zh Esirkepov, and Masaki Kando. High-energy ions from near-critical density plasmas via magnetic vortex acceleration. *Physical review letters*, 105(13):135002, 2010.

[85] SV Bulanov and T Zh Esirkepov. Comment on "collimated multi-mev ion beams from high-intensity laser interactions with underdense plasma". *Physical review letters*, 98(4):049503, 2007.

[86] A Pukhov and J Meyer-ter Vehn. Relativistic magnetic self-channeling of light in near-critical plasma: three-dimensional particle-in-cell simulation. *Physical review letters*, 76(21):3975, 1996.

[87] David Burgess and Manfred Scholer. *Collisionless shocks in space plasmas: structure and accelerated particles*. Cambridge University Press, 2015.

[88] SF Martins, RA Fonseca, LO Silva, and WB Mori. Ion dynamics and acceleration in relativistic shocks. *The Astrophysical Journal Letters*, 695(2):L189, 2009.

[89] A Stockem Novo, MC Kaluza, RA Fonseca, and LO Silva. Optimizing laser-driven proton acceleration from overdense targets. *Scientific reports*, 6(1):1–7, 2016.

[90] Sergei Vladimirovich Bulanov, Jan J Wilkens, T Zh Esirkepov, Georg Korn, G Kraft, Stephan D Kraft, Michael Molls, and Vladimir Sergeevich Khoroshkov. Laser ion acceleration for hadron therapy. *Physics-Uspekhi*, 57(12):1149, 2014.

[91] Luís O Silva, Michael Marti, Jonathan R Davies, Ricardo A Fonseca, Chuang Ren, Frank S Tsung, and Warren B Mori. Proton shock acceleration in laser-plasma interactions. *Physical Review Letters*, 92(1):015002, 2004.

[92] Matthew Zepf, EL Clark, FN Beg, RJ Clarke, AE Dangor, A Gopal, K Krushelnick, PA Norreys, M Tatarakis, U Wagner, et al. Proton acceleration from high-intensity laser interactions with thin foil targets. *Physical review letters*, 90(6):064801, 2003.

[93] Emmanuel d'Humières, Erik Lefebvre, Laurent Gremillet, and Victor Malka. Proton acceleration mechanisms in high-intensity laser interaction with thin foils. *Physics of plasmas*, 12(6):062704, 2005.

[94] Min Chen, Zheng-Ming Sheng, Quan-Li Dong, Min-Qing He, Yu-Tong Li, Muhammad Abbas Bari, and Jie Zhang. Collisionless electrostatic shock generation and ion acceleration by ultraintense laser pulses in overdense plasmas. *Physics of plasmas*, 14(5):053102, 2007.

[95] K Nishihara, H Amitani, M Murakami, SV Bulanov, and T Zh Esirkepov. High energy ions generated by laser driven coulomb explosion of cluster. *Nuclear Instruments and Methods in Physics Research Section A: Accelerators, Spectrometers, Detectors and Associated Equipment*, 464(1-3):98–102, 2001.

[96] V Yu Bychenkov and VF Kovalev. Coulomb explosion in a cluster plasma. *Plasma physics reports*, 31(2):178–183, 2005.

[97] Isidore Last and Joshua Jortner. Dynamics of the coulomb explosion of large clusters in a strong laser field. *Physical Review A*, 62(1):013201, 2000.

[98] E Fourkal, I Velchev, and C-M Ma. Coulomb explosion effect and the maximum energy of protons accelerated by high-power lasers. *Physical Review E*, 71(3):036412, 2005.

[99] Stepan Bulanov, Qing Ji, Thomas Schenkel, Sven Steinke, Wim Leemans, and Eric Esarey. Advanced acceleration mechanisms for laser driven ions by pw-lasers. 2016.

[100] Paul Gibbon. *Short pulse laser interactions with matter: an introduction*. World Scientific, 2005.

[101] GJ Pert. Inverse bremsstrahlung in strong radiation fields at low temperatures. *Physical Review E*, 51(5):4778, 1995.

[102] J Velechovský. Modelování absorpce laserového záěení v plazmatu. 2010.

[103] GJ Pert. The analytic theory of linear resonant absorption. *Plasma Physics*, 20(3):175, 1978.

[104] W Rozmus, VT Tikhonchuk, and R Cauble. A model of ultrashort laser pulse absorption in solid targets. *Physics of Plasmas*, 3(1):360–367, 1996.

[105] Paul Gibbon and AR Bell. Collisionless absorption in sharp-edged plasmas. *Physical review letters*, 68(10):1535, 1992.

[106] Q Dong and J Zhang. Vacuum heating of solid target irradiated by femtosecond laser pulses. *Science in China Series G: Physics, Mechanics and Astronomy*, 46(1):71–77, 2003.

[107] AA Andreev, J Limpouch, and AN Semakhin. Absorption of the energy of a short laser pulse obliquely incident on a highly inhomogeneous plasma. *Bulletin of the Russian Academy of Sciences-Physics*, 58(6):1056, 1994.

[108] B Bezzerides, SJ Gitomer, and DW Forslund. Randomness, maxwellian distributions, and resonance absorption. *Physical Review Letters*, 44(10):651, 1980.

[109] Kent Estabrook and William L Kruer. Properties of resonantly heated electron distributions. *Physical Review Letters*, 40(1):42, 1978.

[110] G Malka, J Fuchs, F Amiranoff, SD Baton, R Gaillard, JL Miquel, H Pépin, C Rousseaux, G Bonnaud, M Busquet, et al. Suprathermal electron generation and channel formation by an ultrarelativistic laser pulse in an underdense preformed plasma. *Physical review letters*, 79(11):2053, 1997.

[111] DW Forslund, JM Kindel, and K Lee. Theory of hot-electron spectra at high laser intensity. *Physical Review Letters*, 39(5):284, 1977.

[112] FN Beg, AR Bell, AE Dangor, CN Danson, AP Fews, ME Glinsky, BA Hammel, P Lee, PA Norreys, and Ma Tatarakis. A study of picosecond laser–solid interactions up to 1019 w cm- 2. *Physics of plasmas*, 4(2):447–457, 1997.

[113] MG Haines, MS Wei, FN Beg, and RB Stephens. Hot-electron temperature and laser-light absorption in fast ignition. *Physical Review Letters*, 102(4):045008, 2009.

[114] T Kluge, T Cowan, A Debus, U Schramm, K Zeil, and M Bussmann. Electron temperature scaling in laser interaction with solids. *Physical review letters*, 107(20):205003, 2011.

[115] Arnaud Debayle. *Theoretical study of ultra high intensity laser-produced high-current relativistic electron beam transport through solid targets*. PhD thesis, Bordeaux 1, 2008.

[116] Hannes Alfvén. On the motion of cosmic rays in interstellar space. *Physical Review*, 55(5):425, 1939.

[117] AR Bell, JR Davies, S Guerin, and H Ruhl. Fast-electron transport in high-intensity short-pulse laser-solid experiments. *Plasma physics and controlled fusion*, 39(5):653, 1997.

[118] HM Milchberg, RR Freeman, SC Davey, and RM More. Resistivity of a simple metal from room temperature to 10 6 k. *Physical review letters*, 61(20):2364, 1988.

[119] Matthias Schnürer, MP Kalashnikov, PV Nickles, Th Schlegel, W Sandner, N Demchenko, R Nolte, and P Ambrosi. Hard x-ray emission from intense short pulse laser plasmas. *Physics of Plasmas*, 2(8):3106–3110, 1995.

[120] Luis O Silva, Ricardo A Fonseca, John W Tonge, Warren B Mori, and John M Dawson. On the role of the purely transverse weibel instability in fast ignitor scenarios. *Physics of Plasmas*, 9(6):2458–2461, 2002.

[121] Yasuhiko Sentoku, Kunioki Mima, Shin-ichi Kojima, and Hartmut Ruhl. Magnetic instability by the relativistic laser pulses in overdense plasmas. *Physics of Plasmas*, 7(2):689–695, 2000.

[122] Kazuo A Tanaka, R Kodama, K Mima, Y Kitagawa, H Fujita, N Miyanaga, K Nagai, T Norimatsu, T Sato, Y Sentoku, et al. Basic and integrated studies for fast ignition. *Physics of Plasmas*, 10(5):1925–1930, 2003.

[123] Andrea Macchi. *A Superintense Laser-Plasma Interaction Theory Primer*. Springer Science & Business Media, 2013.

[124] P Sprangle, E Esarey, and A Ting. Nonlinear theory of intense laser-plasma interactions. *Physical review letters*, 64(17):2011, 1990.

[125] AB Borisov, OB Shiryaev, A McPherson, K Boyer, and CK Rhodes. Stability analysis of relativistic and charge-displacement self-channelling of intense laser pulses in underdense plasmas. *Plasma physics and controlled fusion*, 37(5):569, 1995.

[126] AB Borisov, AV Borovskiy, VV Korobkin, AM Prokhorov, CK Rhodes, and OB Shiryaev. Stabilization of relativistic self-focusing of intense subpicosecond ultraviolet pulses in plasmas. *Physical review letters*, 65(14):1753, 1990.

[127] F Wagner, C Brabetz, O Deppert, M Roth, T Stöhlker, An Tauschwitz, A Tebartz, B Zielbauer, and V Bagnoud. Accelerating ions with high-energy short laser pulses from submicrometer thick targets. *High power laser science and engineering*, 4, 2016.

[128] Pascal Monot, Gilles Doumy, Sundrine Dobosz, Michel Perdrix, Pascal Dâ€™Oliveira, Fabion Quéré, Fabrice Réau, Philippe Martin, Patrick Audebert, Jean-Claude Gauthier, et al. High-order harmonic generation by nonlinear reflection of an intense high-contrast laser pulse on a plasma. *Optics letters*, 29(8):893–895, 2004.

[129] Malte Kaluza, Jörg Schreiber, Marko IK Santala, George D Tsakiris, Klaus Eidmann, Jürgen Meyer-ter Vehn, and Klaus J Witte. Influence of the laser prepulse on proton acceleration in thin-foil experiments. *Physical review letters*, 93(4):045003, 2004.

[130] Paul McKenna, Filip Lindau, Olle Lundh, David Neely, Anders Persson, and Claes-Göran Wahlström. High-intensity laser-driven proton acceleration: influence of pulse contrast. *Philosophical Transactions of the Royal Society A: Mathematical, Physical and Engineering Sciences*, 364(1840):711–723, 2006.

[131] D Batani, R Jafer, Mina Veltcheva, R Dezulian, Olle Lundh, Filip Lindau, Anders Persson, K Osvay, CG Wahlström, DC Carroll, et al. Effects of laser prepulses on laser-induced proton generation. *New Journal of Physics*, 12(4):045018, 2010.

[132] VM Ovchinnikov, DW Schumacher, M McMahon, EA Chowdhury, CD Chen, A Morace, and RR Freeman. Effects of preplasma scale length and laser intensity on the divergence of laser-generated hot electrons. *Physical review letters*, 110(6):065007, 2013.

[133] VM Ovchinnikov, DW Schumacher, GE Kemp, AG Krygier, LD Van Woerkom, KU Akli, RR Freeman, RB Stephens, and A Link. Using time-integrated kα images to study refluxing and the extent of pre-plasmas in intense laser-plasma experiment. *Physics of Plasmas*, 18(11):112702, 2011.

[134] A Debayle, JJ Honrubia, E dâ€™Humieres, and VT Tikhonchuk. Divergence of laser-driven relativistic electron beams. *Physical Review E*, 82(3):036405, 2010.

[135] AJ Mackinnon, Marco Borghesi, S Hatchett, MH Key, PK Patel, H Campbell, A Schiavi, R Snavely, SC Wilks, and O Willi. Effect of plasma scale length on multi-mev proton production by intense laser pulses. *Physical Review Letters*, 86(9):1769, 2001.

[136] V Yu Bychenkov, Y Sentoku, Sergei Vladimirovich Bulanov, K Mima, Gérard Mourou, and Sergei Vladimirovich Tolokonnikov. Pion production under the action of intense

ultrashort laser pulse on a solid target. *Journal of Experimental and Theoretical Physics Letters*, 74(12):586–589, 2001.

[137] Y Sentoku, V Yu Bychenkov, K Flippo, Anatoly Maksimchuk, K Mima, G Mourou, ZM Sheng, and Donald Umstadter. High-energy ion generation in interaction. of short laser pulse with high-density plasma. *Applied Physics B*, 74(3):207–215, 2002.

[138] P McKenna, DC Carroll, Olle Lundh, F Nürnberg, Keith Markey, S Bandyopadhyay, D Batani, RG Evans, R Jafer, Saty Kar, et al. Effects of front surface plasma expansion on proton acceleration in ultraintense laser irradiation of foil targets. *Laser and Particle Beams*, 26(4):591–596, 2008.

[139] Timur Zh Esirkepov, James K Koga, Atsushi Sunahara, Toshimasa Morita, Masaharu Nishikino, Kei Kageyama, Hideo Nagatomo, Katsunobu Nishihara, Akito Sagisaka, Hideyuki Kotaki, et al. Prepulse and amplified spontaneous emission effects on the interaction of a petawatt class laser with thin solid targets. *Nuclear Instruments and Methods in Physics Research Section A: Accelerators, Spectrometers, Detectors and Associated Equipment*, 745:150–163, 2014.

[140] Pengjie Wang, Y Gao, Y Shou, Z Pan, S Xu, D Wang, Jianbo Liu, Z Cao, Z Mei, D Kong, et al. A simple way to introduce an adjustable femtosecond pre-pulse to enhance laser-driven proton acceleration. In *Journal of Physics: Conference Series*, volume 1350, page 012063. IOP Publishing, 2019.

[141] ML Zhou, JH Bin, D Haffa, XQ Yan, and J Schreiber. The impact of femtosecond pre-pulses on nanometer thin foils for laser-ion acceleration. *Plasma Physics and Controlled Fusion*, 59(5):055020, 2017.

[142] Robert Babjak and Jan Psikal. The role of standing wave in the generation of hot electrons by femtosecond laser beams incident on dense ionized target. *Physics of Plasmas*, 28(2):023107, 2021.

[143] MG Haines. Saturation mechanisms for the generated magnetic field in nonuniform laser-matter irradiation. *Physical review letters*, 78(2):254, 1997.

[144] M Borghesi, AJ Mackinnon, R Gaillard, O Willi, A Pukhov, and J Meyer-ter Vehn. Large quasistatic magnetic fields generated by a relativistically intense laser pulse propagating in a preionized plasma. *Physical review letters*, 80(23):5137, 1998.

[145] JA Stamper and BH Ripin. Faraday-rotation measurements of megagauss magnetic fields in laser-produced plasmas. *Physical Review Letters*, 34(3):138, 1975.

[146] A Raven, O Willi, and PT Rumsby. Megagauss magnetic field profiles in laser-produced plasmas. *Physical Review Letters*, 41(8):554, 1978.

[147] RJ Mason and M Tabak. Magnetic field generation in high-intensity-laser–matter interactions. *Physical review letters*, 80(3):524, 1998.

[148] M Tatarakis, A Gopal, I Watts, FN Beg, AE Dangor, K Krushelnick, U Wagner, PA Norreys, EL Clark, M Zepf, et al. Measurements of ultrastrong magnetic fields during relativistic laser–plasma interactions. *Physics of Plasmas*, 9(5):2244–2250, 2002.

[149] AR Bell, FN Beg, Z Chang, AE Dangor, CN Danson, CB Edwards, AP Fews, MHR Hutchinson, S Luan, P Lee, et al. Observation of plasma confinement in picosecond laser-plasma interactions. *Physical Review E*, 48(3):2087, 1993.

[150] AR Bell. Magnetohydrodynamic jets. *Physics of plasmas*, 1(5):1643–1652, 1994.

[151] A Pukhov and J Meyer-ter Vehn. Laser hole boring into overdense plasma and relativistic electron currents for fast ignition of icf targets. *Physical review letters*, 79(14):2686, 1997.

[152] John M Dawson. Nonlinear electron oscillations in a cold plasma. *Physical Review*, 113(2):383, 1959.

[153] Helmut Wiedemann. *Particle accelerator physics*, volume 2. Springer Science & Business Media, 2003.

[154] Martin Reiser and Patrick O'Shea. *Theory and design of charged particle beams*, volume 312. Wiley Online Library, 1994.

[155] Andrzej Wolski. Maxwell's equations for magnets. *arXiv preprint arXiv:1103.0713*, 2011.

[156] Eugene Hecht. *Optics, 5e*. Pearson Education India, 2002.

[157] Helmut Wiedemann. *Particle accelerator physics*. Springer, 2015.

[158] Richard L Taylor. Magnetic measurements of quadrupole focusing magnets at slac. Technical report, 1991.

[159] Xiangxue Zhao, Shancai Zhang, Hong-liang Xu, Wei-min Li, Guangyao Feng, and Lin Wang. Design study of combined magnet with combined function method. 2010.

[160] Eriko Urakabe, Yuzo Fujita, Kazuo Hiramoto, Makoto Inoue, Yoshihisa Iwashita, Mitsutaka Kanazawa, Akio Morita, Masatsugu Nishi, Tetsuro Norimine, Akira Noda, et al. Beam-profile control using an octupole magnet. *Japanese journal of applied physics*, 38(10R):6145, 1999.

[161] Jack T Tanabe. *Iron dominated electromagnets: design, fabrication, assembly and measurements*. World Scientific Publishing Company, 2005.

[162] F Schillaci, M Maggiore, D Rifuggiato, GAP Cirrone, G Cuttone, and D Giove. Errors and optics study of a permanent magnet quadrupole system. *Journal of Instrumentation*, 10(05):T05001, 2015.

[163] DN Jamieson and GJF Legge. The measurement and correction of spherical aberration in a magnetic quadrupole quadruplet lens system. *Nuclear Instruments and Methods in Physics Research Section B: Beam Interactions with Materials and Atoms*, 34(3):411–422, 1988.

[164] David H Dowell, Feng Zhou, and John Schmerge. Exact cancellation of emittance growth due to coupled transverse dynamics in solenoids and rf couplers. *Physical Review Accelerators and Beams*, 21(1):010101, 2018.

[165] Pavel Vagin and Markus Tischer. Variable period undulator with tunable polarization. In *AIP Conference Proceedings*, volume 2054, page 030024. AIP Publishing LLC, 2019.

[166] Bruce Cork and Emery Zajec. *Quadrupole focusing lenses for charged particles.* University of California Radiation Laboratory, 1953.

[167] R Tomás, O Brüning, M Giovannozzi, P Hagen, M Lamont, F Schmidt, G Vanbavinckhove, M Aiba, R Calaga, and R Miyamoto. Cern large hadron collider optics model, measurements, and corrections. *Physical review special topics-Accelerators and Beams*, 13(12):121004, 2010.

[168] JEAN-PIERRE Koutchouk. Correction of the betatron coupling in the lhc. *Part. Accel.*, 55:183–191, 1996.

[169] G Volpini, F Alessandria, G Bellomo, F Broggi, A Paccalini, D Pedrini, A Leone, M Quadrio, L Somaschini, M Sorbi, et al. Nbti superferric corrector magnets for the lhc luminosity upgrade. *IEEE Transactions on Applied Superconductivity*, 25(3):1–5, 2014.

[170] Alexander Wu Chao, Karl Hubert Mess, et al. *Handbook of accelerator physics and engineering.* World scientific, 2013.

[171] Kimberley Lementino. Quadrupole strong focusing for space-charge dominated electron beams in traveling-wave tubes. 2015.

[172] Paul Leroy, Christophe Coillot, Alain F Roux, and Gérard M Chanteur. High magnetic field amplification for improving the sensitivity of hall sensors. *IEEE Sensors Journal*, 6(3):707–713, 2006.

[173] First 4 Magnets. Techcentre: How is the strength of a magnet measured.

[174] Neil Marks. Conventional magnets for accelerators. In *CERN Accelerator School*, 2006.

[175] FH Harlow. A machine calculation method for hydrodynamic problems, technical report lams-1956. 1955.

[176] Charles K Birdsall. Particle-in-cell charged-particle simulations, plus monte carlo collisions with neutral atoms, pic-mcc. *IEEE Transactions on plasma science*, 19(2):65–85, 1991.

[177] Charles K Birdsall and A Bruce Langdon. *Plasma physics via computer simulation.* CRC press, 2004.

[178] Rudolf Hrach. *Počítačová fyzika.* Univerzita JE Purkyně, 2003.

[179] Gianpiero Colonna and Antonio D'Angola. *Plasma Modeling; Methods and Applications.* 2016.

[180] Nicholas A Krall and Alvin W Trivelpiece. Principles of plasma physics. *American Journal of Physics*, 41(12):1380–1381, 1973.

[181] SA Ledvina, Y-J Ma, and E Kallio. Modeling and simulating flowing plasmas and related phenomena. In *Comparative Aeronomy*, pages 143–189. Springer, 2008.

[182] Francis H Harlow. Numerical methods for fluid dynamics, an annotated bibliography. Technical report, Los Alamos Scientific Lab., N. Mex., 1969.

[183] Bruce Archambeault, Colin Brench, and Omar M Ramahi. The finite-difference time-domain method. In *EMI/EMC Computational Modeling Handbook*, pages 35–70. Springer, 2001.

[184] Vahid Vahedi and Maheswaran Surendra. A monte carlo collision model for the particle-in-cell method: applications to argon and oxygen discharges. *Computer Physics Communications*, 87(1-2):179–198, 1995.

[185] Hong Qin, Shuangxi Zhang, Jianyuan Xiao, Jian Liu, Yajuan Sun, and William M Tang. Why is boris algorithm so good? *Physics of Plasmas*, 20(8):084503, 2013.

[186] Mathias Winkel, Robert Speck, and Daniel Ruprecht. A high-order boris integrator. *Journal of computational physics*, 295:456–474, 2015.

[187] Takayuki Umeda. Multi-step boris rotation schemes for lorentz force equation of charged particles. *Computer Physics Communications*, 237:37–41, 2019.

[188] M Žáková. *Reduction of angular divergence of laser-driven ion beams during their acceleration and transport*. FNSPE Departement of Physics, 2014.

[189] Brendan B Godfrey. Review and recent advances in pic modeling of relativistic beams and plasmas. In *AIP Conference Proceedings*, volume 1777, page 020004. AIP Publishing LLC, 2016.

[190] Kane Yee. Numerical solution of initial boundary value problems involving maxwell's equations in isotropic media. *IEEE Transactions on antennas and propagation*, 14(3):302–307, 1966.

[191] John Villasenor and Oscar Buneman. Rigorous charge conservation for local electromagnetic field solvers. *Computer Physics Communications*, 69(2-3):306–316, 1992.

[192] David Tskhakaya. The particle-in-cell method. In *Computational Many-Particle Physics*, pages 161–189. Springer, 2008.

[193] John P Verboncoeur. Particle simulation of plasmas: review and advances. *Plasma Physics and Controlled Fusion*, 47(5A):A231, 2005.

[194] Leslie Greengard. The numerical solution of the n-body problem. *Computers in physics*, 4(2):142–152, 1990.

[195] Roger W Hockney and James W Eastwood. *Computer simulation using particles*. crc Press, 2021.

[196] Computer cluster: Eclipse.

[197] VSB-Technical University of Ostrava. It4innovations national supercomputing center. https://www.it4i.cz/?lang=en, 2017. online, accessed 27-10-2017.

[198] CESNET. Metacentrum. http://www.metacentrum.cz/, 2012. online, accessed 27-10-2017.

[199] Holger Fehske, Ralf Schneider, and Alexander Weiße. *Computational many-particle physics*, volume 739. Springer, 2007.

[200] D Tskhakaya, K Matyash, R Schneider, and F Taccogna. The particle-in-cell method. *Contributions to Plasma Physics*, 47(8-9):563–594, 2007.

[201] Lev Davidovich Landau. On the vibrations of the electronic plasma. *Zh. Eksp. Teor. Fiz.*, 10:25, 1946.

[202] DD Ryutov. Landau damping: half a century with the great discovery. *Plasma physics and controlled fusion*, 41(3A):A1, 1999.

[203] Hideo Okuda. Nonphysical noises and instabilities in plasma simulation due to a spatial grid. *Journal of Computational Physics*, 10(3):475–486, 1972.

[204] A Bruce Langdon. Effects of the spatial grid in simulation plasmas. *Journal of Computational Physics*, 6(2):247–267, 1970.

[205] BF McMillan. Is it necessary to resolve the debye length in standard or δ f pic codes? *Physics of Plasmas*, 27(5):052106, 2020.

[206] Estelle Cormier-Michel, Bradley Allan Shadwick, Cameron Guy Robinson Geddes, Eric Esarey, Carl B Schroeder, and Wim P Leemans. Unphysical kinetic effects in particle-in-cell modeling of laser wakefield accelerators. *Physical Review E*, 78(1):016404, 2008.

[207] Brendan B Godfrey and Jean-Luc Vay. Numerical stability of relativistic beam multidimensional pic simulations employing the esirkepov algorithm. *Journal of Computational Physics*, 248:33–46, 2013.

[208] Michael D Meyers, C-K Huang, Yong Zeng, SA Yi, and Brian J Albright. On the numerical dispersion of electromagnetic particle-in-cell code: Finite grid instability. *Journal of Computational Physics*, 297:565–583, 2015.

[209] Yuxi Chen, Gábor Tóth, Paul Cassak, Xianzhe Jia, Tamas I Gombosi, James A Slavin, Stefano Markidis, Ivy Bo Peng, Vania K Jordanova, and Michael G Henderson. Global three-dimensional simulation of earth's dayside reconnection using a two-way coupled magnetohydrodynamics with embedded particle-in-cell model: Initial results. *Journal of Geophysical Research: Space Physics*, 122(10):10–318, 2017.

[210] Gábor Tóth, Xianzhe Jia, Stefano Markidis, Ivy Bo Peng, Yuxi Chen, Lars KS Daldorff, Valeriy M Tenishev, Dmitry Borovikov, John D Haiducek, Tamas I Gombosi, et al. Extended magnetohydrodynamics with embedded particle-in-cell simulation of ganymede's magnetosphere. *Journal of Geophysical Research: Space Physics*, 121(2):1273–1293, 2016.

[211] Kirit Makwana, Rony Keppens, and Giovanni Lapenta. Two-way coupled mhd-pic simulations of magnetic reconnection in magnetic island coalescence. In *Journal of Physics: Conference Series*, volume 1031, page 012019. IOP Publishing, 2018.

[212] Allard Jan Van Marle, Alexandre Marcowith, and Fabien Casse. Using a combined pic-mhd code to simulate particle acceleration in astrophysical shocks. *PoS*, page 569, 2017.

[213] L Giuffrida, K Svensson, J Psikal, et al. Manipulation of laser-accelerated proton beam profiles by nanostructured and microstructured targets. *Physical Review Accelerators and Beams*, 20(8):081301, 2017.

[214] D Margarone, O Klimo, IJ Kim, J Prokupek, J Limpouch, TM Jeong, T Mocek, J Pšikal, HT Kim, J Proška, et al. Laser-driven proton acceleration enhancement by nanostructured foils. *Physical review letters*, 109(23):234801, 2012.

[215] Daniele Margarone, I Jong Kim, J Psikal, J Kaufman, T Mocek, Il Woo Choi, L Stolcova, J Proska, A Choukourov, I Melnichuk, et al. Laser-driven high-energy proton beam with homogeneous spatial profile from a nanosphere target. *Physical Review Special Topics-Accelerators and Beams*, 18(7):071304, 2015.

[216] S Kar, K Markey, PT Simpson, C Bellei, JS Green, SR Nagel, S Kneip, DC Carroll, B Dromey, L Willingale, et al. Dynamic control of laser-produced proton beams. *Physical review letters*, 100(10):105004, 2008.

[217] Satyabrata Kar, Hamad Ahmed, Rajendra Prasad, Mirela Cerchez, Stephanie Brauckmann, Bastian Aurand, Giada Cantono, Prokopis Hadjisolomou, Ciaran LS Lewis, Andrea Macchi, et al. Guided post-acceleration of laser-driven ions by a miniature modular structure. *Nature communications*, 7(1):1–7, 2016.

[218] Toma Toncian, Marco Borghesi, Julien Fuchs, Emmanuel d'Humières, Patrizio Antici, Patrick Audebert, Erik Brambrink, Carlo Alberto Cecchetti, Ariane Pipahl, Lorenzo Romagnani, et al. Ultrafast laser-driven microlens to focus and energy-select mega-electron volt protons. *Science*, 312(5772):410–413, 2006.

[219] KD Xiao, CT Zhou, B Qiao, and XT He. Guiding and collimation of laser-accelerated proton beams using thin foils followed with a hollow plasma channel. *Physics of Plasmas*, 22(9):093112, 2015.

[220] DB Zou, HB Zhuo, XH Yang, TP Yu, FQ Shao, and A Pukhov. Control of target-normal-sheath-accelerated protons from a guiding cone. *Physics of plasmas*, 22(6):063103, 2015.

[221] Maksym Tryus, Filip Grepl, Timofej Chagovets, Andriy Velyhan, Lorenzo Giuffrida, Stanislav Stancek, Vasiliki Kantarelou, Valeria Istokskaia, Francesco Schillaci, Martina Zakova, et al. Teresa target area at eli beamlines. *Quantum Beam Science*, 4(4):37, 2020.

[222] NP Dover, M Nishiuchi, H Sakaki, Ko Kondo, MA Alkhimova, A Ya Faenov, M Hata, N Iwata, H Kiriyama, JK Koga, et al. Effect of small focus on electron heating and proton acceleration in ultrarelativistic laser-solid interactions. *Physical Review Letters*, 124(8):084802, 2020.

[223] Frank Detering, W Rozmus, A Brantov, V Yu Bychenkov, CE Capjack, and R Sydora. Particle-in-cell simulations of heat flux driven ion acoustic instability. *Physics of plasmas*, 12(1):012321, 2005.

[224] Ondrej Klimo, VT Tikhonchuk, and A Debayle. High-current fast electron beam propagation in a dielectric target. *Physical Review E*, 75(1):016403, 2007.

[225] M Manclossi, JJ Santos, D Batani, Jérôme Faure, A Debayle, VT Tikhonchuk, and Victor Malka. Study of ultraintense laser-produced fast-electron propagation and filamentation in insulator and metal foil targets by optical emission diagnostics. *Physical review letters*, 96(12):125002, 2006.

[226] J Fuchs, TE Cowan, P Audebert, H Ruhl, L Gremillet, A Kemp, M Allen, A Blazevic, J-C Gauthier, M Geissel, et al. Spatial uniformity of laser-accelerated ultrahigh-current mev electron propagation in metals and insulators. *Physical review letters*, 91(25):255002, 2003.

[227] MN Quinn, DC Carroll, XH Yuan, M Borghesi, RJ Clarke, RG Evans, J Fuchs, P Gallegos, L Lancia, K Quinn, et al. On the investigation of fast electron beam filamentation in laser-irradiated solid targets using multi-mev proton emission. *Plasma Physics and Controlled Fusion*, 53(12):124012, 2011.

[228] Marius Schollmeier, M Roth, A Blazevic, E Brambrink, JA Cobble, JC Fernandez, KA Flippo, DC Gautier, D Habs, K Harres, et al. Laser ion acceleration with micro-grooved targets. *Nuclear Instruments and Methods in Physics Research Section A: Accelerators, Spectrometers, Detectors and Associated Equipment*, 577(1-2):186–190, 2007.

[229] M Afshari, J Hornung, A Kleinschmidt, P Neumayer, D Bertini, and V Bagnoud. Proton acceleration via the tnsa mechanism using a smoothed laser focus. *AIP Advances*, 10(3):035023, 2020.

[230] DC Carroll, P McKenna, Olle Lundh, Filip Lindau, C-G Wahlström, S Bandyopadhyay, D Pepler, D Neely, S Kar, PT Simpson, et al. Active manipulation of the spatial energy distribution of laser-accelerated proton beams. *Physical Review E*, 76(6):065401, 2007.

[231] F Schillaci, GAP Cirrone, G Cuttone, M Maggiore, L Andó, A Amato, M Costa, G Gallo, G Korn, G Larosa, et al. Design of the elimaia ion collection system. *Journal of Instrumentation*, 10(12):T12001, 2015.

[232] Bruno Gonzalez-Izquierdo, Martin King, Ross J Gray, Robbie Wilson, Rachel J Dance, Haydn Powell, David A Maclellan, John McCreadie, Nicholas MH Butler, Steve Hawkes, et al. Towards optical polarization control of laser-driven proton acceleration in foils undergoing relativistic transparency. *Nature communications*, 7(1):1–10, 2016.

[233] Z Gong, APL Robinson, XQ Yan, and AV Arefiev. Highly collimated electron acceleration by longitudinal laser fields in a hollow-core target. *Plasma Physics and Controlled Fusion*, 61(3):035012, 2019.

[234] DASSAULT SYSTEMES. 3d simulia, opera - electromagnetic and electromechanical simulation sw.

[235] NU Crooker, SW Kahler, DE Larson, and RP Lin. Large-scale magnetic field inversions at sector boundaries. *Journal of Geophysical Research: Space Physics*, 109(A3), 2004.

[236] Yohei Yamauchi, Steven T Suess, John T Steinberg, and Takashi Sakurai. Differential velocity between solar wind protons and alpha particles in pressure balance structures. *Journal of Geophysical Research: Space Physics*, 109(A3), 2004.

[237] SD Bale, ST Badman, JW Bonnell, TA Bowen, D Burgess, AW Case, CA Cattell, BDG Chandran, CC Chaston, CHK Chen, et al. Highly structured slow solar wind emerging from an equatorial coronal hole. *Nature*, 576(7786):237–242, 2019.

[238] Viviane Pierrard, Milan Maksimovic, and Joseph Lemaire. Core, halo and strahl electrons in the solar wind. *Astrophysics and Space Science*, 277(1):195–200, 2001.

[239] WC Feldman, JR Asbridge, SJ Bame, JT Gosling, and DS Lemons. Electron heating within interaction zones of simple high-speed solar wind streams. *Journal of Geophysical Research: Space Physics*, 83(A11):5297–5303, 1978.

[240] LF Burlaga, RP Lepping, KW Behannon, LW Klein, and FM Neubauer. Large-scale variations of the interplanetary magnetic field: Voyager 1 and 2 observations between 1–5 au. *Journal of Geophysical Research: Space Physics*, 87(A6):4345–4353, 1982.

[241] Allan R Macneil, Mathew J Owens, Robert T Wicks, Mike Lockwood, Sarah N Bentley, and Matthew Lang. The evolution of inverted magnetic fields through the inner heliosphere. *Monthly Notices of the Royal Astronomical Society*, 494(3):3642–3655, 2020.

[242] Stephan Russenschuck. Roxie: Routine for the optimization of magnet x-sections, inverse field calculation and coil end design. proceedings. 1999.

[243] LL Ji, BF Shen, XM Zhang, FC Wang, ZY Jin, CQ Xia, M Wen, WP Wang, JC Xu, MY Yu, et al. Generating quasi-single-cycle relativistic laser pulses by laser-foil interaction. *Physical review letters*, 103(21):215005, 2009.

[244] Thomas Brabec and Ferenc Krausz. Intense few-cycle laser fields: Frontiers of nonlinear optics. *Reviews of Modern Physics*, 72(2):545, 2000.

[245] Robert E Collin. *Field theory of guided waves*, volume 5. John Wiley & Sons, 1990.

[246] George V Eleftheriades, Abbas S Omar, Linda PB Katehi, and Gabriel M Rebeiz. Some important properties of waveguide junction generalized scattering matrices in the context of the mode matching technique. *IEEE Transactions on Microwave Theory and Techniques*, 42(10):1896–1903, 1994.

[247] Oleg Mitrofanov and James A Harrington. Dielectric-lined cylindrical metallic thz waveguides: mode structure and dispersion. *Optics express*, 18(3):1898–1903, 2010.

[248] Site Zhang. Virtuallab fusion: A physical optics simulation platform. In *SPIE Exhibition Product Demonstrations*, page OP20EX0G. International Society for Optics and Photonics, 2020.

[249] Bruno Gonzalez-Izquierdo, Ross J Gray, Martin King, Rachel J Dance, Robbie Wilson, John McCreadie, Nicholas MH Butler, Remi Capdessus, Steve Hawkes, James S Green, et al. Optically controlled dense current structures driven by relativistic plasma aperture-induced diffraction. *Nature Physics*, 12(5):505–512, 2016.

[250] T Ceccotti, V Floquet, Andrea Sgattoni, A Bigongiari, O Klimo, M Raynaud, C Riconda, A Heron, F Baffigi, L Labate, et al. Evidence of resonant surface-wave excitation in the relativistic regime through measurements of proton acceleration from grating targets. *Physical review letters*, 111(18):185001, 2013.

[251] S Vallières, M Salvadori, A Permogorov, G Cantono, K Svendsen, Z Chen, S Sun, F Cbonsoli, E dâ€™Humières, C-G Wahlström, et al. Enhanced laser-driven proton acceleration using nanowire targets. *Scientific Reports*, 11(1):1–11, 2021.

[252] Dimitri Khaghani, Mathieu Lobet, Björn Borm, Loïc Burr, Felix Gärtner, Laurent Gremillet, Liana Movsesyan, Olga Rosmej, Maria Eugenia Toimil-Molares, Florian Wagner, et al. Enhancing laser-driven proton acceleration by using micro-pillar arrays at high drive energy. *Scientific reports*, 7(1):1–9, 2017.

[253] M Bailly-Grandvaux, D Kawahito, C McGuffey, J Strehlow, B Edghill, MS Wei, N Alexander, A Haid, C Brabetz, V Bagnoud, et al. Ion acceleration from microstructured targets irradiated by high-intensity picosecond laser pulses. *Physical Review E*, 102(2):021201, 2020.

[254] Jin-Lu Liu, Min Chen, Jun Zheng, Zheng-Ming Sheng, and Chuan-Sheng Liu. Three dimensional effects on proton acceleration by intense laser solid target interaction. *Physics of Plasmas*, 20(6):063107, 2013.

[255] E d'Humières, A Brantov, V Yu. Bychenkov, and VT Tikhonchuk. Optimization of laser-target interaction for proton acceleration. *Physics of Plasmas*, 20(2):023103, 2013.

[256] David James Stark, Lin Yin, Brian James Albright, and Fan Guo. Effects of dimensionality on kinetic simulations of laser-ion acceleration in the transparency regime. *Physics of Plasmas*, 24(5):053103, 2017.

[257] F Ziaie, H Afarideh, SM Hadji-Saeid, and SA Durrani. Investigation of beam uniformity in industrial electron accelerator. *Radiation measurements*, 34(1-6):609–613, 2001.

[258] HA Davis, BP Wood, CP Munson, LJ Bitteker, MA Nastasi, DJ Rej, WJ Waganaar, KC Walter, DM Coates, and HM Schleinitz. Ion beam and plasma technology development for surface modification at los alamos national laboratory. *Materials chemistry and physics*, 54(1-3):213–218, 1998.

[259] WJ Zhao, Gennady Efimovich Remnev, S Yan, MS Opekounov, XY Le, VM Matvienko, BX Han, JM Xue, and YG Wang. Intense pulsed ion beam sources for industrial applications. *Review of Scientific Instruments*, 71(2):1045–1048, 2000.

[260] W Xiang, WJ Zhao, S Yan, and BQ Zeng. Simulations of intense pulsed ion beam uniformity in a planar magnetically insulated ion diode. *Review of scientific instruments*, 73(2):857–859, 2002.

[261] Huan Wang, Lihua Cao, and Xian Tu He. Collimated proton beams by ultra-short, ultra-intense laser pulse interaction with a foil-ramparts target. *Laser and Particle Beams*, 33(4):765, 2015.

[262] J Psikal and M Matys. Dominance of hole-boring radiation pressure acceleration regime with thin ribbon of ionized solid hydrogen. *Plasma Physics and Controlled Fusion*, 60(4):044003, 2018.

[263] DW Forslund, JM Kindel, WB Mori, C Joshi, and JM Dawson. Two-dimensional simulations of single-frequency and beat-wave laser-plasma heating. *Physical review letters*, 54(6):558, 1985.

[264] GA Askar'Yan, SV Bulanov, Francesco Pegoraro, and AM Pukhov. Magnetic interaction of self-focusing channels and fluxes of electromagnetic radiation: their coalescence, the accumulation of energy, and the effect of external magnetic fields on them. *JETP Letters*, 60(4):251–257, 1994.

[265] M Roth, A Blazevic, Matthias Geissel, Theodor Schlegel, TE Cowan, M Allen, J-C Gauthier, Patrick Audebert, J Fuchs, J Meyer-ter Vehn, et al. Energetic ions generated by laser pulses: A detailed study on target properties. *Physical Review Special Topics-Accelerators and Beams*, 5(6):061301, 2002.

[266] AA Andreev, R Sonobe, S Kawata, S Miyazaki, K Sakai, K Miyauchi, T Kikuchi, K Platonov, and K Nemoto. Effect of a laser prepulse on fast ion generation in the interaction of ultra-short intense laser pulses with a limited-mass foil target. *Plasma physics and controlled fusion*, 48(11):1605, 2006.

[267] HJ Lee, KH Pae, H Suk, and SJ Hahn. Enhancement of high-energy ion generation by preplasmas in the interaction of an intense laser pulse with overdense plasmas. *Physics of Plasmas*, 11(4):1726–1729, 2004.

[268] A Yu Krukovskiy, VG Novikov, and IP Tsygvintsev. 3d simulation of the impact made by a noncentral laser pulse on a spherical tin target. *Mathematical Models and Computer Simulations*, 9(1):48–59, 2017.

[269] R Benattar, P Ney, A Nikitin, SV Zakharov, AA Otochin, AN Starostin, AE Stepanov, VK Roerich, AF Nikiforov, VG Novikov, et al. Implosion dynamics of a radiative composite z-pinch. *IEEE transactions on plasma science*, 26(4):1210–1223, 1998.

[270] A Iacob, AF Nikiforov, VG Novikov, and VB Uvarov. Quantum-statistical models of hot dense matter, methods for computation opacity and equation of state. *Progress in Mathematical Physics (Birkheauser Verlag, 2006)*, 2006.

[271] Dmitrii Aleksandrovich Krestovskikh, Konstantin Anatol'evich Ivanov, Ivan Nikolaevich Tsymbalov, Sergei Anatol'evich Shulyapov, Vladimir Valentinovich Bukin, Roman Valentinovich Volkov, Aleksandr Aleksandrovich Rupasov, and Andrei Borisovich Savelâ€™ev. Postionisation of a spatially nonuniform plasma plume under high-intensity femtosecond laser irradiation. *Quantum Electronics*, 47(1):42, 2017.

[272] J Fuchs, CA Cecchetti, M Borghesi, T Grismayer, E dâ€™Humières, P Antici, S Atzeni, P Mora, A Pipahl, L Romagnani, et al. Laser-foil acceleration of high-energy protons in small-scale plasma gradients. *Physical Review Letters*, 99(1):015002, 2007.

[273] Ju Tae Seo, Seung Hoon Yoo, and Sang June Hahn. Effects of underdense preplasma on the energetic proton generation in ultraintense short laser pulse interaction with an overdense plasma slab. *Journal of the Physical Society of Japan*, 76(11):114501–114501, 2007.

[274] J Psikal, VT Tikhonchuk, J Limpouch, AA Andreev, and AV Brantov. Ion acceleration by femtosecond laser pulses in small multispecies targets. *Physics of Plasmas*, 15(5):053102, 2008.

[275] Rajeev Pattathil. Clf gemini.

[276] Vega pw laser system - technical features.

[277] Ivo Utke, Stanislav Moshkalev, and Phillip Russell. *Nanofabrication using focused ion and electron beams: principles and applications*. Oxford University Press, 2012.

[278] Markku Tilli, Mervi Paulasto-Kröckel, Matthias Petzold, Horst Theuss, Teruaki Motooka, and Veikko Lindroos. *Handbook of silicon based MEMS materials and technologies*. Elsevier, 2020.

[279] Chih Jen Lo, Thomas Aref, and Alexey Bezryadin. Fabrication of symmetric sub-5 nm nanopores using focused ion and electron beams. *Nanotechnology*, 17(13):3264, 2006.

[280] J Psikal, J Grym, L Stolcova, and J Proska. Hollow target for efficient generation of fast ions by ultrashort laser pulses. *Physics of Plasmas*, 23(12):123121, 2016.

[281] L Giuffrida, K Svensson, J Psikal, D Margarone, P Lutoslawski, V Scuderi, G Milluzzo, J Kaufman, T Wiste, M Dalui, et al. Nano and micro structured targets to modulate the spatial profile of laser driven proton beams. *Journal of Instrumentation*, 12(03):C03040, 2017.

[282] Lorenzo Valdevit and Jens Bauer. Fabrication of 3d micro-/nanoarchitected materials. *Three-Dimensional Microfabrication Using Two-Photon Polymerization*, pages 541–576, 2020.

[283] TP Bernat, JH Campbell, N Petta, I Sakellari, S Koo, J-H Yoo, and C Grigoropoulos. Fabrication of micron-scale cylindrical tubes by two-photon polymerization. *Fusion Science and Technology*, 70(2):310–315, 2016.

[284] J Meyer-ter Vehn. Fast ignition of icf targets: an overview. *Plasma physics and controlled fusion*, 43(12A):A113, 2001.

[285] D Habs, T Tajima, J Schreiber, CPJ Barty, M Fujiwara, and PG Thirolf. Vision of nuclear physics with photo-nuclear reactions by laser-driven γ beams. *The European Physical Journal D*, 55(2):279–285, 2009.

[286] F Negoita, M Roth, Peter G Thirolf, S Tudisco, F Hannachi, S Moustaizis, I Pomerantz, P McKenna, J Fuchs, K Sphor, et al. Laser driven nuclear physics at eli–np. *Romanian Reports in Physics*, 68(Supple):S37–S144, 2016.

[287] D Margarone, Antonino Picciotto, A Velyhan, J Krasa, M Kucharik, A Mangione, A Szydlowsky, A Malinowska, Giuseppe Bertuccio, Yongbiao Shi, et al. Advanced scheme for high-yield laser driven nuclear reactions. *Plasma Physics and Controlled Fusion*, 57(1):014030, 2014.

[288] Sophie Le Caër. Water radiolysis: influence of oxide surfaces on h2 production under ionizing radiation. *Water*, 3(1):235–253, 2011.

[289] Marianna Barberio, S Veltri, M Scisciò, and P Antici. Laser-accelerated proton beams as diagnostics for cultural heritage. *Scientific Reports*, 7(1):1–8, 2017.

[290] MS Rihawy, EH Bakraji, S Aref, and R Shaban. Elemental investigation of syrian medicinal plants using pixe analysis. *Nuclear Instruments and Methods in Physics Research Section B: Beam Interactions with Materials and Atoms*, 268(17-18):2790–2793, 2010.

[291] W Maenhaut and K Akilimali. Study of the atmospheric aerosol composition in equatorial africa using pixe as analytical technique. *Nuclear Instruments and Methods in Physics Research Section B: Beam Interactions with Materials and Atoms*, 22(1-3):254–258, 1987.

[292] Thomas A Cahill. Analysis of air pollutants by pixe: The second decade. *Nuclear Instruments and Methods in Physics Research Section B: Beam Interactions with Materials and Atoms*, 49(1-4):345–350, 1990.

[293] KWD Ledingham, W Galster, and R Sauerbrey. Laser-driven proton oncologyâ€"a unique new cancer therapy? *The British journal of radiology*, 80(959):855–858, 2007.

[294] KWD Ledingham, PR Bolton, N Shikazono, and C-M C Ma. Towards laser driven hadron cancer radiotherapy: A review of progress. *Applied Sciences*, 4(3):402–443, 2014.

[295] Giuseppe AP Cirrone, Giacomo Cuttone, Luigi Raffaele, Vincenzo Salamone, Teresio Avitabile, Giuseppe Privitera, Corrado Spatola, Antonio G Amico, Giuseppina Larosa, Renata Leanza, et al. Clinical and research activities at the catana facility of infn-lns: from the conventional hadrontherapy to the laser-driven approach. *Frontiers in oncology*, 7:223, 2017.

[296] Ute Linz and Jose Alonso. Laser-driven ion accelerators for tumor therapy revisited. *Physical Review Accelerators and Beams*, 19(12):124802, 2016.

[297] GAP Cirrone, L Manti, D Margarone, G Petringa, L Giuffrida, A Minopoli, A Picciotto, G Russo, F Cammarata, P Pisciotta, et al. First experimental proof of proton boron capture therapy (pbct) to enhance protontherapy effectiveness. *Scientific reports*, 8(1):1–15, 2018.

[298] G Milluzzo, J Pipek, AG Amico, GAP Cirrone, G Cuttone, G Korn, G Larosa, R Leanza, D Margarone, G Petringa, et al. Geant4 simulation of the elimed transport and dosimetry beam line for high-energy laser-driven ion beam multidisciplinary applications. *Nuclear Instruments and Methods in Physics Research Section A: Accelerators, Spectrometers, Detectors and Associated Equipment*, 909:298–302, 2018.

[299] Antonio Giulietti. *Laser-driven particle acceleration towards radiobiology and medicine*. Springer, 2016.

[300] D Doria, KF Kakolee, S Kar, SK Litt, F Fiorini, H Ahmed, S Green, JCG Jeynes, J Kavanagh, D Kirby, et al. Biological effectiveness on live cells of laser driven protons at dose rates exceeding 109 gy/s. *AIP Advances*, 2(1):011209, 2012.

[301] V Ullmann. Fyzika a nukleární medicína - braggův pík. http://astronuklfyzika.cz/JadRadFyzika6.htm, 2013. online, accessed 12-12-2014.

[302] GAP Cirrone. Hadrontherapy in the ocular melanoma tumor treatment: Experience from the first italian protontherapy center. http://pablocirrone.wikispaces.com/file/view/Medicine-Talks+on+Hadrontherapy-Scientific+English_2.pdf, 2012. online, accessed 19-03-2015.

[303] F Schillaci, M Maggiore, L Andó, GAP Cirrone, G Cuttone, F Romano, V Scuderi, L Allegra, A Amato, G Gallo, et al. Design of a large acceptance, high efficiency energy selection system for the elimaia beam-line. *Journal of Instrumentation*, 11(08):P08022, 2016.

[304] Chang-Ming Charlie Ma, Richard L Maughan, and Colin G Orton. Within the next decade conventional cyclotrons for proton radiotherapy will become obsolete and replaced by far less expensive machines using compact laser systems for the acceleration of the protons. *Medical physics*, 33(3):571–573, 2006.

[305] Particle therapy co-operative group - a non-profit organisation for those interested in proton, light ion and heavy charged particle radiotherapy. http://www.ptcog.ch/, 2013. online, accessed 08-12-2014.

[306] Florian Kroll, Florian-Emanuel Brack, Elisabeth Bodenstein, Kerstin Brüchner, Leonhard Karsch, Stephan D Kraft, Elisabeth Lessmann, Sebastian Meister, Josefine Metzkes-Ng, Alexej Nossula, et al. First systematic in vivo tumor irradiation in mice with laser-accelerated and dose-homogenized proton beams from the draco pw laser. In *Laser Acceleration of Electrons, Protons, and Ions VI*, volume 11779, page 117790I. International Society for Optics and Photonics, 2021.

[307] Ulrich Schramm. High dose-rate in-vivo proton irradiation at draco-pw pilot study results and prerequisites. In *Applying Laser-driven Particle Acceleration II, Medical and Nonmedical Uses of Distinctive Energetic Particle and Photon Sources: SPIE Optics+ Optoelectronics Industry Event*, volume 11790, page 117900C. International Society for Optics and Photonics, 2021.

[308] Vincent Favaudon, Laura Caplier, Virginie Monceau, Frédéric Pouzoulet, Mano Sayarath, Charles Fouillade, Marie-France Poupon, Isabel Brito, Philippe Hupé, Jean Bourhis, et al. Ultrahigh dose-rate flash irradiation increases the differential response between normal and tumor tissue in mice. *Science translational medicine*, 6(245):245ra93–245ra93, 2014.

[309] Hilbert C Christensen, G Nilsson, K-Å Thuomas, and T Reitberger. Proton pulse radiolysis. *Chemical Physics Letters*, 22(3):533–536, 1973.

[310] Thomas E Schmid, Günther Dollinger, Volker Hable, Christoph Greubel, Olga Zlobinskaya, Dörte Michalski, Michael Molls, and Barbara Röper. Relative biological effectiveness of pulsed and continuous 20 mev protons for micronucleus induction in 3d human reconstructed skin tissue. *Radiotherapy and Oncology*, 95(1):66–72, 2010.

[311] Aubert Maquille, Jean-Louis Habib Jiwan, and Bernard Tilquin. Radiosterilization of drugs in aqueous solutions may be achieved by the use of radioprotective excipients. *International journal of pharmaceutics*, 349(1-2):74–82, 2008.

[312] Zhaobing Guo, Dengyong Tang, Xiaguo Liu, and Zheng Zheng. Gamma irradiation-induced cd2+ and pb2+ removal from different kinds of water. *Radiation Physics and chemistry*, 77(9):1021–1026, 2008.

[313] Tsuyoshi Katayama, Makoto Nakauma, Setsuko Todoriki, Glyn O Phillips, and Mikiro Tada. Radiation-induced polymerization of gum arabic (acacia senegal) in aqueous solution. *Food hydrocolloids*, 20(7):983–989, 2006.

[314] P Bouniol and Erling Bjergbakke. A comprehensive model to describe radiolytic processes in cement medium. *Journal of Nuclear Materials*, 372(1):1–15, 2008.

[315] Shuzo Uehara and Hooshang Nikjoo. Monte carlo simulation of water radiolysis for low-energy charged particles. *Journal of radiation research*, 47(1):69–81, 2006.

[316] Thomas B Johansson, Roland Akselsson, and Sven AE Johansson. X-ray analysis: Elemental trace analysis at the 10- 12 g level. *Nuclear Instruments and Methods*, 84(1):141–143, 1970.

[317] Sven AE Johansson and John L Campbell. Pixe: A novel technique for elemental analysis. 1988.

[318] Th Calligaro. Pixe in the study of archaeological and historical glass. *X-Ray Spectrometry: An International Journal*, 37(2):169–177, 2008.

[319] AE Pillay. Analysis of archaeological artefacts: Pixe, xrf or icp-ms? *Journal of Radioanalytical and Nuclear Chemistry*, 247(3):593–595, 2001.

[320] O Valković, M Jakšić, S Fazinić, V Valković, G Moschini, and E Menapace. Quality control of pixe and pige nuclear analytical techniques in geological and environmental applications. *Nuclear Instruments and Methods in Physics Research Section B: Beam Interactions with Materials and Atoms*, 99(1-4):372–375, 1995.

[321] Stephen Juma Mulware. Comparative trace elemental analysis in cancerous and non-cancerous human tissues using pixe. *Journal of biophysics*, 2013, 2013.

[322] ML Carvalho, T Magalhães, M Becker, and A Von Bohlen. Trace elements in human cancerous and healthy tissues: A comparative study by edxrf, txrf, synchrotron radiation and pixe. *Spectrochimica Acta Part B: Atomic Spectroscopy*, 62(9):1004–1011, 2007.

[323] AK Wójcik, B Wąs, M Szałkowski, and JW Mietelski. Proton activation analysis using aic-144 cyclotron as a tool for trace element analysis. *DEPARTMENT OF ANALYTICAL CHEMISTRY, CHEMICAL FACULTY, GDANSK UNIVERSITY OF TECHNOLOGY SEPTEMBER 19-23, 2010 GDAŃSK, POLAND*, page 230, 2010.

[324] F Rizzo, GP Cirrone, G Cuttone, A Esposito, S Garraffo, G Pappalardo, L Pappalardo, FP Romano, and S Russo. Non-destructive determination of the silver content in roman coins (nummi), dated to 308–311 ad, by the combined use of pixe-alpha, xrf and dpaa techniques. *Microchemical Journal*, 97(2):286–290, 2011.

[325] G Pappalardo, A Esposito, GA Cirrone, G Cuttone, S Garraffo, L Pappalardo, F Rizzo, FP Romano, and S Russo. Effects of the behaviour of the proton-induced isotopes production on the analysis of ancient alloys. *Nuclear Instruments and Methods in Physics Research Section B: Beam Interactions with Materials and Atoms*, 266(10):2286–2291, 2008.

List of author's publications & granted projects

Granted projects:
Computational projects:

1. *Project title:* Effects of advanced target designs on laser-accelerated ion beams parameters
   Principal investigator: Ing. Martina Greplová Žáková
   Provider: IT4Innovations National Supercomputing Center
   Computational core hours: 308.000
   Project ID: OPEN-19-21

2. *Project title:* Multidimensional simulations of advanced target designs with the aim of improving parameters of laser-accelerated particle beams
   Principal investigator: Ing. Martina Greplová Žáková
   Provider: IT4Innovations National Supercomputing Center
   Computational core hours: 567.000
   Project ID: OPEN-10-9

Experimental projects:

1. *Project title:* Non-destructive methods of monument testing
   Principal investigator: Ing. Martina Greplová Žáková
   Operational programme: OP Prague – Growth Pole of the Czech Republic
   Provider: City of Prague
   Priority axis: 07.1 Strengthening research, technological development and innovation
   Project ID: CZ.07.1.02/0.0/0.0/17_049/0000831
   Time period: 1.3.2019 – 30.6.2022
   Total costs: 19.712.777 CZK
   EU co-financing rate: 50%
   Cooperation with physical or historical/archaeological science institutes:

   - Czech National Gallery
   - Institute of Archaeology of the CAS
   - The city of Prague Museum
   - Istituto Nazionale di Fisica Nucleare - Laboratori Nazionali del Sud (INFN LNS)
   - private subjects

Publications related to the scope of this thesis:
First author:

1. Zakova, M. G., Psikal, J., Schillaci, F., & Margarone, D. (2021). Improving laser-accelerated proton beam divergence by electric and magnetic fields induced in flat channel-like targets. Plasma Physics and Controlled Fusion, 63(8), 085005.

Co-author:

1. Cirrone, G. A., Petringa, G., Catalano, R., Schillaci, F., Allegra, L., Amato, A., ... & Margarone, D. (2020). ELIMED-ELIMAIA: The First Open User Irradiation Beamline for Laser-Plasma-Accelerated Ion Beams. Frontiers in Physics, 8, 564907.

2. Margarone, D., Cirrone, G. A., Cuttone, G., Amico, A., Ando, L., Borghesi, M., ... & Korn, G. (2018). ELIMAIA: A laser-driven ion accelerator for multidisciplinary applications. Quantum Beam Science, 2(2), 8.

In the review process:

1. D. Margarone, D.,Ahmed, H., Chatain, D., Martin, P., Grepl, F., Greplova Zakova, M., Doria, D., ... & Borghesi, M. (2021). Enhanced Proton Acceleration by Efficient Hole-Boring Radiation-Pressure in Cryogenic Hydrogen. Physical Review Letters

Proceedings:

1. Psikal, J., Horny, V., Zakova, M., & Matys, M. (2019, April). Comparison of ion acceleration from nonexpanded and expanded thin foils irradiated by ultrashort petawatt laser pulse. In Laser Acceleration of Electrons, Protons, and Ions V (Vol. 11037, p. 1103708). International Society for Optics and Photonics.

2. Zakova, M.; Psikal, J.; Margarone, D.; Korn, G., Decreasing divergence and enhancing particle number of laser-driven ion beams by various target designs and laser parameters, 43rd EPS Conference on Plasma Physics, European Physical Society, 2016

3. Zakova, M., Psikal, J., Margarone, D., Maggiore, M., & Korn, G. (2015, May). Reduction of angular divergence of laser-driven ion beams during their acceleration and transport. In Research Using Extreme Light: Entering New Frontiers with Petawatt-Class Lasers II (Vol. 9515, p. 95151F). International Society for Optics and Photonics.

Others:
Co-author:

1. Tryus, M., Grepl, F., Chagovets, T., Velyhan, A., Giuffrida, L., Stancek, S., ... & Margarone, D. (2020). TERESA Target Area at ELI Beamlines. Quantum Beam Science, 4(4), 37.

2. Bechet, S., Versaci, R., Rollet, S., Olsovcova, V., Fajstavr, A., Zakova, M., & Margarone, D. (2016). Radiation protection of a proton beamline at ELI-Beamlines. Journal of Instrumentation, 11(12), C12019.